

Fabrication of CuInSe₂ and Cu(In,Ga)Se₂ Absorber Layers by Pulse- and Pulse-reverse Electrochemical Techniques for Solar Photovoltaic Applications

Sreekanth Mandati

A Dissertation Submitted to
Indian Institute of Technology Hyderabad
In Partial Fulfillment of the Requirements for
The Degree of Doctor of Philosophy



भारतीय प्रौद्योगिकी संस्थान हैदराबाद
Indian Institute of Technology Hyderabad

Department of Materials Science and Metallurgical Engineering

March, 2015

Declaration

I declare that this written submission represents my ideas in my own words, and where others' ideas or words have been included, I have adequately cited and referenced the original sources. I also declare that I have adhered to all principles of academic honesty and integrity and have not misrepresented or fabricated or falsified any idea/data/fact/source in my submission. I understand that any violation of the above will be a cause for disciplinary action by the Institute and can also evoke penal action from the sources that have thus not been properly cited, or from whom proper permission has not been taken when needed.

Sreekanth Mandati

MS11P1003

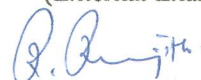
Approval Sheet

This thesis entitled “Fabrication of CuInSe₂ and Cu(In,Ga)Se₂ Absorber Layers by Pulse- and Pulse-reverse Electrochemical Techniques for Solar Photovoltaic Applications” by Sreekanth Mandati is approved for the degree of Doctor of Philosophy from IIT Hyderabad.



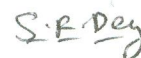
Prof. Juzer Vasi

Department of Electrical Engineering,
Indian Institute of Technology, Bombay
(External Examiner)



Dr. Ranjith Ramadurai

Department of Materials Science and Metallurgical Engineering,
Indian Institute of Technology, Hyderabad
(Internal Examiner)



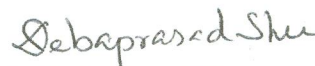
Dr. Suhash Ranjan Dey

Department of Materials Science and Metallurgical Engineering,
Indian Institute of Technology, Hyderabad
(Adviser)



Dr. B. V. Sarada

Centre for Solar Energy Materials,
International Advanced Research Centre for Powder Metallurgy and New Materials (ARCI),
Hyderabad.
(Co-Adviser)



Dr. Debaprasad Shee

Department of Chemical Engineering,
Indian Institute of Technology, Hyderabad
(Chairman)

Acknowledgements

At the outset, I would like to express my sincere gratitude to Dr. G. Sundararajan, Director, Dr. S. V. Joshi, Additional Director, and Dr. G. Padmanabham, Associate Director, ARCI, for providing me an opportunity to work as a senior research fellow at ARCI and for granting me the permission to register for Ph. D. externally at IIT Hyderabad. I sincerely thank Prof. U. B. Desai, Director, IITH, for permitting me to register for Ph. D.

I am greatly indebted to my mentors Dr. B. V. Sarada (CSEM, ARCI) and Dr. Suhash Ranjan Dey (MSME, IITH) for their timely support, valuable guidance and encouragement throughout my doctoral studies. I am privileged to work with Dr. Sarada, who has been guiding me day to day in all the experiments, analyses and discussions. I felt the utmost care and affection from her in and out of the laboratory and the way she supported me even during my tough times is simply exceptional. I am very fortunate to work with Dr. Suhash Ranjan Dey, my internal guide at IITH, who is without doubt an exemplary supervisor. The way he contributed to my thesis work with pertinent suggestions during experiments and analysis of the results is incredible. I am very grateful to him for his personal concern to me during my tough times. I am honored to have Dr. Shrikant V. Joshi, Additional Director, ARCI, as one of my off-screen mentors. I have been fortunate for the last three years to get his time for my research work discussions and doctoral committee meetings. His valuable suggestions and comments contributed significantly to my thesis. He has given a tremendous support and took personal care during the difficult times of Ph. D. I am extremely happy to have worked with above three and I am always obliged to them. I am at loss of words to thank them for their constant support for the last three years.

Partial support under the US-India Partnership to Advance Clean Energy Research (PACE-R) for the Solar Energy Institute for India and the United States (SERIUS), funded jointly by the U. S. Department of Energy (under Subcontract DE-AC36-08GO28308 to the National Renewable Energy Laboratory, Golden, Colorado) and the Government of India, through the Department of Science and Technology (under Subcontract IUSSTF/JCERDC-SERIUS/2012) is gratefully acknowledged.

I would like to thank my doctoral committee (DC) members, Dr. Pinaki Prasad Bhattarjee, Head, MSME, Dr. Ranjith Ramadurai, MSME, Dr. Deepa, Dept. of Chemistry

for their valuable inputs and remarks during DC meetings. I like to thank Dr. SRD, Dr. RR and Dr. Chandra Sekhar Sharma, who taught me during the course work at IITH and it was a nice learning experience from them.

I express my deepest gratitude to Dr. Tata N. Rao, Team leader, Centre for Nanomaterials, ARCI, for his valuable feedbacks and suggestions during the analyses of results and while writing manuscripts. I sincerely thank Dr. G. Ravi Chandra, Team Leader, Centre for Materials Characterization and Testing, for getting the characterizations done and his valuable suggestions related to sample preparation. I would like to thank Mrs. Jyotirmayi, Mr. M. Ramakrishna, Mr. K. Ramesh Reddy, Mr. GVR Reddy and Mr. L. Venkatesh for their great help in the characterization of the samples. I also take this opportunity to thank Dr. S. Sakthivel and Dr. Sanjay Dhage for their help in preparation and characterization of the samples. I thank Mrs. Nirmala and Mrs. Aruna for their valuable support while preparing the samples. I am very thankful to my lab mates Mrs. Ch. L. P. Pavithra, Mrs. Radha and Mr. Venkat who has helped me during experiments.

I would like to thank Mr. R. Prabhakar Rao, CAPO, Mr. R. Vijay Kumar, CFAO and Mr. Srinivas, HRD, ARCI for their administrative and financial supervision during my stay at ARCI. I would like to thank Dr. Dibyendu Chkravathy, ARCI for his personal concern and valuable suggestions. I thank all the scientists and employees who made it a friendly environment to work at ARCI.

I acknowledge the Department of Science and Technology, Govt. of India and the Indo-U. S. Science and Technology Forum, for selecting me for the prestigious Bhaskara Advanced Solar Energy internship award thereby providing an opportunity to work at Prof. Rakesh Agrawal's solar energy research laboratory, Purdue University, USA. I am grateful to Prof. Rakesh Agrawal for his valuable guidance during my BASE internship. I also take this opportunity to thank my lab mates in solar energy research group at Purdue University who have given me a constant support during my BASE internship.

I thank my friend Ms. Alka Pareek who made my stay memorable in Hyderabad. She has been a constant support for me personally and professionally throughout my doctoral studies. I like to thank Ms. Anulekha KH who has also been a part in making my stay fun and frolic. I like to thank my friends Mr. Pramod at ARCI and Mr. Palli Srinivas, Mr. Basanth, and Mr. Bhaskar at IITH for their help in various aspects. I am very fortunate to

have good friends like Deepthi, Srikanth, Subrahmanyam, Parvathala Reddy, Bapanayya, Rajendra and Krishna Mohan for their encouragement and support throughout my life. I am very thankful to my batch mates at ARCI and IITH for their loving support, loyal friendship and pleasant company.

I owe to my parents (Mr. Pulla Reddy and Mrs. Jayamma), my brother (Dr. Vinay Reddy) and my sister (Mrs. Rajeswari Venkat Reddy) who have been a constant source of encouragement and driving force that helped me overcome the rigors of research work.

Dedicated to

Mr. DEPENDABLE, THE WALL
RAHUL SHARAD DRAVID

Abstract

Global energy crisis is one of the major concerns of the humankind due to the limited availability of fossil fuels which accomplish dominant portion of present days' energy. Hence, the need to develop renewable energy resources has come to the forefront of discussion. Solar photovoltaic is one of the major alternatives for future energy harvesting system; however, the utility of this emerging technology depends on the efficiency of the solar cell and viable techniques to commercialize it. Though silicon based photovoltaic technology is the most dominant till date but expensive manufacturing techniques pertaining to it is a major concern. In this context, chalcopyrite Cu(In,Ga)Se_2 (CIGS) thin-film technology has already witnessed high conversion efficiencies due to its suitable bandgap (≈ 1.20 eV) and large optical absorption coefficient ($\approx 10^5 \text{ cm}^{-1}$). The highly efficient CIGS devices are often fabricated using expensive vacuum based technologies; however, efforts to seek an economical and scalable method for the production of stoichiometric CIGS thin-films have been ongoing to realize the commercialization of these devices. In pursuit of this, electrodeposition has been demonstrated to produce CIGS devices with high efficiencies and it is easily amenable for achieving large area films of high quality with efficient material utilization and high deposition rate. The use of multi-steps, complexing agents, organic additives during the deposition using a three-electrode system followed by a conventional selenization step have often been employed to achieve chalcopyrite compact CIGS which make the process more complex and expensive.

In appreciation of the above, the present research proposes a simplified but advanced electrodeposition technique for the fabrication of CIGS thin-films. The technique uses features such as pulse and pulse-reverse plating, avoids the third reference electrode and expensive Pt is substituted by high purity graphite. In addition, it avoids the use of complexing agents and conventional selenization step making it a simple, economic and environmental friendly approach. Pulse electrodeposition of CuInSe_2 (CIS) thin-films is the first investigation of the present study, which is essentially aimed for the basic optimization of the process so as to ease the method for CIGS films. The parameters are appropriately regulated to produce stoichiometric CIS films with a novel flake-like morphology and resulted in an improved photoelectrochemical (PEC) performance. The process is further optimized to produce compact phase pure stoichiometric CIGS thin-films which have exhibited an enhanced PEC performance over the conventional direct current deposited

CIGS films. The growth mechanism of pulse electrodeposited CIGS is explained which is responsible for yielding a compact morphology. In order to attain a better and easier control over the composition and morphology of the CIGS films and to avoid excess use of less abundant In precursor, a novel sequential pulse electrodeposition approach is proposed which has not only resulted in exceptional control over the composition and morphology but also yielded compact single phase CIGS films exhibiting significantly improved PEC performance. Furthermore, the process is systematically improved to fabricate nanostructured CIGS thin-films consisting of nano-flakes, nano-mesh, etc. which are particularly advantageous due to the high surface area and smaller thickness (of flake/rod) thereby leading to improved light absorption and minimized recombination. Nanostructured CIGS films exhibited high photocurrents in PEC performance showing their potential ability to use in photoelectrochemical cells and thin-films solar cells. Ultimately, the suitability of the pulse electrodeposited CIGS films is tested by constructing the CIGS/CdS heterojunction wherein n-type CdS layer is chemical bath deposited onto CIGS. The junction has yielded photocurrent values that are comparable to the short circuit current densities in conventional solid state device and have shown exceptional stability. In conclusion, a simple, economic and environmental friendly pulse electrodeposition technique is proposed to fabricate high quality CIGS thin-films and can be a potentially viable technique for their commercialization. The possible outlook of the study is to construct a full device by depositing window layers, metal fingers, etc. to determine the conversion efficiency of the device.

Nomenclature

Å	Angstrom
a-Si	Amorphous silicon
BSF	Back surface field
C	Capacitance
C_0	Bulk concentration of species
CBD	Chemical bath deposition
CdS	Cadmium sulfide
CdTe	Cadmium telluride
CE	Current efficiency
CIGS	Copper indium gallium (di)selenide
CIGSS	Copper indium gallium sulphide/selenide
CIS	Copper indium (di)selenide
c-Si	Crystalline silicon
Cu-Se or Cu_2Se	Copper selenide
CV	Cyclic voltammetry
D	Diffusion coefficient
DC	Direct current
DSSC	Dye sensitized solar cell
E	Electrode potential
E_0	Standard Electrode potential
EC	Conduction band edge
ED	Electrodeposition
EDTA	Ethylene diamene tetra-acetic acid
EDX or EDS	Energy dispersive X-ray spectroscopy
EF	Fermi energy
E _{FB}	Flat-band potential
E_g	Bandgap
EV	Valence band edge
F	Faraday's constant

FESEM	Field emission scanning electron microscope
FF	Fill factor
FIB	Focused ion beam
G	Generation rate of electron hole pairs
Ga ₂ Se ₃	Gallium selenide
GIXRD	Grazing incidence X-ray diffraction
HER	Hydrogen evolution reaction
HRTEM	High-resolution transmission electron microscope
I _M	Maximum current density (output)
I _m	Peak current
IN	Instantaneous nucleation
In ₂ Se ₃	Indium selenide
ITO	Indium doped tin-oxide
J	Diode current
J ₀	Saturation current density
JCPDS	Joint Committee on Powder Diffraction Standards
J _L	Photocurrent
J _{sc}	Short circuit current density
k _B	Boltzmann's constant
L _e	Electron diffusion length
L _h	Hole diffusion length
MBE	Molecular beam epitaxy
m _e [*]	Electron effective mass
m _h [*]	Hole effective mass
MIS	Metal-insulator-semiconductor
Mo	Molybdenum
MoSe ₂	Molybdenum selenide
MS	Mott-Schottky
ms	milli-second
MSE	Mercurous sulphate electrode
MTOE	Million tons of oil equivalent

n	Diode ideality factor
N	Carrier density
N_a	Acceptor density
NHE	Normal hydrogen electrode
OCP	Open circuit potential
PEC	Photoelectrochemical
PED	Pulse electrodeposition
P_{in}	Incident power
PN	Progressive nucleation
poly-Si	Polycrystalline silicon
PRC	Pulse-reverse current
PRED	Pulse-reverse electrodeposition
q	Charge
R_a	Average roughness
R_s	Series resistance
R_{SH}	Shunt resistance
RTP	Rapid thermal processing
SAED	Selected area electron diffraction
SCE	Saturated calomel electrode
SEM	Scanning electron microscopy
SLG	Soda lime glass
T	Temperature
t	Time
t_a	Anodic pulse time
t_c	Cathodic pulse time
TCO	Transparent conducting oxide
TEM	Transmission electron microscopy
T_m	Time at peak current
t_{off}	Off-time
t_{on}	On-time
TSC	Tri-sodium citrate

UV-Vis-NIR	Ultraviolet-visible-near infra-red
V	Voltage
V_m	Maximum voltage (output)
V_{oc}	Open circuit voltage
W	Width of depletion layer
XRD	X-ray diffraction
XRF	X-ray fluorescence
α	Absorption coefficient
ϵ	Dielectric constant
ϵ_0	Permittivity of free space
η	Efficiency
λ	Wavelength
ν	Frequency

Contents

Declaration.....	ii
Approval Sheet	iii
Acknowledgements.....	iv
Abstract.....	viii
Nomenclature	x
1 Introduction	1
1.1 Energy.....	1
1.2 Solar Energy	2
1.3 Solar Photovoltaics	3
1.4 Solar Cell	4
1.5 Solar Cell Technologies.....	10
1.5.1 First Generation Solar Cells.....	10
1.5.2 Second Generation Solar Cells	11
1.5.3 Third Generation Solar Cells	13
1.5.4 Fourth Generation Solar Cells	13
1.6 CuInSe ₂ (CIS) and Cu(In,Ga)Se ₂ (CIGS)	15
1.7 Design of CIGS Solar Cell: Role of Different Layers	18
1.7.1 Back Contact.....	19
1.7.2 Absorber Layer	20
1.7.3 Buffer Layer.....	20
1.7.4 Front Contact	21
1.7.5 Band Diagram and Other Device Aspects	21
1.8 Synthesis Methods of CIGS Absorber Layer.....	23
1.8.1 Vacuum based Techniques	24
1.8.2 Non-vacuum-based Techniques.....	25
1.9 Electrodeposition	27
1.9.1 Direct Current (DC) Electrodeposition.....	29
1.9.2 Pulse Electrodeposition (PED)	29
1.9.3 Pulse Reverse Electrodeposition (PRED).....	31
1.10 Literature: Electrodeposition of ternary/quarternary Chalcopyrites	32
1.11 Objective of the Present Work.....	44

2 Materials and Methods	46
2.1 Materials	47
2.2 Methods	47
2.2.1 Electrodeposition of CIS/CIGS films	48
2.2.2 Chemical bath deposition of CdS	51
2.3 Characterization techniques	52
2.3.1 Scanning electron microscopy (SEM)	52
2.3.2 X-ray fluorescence spectroscopy (XRF).....	53
2.3.3 X-ray diffraction (XRD).....	54
2.3.4 Raman spectroscopy	55
2.3.5 Transmission electron microscopy (TEM)	56
2.3.6 Focused ion beam (FIB) milling and imaging	57
2.3.7 Cyclic voltammetry (CV)	58
2.3.8 UV-Vis-NIR Absorption spectroscopy.....	59
2.3.9 Mott-Schottky analysis	60
2.3.10 Photoelectrochemical (PEC) characterization	62
3 Pulse electrodeposition of CuInSe₂	64
3.1 Direct current (DC) electrodeposition of CIS thin-films	64
3.2 Pulse electrodeposition (PED) of CIS thin-films.....	67
3.2.1 Compositional analysis	68
3.2.2 Morphological characterization	69
3.2.3 X-ray diffraction of PED CIS films.....	70
3.2.4 Micro-Raman analysis of PED CIS films.....	71
3.2.5 Cross-sectional analysis using FIB	72
3.2.6 Optical studies – Determination of bandgap.....	73
3.2.7 Photoelectrochemical analysis.....	74
3.3 Conclusions.....	76
4 Pulse electrodeposition of Cu(In,Ga)Se₂	77
4.1 Cyclic voltammetry (CV) of Cu-In-Ga-Se system	77
4.1.1 CV of Cu-Se, In-Se, Ga-Se, Cu-In-Se, Cu-Ga-Se and Cu-In-Ga-Se	77
4.1.2 CV of Cu-In-Se and Cu-In-Ga-Se: Multiple sweeps	80
4.2 Pulse electrodeposition of CIGS.....	82
4.2.1 Compositional analysis of CIGS thin-films.....	82
4.2.2 Morphology of CIGS thin-films	84
4.2.3 CIGS thin-films with increased deposition time.....	87

4.2.4	X-ray diffraction studies of DC and PED deposited CIGS thin-films	88
4.2.5	Micro-Raman analysis of DC and PED deposited CIGS thin-films	90
4.2.6	Cross-sectional studies of DC and PED deposited CIGS thin-films	92
4.2.7	Optical absorption studies of DC and PED deposited CIGS thin-films	93
4.2.8	Mott-Schottky studies of DC and PED deposited CIGS thin-films	94
4.2.9	Photoelectrochemical (PEC) analysis of DC and PED deposited CIGS thin-films	95
4.3	Growth mechanism studies	96
4.3.1	Theory of nucleation mechanism during electrodeposition	97
4.3.2	Types of nucleation mechanism	98
4.3.3	I-t curves – DC and PED deposited CIGS films	100
4.3.4	Growth mechanism of DC and PED deposited CIGS films	101
4.3.5	Simulated and experimental models of DC and PED deposited CIGS films	103
4.4	Conclusions.....	104
5	Sequential Pulsed electrodeposition of Cu(In,Ga)Se₂	106
5.1	Two-stage deposited CIGS films	107
5.1.1	Compositional analysis of two-stage PED deposited CIGS thin-films.....	107
5.1.2	Morphology of two-stage PED deposited annealed CIGS thin-films.....	108
5.1.3	Phase constitution of two-stage PED deposited annealed CIGS thin-films.....	109
5.1.4	Band gap of two-stage PED deposited annealed CIGS thin-films	110
5.1.5	Photoelectrochemistry of two-stage PED deposited annealed CIGS thin-films	111
5.2	Deposition of Cu-Ga-Se films – optimization of applied voltage	112
5.2.1	Compositional analysis of Cu-Ga-Se thin-films	112
5.2.2	Morphological and profilometry studies of Cu-Ga-Se thin-films.....	114
5.2.3	Micro-Raman spectra of Cu-Ga-Se thin-films.....	115
5.3	Fabrication of CIGS thin-films	116
5.3.1	Elemental composition of sequentially deposited annealed CIGS thin-films....	116
5.3.2	Morphology of sequentially deposited annealed CIGS thin-films.....	117
5.3.3	XRD patterns of sequentially deposited annealed CIGS thin-films	118
5.3.4	Raman spectra of sequentially deposited annealed CIGS thin-films	119
5.4	Characterization of optimized CIGS thin-films	120
5.4.1	Compositional analysis of optimized CIGS thin-films by XRF	120
5.4.2	Structural analysis of optimized CIGS thin-films by TEM	120
5.4.3	Cross-section analysis of optimized CIGS thin-films by SEM.....	121
5.4.4	Optical studies of optimized CIGS thin-films	122

5.4.5	Mott-Schottky analysis of optimized CIGS thin-films	123
5.4.6	I-V characteristics of optimized CIGS thin-films by PEC.....	124
5.5	Conclusions.....	125
6	Fabrication of Cu(In,Ga)Se₂ nano-flakes by pulsed electrodeposition.....	126
6.1	Effect of tri-sodium citrate (TSC) on pulse electrodeposition of CIGS	127
6.1.1	Variation in composition of CIGS thin-films with varied TSC concentration ..	127
6.1.2	Morphology of annealed CIGS thin-films with varied TSC concentration	130
6.1.3	XRD analysis of annealed CIGS thin-films with varied TSC concentration.....	133
6.1.4	Raman spectra of annealed CIGS thin-films with varied TSC concentration ...	135
6.1.5	Optical studies of CIGS thin-films deposited with 100 mM TSC	136
6.1.6	Mott-Schottky analysis of CIGS thin-films deposited with 100 mM of TSC ...	137
6.1.7	PEC studies of CIGS thin-films deposited with 100 mM TSC	137
6.2	Fabrication of hierarchical CIGS nano-flakes	138
6.2.1	Variation in composition of CIGS thin-films with varied deposition time.....	139
6.2.2	Morphology of CIGS thin-films with varied deposition time.....	140
6.2.3	Phase constitution of CIGS thin-films by XRD.....	143
6.2.4	Raman analysis of CIGS thin-films	144
6.2.5	Optical absorption studies of CIGS thin-films	145
6.3	Characterization of stoichiometric CIGS nano-flakes	146
6.3.1	TEM analysis of CIGS thin-films.....	146
6.3.2	Cross-section analysis of CIGS nano-flakes by SEM.....	147
6.3.3	Optical studies of CIGS nano-flakes	148
6.3.4	Mott-Schottky analysis of CIGS nano-flakes	149
6.3.5	I-V characteristics of optimized CIGS thin-films by PEC.....	150
6.4	Conclusions.....	151
7	Pulse-reverse electrodeposition of Cu(In,Ga)Se₂.....	153
7.1	Pulse-reverse electrodeposition (PRED) of CIGS thin-films	154
7.1.1	Compositional analysis of PR electrodeposited CIGS films	155
7.1.2	Morphology of PR electrodeposited CIGS films.....	156
7.1.3	Micro-Raman analysis of PR electrodeposited CIGS films	158
7.2	Characterization of the fishbone like CIGS nano-mesh deposited by PRED	159
7.2.1	FESEM characterization of fishbone like CIGS nano-mesh	159
7.2.2	Phase constitution of fishbone like CIGS nano-mesh.....	160
7.2.3	Micro-structural characteristics of fishbone like CIGS by TEM.....	161
7.2.4	Optical absorption studies of the CIGS nano-mesh.....	162

7.2.5	Mott-Schottky analysis of fishbone like CIGS nano-mesh.....	163
7.2.6	Photoelectrochemical studies of fishbone like CIGS nano-mesh	165
7.3	Conclusions.....	166
8	Fabrication and characterization of CIGS/CdS heterojunction	168
8.1	Fabrication of CIGS/CdS heterojunction.....	169
8.2	Characterization of CIGS/CdS heterojunction.....	170
8.2.1	Morphology and phase constitution of CIGS/CdS heterojunction	170
8.2.2	Photoelectrochemical characterization of CIGS/CdS heterojunction	171
8.3	Conclusions.....	174
	Summary and Outlook	176
	References	181

Chapter 1

Introduction

1.1 Energy

“Energy”, can never be created nor destroyed, can only be converted from one form to other form. Energy plays the most important role in today’s human survival and its progress and is the major factor in the development of a country. It is available in many varieties in nature however the accessibility is rather limited in its present forms. Therefore, the best way to access this available energy is to convert it into familiar forms such as light, heat, electricity, etc. since human’s energy needs are mainly in the form electricity and heat. Till now the maximum energy used is transformed from easy-to-use non-renewable resources like fossil fuels (coal, natural gas, liquid petroleum, etc.). However, the inherent problems associated with the use of fossil fuels such as their limited availability and the environmental issues force the mankind to look for new, more sustainable long-term energy solutions to provide the future energy supply.

Indian economy has experienced unprecedented economic growth over the last decade. Today, India is the ninth largest economy in the world, driven by a real GDP growth of 8.7% in the last 5 years (7.5% over the last 10 years). In 2010 itself, the real GDP growth of India was the 5th highest in the world. This high order of sustained economic growth is placing enormous demand on its energy resources. The demand and supply imbalance in energy is pervasive across all sources requiring serious efforts by Government of India to augment energy supplies to deal with possible severe energy supply constraints in future. A projection in the Twelfth Plan document of the Planning Commission indicates that total domestic energy production of 669.6 million tons of oil equivalent (MTOE) will be reached by 2016-17 and 844 MTOE by 2021-22. This will meet around 71 per cent and 69 per cent of expected energy consumption, with the balance to be met from imports, projected to be

about 267.8 MTOE (≈ 3.11 TWh) by 2016-17 and 375.6 (4.37 TWh) MTOE by 2021-22 [1].

The above required energy figures clearly demonstrate the need to develop renewable energy resources which has come to the forefront of discussion. Increased demand from developing countries like India and China coupled with plateauing and decreasing supply have led to huge leaps in fossil fuel prices. Power demand projections have the world needing nearly 35 TW by the year 2050. In this context, solar energy, which is the major form of renewable energy, becomes one of the crucial alternatives to suffice the world's energy demand.

1.2 Solar Energy

Sun produces huge amount of energy that enter the earth atmosphere in form of electromagnetic radiations and heat. The earth captures a very small part typically about 2 billionths of the sun's immense output during its revolution around the sun [2]. Typical solar spectrum on the earth's surface is shown in Figure 1.1. This radiation from sun can be extracted and transferred into the two leading forms as heat and electricity. Conversion of sunlight into heat is the concept of solar thermal whereas conversion into electricity is the phenomenon of solar photovoltaics. Both of these are low-cost, environmentally friendly technologies. Solar thermal power generation systems use mirrors to collect sunlight and produce steam by solar heat to drive turbines for generating power. This system generates power by rotating turbines like thermal and nuclear power plants, and therefore, is suitable for large-scale power generation. For its ability to generate power round-the-clock by use of stored heat, as well as high energy conversion efficiency, solar thermal power generation is now attracting increasing attention as one of the promising next-generation systems. Solar thermal delivers thermal energy that is used to heat water or other fluids, and can also power solar cooling systems. Solar photovoltaics, on the other hand, uses the concept of conversion of sunlight into electricity. Solar photovoltaic power generation has been one of the cleanest sustainable energy technologies. It has been growing quite rapidly that, in 2013, its fast-growing capacity increased by 38 % to a running total of 38 GW worldwide [3]. The topic of interest for the present work is the phenomenon of solar photovoltaics and is explained in detail in the next section.

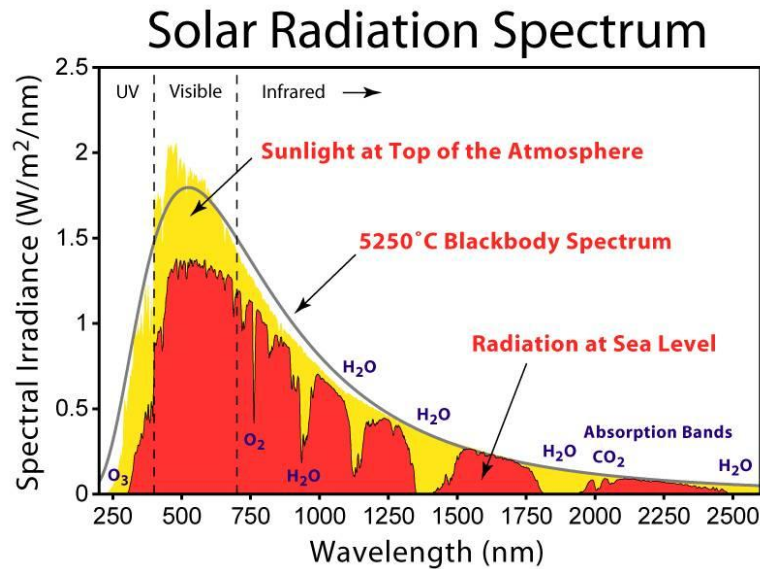


Figure 1.1: Spectrum of solar radiation reaching the earth's atmosphere [4]

1.3 Solar Photovoltaics

The French physicist Edmond Becquerel, in 1839 discovered the photovoltaic effect while studying the behavior of solids in electrolytes. When metal plates (silver or platinum) immersed in a solution were exposed to light, a small voltage and current were produced. Few years later, Charles Fritts fabricated the first thin selenium solar cell, predicting the potential of this energy source [5]. The advances in solid state electronic technology in the 1950's lead to the fabrication of the silicon solar cell, developed in the Bell Telephone Laboratories by Chapin, Fuller and Pearson [6]. The first silicon solar cell had an efficiency of 6 %. This discovery was the beginning of the active research in high efficient and low cost photovoltaic devices. The market areas of the first commercialized cells in the fifties corresponded to smaller power requirements, such as telephone repeaters requiring tens of Watts. The first impacts of the solar photovoltaics were realized for space applications when the satellite Vanguard-I was launched in 1958, containing a small six silicon cell panel, providing about 5 mW of power. Two months after the Vanguard launch, the USSR launched a much larger solar powered satellite, which worked for over two years. Since then, practically all spacecrafts have been powered by solar cells. The limitations in the fossil-fuel resources and the oil embargo in 1973 turned the industry to support the terrestrial requirements.

During the last decades of the 20th century, the technology and industry developed extensively, with module shipment exceeding 200 MW/year and installations of remote and

central power stations producing hundreds of megawatts [3]. While silicon technology achieved efficiencies close to the theoretical limits ($\approx 33\%$), new approaches were investigated in order to reduce the high costs involved in crystalline cells. Therefore, since the eighties an intense activity in the research of new materials for the production of large-scale high efficiency cells took place. As a result, new emerging technologies have penetrated in the photovoltaics market, which up to some years ago was absolutely dominated by crystalline silicon technologies. Among these technologies, amorphous silicon (a-Si), polycrystalline and multicrystalline silicon (p-Si), II-VI compounds, copper indium diselenide (CISe) and copper indium gallium diselenide (CIGS) have already achieved commercial maturity.

1.4 Solar Cell

A solar cell is an electronic device designed for converting the irradiated Sun light into electricity. The temperature difference between the surface of the sun with a temperature of $T = 5800$ K and the surface of the earth ($T = 300$ K) is the driving force of any solar energy conversion. Solar cells and solar modules directly convert the solar light into electricity using the photovoltaic effect. Thus, a solar cell needs a photovoltaic absorber material (semiconductor) that not only absorbs the incoming light efficiently but also able to create mobile charge carriers, electrons and holes, which are separated at the terminals of the device without significant loss of energy. The simplest way to achieve this is by constructing a p-n homojunction, although there are other structures, such as metal/semiconductor (MS), metal/insulating/semiconductor (MIS) and complex heterojunctions that have been used as solar cells. The operation of the usual photovoltaic cell involves four different steps. First, the photons with energy greater than the bandgap of the material are absorbed to generate electron/hole pairs. These photogenerated carriers diffuse to the edge of the depletion region of the junction, where they are separated and swept by the internal electrical field of the junction (shown in Figure 1.2). Finally, the separated carriers are collected via ohmic contacts with grid structures. The electrical behavior depends on the type of cell, and the electronic properties of the material.

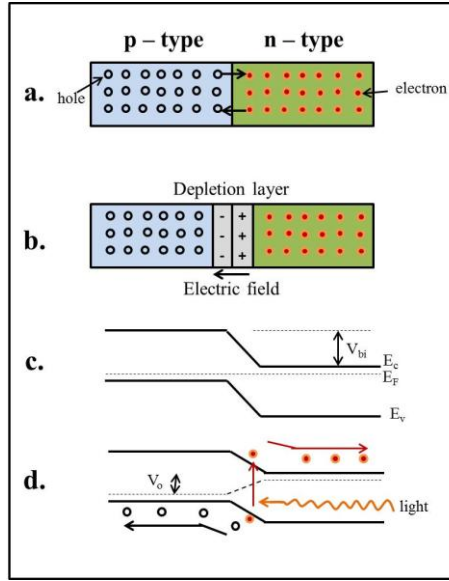


Figure 1.2: p-n junction formation and separation of electrons and holes

Ideal solar cells under illumination:

Generation of photocurrent upon light incidence on the semiconductor absorber is explained above. The generated photocurrent is mathematically formulated using the junction characteristics of the diode. A mathematical model is generally constructed to understand the concept of photocurrent generation by the absorption of photons wherein it is assumed that the generation rate of electron-hole pairs by illumination is uniform throughout the device to simplify the model [7]. The output photocurrent of the solar cells under illumination is the superimposed mixture of diode current and a constant photocurrent (J_L) and is given by the equation:

$$J = J_0 \left(e^{\frac{qV}{kT}} - 1 \right) - J_L \tag{1.1}$$

$$J_L = qG(L_e + W + L_h) \tag{1.2}$$

where J_0 is the saturation current density, V is bias voltage, k is Boltzmann constant, T is temperature, J_L is photocurrent density, G is generation rate of electron hole pairs, W is width of the depletion layer, L_e and L_h are the electron and hole diffusion lengths.

Note that the photocurrent J_L contains the photo-generated carriers by light in the depletion region of the diode and a minority carrier diffusion length on either side [7]. Therefore it is

straightforward to conclude that longer minority carrier lifetimes and wider depletion width lead to higher photocurrent.

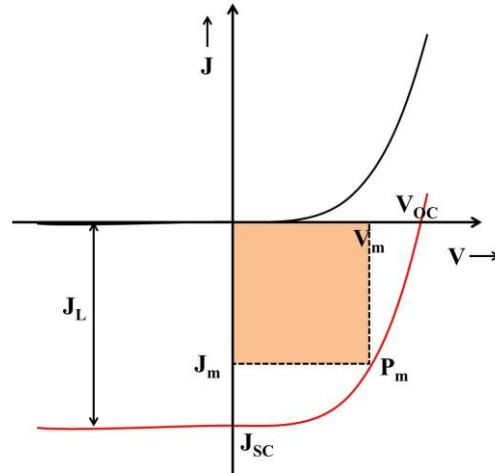


Figure 1.3: Typical J-V characteristics of solar cell

Current density-voltage characteristics of solar cells in the dark and under illumination are illustrated in Figure 1.3. Several parameters are used to characterize solar cell output such as open-circuit voltage, short circuit current density, fill factor and conversion efficiency, etc. These parameters are critical to the performance of the solar cell and understanding them is the key to improve the device performance. In this context, these parameters are defined as follows.

The short-circuit current is the current through the solar cell when the voltage across the solar cell is zero (i.e., when the solar cell is short circuited). The short-circuit current is due to the generation and collection of light-generated carriers. For an ideal solar cell at most moderate resistive loss mechanisms, the short-circuit current and the light-generated current are identical. Therefore, the short-circuit current is the largest current which may be drawn from the solar cell. I_{sc} depends significantly on the area of the solar cell which is the reason often it is expressed in terms of short circuit current density (J_{sc}), as shown in Figure 1.3, to avoid the area dependence in the calculations. (J_{sc}) depends on several parameters such as the incident power of sun light (essentially defines the number of photons incident on the sample), the spectrum of sun light (like AM 1.5, AM 1.0, etc.), the optical properties of solar cell and the photo-generated carrier collection probability. J_L is the light generated current density inside the solar cell and is the correct term to use in the solar cell equation, as shown in equation 1.1. At short circuit conditions the externally measured current density

is J_{sc} . Since J_{sc} is usually equal to J_L , the two are used interchangeably and for simplicity and the solar cell equation is written with J_{sc} in place of J_L . However, in the case of very high series resistance ($> 10 \Omega\text{cm}^2$) J_{sc} is less than J_L and writing the solar cell equation with J_{sc} is incorrect.

The open-circuit voltage, V_{oc} , is the maximum voltage available from a solar cell, and this occurs at zero current. The open-circuit voltage is shown on the J-V curve in Figure 1.3. The V_{oc} can be obtained by setting J to be zero in equation 1.1 and is formulated as:

$$V_{oc} = \ln\left(\frac{J_L}{J_0} + 1\right) \quad (1.3)$$

From Figure 1.3, a parameter P_m is observed which corresponds to the maximum power output of the solar cell. From the P_m value the corresponding V_m and J_m can be inferred from the figure, which are then used to define a parameter called Fill Factor. The short-circuit current and the open-circuit voltage are the maximum current and voltage respectively from a solar cell. However, at both of these operating points, the power from the solar cell is zero. The fill factor, more commonly known by its abbreviation "FF", is a parameter which, in conjunction with V_{oc} and I_{sc} , determines the maximum power from a solar cell. The FF is defined as the ratio of the maximum power from the solar cell to the product of V_{oc} and I_{sc} . Graphically, the FF is a measure of the "squareness" of the solar cell and is also the area of the largest rectangle which will fit in the IV curve.

$$FF = \frac{V_M I_M}{I_{sc} V_{oc}} \quad (1.4)$$

The efficiency is the most commonly used parameter to compare the performance of one solar cell to another. Efficiency is defined as the ratio of energy output from the solar cell to input energy from the sun. In addition to reflecting the performance of the solar cell itself, the efficiency depends on the spectrum and intensity of the incident sunlight and the temperature of the solar cell. Therefore, conditions under which efficiency is measured must be carefully controlled in order to compare the performance of one device to another. Terrestrial solar cells are measured under AM1.5 conditions and at a temperature of 25°C. Solar cells intended for space use are measured under AM0 conditions. The energy-conversion efficiency, η , is given by:

$$\eta = \frac{FF I_{SC} V_{OC}}{P_{in}} \quad (1.5)$$

where P_{in} is the total power of the light incident on the solar cell.

Non-ideal solar cells

The solar cells in practical usage have several issues such as grain boundary and defects in devices making them non-ideal. In order to characterize solar cells more precisely, an equivalent circuit containing series resistance R_S and shunt resistance R_{SH} is usually employed to describe the diode performance (Figure 1.4). The major causes of the series resistance are the bulk resistance of the semiconductor materials, metallic contacts and interconnections, and the contact resistance between the metallic contacts and semiconductor. The shunt resistance is influenced by the leakage across the p-n junction via crystal defects and impurities. High series resistance and low shunt resistance can reduce V_{OC} and J_{SC} .

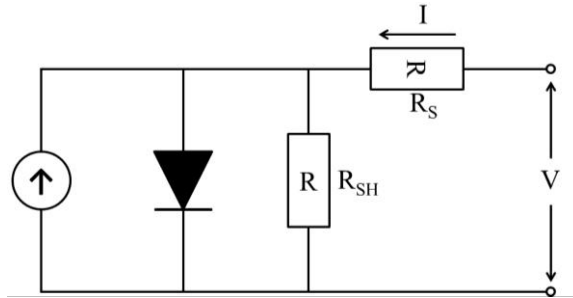


Figure 1.4: Equivalent circuit for non-ideal solar cells

Based on the equivalent circuit the current density-voltage relation can be inferred as:

$$J = J_0 \left(e^{\frac{q(V-JR_S)}{nkT}} - 1 \right) + \frac{V - JR_S}{R_{SH}} - J_L \quad (1.6)$$

where n is the diode ideality factor.

The saturation current density J_0 may be written as:

$$J_0 = J_{00} e^{\left(\frac{-E_a}{nkT}\right)} \quad (1.7)$$

where E_a is the activation energy and the pre-factor J_{00} is only weakly temperature dependent. The diode quality factor $n = 1$ for recombination at back surface, in the quasineutral region, and at the absorber/buffer interface, whereas for space charge recombination $n = 2$. Pictorial representation of J-V characteristics with varied R_S and R_{SH} are shown in Figure 1.5.

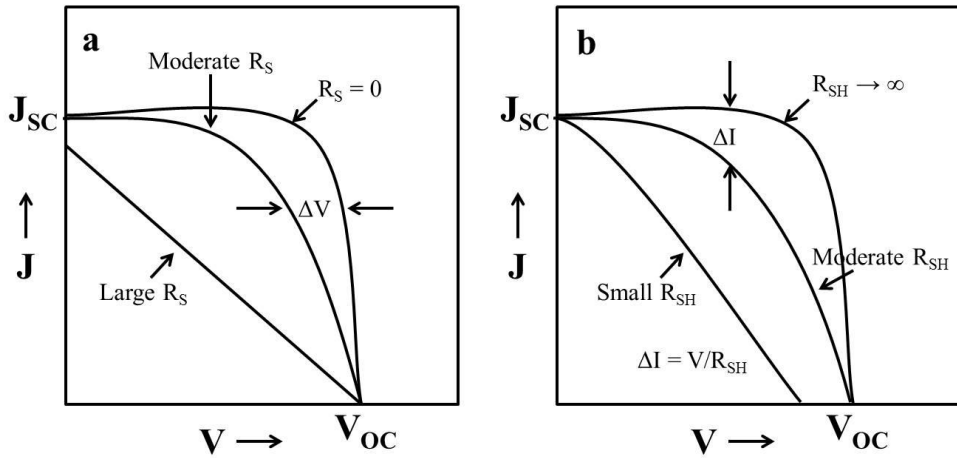


Figure 1.5: J-V characteristics of a solar cell with a) varied series and b) shunt resistances. Reproduced from [7].

Based on the above analysis, for a semiconductor to be used as a photovoltaic absorber, its bandgap energy E_g is the primary quantity defining how many charge carriers are generated from solar photons with energy $E \geq E_g$. Maximizing the number of photons contributing to the short-circuit current density of a solar cell would require minimizing E_g . Since photogenerated electron hole pairs thermalize to the conduction-band and valence band edges after light absorption, the generated energy per absorbed photon corresponds to E_g regardless of the initial photon energy E . Thus, maximizing the band-gap energy E_g maximizes the available energy per absorbed photon. Therefore, one intuitively expects that an optimum band-gap energy exists between $E_g = 0$, maximizing the generated electron-hole pairs, and $E_g \rightarrow \infty$, maximizing the generated energy contained in a single electron-hole pair. Quantitatively, this consideration is reflected in the dependence of the maximum achievable conversion efficiency of a single band-gap photovoltaic absorber material [8].

The typical requirements that need to be met by the photovoltaic absorber layers to ensure the maximum efficiency of the device [7-9], are as follows:

1. A direct band gap with nearly optimum values for either homojunction or heterojunction devices.
2. A high optical absorption coefficient, which minimizes the requirement for high minority carrier lengths.
3. The possibility of producing n and p-type material, so that the formation of homojunction as well as heterojunction devices is feasible.
4. A good lattice and electron affinity match with large band gap window layer materials so that heterojunctions with low interface state densities can be formed and deleterious band spikes can be avoided.

A number of materials satisfy the above requirements and are explored as the absorber layers in solar cells, are discussed in the next sections.

1.5 Solar Cell Technologies

Photovoltaic cells are broadly classified into four types based on the usage of absorber materials for the cell production. They are:

1. First generation solar cells (single silicon crystal wafers, c-Si)
2. Second generation solar cells
 - a. Amorphous silicon (a-Si)
 - b. Polycrystalline silicon (poly-Si)
 - c. Cadmium Telluride (CdTe)
 - d. Copper indium gallium diselenide (CIGS)
3. Third generation solar cells
 - a. Nanocrystal solar cells
 - b. Photoelectrochemical cells (Grätzel cells)
 - c. Polymer cells
 - d. Dye sensitized solar cells
4. Fourth generation solar cells (Hybrid – inorganic crystals with a polymer matrix)

These different types of materials have their own advantages and disadvantages which resulted in different cell efficiencies. The relevant particulars of these materials have been explored here.

1.5.1 First Generation Solar Cells

First generation photovoltaic cells are the dominant technology in the commercial production of solar cells, accounting for more than 80 % of the solar cell market. Cells are typically made using a crystalline silicon wafer and consists of a large-area, single layer p-n junction diode. Silicon has been and continues to be the foundation of the photovoltaics industry. Silicon's properties are well known and the technological aspects of the growth of crystalline silicon have been profusely studied during the development of the electronic industry. Moreover, silicon comprises about the 20 % of the Earth's crust, which makes this element a good choice for large productions. A most common approach to fabricate these cells is to process discrete cells on wafers sawed from silicon ingots. There are other approaches including make of ingots into either mono-crystalline or multi-crystalline and cutting of silicon wafers from multi-crystalline ribbons. This recent approach saves energy to process discrete cells. The band gap range of 1.11 eV aids in efficient broad spectral absorption, however, its indirect nature leads to lower absorption coefficient and often requires thicker wafers to improve the efficiency. Efficiencies have reached up to 25.6 % on the laboratory scale and 23 % for the module scale [10]. In addition to broad spectral absorption range, high carrier mobilities are another significant advantage of the first generation solar cells. However, they require expensive manufacturing technologies such as growing and sawing of ingots which is a highly energy intensive process. In addition, most of the higher energy photons, at the blue and violet end of the spectrum, are wasted as heat.

1.5.2 Second Generation Solar Cells

The second generation solar cells use thin-film deposits of semiconductors as absorber layers. A thin film is a material created by the random nucleation and growth processes of individually condensing/reacting atomic/ionic/molecular species on a substrate. The structural, chemical, metallurgical and physical properties of such materials are strongly dependent on a number of deposition parameters and thickness. Thin-films encompass a considerable thickness range, varying from few nanometers to tens of micrometers and thus are best defined in terms of 'birth processes' rather than thickness. The atomistic random nucleation and growth processes bestow new exotic properties to thin-film materials. The following features of thin-film processes are of specific interest for thin-film based solar cells:

1. Several varieties of techniques such as physical, chemical, electrochemical, plasma based and hybrid methods are available for depositing thin-films

2. Varying the deposition parameters and/or substrate, the microstructure and other properties of the thin-films of most materials can be varied from one extreme of amorphous/nanocrystalline to highly oriented and/or epitaxial growth
3. A wide range of shapes, sizes, areas and substrates are available for thin-film deposition
4. Doping and alloying even with incompatible materials can be obtained due to the relaxed solubility conditions
5. Suitable materials can be used during deposition to passivate surfaces and grain boundaries
6. Different types of electronic junctions, single and tandem junctions, are feasible
7. Graded bandgap, composition and lattice constants can be obtained to meet the requirements for a designer solar cell
8. Composition in case of multicomponent materials, bandgap and other optoelectronic properties, can be graded in desired manner
9. Surfaces can be modified to achieve desired optical reflectance/transmission characteristics, haze and optical trapping effects
10. Besides conservation of energy and materials, thin-film processes are in general eco-friendly [For example, the chemical bath deposition process accepted for depositing CdS window layer] and qualify as 'Green' processes

Various materials like amorphous Si, poly-crystalline Si, GaAs, CdTe, CIGS, CZTS, CIAS, etc. are under intense research for the application in thin-film solar cells. Among these multinary compound semiconductors often possess a direct band-gap and hence a large optical absorption coefficient leading to high cell efficiencies. GaAs is the leading candidate among thin-films solar cells with a highest cell efficiency of 28.8 % [10]. Thin-films solar cells offer several advantages compared to the other conventional materials as following:

1. Lower manufacturing costs
2. Lower cost per watt can be achieved
3. Reduced mass
4. Less support is needed when placing the samples on rooftops
5. Allows fitting panels on light or flexible materials, even textiles

However, the efficiencies of thin-film solar cells are lower compared silicon wafer based solar cells. Increased toxicity due to the elements like Cd and Se is another disadvantage of thin-film technology.

1.5.3 Third Generation Solar Cells

These devices do not rely on a traditional p-n junction to separate photogenerated charge carriers compared to the previous semiconductor devices. They include devices based on nanocrystal solar cells, photoelectrochemical cells, dye-sensitized solar cells (DSSC), polymer solar cells, etc. Cell efficiency has reached up to 12 % for laboratory scale for the case of DSSC and the module efficiency is in the range of 8 % [11]. However, a path breaking record efficiency of 15 % is reported for DSSC wherein a perovskite based solid state dye is being used [12]. Third generation materials have several advantages such: low-energy and high throughput processing technologies; polymer cells – solution processable, chemically synthesized, low materials cost; Grätzel cells – attractive replacement for existing technologies in low density applications like rooftop solar collectors, work even in low-light conditions; DSSC – potentially rechargeable (upgradeable). However, similar to second generation cells the efficiencies are lower compared to silicon based solar cells. In addition, degradation effects i. e. efficiency decreases with time due to environmental effects. Materials possess large bandgap which often leads to lower absorption of the solar spectrum. PEC cells suffer the degradation of electrodes from the electrolyte, often termed as photo-corrosion.

1.5.4 Fourth Generation Solar Cells

These solar cells make use of polymers with nanoparticles mixed together to make a single multispectrum layer. Significant advances in hybrid solar cells have followed the development of elongated nanocrystal rods and branched nanocrystals. Due to these aspects a significant improvement in the charge transport characteristics is observed. Incorporation of nanostructures into polymers required optimization of blend morphology using solvent mixtures. Cell design involves solid state nanocrystals (Si, In, CuInS₂, CdSe), embedded in light absorbing polymer with p-type conductivity, such as PEDOT:PS, which carries holes to the counter electrode, coated on a transparent semi-conducting oxide (ITO). Cell efficiency is of the order of 6 % for laboratory scale and hasn't reached the module scale production [10]. These materials are solution processable, low cost, possibility of self-assembly. Nanocrystals can also be printable on a polymer film which always leads to a potential possibility for improved conversion efficiency. However, efficiencies are lower compared to silicon based solar cells and potential degradation problems similar to polymer cells.

Efficiencies achieved by various technologies from different institutions across the world are shown in Figure 1.6.

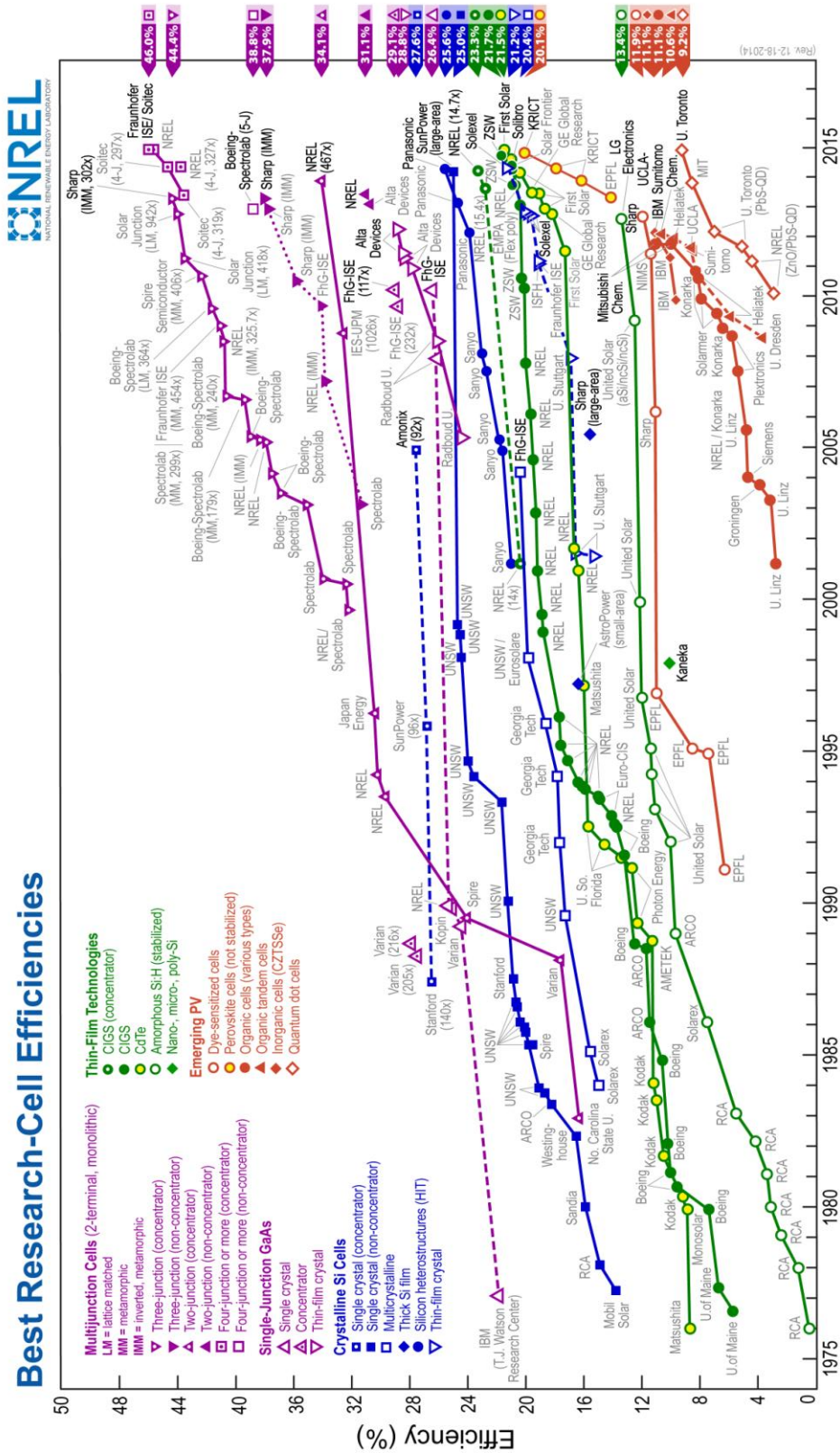


Figure 1.6: Efficiencies achieved by different technologies. Courtesy: NREL

Among these materials, CuInSe_2 and Cu(In,Ga)Se_2 thin-films based technologies have been under the intense research for the past two decades owing to their suitable direct bandgap and resulting high optical absorption coefficient. The large absorption of these materials often results in the use of thin-films of 1 – 3 μm instead of thick slices of Si of 300 μm . CIGS based technologies have already achieved efficiencies close to 21 % indicating their promise for the solar photovoltaic energy generation. However, as discussed previously, the commercialization of these solar cells has been limited due to the lack of an economic method to produce large area high quality films. In this context, the present work focuses on these technologies which are discussed in detail in the next sections.

1.6 CuInSe_2 (CIS) and Cu(In,Ga)Se_2 (CIGS)

Current trend in photovoltaics requires the development of high performance inexpensive solar cells that can serve in the long term as viable alternatives to the single crystal silicon technology. A wide range of II-IV compounds and a variety of multinary semiconductors satisfy the above requirements as discussed in section 1.4. Copper based ternary compounds with the chalcopyrite structure are one of the leading technologies due to their superior properties that are required for a typical solar absorber layer over other materials [13]. Foremost among those copper ternaries, that has emerged as leading candidates are the chalcopyrite-type CuInSe_2 .

CuInSe_2 (CIS) is a ternary semiconductor belonging to the I-III-VI class, crystallizes to a chalcopyrite structure, possesses a direct bandgap of 1.04 eV and an absorption coefficient of $\approx 10^5 \text{ cm}^{-1}$ [13, 14]. The CIS-based solar cells are simple to produce and they also exhibit features like chemical stability, stability with time, and doping versatility. The absorbing layer is the key element of solar converters, which is produced mainly from the p-type semiconductor. CIS crystallizes in the tetragonal structure as shown in Figure 1.7, which is primarily a diamond like lattice with a face centered tetragonal unit cell [15]. Each selenium atom serves as the center of a tetrahedron of two copper and indium atoms. In turn, each metallic atom is surrounded by a tetrahedron of chalcogen atoms [16].

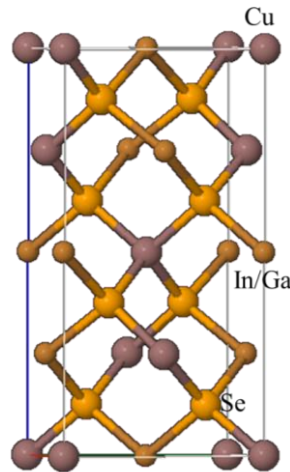


Figure 1.7: Tetragonal chalcopyrite structure of CIGS

The electrical properties of Cu ternary semiconductors are basically determined by native defects [17]. The determined characteristic of electrical properties of CIS films is due to the compensation between native donors and acceptors. There are three possible electrically active defects namely, vacancies, interstitials and antisite defects [18-20]. It is these defects which determine the nature of the conductivity of CIS films whether n type or p type. Intrinsic copper vacancies (V_{Cu}) and copper on indium antisite defects (Cu_{In}) are the electrically active defects for a typical p-type CIS film. On the other hand, intrinsic selenium vacancies (V_{Se}) and indium on copper antisite defects (In_{Cu}) makes the CIS n-type. This kind of material is not preferred mainly because of the formation of copper selenide (Cu_2Se). Cu_2Se being highly conductive, shorts out the junction. Adding more Indium than copper reduces the formation of Cu_2Se but it causes other defects like V_{Cu} and In_{Cu} which are compensating in nature [21]. Hence, the copper to indium ratio (Cu/In) is always maintained around unity. Samples with p-type conductivity are grown if the material is Cu-poor and is annealed under high Se vapor pressure, whereas Cu-rich material with Se deficiency tends to be n-type. CIS films when suitably manufactured tend to be p-type because of the low energy of formation of copper vacancies which give the material its conductivity [17, 20, 22].

CIS solar cells often yielded relatively lower open circuit potentials due to its small bandgap. This limitation is overcome by adding controlled amounts of gallium to replace indium in the CIS structure [23]. The band gap of $CuIn_{1-x}Ga_xSe_2$ varies according to the equation[24]

$$E_g = 1.011 + 0.664x + 0.249x(1 - x) \quad (1.8)$$

Depending on the [Ga]/[In+Ga] ratio, the bandgap of CIGS can be varied continuously between 1.02 eV and 1.68 eV [23, 25]. Employing CIGS together with CIS extends the spectral range to the IR region. The quantum response of CIGS solar cell is shown in Figure 1.8. The addition of about 30% Ga in CIS increases the bandgap to 1.2 eV which has a closer match with the AM 1.5 solar spectrum as observed in Figure 1.8 [8, 25]. Addition of gallium not only increases the band gap but also has other beneficial effects [25]. The addition of Ga improves the adhesion of the film to the Mo substrate. The carrier concentration in the absorber is also reported to increase with addition of gallium. Moreover, defect chemistry, electron and hole affinities, film morphologies and lattice constants are also affected by the addition of Ga [8, 25].

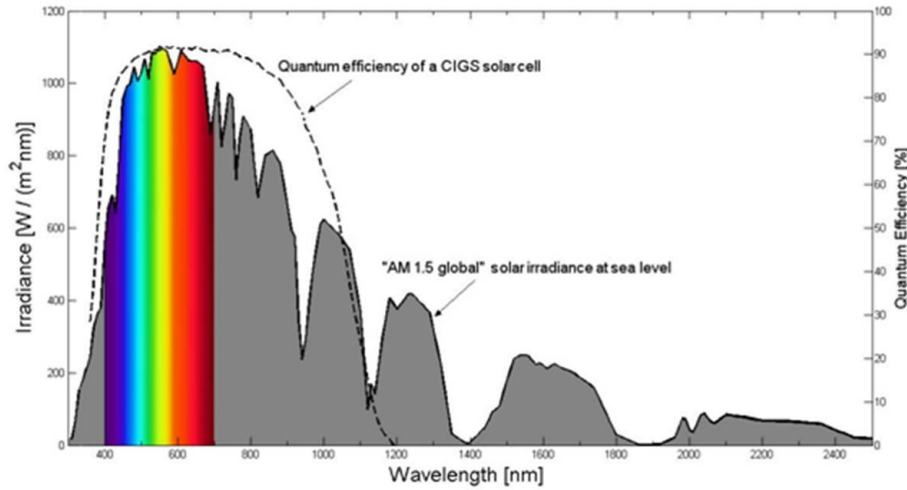


Figure 1.8: Quantum response of CIGS solar cell for AM 1.5 G irradiance

The addition of Ga in the film can be carried out in a way that the concentration of Ga is the same throughout, resulting in homogenous films with uniform bandgap everywhere. The Ga profile in the absorber can also be varied resulting in graded band gap structures. By using graded compositional profiles, i.e. higher gallium concentration towards the back contact, a back-surface field (BSF) is achieved since a higher concentration of gallium mainly increases the conduction band level in the CIGS layer [26, 27]. A reduced back-contact recombination has earlier been demonstrated by the use of such a BSF. Band-gap grading creates a quasi-electric field due to the conduction band bending, moving the electrons towards the junction thereby increasing the probability of their collection. Further, graded

band gap structures could be developed which could result in an improvement in V_{OC} without reduction in I_{SC} [28]. Though it is beneficial to add Ga to improve the properties of CIS, there is a limit to which it serves favorable. Higher Ga content of 40% has a detrimental effect on the device performance, because it negatively impacts the transport properties of the CIGS absorber film. The current, high-efficiency devices are prepared with bandgaps in the range 1.20–1.25 eV, which corresponds to a Ga/(In+Ga) ratio between 25 and 30% [28-32].

To summarize, CIS and CIGS materials have specific advantages over other materials owing to above properties for solar cell applications. To name a few:

1. Well-adapted direct bandgaps which are suitably controlled by alloying
2. Possibility of p-type and n-type doping
3. Extremely good stability
4. Large absorption coefficients
5. Well-suited lattice and electron affinity for common window layers such as ITO, ZnO, etc.

Disadvantages:

1. Complex stoichiometry
2. Less abundance of materials
3. Toxicity of Se

1.7 Design of CIGS Solar Cell: Role of Different Layers

Thin film technology based on CIS appeared at the end of the seventies [33]. In 1982 a CIS/CdS cell was confirmed, with efficiencies greater than 10 % [34]. Incorporation of Ga in the CIS compound made possible to reach efficiencies over 20 % [29-31]. Furthermore, these devices show excellent stability. Most commonly CIGS based solar cells are grown in substrate configuration as shown in Figure 1.9. This configuration gives the highest efficiency owing to a favorable process conditions and material compatibility. Device fabrication is usually done in a substrate configuration starting with the deposition of back contact, usually Mo, on glass, followed by the p-type CIGS absorber, CdS buffer layer, undoped ZnO, n-type transparent conductor (usually Al: ZnO), metal grid, and antireflection coating. In addition, it requires an encapsulation layer and/or glass to protect the cells surface. The structure of CIGS solar cell is quite complex because it contains several compounds as stacked films that may react with each other. Fortunately, all detrimental

interface reactions are either thermodynamically or kinetically inhibitive at ambient temperature. The role of each of the layers is explained in detail in the following sections.

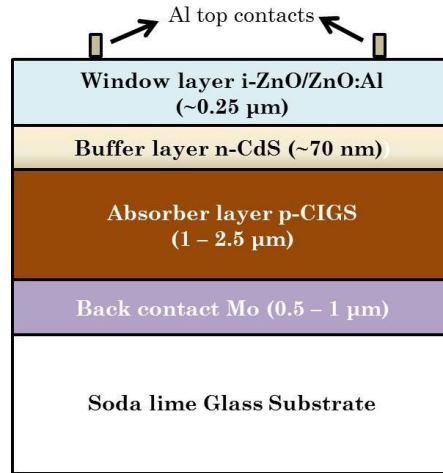


Figure 1.9: Typical CIGS solar cell configuration

1.7.1 Back Contact

The back contact made out of a metal, covers the entire back surface of the solar cell and acts as a conductor to extract the holes from the solar cell. Molybdenum (Mo) is the most common metal used as a back contact for CIGS solar cells. Several metals Pt, Au, Ag, Cu and Mo, have been investigated as back contacts [35-37]. In addition, polyimide (flexible) has also been explored [32]. Among these, Mo emerged as the dominant choice for back contact due to its relative stability at the processing temperature, resistance to alloying with Cu and In, and its low contact resistance with CIGS. The typical value of resistivity of Mo is nearly $5 \times 10^{-5} \Omega \text{ cm}$ or less. Mo is typically deposited by e-gun evaporation [38] or sputtering [39-42] on soda lime glass which ideally provides inert and mechanically durable substrate at temperatures below 500-600 °C. In addition, formation of a thin p-type MoSe_2 layer between Mo and CIGS during the annealing at temperatures higher than 500 °C is beneficial for the cell performance for several reasons [43, 44]. First, it forms a proper ohmic back contact. The Mo/CIGS contact without MoSe_2 is a not an ohmic but Schottky contact which causes resistive losses [43, 45]. Another advantage is the improved adhesion of the absorber to the Mo back contact. Further, since the bandgap of the MoSe_2 is wider (about 1.4 eV [43]) than that of a typical CIGS absorber, it forms a back surface field for the photogenerated electrons [43, 45, 46], providing simultaneously a low resistivity contact for holes [47]. The back surface field reduces recombination at the back contact since the insertion of a wider bandgap layer (of the same conductivity type as the absorber) between

the back contact and the absorber creates a potential barrier that confines minority carriers in the absorber. Finally, the MoSe₂ layer prevents further reactions between Mo and CIGS [48]. Typically, MoSe₂ has a thickness in the range of 10 – 40 nm for devices with high efficiencies [44].

1.7.2 Absorber Layer

Absorber layer is the heart of the solar cell which plays the important role of photovoltaic effect. The primary function of the absorber layer is to generate the electron-hole pairs upon exposure to sunlight. CIS or CIGS, play the role of absorber layer, are often simply referred to as chalcopyrites because of their crystal structure. These materials are easily prepared in a wide range of compositions as discussed in the later sections. However, for the preparation of the solar cells, only slightly Cu-deficient compositions of p-type conductivity are suited. CIS/CIGS material properties have been mentioned in previous sections and are not discussed here.

1.7.3 Buffer Layer

Semiconductor compounds with n-type conductivity and band gaps between 2.0 and 3.6 eV have been applied as buffer for CIGS solar cells. However, CdS remains the most widely investigated buffer layer, as it has continuously yielded high-efficiency cells [30, 31]. CdS for high-efficiency CIGS cells is generally grown by a chemical bath deposition (CBD), which is a low-cost, large-area process. However, incompatibility with in-line vacuum-based production methods is a matter of concern. One advantage of the CBD method as compared to evaporation is that a complete, conformal coverage of the CIGS surface can be obtained at very low thicknesses [49].

The role of the CdS buffer layer is twofold: it affects both the electrical properties of the junction and protects the junction against chemical reactions and mechanical damage. From the electric point of view the CdS layer optimizes the band alignment of the device and builds a sufficiently wide depletion layer that minimizes tunneling and establishes a higher contact potential that allows higher open circuit voltage value [49]. The buffer layer also plays a very important role as a “mechanical buffer” because it protects the junction electrically and mechanically against the damage that may otherwise be caused by the oxide deposition (especially by sputtering). Moreover, in large-area devices the electric quality of the CIGS film is not necessarily the same over the entire area, and recombination may be enhanced at grain boundaries or by local shunts. Together with the undoped ZnO layer, CdS

enables self-limitation of electric losses by preventing defective parts of the CIGS film from dominating the open circuit voltage of the entire device. In addition to the CdS, several other buffer layers such as $\text{Cd}_{1-x}\text{Zn}_x\text{S}$ [50], ZnS [51], ZnSe [52], (Zn,Mg)O [53], In_2S_3 [54, 55], In_2Se_3 [56], InZnSe_x [57], etc. have also been explored to essentially avoid toxic Cd in the device fabrication.

1.7.4 Front Contact

There are two main requirements for the electric front contact of a CIGS solar cell device: sufficient transparency in order to let enough light through to the underlying parts of the device, and sufficient conductivity to be able to transport the photo-generated current to the external circuit without too much resistance losses. Transparent conducting metal oxides (TCO) are used almost exclusively as the top contacts. Narrow lined metal grids (Ni–Al) are usually deposited on top of the TCO in order to reduce the series resistance. The quality of the front contact is thus a function of the sheet resistance, absorption and reflection of the TCO as well as the spacing of the metal grids.

Today, CIGS solar cells employ either tin doped In_2O_3 ($\text{In}_2\text{O}_3:\text{Sn}$) or, more frequently, RF sputtered Al-doped ZnO. A combination of an intrinsic and a doped ZnO layer is commonly used, although this double layer yields consistently higher efficiencies, the beneficial effect of intrinsic ZnO is still under discussion. It has been shown that device performance increases due to the increase in V_{OC} by 20 – 40 mV. Resistive oxide layer provides, together with buffer, a series resistance that protects the device from local electrical losses that may originate from inhomogenities of the absorber. Doping of the conducting ZnO layer is achieved by group III elements, particularly with aluminum. For high-efficiency cells the TCO deposition temperature should be lower than 150 °C in order to avoid the detrimental inter-diffusion across CdS/CIGS interface.

1.7.5 Band Diagram and Other Device Aspects

CIGS solar cell consists of different layers as explained above; the band diagram of the cell has become complex due to the presence of these layers. The band diagram of CIGS based solar cell is shown in Figure 1.10. The built-in field constituted by the CIGS/CdS heterojunction is responsible for the separation of photo-generated carriers, thereby, inducing photocurrent from the cell. The heterojunction is in fact so complex that several approaches have been used to model its electrical behavior. The first CIS/CIGS-based cells used a thick CdS window layer, which was responsible for the important electronic losses in

these early devices, due to the recombination at the CdS/absorber interface [58]. The introduction of a highly doped ZnO window layer, together with the thickness decrease of the CdS layer, increased the band bending in the absorber and decreased the recombination rate of electrons at the heterointerface such that in the actual state-of-the-art, it is accepted that recombination at the interface does not limit the V_{OC} of the device. Probably the recombination at the space charge region in the bulk of the absorber constitutes the dominant electronic loss mechanism in high efficiency devices [47].

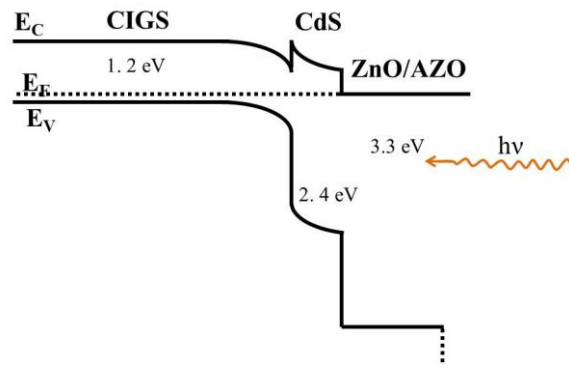


Figure 1.10: Band diagram of CIGS solar cell

There are several aspects of the chalcopyrite-based solar cells that are not totally understood. For example, it is generally accepted that the presence of Na in appropriate amounts (0.1 %) in the CIGS films improves the device performance [59]. The benefits of the Na are probably a result of manifold consequences. Moreover, the formation of NaSe_x compounds during the formation of the film slows down the growth of the CIGS grains, facilitating the incorporation of Se and widening the existence range of the chalcopyrite CIGS compound in the equilibrium phase diagram [60]. The diminishment of the number of V_{Se} defects and the Na-promoted oxygenation and passivation of grain boundaries are other mechanisms influencing the properties of the resultant absorbers [59]. Therefore, it is necessary to control the incorporation of Na in the absorbers, which is either externally introduced or through the utilization of soda-lime glass substrates.

Another example of the complex physical problems concerning these devices is the influence of the surface phases. The presence of Cu_{2-x}Se crystalline phase in the surface of the CIGS films has a great influence on the electronic properties of CIGS films. This secondary copper selenide phase has an equivalent free energy as that of CIGS and is stable even at the elevated temperature that is being used for the improved crystallinity of CIGS.

Cu_{2-x}Se is a degenerate semiconductor and is expected to segregate to the grain boundaries and/or to the surface thereby leading to higher dark currents of the cell [24, 61, 62]. Therefore, it is crucial to avoid these secondary phases during the formation of CIGS from any method.

Best CIGS-based cells are obtained with the utilization of $\text{Cu}(\text{In,Ga})(\text{S,Se})_2$ pentenary absorbers [63, 64]. Ga and S are added in order to tune the gap of the absorber. As previously mentioned, Ga increases the bandgap of CIGS up to 1.2 eV, as a consequence, the open-circuit voltage of the cells increases, achieving values above 0.7 V without decreasing cell efficiency [28]. High Ga contents increases $(E_g - eV_{OC})$. This is due to either unfavorable band alignment or Fermi level pinning. In addition to the effect upon the bandgap, the incorporation of Ga has similar effects like that of the introduction of Na. The existence of the chalcopyrite phase is substantially widened, decreasing the sensitivity of the cell performance to stoichiometric deviations. The Ga addition also increases the free carrier density, increasing the conductivity one order of magnitude [25], which has been explained in terms of defect physics considerations [63].

Sulphur constitutes another alloying element commonly employed in the commercial cells. The incorporation of S in the films promotes the surface segregation of CuS, which must be removed by an additional step in the industrial process. Despite this drawback, the improvement in the open circuit voltage achieved is in the range of 100 mV [65]. This increase is mainly attributed to a passivation of recombination centers, which strongly affects the electrical transport properties of the material.

Knowing the material properties of CIGS and various device aspects, the next important step is to make these materials. In this context, various techniques explored for the preparation of CIGS absorber layers are discussed in the following sections.

1.8 Synthesis Methods of CIGS Absorber Layer

The construction, working and several other aspects concerning CIGS based solar cells are briefed in the previous section. However, the essential task is to look at the methods for the synthesis of CIGS absorber layer since technique used for production decides the economic viability of CIGS solar cell. A wide variety of thin-film deposition methods have been used to deposit CIGS thin-films. To determine the most promising technique for the commercial manufacturing of modules, the overriding criteria are: (i) low cost, (ii) scalability, (iii)

reproducibility and (iv) manufacturability. Ultimately, the techniques should be capable of cutting down the costs of solar panels drastically in the future. For CIGS, device considerations dictate that the layer should be at least 1 μ m thick and that the relative compositions of the constituents are kept within the bounds determined by the phase diagram. The promising deposition methods for the commercial manufacturing of modules can be divided into two general categories namely vacuum-based and non-vacuum based approaches.

1.8.1 Vacuum based Techniques

Methods which adopt vacuum for the deposition of CIGS thin-films are termed under vacuum-based approach category. Physical vapor deposition techniques including co-evaporation, sputtering, molecular beam epitaxy, pulsed laser deposition, etc. have been investigated for the formation of CIGS thin-films. Though vacuum is involved, these methods are the most promising for deposition of high efficiency CIGS devices and are explored for commercial manufacture of CIGS modules. The most successful technique for deposition of CIGS absorber layers for highest efficiency small area cells is the simultaneous evaporation of the constituent elements from multiple sources in single process where Se is offered in excess during the whole deposition process [36, 83]. Typical co-evaporation set-up is shown in Figure 1.11. Deposition is often performed under ultra-high vacuum conditions using a molecular beam epitaxy (MBE) system which is either a two-stage or a three-stage process. Two-stage process involves co-evaporation of Cu-rich CIGS layer at a lower substrate temperature (450 °C), followed by In-rich layer at a higher temperature (550 °C). The layers intermix, forming a homogeneous film with a slightly Cu-deficient overall composition. The three-stage process involves first the deposition of (In,Ga)₂Se₃ at a lower substrate temperature (about 300-350 °C) and then the evaporation of Cu and Se at a higher temperature (500-560 °C) to yield Cu-rich CIGS. After adding more (In,Ga)₂Se₃, a slightly Cu-deficient final film composition is achieved. Co-evaporated CIGS films yielded highest conversion efficiencies with the world record being 20.8 % by Jackson et al. wherein a potassium doping in the CIGS films was performed [30]. Several groups have reported CIGS cells with high efficiencies using co-evaporation method [29-32, 65-67].

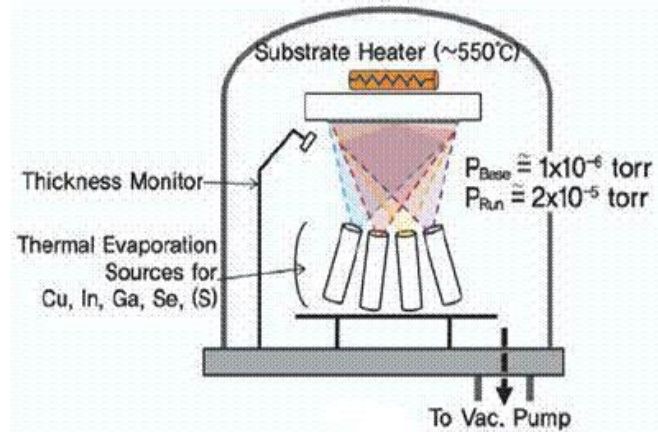


Figure 1.11: Schematic of co-evaporation set-up for CIGS thin-films [68]

Despite its indisputable power in preparing high-quality material on small areas, co-evaporation has problems in upscaling. Co-evaporation requires a strict control of the evaporation fluxes to achieve the desired film properties such as composition, texture, and electrical properties making it a difficult choice for large area modules. As an inevitable consequence, the conversion efficiencies of large area cells and modules are considerably lower than those of the smaller-area devices. High-vacuum deposition methods typically waste expensive raw materials through unintentional deposition on the vacuum chamber walls and therefore, achieve relatively low materials-utilization efficiency. Even advanced, relatively high efficiency vacuum techniques such as dual rotatable magnetron sputtering only achieve materials utilization efficiencies of 75–80%. This low utilization of source materials will limit the potential for cost reductions.

Although thin-film CIGS solar cells with power conversion efficiencies over 20 % have been demonstrated, the vacuum-based processes used to deposit the absorber layers in these devices pose cost and technological barriers in the production of low-cost PV modules. Hence, efforts to seek an economical and scalable method for the production of stoichiometric CIGS thin-films have been ongoing to realize the commercialization of these devices. Several non-vacuum based methods have been explored for this purpose and are discussed in the following section.

1.8.2 Non-vacuum-based Techniques

The development of non-vacuum process for CIGS deposition offers a number of potential advantages over the continued use of vacuum approaches [69]:

1. The equipment required for large-area device processing is significantly simplified and costs are reduced as vacuum is avoided.
2. Materials utilization efficiencies close to 100% are achievable by non-vacuum processes that precisely direct materials to the desired location on the substrate surface.
3. Solution-based deposition processes are potentially less energy intensive relative to vacuum-based approaches. Many solution-based approaches have low energy input and can deposit precursor layers at room temperature and utilize a short heat treatment technique, such as rapid thermal processing (RTP) to form CIGS.
4. For several solution-based approaches, such as printing, doctor blade coating and stamping, one high-speed pass is sufficient to coat the substrate with a precursor film, meaning the processes can readily be made high throughput and are compatible with roll-to-roll processing of flexible substrates.

Despite these advantages, unless low-cost PV modules maintain good power conversion efficiency the balance-of system costs associated with installed modules will lead to little or no reduction in the electricity cost as compared to vacuum deposited modules. With this requirement in mind, development of a non-vacuum deposition method to fabricate CIGS has become an intensively pursued goal in PV research and a variety of solution-based approaches have been demonstrated.

Non-vacuum approaches, explored for the deposition of CIGS, can be roughly divided into three different categories depending on the deposition method and the scale mixing of the precursor materials.

- i) Electro-, electroless and chemical bath deposition where electrochemical/chemical reactions in a solution lead to the coating on an immersed substrate.
- ii) Particulate based processes that use solid particles dispersed in a solvent to form an ink, which can be coated on a substrate.
- iii) Processes that coat molecular precursor solutions onto a substrate by mechanical means such as spraying or spin coating.

The efficiency gap between vacuum and non-vacuum deposited CIGS has been reduced in past years and processes from the above categories have now reported cells with efficiencies of 11 – 15%, thereby, showing promise for commercialization. Among these methods,

electrochemical deposition is the most extensively explored technique for the deposition of CIGS absorber layers and has witnessed in high efficiency devices [70-74]. Of the non-vacuum methods, ink-jet printing can certainly be a choice for the production of CIGS thin-films owing to its simplicity and low cost. However, several problems associated with it such as formation of CIGS films with surface cracks need to be solved prior to the commercialization of these devices. The present study is focused on exploring electrochemical techniques for the deposition of CIGS which is discussed in detail in the following sections.

1.9 Electrodeposition

Electrodeposition, is an electrochemical plating process, uses an electric current or potential to reduce the desired metal ions from the solution onto a conducting object to form a thin layer of the material. In general, a conventional electrodeposition set-up contains three electrodes, namely, anode, cathode and reference electrode which are immersed in an electrolyte as shown in Figure 1.12. Saturated calomel electrode (SCE), Ag/AgCl, mercurous sulphate electrode (MSE), etc. are the most commonly used reference electrodes, which have a standard electrode potential vs. normal hydrogen electrode (NHE). A reference electrode is used to maintain the constant potential difference between the counter and the working electrodes. However, the use of reference electrode makes the process expensive for commercialization and has additional effects as explained later in experimental section. When an electric current/potential is supplied between the electrodes, the metal ions from the solution get reduced onto cathode by the use of potential difference between the electrodes. The electrode on which reduction takes place is a cathode or a working electrode and, in general, is the substrate of interest. At anode oxidation takes place. Anode is highly inert or noble material and does not take part in any reaction with the precursor solution or undergo any changes to the applied potential. Platinum is the most conventionally used anode in electrodeposition. However, high purity graphite can replace platinum to make the process more economical and scalable.

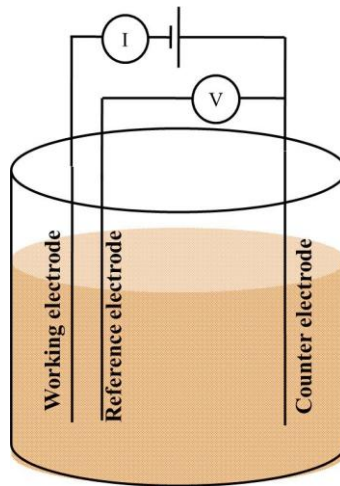


Figure 1.12: Typical electrodeposition set-up containing three electrodes

Electrodeposition is a promising economic approach to fabricate the absorber layers in thin-film solar cells due to following advantages [9, 70, 72, 73]:

1. Production of high quality films with very low capital investment
2. Low cost and high rate process
3. Use of very low cost starting materials e.g., low purity salts, solvents, based on automatic purification of the deposited materials during plating
4. Continuous deposition of multi-components on large areas
5. Uses low temperature for deposition
6. Deposition of films on a variety of shapes and forms of wires, tapes, coils, and cylinders
7. Controlled deposition rates and effective material use as high as 98%
8. Minimum waste generation i. e. solution can be recycled

Owing to these advantages, electrodeposition satisfies all the necessary criteria for the research and development of PV solar cells. It is a low cost, scalable and manufacturable technique and therefore, is capable of cutting down costs of solar panels drastically in the future.

In addition to the above mentioned advantages, electrodeposition involves unique techniques such as direct current plating and pulse plating. Among these, pulse plating again has two advanced features namely, pulse electrodeposition and pulse-reverse electrodeposition. These advanced techniques are unique in themselves that they provide additional process control variables and make electrodeposition an attractive tool for the deposition of semiconductors [75].

1.9.1 Direct Current (DC) Electrodeposition

A constant current or potential is applied continuously during the deposition to coat the desired materials. Figure 1.13 shows the schematic of the direct current applied and the typical growth process corresponding to it. As it can be seen, DC technique has only two variables, namely, applied potential/current and time of deposition. However, the precursor concentration and electrolyte pH are the common variables for all techniques in electrodeposition. The morphology, composition and thickness of the deposit can be varied by varying the above mentioned parameters. However, the continuous use of constant potential/current leads to continuous deposition of films without any relaxation. The growth of existing nucleation sites takes place rather than generating new nucleation sites leading to a rough and porous deposit (Figure 1.13). In addition, hydrogen evolution reaction (HER) competes along with the deposition of desired materials as often aqueous electrolytes are used for the deposition. The HER not only influences the current efficiency of the technique but also the deposited film properties. The evolved hydrogen gets entrapped into the deposited films making it more porous during DC deposition. However, the use of additives in this conventional DC deposition has improved the morphology of the deposited films. Despite having several disadvantages, DC electrodeposition is still a leading technique for the production of single element deposits and binary alloys.

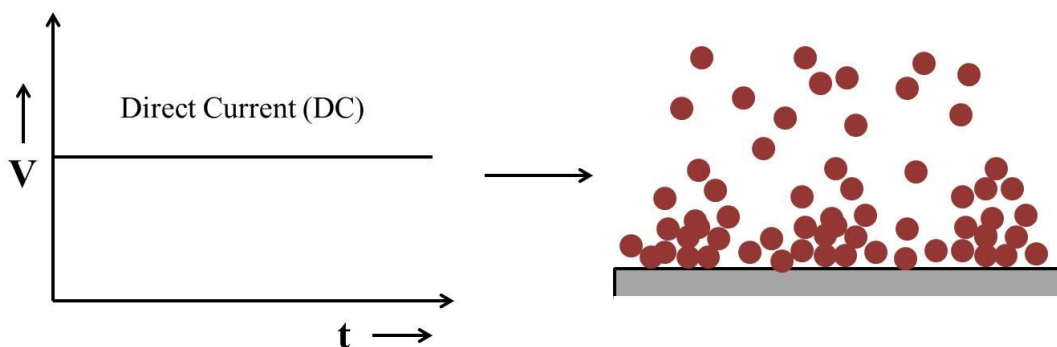


Figure 1.13: Schematic of direct current (DC) electrodeposition and resulting growth process of the deposit

1.9.2 Pulse Electrodeposition (PED)

In a pulse electrodeposition (PED), current/potential is applied in the form of modulated waves. Figure 1.14 shows the typical waveform used during a PED. In contrast to the DC electrodeposition, pulse current helps to control on-time (t_{on}) and off-time (t_{off}).

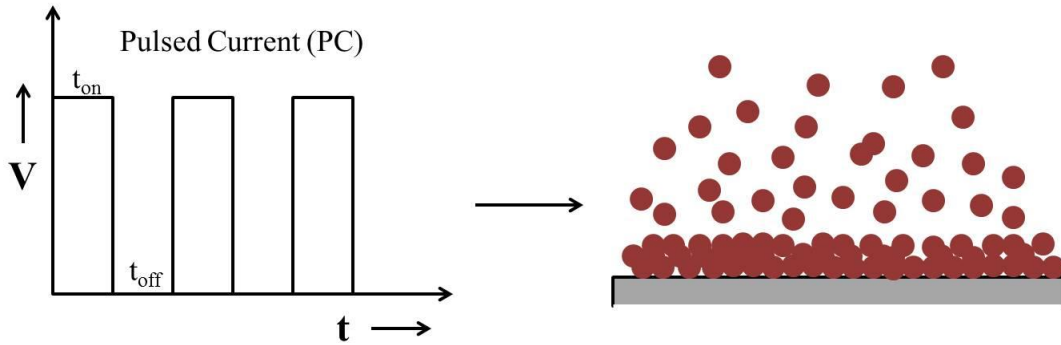


Figure 1.14: Schematic of waveform in pulse electrodeposition (PED) and resulting growth process of the deposit

Often, the variation in t_{on} and t_{off} is expressed using a common parameter known as duty cycle, which is defined by the equation:

$$Duty\ Cycle\ (\%) = \frac{t_{on}}{t_{on} + t_{off}} \times 100 \quad (1.9)$$

The precise variation in duty cycle provides us to control electrochemical process by affecting the diffusion layer, grain size and nucleation. Usually in electroplating a negatively charged layer is formed around the cathode which gets charged to a known thickness and prevents the ions from the bulk (see Figure 1.15). The charged diffusion layer gets discharged and helps easier passage of the ions through the layer and onto the cathode during pulse electrodeposition wherein the output is periodically turned off. Moreover, higher current density areas in the bath become more depleted than low current areas. Migration of ions to depleted areas in the bath during off-time makes the even distribution of ions for the easy availability of deposition during on-time. Off-time is also called as relaxation time as there is no deposition. The presence of relaxation time between two successive intervals of deposition aids in the relaxation and the rearrangement of deposited atoms leading to the possibility of new nucleation sites during the subsequent deposition. This, in turn, not only improves the uniformity of deposition but also reduces the porosity and roughness of the deposit (see Figure 1.14). In addition, the entrapped hydrogen and impurities during the deposition diffuse out during the relaxation time. Complex stoichiometry of ternary/quarternary systems can be relatively easily controlled using PED deposition by the variation of t_{on} and t_{off} .

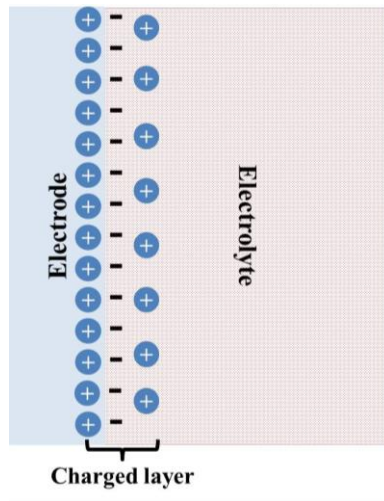


Figure 1.15: Charged layer at the electrode-electrolyte interface during the deposition

Advantages of PED [76, 77]:

1. Increase of the deposit homogeneity due to a higher throwing power even at complex shaped parts
2. Dramatic improvement of the layer properties e.g. minority carrier diffusion
3. By short cathodic pulses with a higher current density, nucleation process can be increased
4. By very short anodic pulses with a higher current density leveling and smoothening effect can be achieved
5. Controlling composition of ternary/quarternary systems by altering the pulse sequence
6. Reduction in porosity can be achieved by eliminating the entrapped hydrogen during the deposition

1.9.3 Pulse Reverse Electrodeposition (PRED)

A pulse-reverse electrodeposition technique possesses all the features as that of pulse current electrodeposition. In addition, a small reverse/anodic pulse is applied between two successive forward pulses as in PED deposition. Figure 1.16 shows the typical pulse waveform used in a PRED technique and growth process of the deposit. The small anodic pulse is specifically advantageous since it oxidizes/removes a small layer from the surface of the deposited film. This will help in smoothening of the deposit, removing the impurities as well as the entrapped hydrogen. However, the anodic pulse plays a crucial role in the

deposition of systems like CIS and CIGS, wherein an undesired secondary Cu-Se phase exists on the surface, as previously discussed. With the appropriate control of the anodic pulse, excess copper and hence the undesired phases can be easily eliminated from the deposited films thereby, forming a phase-pure CIS/CIGS. Similar to PED deposition, the variation in pulse parameters is expressed using a common parameter known as duty cycle, which is defined by the equation:

$$Duty\ Cycle\ (\%) = \frac{t_c}{t_a + t_c} \times 100 \quad (1.10)$$

where t_c is the total cathodic pulse time and t_a is the anodic pulse time.

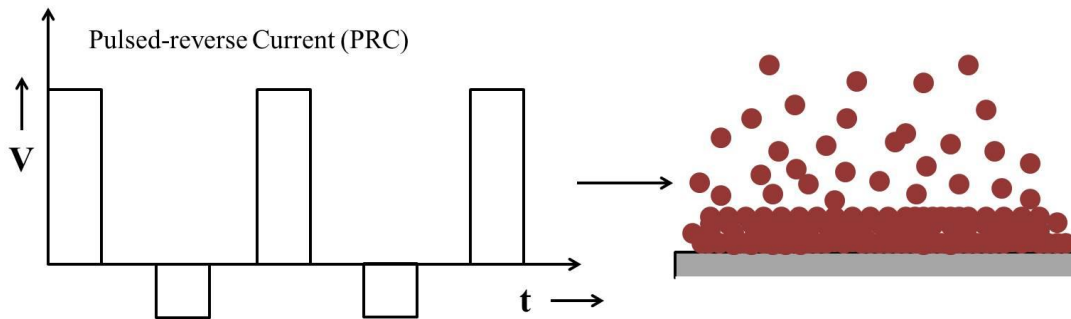


Figure 1.16: Schematic of waveform in pulse-reverse electrodeposition (PRED) and resulting growth process of the deposit

These different electrodeposition techniques and their advantages make electrodeposition an attractive tool in the field of macro-electronics such as photovoltaics, large-area display devices and to the newly emerging field of nanotechnology. In addition, it's simple, economical and scalable which makes it a viable choice for the commercialization of PV solar modules.

1.10 Literature: Electrodeposition of ternary/quarternary Chalcopyrites

The goal of the electrodeposition (ED) is to assure an adherent, compact and a laterally uniform film with the desired stoichiometry. Lateral compositional uniformity is essential over large areas for commercialization of devices. The properties of the deposit solely depend on the control of individual parameters during ED such as electrode material, precursor concentration in electrolyte, applied potential/current and temperature. For single metallic systems like Cu or Zn these properties are well understood. However, the system becomes complex when two or more elements are being deposited. Deposition of CIGS

contains multiple elements including a chalcogen making the ED process substantially complex. Despite that electrochemical deposition appears to be a promising technique for the low-cost solution preparation of semiconductors [78-80]. Indeed, electrochemical deposition has been widely investigated for CIGS deposition since the pioneering work by Bhattacharya et al. in 1983 [81]. More than 250 papers have been devoted to the electrochemical preparation of CIGS and several review papers have appeared [69, 78, 79], making electrodeposition the most intensely studied non-vacuum deposition method for CIGS. In light of this, this section will focus on previously published work.

The first electrochemical approach to deposit a polycrystalline CuInSe₂ (CIS) was reported by Bhattacharya in 1983, wherein Cu, In and Se were simultaneously deposited from an acidic solution [81]. Quickly after the first report, several approaches have been proposed for the synthesis of CIS thin films. Hodes et al. deposited an alloy of Cu-In and annealed to form CIS [82]. Kapur et al. have followed a similar annealing of Cu-In films; however, here a stacked Cu-In layer has been deposited. Bhattacharya et al. have also annealed the stack of In-Se and Cu-Se to form CIS films. Such an approach has been used for long time for preparing copper/indium bilayers which are then reacted thermally with a selenium atmosphere to form CIGS or In/Se bilayers for indium selenide. Two elements (Cu-In) were co-deposited by Herrero et al. [83]. In that case the precursor film is intimately mixed “electrochemically” which can be an advantage with respect to stacked elemental layers. The deposition takes place for potentials more negative than that of the less noble element, here In. Moving a step further, in 1996, Massaccioli et al. have developed the approach of formation of binary metal selenides to ultimately form CIS films [84]. The basis for such an approach was the formation of many metallic selenides at relatively lower potentials than the individual elements due to their large formation energies (-386 kJ/mol for In₂Se₃, -418 kJ/mol for Ga₂Se₃, -104 kJ/mol for Cu₂Se). This concept led to new deposition domains in terms of the applied potential (see Figure 1.17) [78]. The redox potential of the reaction In³⁺ to In₂Se₃ involves 6e⁻ and is shifted by an amount of $-\Delta G/6F = 0.65$ V, with respect to the deposition of metallic indium. This leads to an inference of plausible deposition of indium selenide can theoretically take place below 0.35 V [84]. A similar mechanism is applied for copper and gallium selenides. This mechanism, known as the Kroger's mechanism, is a key point for the electrodeposition of good quality materials, since it allows self-regulating the composition of the film and is highly beneficial for improving the structural quality. This mechanism has been used by several researchers to form the stacked layers of binary metallic selenides which was then annealed to form stoichiometric CIS thin-films.

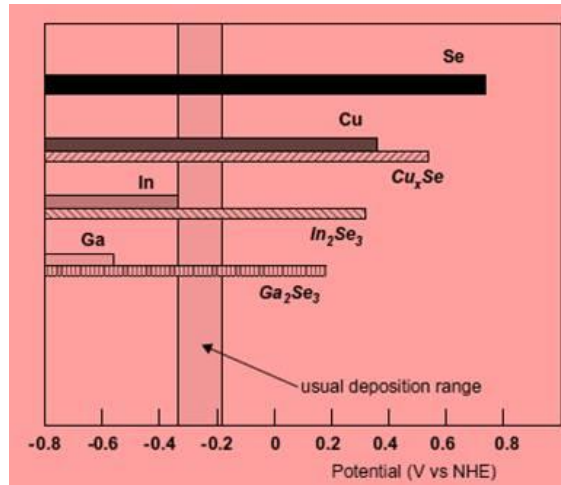
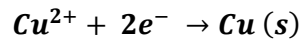
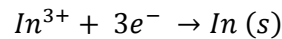


Figure 1.17: Electrochemical diagram showing the deposition domains of binary selenides (Cu_xSe , In_2Se_3 , Ga_2Se_3) and individual elements (Cu, In, Ga, Se). Reproduced from [78].

However, it is of general interest to perform a simultaneous codeposition of all three elements together to reduce the number of steps in achieving stoichiometric chalcopyrite CIS and CIGS thin-films. Such an approach was first initiated by Bhattacharya [81], which is by far the most investigated case as it involves only one electrochemical process, often termed as one-step electrodeposition. However, due to the distinct electrochemical aspects of the three ions the system becomes more complex since there may be a possibility of formation of elements in their elemental form or as binary compounds in addition to the desired ternary CIS phase. Typical electrochemical reactions involving the reduction of elements and formation of CIS/CIGS phase are as follows [71]:



$$E = E_{\text{Cu}}^0 + \frac{RT}{2F} \ln[\text{Cu}^{2+}] = 0.337 + 0.0295 \log[\text{Cu}^{2+}] \quad (1.11)$$



$$E = E_{\text{In}}^0 + \frac{RT}{3F} \ln[\text{In}^{3+}] = -0.342 + 0.0197 \log[\text{In}^{3+}] \quad (1.12)$$

$$Ga^{3+} + 3e^{-} \rightarrow Ga (s)$$

$$E = E_{Ga}^0 + \frac{RT}{3F} \ln[Ga^{3+}] = -0.529 + 0.0197 \log[Ga^{3+}] \quad (1.13)$$

$$H_2SeO_3 + 4H^{+} + 4e^{-} \rightarrow Se + 3H_2O$$

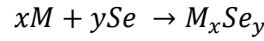
$$E = 0.741 - 0.0591 pH + 0.0148 \log[H_2SeO_3]$$

$$HSeO_3^{-} + 5H^{+} + 4e^{-} \rightarrow Se + 3H_2O$$

$$E = 0.778 - 0.0739 pH + 0.0148 \log[HSeO_3^{-}] \quad (1.14)$$

$$SeO_3^{2-} + 6H^{+} + 4e^{-} \rightarrow Se + 3H_2O$$

$$E = 0.875 - 0.0886 pH + 0.0148 \log[SeO_3^{2-}]$$



where E is the electrode equilibrium potential with respect to the standard hydrogen electrode; and E_{Cu}^0 , E_{In}^0 , and E_{Ga}^0 are the standard electrode potentials of Cu, In, and Ga, respectively. F is Faraday's constant equals to 96,485 C/mol. The concentration of H^{+} is converted to a pH scale and shown in the equations. The logarithmic of concentrations of the different chemical species shifts the electrode equilibrium potential at the specific concentration. An electrochemical phase diagram involving formation of various phases with the variation in deposition potential is shown in Figure 1.18 [85].

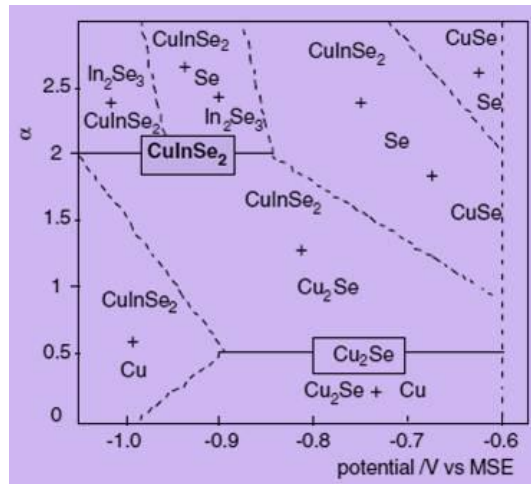


Figure 1.18: Electrochemical phase diagram showing various phases in the Cu-In-Se system as a function of deposition potential and flux ratio of Se(IV) and Cu(II). The In(III) is assumed

excess. The potentials are referred to Mercurous Sulfate Electrode (-0.65V vs. NHE). Reproduced from [78].

One-step electrodeposition of CIS is usually carried out in an aqueous solution often containing chloride/sulfate precursors of Cu^{2+} or Cu^+ , In^{3+} , and $\text{SeO}_2/\text{H}_2\text{SeO}_3$. Owing to the limited solubility of Cu^+ compounds and the instability of the free Cu^+ ions in aqueous solutions, Cu^{2+} compounds are considerably more frequently used than Cu^+ compounds. The deposition solution contains often a complexing agent in order to shift the reduction potentials of Cu and In closer together to improve the film quality. Complexing agents such as citric acid/citrate [86-89], ammonia [81], triethanolamine [81, 90], ethylenediamine [91], ethylene diamene tetra acetic acid (EDTA) [92], thiocyanate [61, 93, 94], etc. are used during the one-step electrodeposition of CIS thin-films. In addition, a supporting electrolyte such as chloride (LiCl [71-73, 95] or NaCl [92]) or sulfate (K_2SO_4 [85, 89, 96]) is added which results in an improved conductivity of the electrolyte leading to easier mobility of the precursor ions. Often amorphous or poorly crystalline CIS films were observed from electrodeposition which contains frequently degenerate Cu_{2-x}Se phases that are detrimental to the device performance [61, 79]. Also, Cu-rich films have generally larger grain sizes than stoichiometric or In-rich films. Due to these reasons, the electrodeposited CIS films often require an annealing step under an inert atmosphere to improve the crystallinity of the films and to increase the grain size. In addition, electrodeposited CIS/CIGS films are often non-stoichiometric and need to be annealed in a selenium atmosphere to correct for the stoichiometry.

Co-electrodeposition of CIS thin-films was first performed by Bhattacharya wherein 0.018 M In^{3+} , 0.018 M Cu^+ and 0.025 M SeO_2 were used as precursors. In addition, 0.006 vol.% triethanolamine and 0.007 vol.% NH_3 were used as complexing agents and the pH was maintained at 1. The films were deposited on FTO coated glass substrates at -0.7 V vs. SCE at room temperature, and the solution was stirred during the deposition. Films had shown several peaks corresponding to chalcopyrite phase after annealing though the compositional analysis was not performed [81]. Vedel et al. explored the systematic reaction mechanism of electrodeposition of CIS thin-films wherein films were deposited on SnO_2 electrodes by cyclic voltammetry as well as deposition experiments which predicts the formation binary Cu-Se prior to formation of CIS phases [97]. As the CIS phase formation occurs preceding the Cu-Se phase, several researchers have studied the Cu-Se phase alone by electrodeposition for possible mechanisms [98]. Presence of Cu^{2+} ions in the solution shifted

the reduction potential of Se^{4+} to the positive direction considerably resulting in reasonable quantities of Se deposition. This leads to the fact that Cu-Se formation enables the deposition of Se in electrodeposition. When In^{3+} concentration is not high enough, the electrodeposition process is limited by diffusion of all the three ions. Consequently, the film composition is determined by both flux ratios $\text{Se}^{4+}/\text{Cu}^{2+}$ and $\text{In}^{3+}/\text{Cu}^{2+}$ [91].

Pottier and Maurin studied the electrodeposition of Cu-In, Cu-Se and CIS thin films on Ti and Ni rotating disc electrodes using 0-80 mM Na-citrate as complexing agent [89]. The presence of citrate was found to decrease reduction rate of Cu^{2+} resulting in better control over the Cu content in the as-deposited films. In addition, lower concentration of citrate resulted in the formation of smooth films, whereas large concentrations led to powdery deposits. Thus the main function of the complexing agent was to promote the formation of well-defined crystallized compounds [89]. Molin et al. studied the reactions in the citrate system on Ti electrodes [99, 100]. They have observed the formation of different compounds such as CuSe, Cu_3Se_2 , CIS, and In-enriched CuInSe_2 from the same deposition solution by varying the deposition potential [100]. Herein the group proposed the mechanism of formation of CIS by the reaction of In^{3+} with Cu_3Se_2 [99]. This study, however, led to an interesting aspect of widened potential range for the formation of CIS thin-films when the solution was stirred during the deposition. Moreover, the deposition rate and the current efficiency were found to increase but the film morphology did not change. It is generally known that the potential ranges for the formation of the various compounds depend on the total conductivity of the solution, cathode surface area (ohmic drops) and electrolyte temperature. Therefore, use of a suitable electrolyte to increase the conductivity of solution was explored wherein Na_2SO_4 was used as a supporting electrolyte resulting in the narrow potential range of CIS formation due to increase of the solution conductivity [101, 102].

Herrero et al. deposited CIS films on Mo substrates by using citric acid as the complexing agent [103]. In rich CIS films were result of the deposition, however, Cu_xSe was also found to be present in the samples. They also studied the effects of post-deposition treatments such as annealing for 15 min under Ar (at 200 to 600 °C) and etching in 0.5 M KCN at 40 °C for 2 min. The film characteristics were found to depend on the sequence of post-deposition treatments. Etching of the as-deposited films resulted always in In-rich films, whereas etching after annealing resulted in more stoichiometric films due to the removal of small amounts of Cu and Se [103].

Calixto et al unraveled the mechanism of CIS deposition by using a pH 1.5 solution at a deposition potential of -0.5 V [104, 105]. The as-deposited semi-crystalline films became polycrystalline after annealing at 500 °C under Ar for 30 min. Also the grain size increased upon annealing. The bulk of the film was found to be Cu-rich which was attributed to the growth mechanism: Cu and Se deposit during the first seconds, forming a Cu_xSe layer which enables the assimilation of In^{3+} ions. At the beginning, more Cu is deposited than In, but the amount of In increases as the deposition proceeds. That is why the film surface is poor in Cu [104]. This explains why photoelectrochemical (PEC) measurements showed p-type conductivity and C-V measurements n-type conductivity [105]. PEC measurements mostly characterize the bulk of the film where the light is mainly absorbed, whereas C-V measurements give information about the surface since the depletion region is on the film surface [105]. Ueno et al. deposited CIS films on Ti substrates and observed the codeposition of In with Cu and Se at -0.6 V [106]. The as-deposited films deposited below -0.6 V showed CIS and Cu_3Se_2 phases whereas only CIS phase was found for films deposited at -0.8 V. Films deposited at -1.0 V resulted in metallic In in addition to CIS. The films were compositionally non-uniform and exhibited poor surface morphologies. Photoelectrochemical measurements evidenced the high dark currents due to metal rich CIS films. Deposition of CIS films was performed on rotating Ti electrodes at -0.8 V vs. SCE by Khare et al. exhibited binary phases such as In_6Se_7 together with CIS [107]. The films were n-type and had rough surface morphologies and were thus potentially suitable for photoelectrochemical (liquid junction) solar cells [107]. Chemical treatments in Br_2 (0.05-0.1 vol.%) / MeOH and 0.1-0.5 M KCN solutions were also studied to remove the undesired secondary phases present in the annealed CIS films [108]. The Br_2 treatment caused surface leveling but did not change the film composition whereas KCN was found to dissolve selectively Cu and Se. The sequence of the post-deposition treatments was again found to be of importance and the results obtained were similar to those in [108]. Ugarte et al. used EDTA as the complexing agent for the deposition of CIS films [92]. The as-deposited films showed amorphous CIS and the crystallinity improved upon annealing. The films were etched in a cyanide solution prior to the photoelectrochemical measurements that were performed in 0.5 M K_2SO_4 at pH 4.5. Despite the high dark currents (caused by the metal-rich film composition as stated earlier by Ueno et al. [106]), the measurements revealed that the films were p-type. The best photoresponse was achieved when the deposition solution contained EDTA [92]. In addition to these studies, several researchers have reported about the variation in composition and morphology of the CIS films by varying the concentration

of precursors, deposition potential, pH, annealing conditions and using various complexing agents to ultimately achieve stoichiometric chalcopyrite CIS thin-films in the recent past [90, 109-129].

In addition to the synthesis of CIS thin films by direct current (DC) electrodeposition a pulse electrodeposition (PED) techniques has been studied for the formation of CIS thin-films. Pulse electrodeposition is an advanced form of electrodeposition which offers better control over the deposit properties by controlling the interfacial electrochemical reaction for the formation of thin film. PED technique is usually used to improve the quality of thin films via the application of current or potential with high instantaneous densities in pulses. This process has several advantages over DC electrodeposition since it lends itself to improved process control by virtue of the possibility of manipulating parameters such as deposition potential, duty cycle and period. It can produce a more homogeneous surface with good adhesion to the substrate because the rate-determining step of the electrodeposition process is controlled by a mass-transfer process. It also offers a better control over stoichiometry during the deposition of a ternary or a quaternary system as rearrangement and partial dissolution of the film occur during the off-time. The duty cycle defined in equation 1.9, is thus an important variable. Appropriate regulation of duty cycle provides a better control over the composition of individual elements and hence, stoichiometry of the films. Further, morphology of the films and the grain size distribution can also be conveniently controlled with the variation in on- and off-time during a pulse electrodeposition technique. These advantages not only result in superior quality thin-films but also enable one to avoid additional steps of deposition and/or the use of complexing agents. In addition, the process such as etching using a KCN to remove undesired Cu-Se secondary phase can be avoided by the suitable optimization of pulse parameters to eliminate this undesired phase in the as-deposited CIS thin-films. Several studies have already been reported on the pulse electrodeposition of CIS thin-films.

Kang et al. reported the preparation of CIS thin-films by pulse-reverse electrodeposition technique followed by selenization. Stoichiometric CIS films with higher adhesion and rough surface morphology were reported which were then used to fabricate the CIS-solar cell resulting in an efficiency of 1.42% [130]. Xiao Li et al. employed a square wave modulated by a bell-like wave during the pulse plating for the fabrication of CIS thin-films. The study reported well adherent chalcopyrite CIS films with a uniform morphology [86]. A three-step pulse electrodeposition method was used for the fabrication of CIS thin-films

reporting a mixture of phases such as Cu-Se, In-Se, CIS, etc. as confirmed from Raman and optical studies of the samples [131]. Deposition performed in three segments of pulse potentials could have resulted in these various phases. As a result the films showed an extremely poor photoresponse with the photocurrents of the order of 1-3 μA at -0.2 V. However, the study notes the presence of secondary phases to be advantageous since they absorb the light in UV range which could contribute to extra carrier generation. Valdes et al. employed different potentials during the pulses which resulted in chalcopyrite p-type CIS thin-films with different morphologies and composition of samples [132]. Murali et al. prepared CIS thin-films using pulse electrodeposition with varied duty cycle from 6- 50 % and reported the p-type phase pure CIS films with resistivities in the range of 1 to 10 ohm-cm [133]. Hu et al. employed the deposition of CIS films by pulse electrodeposition wherein multi potentials were used to control the composition of the films which also resulted in the improved deposition uniformity without any secondary phases [134]. Similar reports on the compositional control of CIS thin-films by the variation of pulse parameters have appeared in the recent past [135-138].

Incorporation of Ga into the CIS thin-films, to improve the desired properties, was a challenging task for long time for the formation of quaternary CIGS thin-films. Ga has more negative reduction potential compared to the other three elements in the system and was extremely difficult to incorporate using the potential regime that has been employed for the deposition of CIS thin-films [78]. The incorporation of Ga by electrodeposition is yet more difficult than that of In due to its higher electronegativity. In addition, gallium selenide compounds also require more negative redox potential than those of indium selenides which makes it a challenging task for researchers unlike the case for CIS films wherein copper and indium selenides were successfully deposited and annealed to form chalcopyrite CIS thin-films. However, this bottleneck has been overcome in the recent past. Several researchers have reported the successful incorporation of Ga in the films up to desired range of amounts (6 – 10%) for the preparation of high efficiency cells [71, 72]. Formation of CIGS films upon incorporation of Ga into CIS films was observed, interestingly, by a shift in the preferred (112) orientation from XRD studies [139]. This is essentially due to the lower atomic radius of Ga, the crystal structure of CIGS gets contracted as a whole leading to a decrease in the lattice parameter and hence, inter-planar spacing. This decrease in inter-planar spacing in turn leads to a shift in the 2θ of XRD to higher values. Raman analysis of CIGS films predicted a similar shift to higher wavenumbers for the A1 mode [140]. It is also

known that incorporation of Ga increases the bandgap of chalcopyrite films which was observed from optical studies of CIGS films [26, 141-143].

Bhattacharya et al. were the first to report the insertion of Ga from a chloride bath but to a very low content $\text{Ga/In} \approx 0.1$ wherein a superimposed alternating voltages has been used at 20 kHz [144]. But the breakthrough for the incorporation of Ga has been realized a little later when the group had used a pH buffer in the chloride bath, also known as Hydrion buffer ($\text{pH} = 3$) consisting of sulphamic acid and potassium hydrogen phthalate. The deposition potential was kept constant while the solution composition has been varied to realize the real possibility of incorporating Ga with the ratio Ga/In from 0.3 to 0.7. This process demonstrated the formation of CIGS films over a wide range of compositions suitable for efficient solar cells by one-step electrodeposition technique. CIGS layers generally deposited from the above mentioned electrodeposition technique often used an additional PVD step to achieve the required composition to form stoichiometric films [74, 145]. However, the use of Hydrion buffer reduced the use of additional PVD processing to large extent since considerable amounts of Ga was incorporated into the films. Bhattacharya et al demonstrated a cell efficiency of 9.4 % by using a similar PVD step to improve the composition of In and Ga in the as-deposited CIGS thin-films [95]. Valderrama et al explored a similar electrodeposition technique followed by PVD step to achieve stoichiometric chalcopyrite CIGS films and additionally demonstrated the use of CIGS films to produce hydrogen by the use of photoelectrochemical testing of the films in H_2SO_4 [145]. On the other hand, Fahoume et al achieved the co-electrodeposition Cu, In, Ga and Se by shifting the deposition potential to more negative values. The ratio of In/Ga was observed to be 0, 0.4 and 1 for the deposition potential of -0.38, -0.68 and -0.78 V, respectively. Kampmann et al. also succeeded by incorporating Ga into CIS films achieving a Ga/In ratio of 0.11 [96]. Calixto et al further improved the method by avoiding the PVD step to electrodeposit CIGS layers and reported a cell efficiency of 6.2% after the films were selenized in H_2Se atmosphere [105]. This was truly the first non-vacuum based techniques to have yielded a reasonable efficiency for CIGS based solar cells. Avoiding the formation of secondary phases was essentially a key point to achieve high quality CIGS thin-films and hence, higher efficiency. The formation of secondary phases was successfully prevented by the pretreatment of Mo substrate wherein a 1 min pre-deposition of CIGS was performed and a multi-potential deposition regime was employed to obtain crack-free CIGS layers [146]. Zhang et al. employed the vacuum annealing treatment to the electrodeposited CIGS to improve the crystalline properties of the as-deposited films [147]. However, the technique

lacked to achieve the desired stoichiometry for CIGS thin-films [147]. Friedfeld et al. varied the deposition and annealing conditions and reported a well-controlled compositional variation to form stoichiometric CIGS thin-films without a further selenization step [148]. This process demonstrates the possibility to avoid the post selenization step, often employed during electrodeposition of CIGS, which can make the process more economical and environment friendly. Several researchers explored one-step electrodeposition technique to achieve stoichiometric CIGS films, however, morphology of the films contained cracks and also presence of secondary phases was still a major concern to improve the quality of films.

In the similar context, addition of Ga seems to cause morphology related problems, often a concern during the electrodeposition of CIGS films. Fernandez et al varied the concentration of precursor solution systematically and achieved a better control over composition and morphology of the CIGS films [95]. The presence of cracks in Ga-containing layers is often a serious problem [95, 146], though it can be reduced through the use of alcohol–aqueous solutions [149] or supporting electrolytes such as LiCl or Li₂SO₄ with gelatin as brightening additive [150]. Complexing agents such as citric acid/citrate [151, 152], thiocyanate [153], sodium sulfamate [154], sulfosalicylic acid [155], etc. were often used to improve the composition and morphology of the CIGS films. These additives often form complexes with the metal ions in the solution such as Cu, thereby limit the deposition of these elements resulting in controlled deposition rates and hence the morphology [87, 88]. Good quality CIGS thin films were also prepared from sulphate–citrate and chloride–citrate solutions [147, 154, 156] and control of the optical band gap by increasing the Ga content in the films was demonstrated [157].

To overcome the difficulty of In and Ga incorporation, alternative strategies to co-electrodeposition have been developed, often involving the deposition of stacked elemental layers or else deposition of alloys, followed by a selenization or sulphurization treatment to provide all of the chalcogen [70, 71]. Deposition of Cu-Ga [148], Cu-In [82, 83, 158, 159], In-Ga [160] and Cu-In-Ga [153] alloys has been demonstrated, with the latter two approaches leading to 6.6% and 4% efficiency cells, respectively. Recently, Solopower explored the layer by layer electrodeposition to form stoichiometric CIGS thin-films [70]. The process also used several varieties of complexing agents, organic additives, etc. to correct for the composition and improve the morphology of the films. In addition, current densities were varied during deposition and annealing temperatures were optimized to achieve high quality compact large grained stoichiometric chalcopyrite CIGS films. Devices

and modules were fabricated using these films which had shown an efficiency of 15.36 % on an area of 5.34 cm² and 13.4 % on an area of 3.8 m². These are the highest efficiencies that were reported for electrodeposited CIGS films till date [70].

In addition to the conventional direct current (DC) electrodeposition above, pulse electrodeposition (PED) has also been explored for the deposition of CIGS thin-films [156, 161]. As previously mentioned, pulse electrodeposition offers extra advantage since it has additional variables such as pulse on-time, off-time which can be conveniently varied to achieve a controlled deposition rate and hence the composition of CIGS thin-films [75, 77]. This technique is particularly advantageous for the complex systems like CIS/CIGS wherein attaining the desired stoichiometry is the key for the ultimate device performance. Though PED technique is typically advantageous for a quaternary system like CIGS, only limited reports are available for pulse electrodeposited CIGS films. Fu et al., have explored different plating techniques including DC, pulse and pulse reverse electrodeposition for the fabrication of CIGS thin films and reported the elimination of undesired secondary phases like Cu_{2-x}Se to obtain single phase pure chalcopyrite CIGS thin films [161]. Liu et al., have employed the PED with the variation of duty cycle to remove the excess In and to avoid In-Se compounds during the deposition for the preparation of single phase CIGS thin films [156]. The use of PED offers the manipulation of various parameters like amplitude of the current/potential, duty cycle, and the time of deposition thereby enables the control over the composition of individual elements in a ternary/quaternary system like CIS/CIGS to ultimately obtain the single phase CIGS by avoiding secondary phases like Cu-Se, In-Se, and Ga-Se, etc. Also, with the variation of duty cycle, morphology of the thin films would evolve into a highly dense and compact form to yield higher performance of the device.

However, most of these pulse electrodeposition studies for CIS/CIGS thin-films still used the complexing agents, employed a three-electrode system, followed by the conventional selenization step and other relevant post deposition treatments such as etching with KCN, etc. to achieve stoichiometric phase-pure chalcopyrite CIS/CIGS thin-films. These processes not only make the technique expensive but might also result in poor quality CIS films. For instance, the use of KCN etching makes the film rough and use of complexing agents might result in impurities in the deposited CIS films. Hence, it would be essential to achieve stoichiometric chalcopyrite CIS/CIGS thin-films without any secondary phases by avoiding the above mentioned aspects.

1.11 Objective of the Present Work

As it has been discussed, CIGS thin-films can effectively yield high efficiency solar devices; however, it is extremely crucial to develop a simple and economical method for the production of CIGS thin-films to ultimately realize the commercialization of these devices. In this context, electrodeposition has already witnessed the CIGS devices with reasonably high efficiency. In a conventional direct current electrodeposition, the number of variables is limited to only the applied voltage/current density and deposition time in addition to the precursor concentration which makes the process arduous to achieve a better control over composition and morphology of CIGS thin-films. Use of multi-steps, complexing agents, organic additives during the deposition followed by a conventional selenization step have been employed to achieve stoichiometric CIGS. These aspects not only makes the process more complex but also expensive. In addition, a three electrode system with Pt being the counter electrode and saturated calomel electrode or Ag/AgCl electrode as the reference electrode has been employed for conventional electrodeposition. The use of these reference electrodes makes the process more expensive when deposition is aimed at large areas.

In this context, the present study explores a two electrode system by avoiding the third reference electrode and expensive Pt is substituted by high purity graphite for the deposition of CIGS thin-films. Advanced techniques such as pulse and pulse-reverse electrodeposition are explored for the fabrication of CIGS thin-films. Variation in pulse parameters aids in better control over composition of individual elements and resulted in stoichiometric chalcopyrite CIGS thin-films. The appropriate regulation of these parameters has resulted in the minimization of the undesired secondary phases in the as-grown films and also resulted in various nanostructured morphologies such as nano-flakes, nano-mesh, etc. which are particularly advantageous as they lead to improved light absorption and minimized recombination. Due to the additional variables possessed by these techniques conventionally used complexing agents and additional step of selenization were also avoided. However, effect of complexing agent (tri-sodium citrate) has been studied on the pulse electrodeposition of CIGS films to unravel the mechanism on the deposition of CIGS thin-films.

Essential developments and the structure of the present research work are as follows:

1. A simplified and novel electrodeposition set-up for the fabrication of CIS/CIGS thin-films

2. Pulse electrodeposition of CIS thin-films – optimization of pulse parameters (desired stoichiometry with minimized secondary phases and novel flake-like morphology)
3. Pulse electrodeposition of CIGS thin-films – duty cycle has been optimized to yield compact phase-pure stoichiometric CIGS thin-films. Additionally, pulse electrodeposited CIGS films are also compared with conventional direct current electrodeposited CIGS films. Furthermore, fundamental growth mechanism studies for pulse electrodeposited CIGS thin-films are also explored.
4. A novel sequential pulse electrodeposition technique for CIGS thin-films – deposition has been performed in two stages (Cu-Ga-Se and In) to achieve better control over the composition of elements and to develop highly dense single phase CIGS thin-films.
5. Effect of complexing agent on the pulse electrodeposition of CIGS thin-films – this study is divided into parts:
 - a. Study of variation in the concentration of complexing agent on the composition and morphology of CIGS thin-films
 - b. Fabrication of novel hierarchical CIGS nano-flakes using a defined concentration of complexing agent
6. Pulse-reverse electrodeposition of CIGS thin-films – optimization of parameters such as reverse potential and duty cycle has resulted in a novel CIGS nano-mesh which exhibited superior properties.
7. Fabrication of CIGS/CdS heterojunction – CdS has been deposited using conventional chemical bath deposition technique onto pulse electrodeposited CIGS thin-films. Significantly improved performance with an excellent stability is observed.

In each case the films were characterized using scanning electron microscopy, X-ray diffraction, Raman spectroscopy, transmission electron microscopy, absorption spectroscopy, Mott-Schottky analysis, focused ion-beam analysis and photoelectrochemical analysis to study various properties of the samples.

Chapter 2

Materials and Methods

Electrodeposition technique, categories and their advantages have been discussed in the previous chapter. In addition, reports pertaining to the electrodeposition of CuInSe_2 (CIS) and Cu(In,Ga)Se_2 (CIGS) thin-films have been extensively reviewed. The knowledge gained from the previous reports has been considered for the initiation of the electrodeposition of CIS and CIGS films. In this context, this chapter focuses on the materials and various experimental aspects that are used to electrodeposit and characterize the CIS and CIGS films. Electrodeposition of CIS/CIGS films involves aspects such as electrodes cleaning, preparation of electrolytic bath, and optimization of pH, etc. prior to performing the final deposition. Figure 2.1 shows the flow chart that is followed to electrodeposit and characterize the CIS/CIGS thin-films.

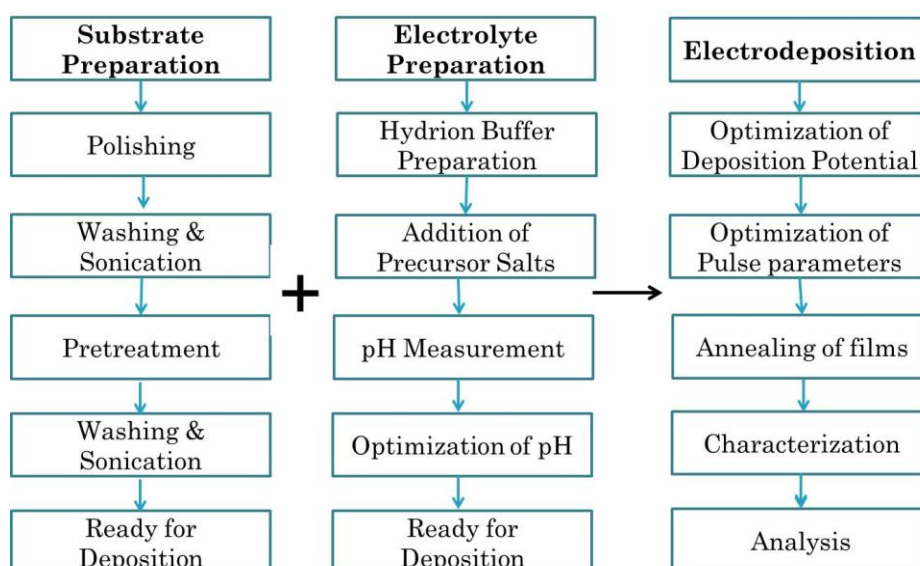


Figure 2.1: Flow-chart of the present work involving electrochemical deposition and characterization of CIS/CIGS thin-films

2.1 Materials

Electrolyte bath often uses the precursor salts such as sulfates, chlorides, nitrates, etc. as discussed earlier. The materials, their purity and relevant concentration ranges used in the present work for the electrodeposition of CIS/CIGS thin-films are tabulated below in Table 2.1. The final concentrations that are used for the electrodeposition are mentioned while discussing the relevant results.

Table 2.1: Different materials, their purity and concentration range used for electrodeposition and other characterizations of CIS/CIGS

Material	Make	Purity (%)	Concentration Range (mM)*
Hydrion buffer	Sigma Aldrich	-	Not specified
Cupric chloride	SD Fine Chem.	99+	2 – 6
Indium chloride	Alfa Aesar	99.99	1 – 6
Gallium chloride	Alfa Aesar	99.999	5 – 10
Selenous acid	Alfa Aesar	97	5 – 10
Lithium chloride	Sisco Res. Lab.	99+	200 – 300
Tri-sodium citrate	Qualigens	99	20 – 140
Hydrochloric acid	Qualigens	35.8 – 38	Very dilute
Sodium hydroxide	Qualigens	98	500 – 1000
Sodium sulfate	Qualigens	99.5	100 – 1000
Sodium sulfide	Qualigens	50	50 – 200
Sodium sulfite	Qualigens	98	20 – 50
Sulfuric acid	Qualigens	98	300 – 500
Cadmium sulfate	Alfa Aesar	99+	5 – 30 mM
Thiourea	Qualigens	99.5	30 – 100

*typical concentrations used for the deposition are mentioned while discussing the results.

2.2 Methods

Methods employed during the fabrication of CIS/CIGS films can be classified into two categories namely, preparation methods and characterization techniques. Electrodeposition with advanced features such as pulse and pulse-reverse potentials is used for the preparation of CIGS thin-films. In addition, CIS/CIGS films have also been fabricated by DC electrodeposition technique for comparative studies. Techniques including scanning electron microscopy with energy dispersive X-ray spectroscopy, X-ray fluorescence, X-ray

diffraction, Raman spectroscopy, transmission electron microscopy, absorption spectroscopy, Mott-Schottky analysis, focused ion-beam analysis and photoelectrochemical analysis, etc. have been used to characterize the CIS/CIGS films to study the morphology, elemental composition, phase constitution, optical properties, flat-band potential, carrier density and photoresponse. In addition, chemical bath deposition used for the deposition of CdS thin-films is also discussed.

2.2.1 Electrodeposition of CIS/CIGS films

Electrodeposition of CIS/CIGS thin-films involves three major steps such as electrodes preparation, chemical bath preparation followed by optimization of pH and finally potentiostatic electrodeposition. It is a usual practice to electrodeposit semiconducting materials using a three-electrode system, namely cathode, anode and a reference electrode. The reference electrode has always been used to measure the cathode voltage with respect to it, since the electrolyte concentrations change during the growth process due to changes of ion concentrations. However, more commonly used reference electrodes such as Ag/AgCl and calomel electrodes are external impurity sources and hence could poison the bath, and drastically reduce the efficiency of solar cells fabricated. For example, it has been reported that the addition of Ag^+ ions in parts per billion, drastically reduce the efficiency of electrodeposited CdTe solar cells [162]. Observation of Nernst equation shows that considerable ionic concentration changes introduce only a few mV shifts in the case of CIS and CIGS films [163, 164]. This variation is negligible when compared to the useful growth range of about 1 to 2 V. In these cases at least, the use of harmful reference electrodes could be avoided. Although there is a salt bridge method used to separate the reference electrode from the electrolyte solution, complete elimination of the reference electrode makes the electrodeposition process simpler and more economical, especially in the case of larger area deposition. Hence, the present work avoids the use of reference electrode and employs a simple two-electrode system for the electrodeposition of CIS/CIGS films. In addition, graphite is equivalently electrochemically inert compared to platinum and in the present study, conventionally used platinum is replaced with a high purity graphite electrode which can reduce the cost drastically when the deposition is aimed at large areas. Typical two-electrode system employed for the deposition of CIS/CIGS films is shown in Figure 2.2.

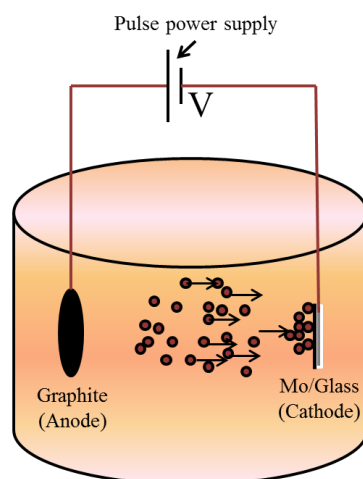


Figure 2.2: Schematic of two-electrode electrodeposition set-up employed for CIS/CIGS thin-film deposition

Preparation of electrodes

In the present work, a graphite electrode with a purity of 99.2% is used as anode (area 5 cm²) and Mo foil or Mo sputtered glass as a cathode or working electrode (substrate, area 1 – 9 cm²). Graphite is ultrasonicated in acetone for 15 min before and after the deposition using Life-Care’s fast clean ultrasonicator. Mo foils are polished using diamond paste prior to electrodeposition. Polished Mo foils are rinsed with distilled water and ultrasonicated in acetone for about 10 minutes. Then the foils are pre-treated using 15 % HCl and 1M NaOH solutions in order to remove the surface oxide layer and impurities on the surface. The pre-treated Mo foils are rinsed again with distilled water thoroughly and sonicated in ethanol for about 10 minutes and are purged with nitrogen gas prior to the deposition. In case of Mo/glass, molybdenum has been DC sputtered onto soda lime glass (SLG) in two steps. First, a seed layer (50 nm) is grown on SLG using a power of 2250 W with an Ar flow of 1000 sccm followed by the growth of bulk layer (150 nm) using 7200 W power and 240 sccm of Ar flow. Sputtered Mo/glass has been ultrasonicated in deionized water, acetone and ethanol for 15 min in each case and is purged with nitrogen in order to further reduce any possibility of oxide layer, prior to the deposition of CIS/CIGS films. Electrodes are inserted vertically into the solution and connected via the crocodile clips to the copper wires of the power source.

Electrolytic bath preparation

Glass beakers (Borosil) of 100 – 1000 ml are used for the electrolytic bath. The electrolyte preparation involves the preparation of Hydrion buffer followed by subsequent addition of

precursor salts to it. As received hydriion buffer (pH = 3) sachet is dissolved in 500 ml of deionized water. The pH of the buffer has been verified by a digital pH mater from Digisun Electronics Systems (model no. 2001). The precursor salts are then added to the buffer solution in the order of copper chloride, indium chloride, gallium chloride and selenous acid. Finally, lithium chloride is added to the above solution as a supporting electrolyte, which is used to improve the ionic conductivity of the electrolyte. The solution is continuously stirred during the addition of salts. After the proper dissolution of the salts is ensured, the pH of the solution is adjusted to the range of 2.00-2.40 for the deposition by the addition of few drops of HCl. As the study aims at the fundamental understanding and hence, the optimization of parameters in pulse and pulse-reverse electrodeposition, a new electrolyte has been prepared for every deposition to ensure the consistency though the solution can be recycled for several depositions.

Potentiostatic electrodeposition

Conventionally electrodeposition is carried out in two ways, namely, potentiostatic and galvanostatic. In potentiostatic technique, the deposition is performed by applying a constant voltage between the electrodes whereas a constant current density is used in a galvanostatic process. The present study employs a potentiostatic technique wherein constant voltage has been employed during the deposition. In addition, as mentioned in section 1.11, pulse and pulse-reverse techniques have been employed for the electrodeposition of CIS/CIGS thin-films. A Dynatronix (DuPR 10-3-6) pulse power supply has been used to electrodeposit the CIS/CIGS thin-films. The deposition parameters have been varied in the ranges as shown in Table 2.2. However, the appropriate variation and optimization of these parameters pertaining to CIS and CIGS films are mentioned while discussing the relevant results.

Table 2.2: Typical variation of parameters employed for electrodeposition of CIS/CIGS thin-films

Deposition Parameter		Variation range
pH of the electrolyte		1.5 – 2.5
Forward Conditions	Cathodic voltage	-0.7 to -1.5 V
	Pulse On-time	0 – 50 ms
	Pulse Off-time	0 – 50 ms
Reverse	Anodic voltage	0 – 0.5 V

Conditions	Pulse-reverse On-time	0 – 3 ms
	Pulse-reverse Off-time	0 – 3 ms
Deposition time		5 – 60 min

Annealing of electrodeposited CIS/CIGS thin-films

Electrodeposited CIS/CIGS thin-films prepared by employing the above variation of parameters are rinsed thoroughly with DI water prior to further processing. These films are finally annealed at 550 °C under Ar atmosphere for 30 min by employing a ramping rate of 30 °/min. Annealing of electrodeposited films is a crucial process in the preparation of absorber layers as it involves following aspects:

1. Formation of chalcopyrite CIS/CIGS thin-films by the inter-diffusion of different elements. This is essential when the deposition is carried out in multiple stages wherein binary metallic selenides are expected to form owing to their lowest formation energies during deposition. These binary selenides react together during ramp of annealing to form chalcopyrite thin-films.
2. When co-electrodeposition of all the elements is performed, annealing process improves the crystallinity of as-deposited films in addition to the above mentioned process.
3. Annealing also increases the grain size of the as-deposited films which ultimately improve the transport properties of the absorber layer.
4. Most importantly, for a system like CIS/Mo or CIGS/Mo, annealing of films at temperatures above 500 °C results in the formation of a crucial thin p-type MoSe₂ layer at the interface of CIS/CIGS and Mo. This MoSe₂ layer not only promotes the adhesion between Mo and CIS/CIGS but also improves the ohmic contact as discussed earlier in section 1.7.1.

These electrodeposited and annealed CIS/CIGS films are now ready to be characterized and tested as absorber layers for thin-films solar cells.

2.2.2 Chemical bath deposition of CdS

As mentioned in section 1.11, the CIGS/CdS heterojunction has been fabricated to perform the junction characteristics. In this context, CdS has been deposited using chemical bath deposition wherein 1.5 mM aqueous solution of cadmium sulfate and 50 mM aqueous solution of thiourea are used as precursors. In one bath cadmium sulfate is complexed by aqueous ammonia. Initially white precipitate is observed which disappeared on further addition of aqueous ammonia, pH of this solution is adjusted to 11, and aqueous solution of

thiourea is then added. The solution is then kept for heating until 65 °C. Once the bath acquired the temperature, CIGS/Mo/glass electrode (substrate) is vertically inserted into the solution and deposition has been carried out for 8 min. The substrate area without CIGS deposition is masked with a scotch tape to avoid the deposition of CdS. CdS deposited CIGS films are then cleaned with DI water and used for further characterization.

2.3 Characterization techniques

Characterization of electrodeposited and annealed CIS/CIGS films has been performed using several techniques to study various properties such as morphology, composition, phase constitution, optical studies, photoresponse, etc. In this context, various techniques have been used for the characterization of CIS/CIGS films and their relevant specifications have been detailed in this section.

2.3.1 Scanning electron microscopy (SEM)

Scanning electron microscopy provides the information about the samples based on the interaction of an accelerated high energetic electron beam with the matter (samples). The interaction results in the emission of secondary electrons, backscattered electrons, X-rays, etc. Knocking out of electrons from the samples by high energetic incident electrons occurs through the momentum transfer results in secondary electrons and without any momentum transfer leads to back scattered electrons. These emissions are then detected to analyze aspects such as surface morphology, particle size, cross-sectional morphology, composition, etc. of the samples. In general, secondary electrons and backscattered electrons provide the information about the morphological aspects and elemental contrast of the samples. The analysis using the energy of emitted X-rays is usually known as energy dispersive X-ray spectroscopy (EDX or EDS) and provides the information about individual atomic composition of the samples since the energy of these X-rays depends directly on the atomic number of the atoms from which it is being emitted. EDX is a common tool to analyze the composition of samples qualitatively as well as quantitatively for atomic numbers above 10. It is also used as a local probe, for most samples, to detect the constituent elements since it spans an interaction volume of $\approx 1 \mu\text{m}^3$.

In the present study, a Hitachi – S4300SE/N field emission scanning electron microscope with an attached EDS (EDAX) detector has been used to study the morphology and composition of the samples. An accelerating voltage of 20kV is used for the electron beam during the analysis. The working distance between the sample surface and electron beam is

maintained in the range of 8 – 15 mm. As-deposited as well as annealed CIS/CIGS films on Mo/glass are coated with gold prior to the analysis and no other procedure is adopted for the sample preparation. The surface morphology of CIGS films obtained using the FESEM in the present study is shown in Figure 2.3.

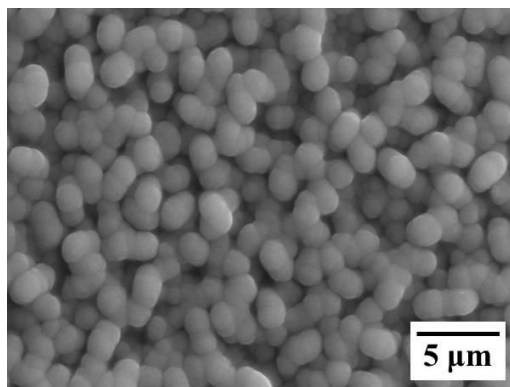


Figure 2.3: Typical SEM image of CIGS films obtained in the present study

2.3.2 X-ray fluorescence spectroscopy (XRF)

In an XRF spectrometer, sample is illuminated by an intense X-ray beam, known as the incident beam, which interacts with the sample by getting scattered or absorbed. When the high energetic X-ray hits the atom inside the sample, the electrons are ejected out of the atom leaving behind a vacant orbital. The electron from high energy states jumps to the vacant orbital by emitting the energy which is equal to the difference of their states. The emitted energy is often in the form of photons and in this case it is X-rays. These are called the characteristic X-rays since the energy of the X-rays is specific to the atom from which it is being generated. The analysis of these characteristic X-rays provide information such as the qualitative and quantitative information about atoms. If a sample has many elements present the use of a wavelength dispersive spectrometer allows the separation of a complex emitted X-ray spectrum into characteristic wavelengths for each element present. XRF is in general used for the bulk analyses of the samples since the spot size cannot be too small as in EDS (1-2 microns). This technique is advantageous when the composition of the bulk sample is required and it can also be used to determine the thickness of the films.

In the present study, a Fisherscope XRF spectrometer (XUV TDD) is used for the measurement. The source of the X-rays is a tungsten filament and a voltage of 50 kV is used to energize the X-ray beam. The spot size of the beam is 150 μm and approximately four spots are considered for the analysis on a typical 1 cm² CIGS samples.

2.3.3 X-ray diffraction (XRD)

XRD is a widely used characterization technique for the determination of crystal structures of materials. The technique uses the Bragg's law of X-ray diffraction which states that when incoming X-rays diffracted constructively by the atoms in the crystal planes, the path difference between the rays diffracted by the successive atomic planes is directly proportional to the integer multiples of incident X-ray wavelength. The powder X-ray diffractometer can be used to analyze thin film samples by means of a change in mechanical arrangement. One such arrangement is Grazing angle incidence X-ray diffractometer, where the angle between the incident X-ray beam and the thin film sample is adjusted to $0.5-1^\circ$. This arrangement exposes the film to X-rays more effectively than the substrate. X-ray diffraction provides information such as the crystallographic structure, crystallite size and preferred orientation in a polycrystalline sample.

Bruker – D8 advanced X-ray diffractometer with Cu K_α radiation ($\lambda = 1.54 \text{ \AA}$) is used to examine the phase constitution of the CIGS thin-films on Mo/glass. The diffraction patterns are collected in the range of $2\theta = 20 - 70^\circ$ with a scan rate of $0.1^\circ/\text{sec}$. The as-grown and annealed samples on Mo/glass are directly used for the XRD characterization. However, CIS thin-films grown on Mo foils did not yield considerable patterns using conventional XRD due to the larger substrate thickness ($\approx 120 \text{ }\mu\text{m}$) than the films thickness ($\approx 1 \text{ }\mu\text{m}$). In this context grazing incidence XRD (GIXRD) is employed to examine the diffraction patterns of the annealed CIS films with the same apparatus. An angle of 1° is used for the grazing incidence XRD. The diffraction patterns are collected in the range of $2\theta = 20 - 70^\circ$ with a scan rate of $1^\circ/\text{min}$. The typical XRD pattern of CIGS films obtained in the present study using Bruker – D8 X-ray diffractometer.

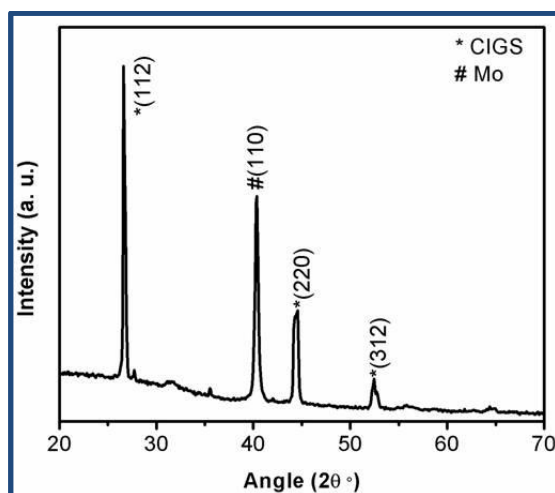


Figure 2.4: Typical XRD pattern of CIGS films obtained in the present study. The peaks are indexed using JCPDS cards.

2.3.4 Raman spectroscopy

Raman spectroscopy is a technique based on the inelastic scattering of monochromatic light, usually from a laser source. Inelastic scattering means that the frequency of photons in monochromatic light changes upon interaction with a sample. Photons of the laser light are absorbed by the sample and then reemitted. Frequency of the reemitted photons is shifted up or down in comparison with original monochromatic frequency, which is called the Raman effect. This shift provides information about vibrational, rotational and other low frequency transitions in molecules. Raman spectroscopy can be used to study solid, liquid and gaseous samples. Raman scattering has been frequently used as a nondestructive, highly sensitive spectroscopic technique in the region of spectro-chemical analysis to investigate the structural characterization of a semiconductor compound.

In the present work, micro-Raman spectroscopy is used to analyze the structure of quaternary chalcopyrite compounds, to discuss about the vibration modes of CIGS crystalline thin film. The specific purpose of the high-resolution micro-Raman studies is also to ascertain the vibrational modes of individual phases and detect any surface dispersed microcrystallites of Cu_{2-x}Se , as detection of phases like CIS, CGS, CIGS, Cu_{2-x}Se is difficult by XRD due to the negligible variation in 2θ values for the dominant (112) orientation of each phase. In the Raman analysis, the incident laser light can be focused on the sample within a spot of 1 micron in diameter. High spatial resolution is required whenever one has to deal with micrometer-size samples. Hence, micro-Raman spectroscopy is suitable for the structural analysis of samples with an active area of a few square micrometers. Micro-

Raman Spectra of CIGS thin-films are recorded using the Horiba Jobin Yvon-Lab Ram HR-800 Raman spectrometer with Ar ion laser of 514 nm, as the light source. The spectra are recorded at room temperature in the scan range of 100 - 600 cm^{-1} . In the present study microscopic focusing is used to detect Cu_{2-x}Se microcrystallites on the surface of CIGS thin-films. As-grown and annealed CIGS films on Mo/glass are directly used for the Raman analysis. Typical Raman spectrum of CIGS films containing the undesired Cu_{2-x}Se phases is shown in Figure 2.5.

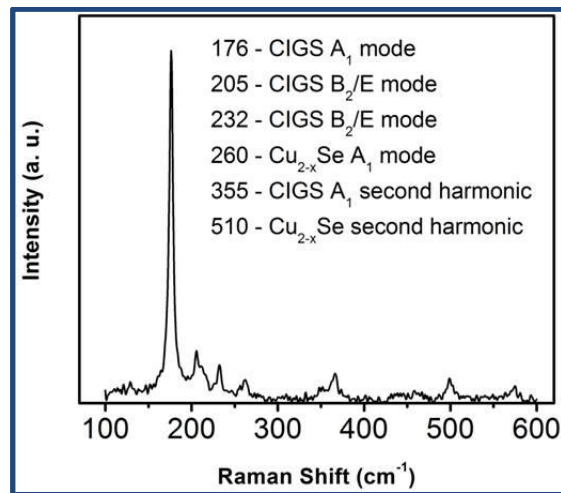


Figure 2.5: Typical Raman spectrum of CIGS films obtained in the present study. The undesired Cu_{2-x}Se secondary phase is also seen.

2.3.5 Transmission electron microscopy (TEM)

TEM is used to produce images from a sample by illuminating the sample with electrons (i.e. the electron beam) within a high vacuum, and by detecting the electrons that are transmitted through the sample. It is an analytical tool allowing visualization and analysis of specimens in the realms of 1nm. TEM reveals levels of detail and complexity inaccessible by light microscopy because it uses a focused beam of high energy electrons. It allows detailed micro-structural examination through high-resolution and high magnification imaging. It also enables the investigation of crystal structures, specimen orientations and chemical compositions of phases, precipitates and contaminants through diffraction pattern, X-ray and electron-energy analysis. Ultimately, using a TEM we can see the columns of atoms present in crystalline samples.

FEI Tecnai G² transmission electron microscope with LaB_6 filament is used to record the HRTEM images of CIGS thin-films in the present study. An accelerating voltage of 200 kV

is used to energize the electrons. The TEM is also equipped with an EDS detector from EDAX which is used for the qualitative and quantitative analysis of elemental composition in the samples. Samples are prepared by scraping the CIGS thin-films into powder form which is dispersed in ethanol. Ethanol suspension is finally dropped onto Cu grid for TEM analysis. TEM image, HRTEM, SAED and TEM-EDS of CIGS films obtained in the present study are shown in Figure 2.6.

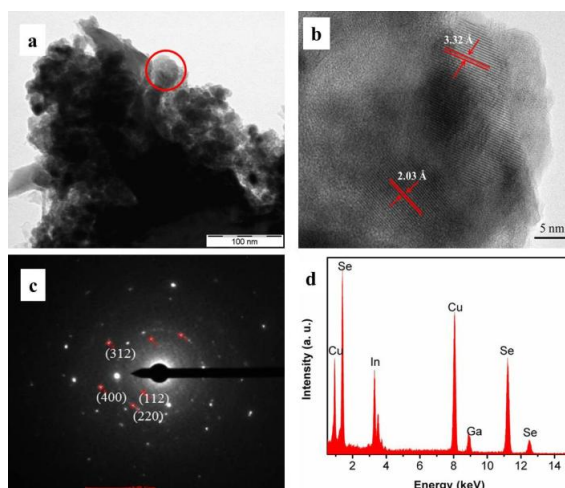


Figure 2.6: a) TEM image, b) HRTEM image, c) SAED and d) TEM-EDS of CIGS obtained in the present study.

2.3.6 Focused ion beam (FIB) milling and imaging

The highly localized sputtering or milling of the sample by the focused ion beam is the most useful feature of the FIB. Beam currents are well controlled during the sputtering of the materials and a trench of desired dimensions can be obtained. This feature allows one to image the sample's cross-section to probe the interface and determine the thickness of the thin-films. FIB imaging is very similar to SEM except that the instrument is equipped with an ion beam in addition to the electron beam to image the samples. The ion beam can be focused to a diameter of approximately 10 nm and it interacts with the material by producing secondary electrons, secondary ions and neutral atoms. The penetration depth of electrons is of the order of 100 nm whereas the ions are restricted to a thin surface layer of the order of 10-20 nm. Thus it is possible to obtain better contrast from thin films with the FIB than the SEM. It has been demonstrated that the FIB is useful for the preparation of specimens from cross sections of coatings, micrometer sized particles, powders, carbon nanotubes and complex three-dimensional specimens for the TEM.

In the present study, it is difficult to distinguish the interface of Mo/CIS due to the ductile nature of Mo foils ($\approx 120 \mu\text{m}$ thick). Hence, FIB milling and imaging is used to observe the cross-section of CIS films on Mo foils. A Carl-Zeiss FIB system (Neon-40) with Ga as the ion source is used for FIB milling and imaging. A trench is milled over the surface of CIS film to view the cross section using 30kV beam voltage. Rough milling of the trench is performed using a 2 nA beam current whereas a 500 pA beam current is used for the final smooth milling of the trench. Cross sectional images are taken by the secondary electron and ion beam at angles of 90° and 54° , respectively, with respect to the film surface. Typical FIB image showing CIS/Mo interface is shown in Figure 2.7.

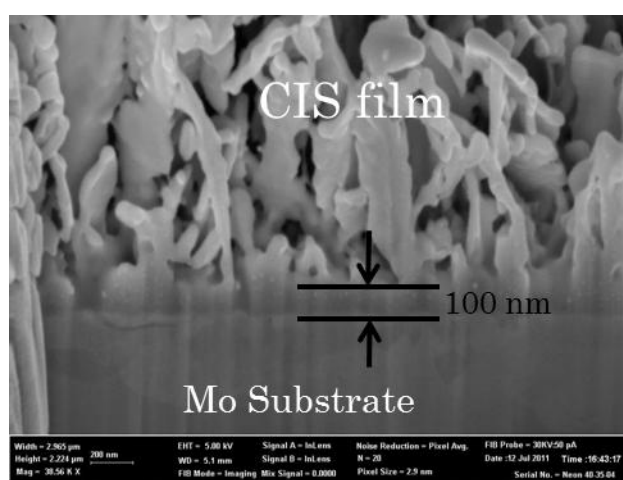


Figure 2.7: Typical FIB cross-sectional image showing CIS/Mo interface

2.3.7 Cyclic voltammetry (CV)

Voltammetry is one of the techniques employed to investigate the mechanism of redox reactions in an electrolyte. There are numerous forms of voltammetry such as potential step, linear sweep, cyclic voltammetry, etc. For each of these cases, a voltage or series of voltages are applied to the electrode and the corresponding current that flows is monitored. In a typical cyclic voltammogram or voltammetry experiments, potential is swept between the two points (V_1 and V_2) with a constant sweep rate and the respective current is observed. The behavior of I-V curve provides information about the redox reactions that happen in the solvent. The peaks observed in the I-V curves represent the reduction and oxidation of elements which are a direct consequence of Faraday's law. In general, reduction of elements happens at negative potentials and oxidation at positive potentials. Using this experiment, the reduction potential of an element or a compound or a system can be determined.

In the present study, CV experiments are performed individually for CuCl_2 , InCl_3 , GaCl_3 , H_2SeO_3 and their relevant combinations to determine the reduction of potential of the elements and their binary/ternary systems. CV experiments are carried out using Solartron electrochemical interface (SI 1287) in a three electrode electrochemical cell. The cell consists of Mo/glass as working electrode, Pt as counter electrode and saturated calomel electrode (SCE) as reference electrode. Potential is swept between -1.0 to 1.0 V with a sweep rate of 10 mV/s. Analysis of the I-V curve and the CV performed on Mo/glass electrode provided the information about the reduction potential of binary/ternary phases. Typical CV of Cu-In-Se system recorded vs. SCE in the present study is shown in Figure 2.8.

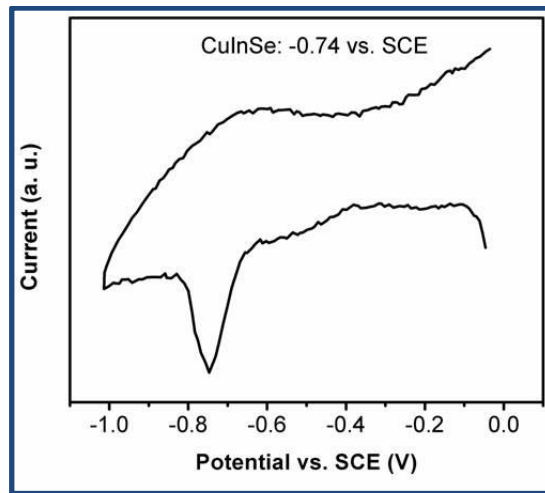


Figure 2.8: Typical CV of Cu-In-Se system recorded in the present study

2.3.8 UV-Vis-NIR Absorption spectroscopy

The optical properties of semiconductors are generally studied by absorption measurements at room temperature with a UV/Visible/NIR absorption spectroscopy. Optical bandgap (E_g) and absorption coefficient are well known related to photon energy by the following relation:

$$\alpha h\nu = A (h\nu - E_g)^n$$

where A is a constant, E_g is the band gap, and h is the Plank constant. And n takes the value 1/2 for direct allowed transition, value 3/2 for direct forbidden, and values 2 and 3 for indirect allowed and forbidden transitions, respectively. By measuring the absorbance of the materials vs. the wavelength of the incident radiation, one can calculate the absorption

coefficient (provided thickness of the film is known) and hence, the bandgap of the material. In general, an integrating sphere apparatus is used to record the reflectance spectra of the thin-films on any metal or metal coated glass substrate. The reflectance can then be converted to absorbance to determine the absorption coefficient.

Varian UV-Vis-NIR spectrophotometer (Cary 5000) is used in the present work to study the absorption properties and to determine the bandgap of the CIS/CIGS thin-films. An integrating sphere apparatus is equipped to measure the diffuse reflectance from the samples. A tungsten halogen lamp is used as the visible source with a quartz window and a deuterium lamp is used as the UV source. The spectra are recorded in the range of 200 – 2500 nm with a scan rate of 1200 nm/min. The samples with a minimum of 4cm² area are used to cover the entire illuminated window. Typical absorption spectra and the corresponding Tauc's plot to determine the bandgap of CIGS films are shown in Figure 2.9.

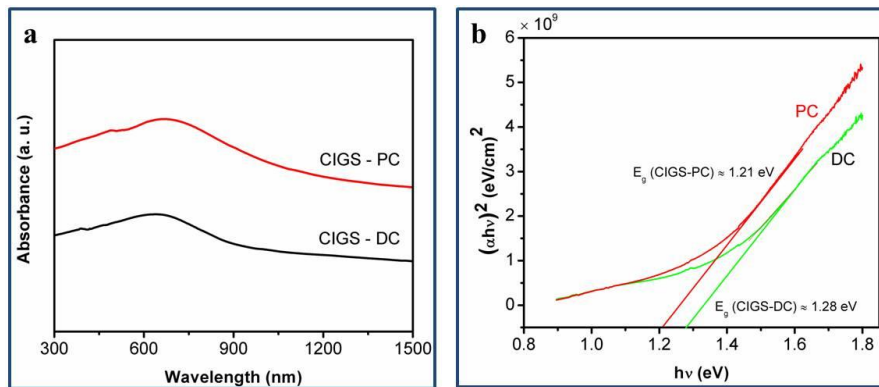


Figure 2.9: Typical absorption spectra and the Tauc's plot of CIGS thin-films.

2.3.9 Mott-Schottky analysis

When a potential is applied to a metal electrode the Fermi level of the metallic electrode shifts based on the variation in applied potential. Similarly for a semiconductor, the band edge energies change with the variation in applied potential. However, this variation is not uniform spatially, when the semiconductor is placed in a liquid or coupled with another semiconductor or metal, leading to the phenomenon called band bending. Therefore, the change in the energies of the band edges on going from the interior of the semiconductor to the interface, and hence the magnitude and the direction of band bending, varies with the applied potential. Based on the nature of the band bending and the applied potential, the double layer capacitance across semiconductor-electrolyte interface varies. Measurement of the double layer capacitance as a function of applied potential under depletion condition

yields the determination of the flat-band potential of the semiconductor by using the Mott-Schottky relationship:

$$\frac{1}{C^2} = \frac{2}{e\epsilon\epsilon_0N} \left(E - E_{FB} - \frac{kT}{e} \right)$$

where, C = capacitance

ϵ = the dielectric constant of the semiconductor

ϵ_0 = permittivity of free space

N = carrier density (electron donor concentration for an n-type semiconductor or hole acceptor concentration for a p-type semiconductor)

E = applied potential

E_{FB} = flat-band potential

The flat-band potential of the semiconductor can be found from the plot of $1/C^2$ vs. E from the above equation. Extrapolation of the curve to $C = 0$ yields E_{FB} and the slope of the curve can be used to determine the donor/acceptor density.

In addition, using the E_{FB} and N_a (acceptor density) values obtained from Mott-Schottky analysis and E_g value from absorption studies, it is possible to calculate the band-edge position by the following relation:

$$E_V = -E_{FB} + k_B T \ln \left(\frac{N_a}{N_V} \right)$$

And the density of states of valence band can be calculated by the relation:

$$N_V = 2 \left(\frac{2\pi m_h^* k_B T}{h^2} \right)^{3/2} = 6.73 \times 10^{18} \text{ cm}^{-3}$$

Using the N_V and E_g , the valence band-edge position can be calculated.

In the present study, Mott-Schottky plots are recorded in a 0.5M H_2SO_4 solution using a Solartron impedance analyzer (SI 1260) with an electrochemical interface (SI 1287) wherein Pt, Saturated Calomel Electrode (SCE) and CIGS/Mo/Glass are used as counter, reference and working electrodes, respectively. A sweep DC measurement is employed wherein the AC amplitude is fixed at 10 mV and the potential is swept in the range of -0.5 to 0.2 V vs. respective open circuit potential (OCP). OCP is noted when the electrodes are inserted for measurement without the application of potential. Measurements are carried out using different frequencies as 10, 50 and 100 kHz. A scan rate of 1 mV/s is employed with a data acquisition rate of 5s per point. Typical Mott-Schottky plot of CIGS films is shown in Figure 2.10.

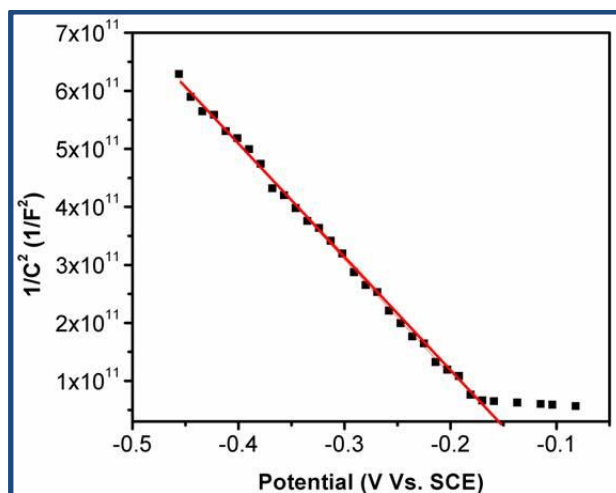


Figure 2.10: Typical Mott-Schottky plot showing the determination of Flat-band potential of CIGS thin-films

2.3.10 Photoelectrochemical (PEC) characterization

Photoelectrochemical characterization is analogous to the solid state I – V characteristics of a semiconductor. In a solid state device, the junction is formed by the p- and n-type solid state materials, whereas, in a PEC test, the junction is often formed by the combination of a semiconductor and an electrolyte. PEC characterization generally involves the interfacial electrochemical characterization of semiconductor-liquid electrolyte interface. To ascertain the performance of CIGS absorber films, devices have often been constructed by sequential deposition of a buffer layer, i-ZnO and TCO layers, followed by deposition of metal fingers. Use of distinct methods to deposit each of these layers makes it a difficult and time consuming process, besides leading to increased time for optimization of the absorber layers. A rapid assessment of photoactivity is often desired for screening semiconductor absorber layers for PV applications. This can be achieved without fabricating an entire device by using an electrolyte contact and carrying out photoelectrochemical (PEC) characterization involving a linear/cyclic potential sweep while illuminating the electrode with chopped light. Typically, a PEC test utilizes a hydrogen evolution reaction (HER), as related to PEC water reduction, to account for the photocurrent. Such a PEC test not only provides the signature of photoactivity but also demonstrates the potential utility of the CIGS based photoelectrochemical solar cells for hydrogen generation. HER requires either significant over-potentials or a suitable electro-catalyst. As CIGS thin-films do not possess either of the above, they have often yielded smaller photocurrent densities when aqueous Na_2SO_4 , K_2SO_4 , H_2SO_4 , etc. have been used as electrolytes. However, due to the simplicity

of the measurement apparatus and cost, PEC has often been used specially for the rapid assessment of CIS/CIGS thin-films.

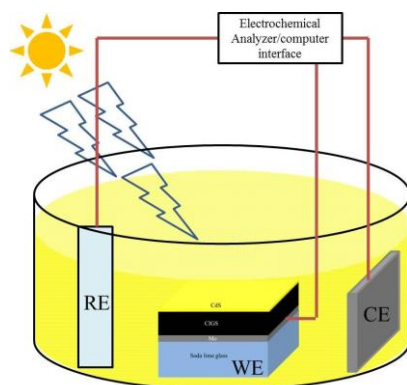


Figure 2.11: Typical photoelectrochemical characterization set-up

In the present work, the photoelectrochemical (PEC) performance of the CIS/CIGS thin films is investigated using the CH Instruments electrochemical analyzer (660A). The measurements are carried out potentiostatically in an electrochemical cell. A classical three-electrode cell with Pt foil as the counter electrode, Saturated Calomel Electrode (SCE) as the reference electrode, and the CIS/CIGS thin-film as the working electrode are used. The typical PEC set-up used in the present study is shown in Figure 2.11. Various electrolytes such as Na_2SO_4 , H_2SO_4 , sulphide + sulphite, etc. have been used as the electrolytes. Newport solar simulator with AM 1.5 Global (100 mW/cm^2) lens is used as the light source for the PEC measurements. Typical PEC I-V and amperometric I-t characteristics of a CIGS film are shown in Figure 2.12.

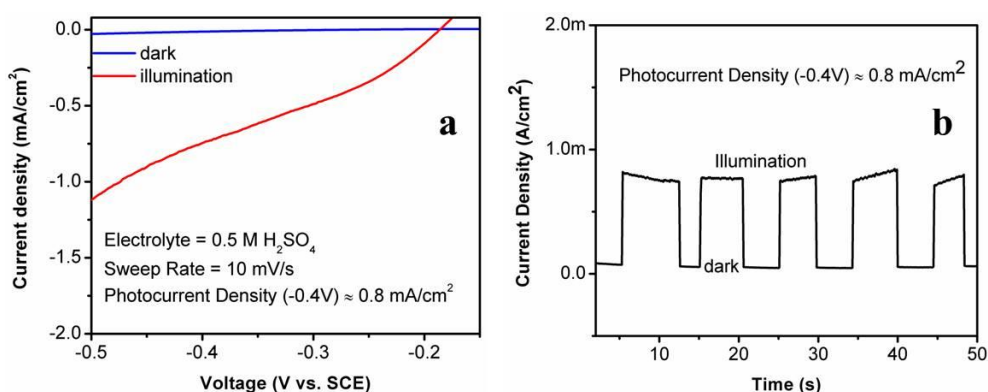


Figure 2.12: Typical PEC I-V and I-t characteristics of a CIGS film

Chapter 3

Pulse electrodeposition of CuInSe_2

Cu(In,Ga)Se_2 (CIGS) thin films are the major interest of the present study, however, the preliminary studies are focused on CuInSe_2 (CIS) thin-films. This is essentially due to the fact that the basic structure of CIGS evolves from the CIS as discussed previously. Hence, understanding the compositional control in CIS films can provide a basis for the CIGS thin-films. In addition, though CIGS films have achieved superior efficiencies over CIS films but the research on CIS has been equally active and efforts are still underway to improve the performance of these films [86, 119-129, 131-137, 165]. Hence, in the present study, pulse electrodeposition of CIS thin-films is initially performed on Mo foils using a two-electrode system. The relevant parameters such as deposition potential, pulse parameters and results pertaining to CIS thin-films are discussed in this chapter. Though the electrodeposition of CIS films is aimed using a pulse current, preliminary experiments are carried out using a direct current (DC). These preliminary studies are important owing to the two-electrode system employed in the present study in addition to the proposed elimination of selenization step.

3.1 Direct current (DC) electrodeposition of CIS thin-films

The DC electrodeposition of CIS thin-films is carried out using the precursors of CuCl_2 (4.35 mM), InCl_3 (5.56 mM), H_2SeO_3 (8.14 mM) and LiCl (0.26 M). These precursors are added to hydron buffer (pH 3) and the final pH of the electrolyte is maintained between 2.15 and 2.25 by addition of HCl. At the first instant, deposition voltage has been varied to study the variation in the content of individual elements of CIS thin-films, with a constant deposition time of 15 min. The variation in content of individual elements of CIS thin-films deposited at various voltages is shown in Table 3.1

Table 3.1: Variation in content of individual elements of CIS thin-films deposited at various applied voltages

Applied Voltage (V)	Content of individual elements (at. %)		
	Cu	In	Se
-0.7	46.21	4.78	49.01
-1.0	35.24	12.86	51.90
-1.5	27.43	21.82	50.75

A deposition voltage of -0.7 V is initially chosen to perform the electrodeposition of CIS thin-films, which is often employed using a three-electrode system, as discussed previously. It can be seen from Table 3.1 that the content of In is very low at -0.7 V with Cu and Se being rich in the films. The deposition is then performed by increasing the negative deposition voltage to -1.0 and -1.5 V. With an increased deposition voltage, the content of In increased from ≈ 5 to 22 at. % while the copper content decreased appreciably with no considerable change in Se content. This increased In content in the deposit clearly demonstrate the need of higher (more negative) deposition voltages using a two-electrode system, which is in agreement with the previously reported findings of Dharmadasa's group [166].

The morphology of the CIS thin-films deposited at different deposition voltages is shown in Figure 3.1. At a lower deposition voltage of -0.7 V, flower like particles are observed which disappeared as the voltage is increased to -1.5 V. In addition, the porosity and roughness seems to be higher at the higher deposition voltage of -1.5 V. The reasons for the porosity and roughness of the films are discussed as follows: Firstly, the continuous use of constant potential/current during the DC method leads to continuous deposition of films without any relaxation. This result in the growth of material at the existing nucleation sites takes place rather than generating new nucleation sites leading to a rough and porous deposit, as discussed for the mechanism of DC deposition in section 1.9.1. In addition, the rapid deposition rate at the higher deposition potential also causes roughness in the electrodeposited films [166]. Another important reason is the competing hydrogen evolution reaction that occurs during the deposition of thin-films at more negative deposition voltages as explained below.

For the deposition voltage of -1.5 V the current density during deposition is observed to be $\approx 30 \text{ mA/cm}^2$. This current density is then utilized to calculate the current efficiency (CE) of

the process using Faraday's law. CE is defined as the ratio between the actual amounts of material deposited to that calculated theoretically from Faraday's law. In this way, one can estimate the amount of current density/charge that is being wasted without getting utilized for the intended material deposition. In the present study, at a deposition voltage of -1.5 V, the CE is calculated to be $\approx 73\%$, indicating the wastage of current involved in the deposition process. In general, evolution of hydrogen and/or the reduction of impurities during deposition account for the wasted current/charge. The hydrogen evolution reaction is expected to be more prominent and competes with the deposition of CIS films in the present study since the deposition is carried out in aqueous electrolytes. The hydrogen bubbles evolved during the deposition get entrapped into the films at the cathode. In addition, due to the continuous supply of constant voltage during the DC deposition and the rapid deposition process, material deposition occurs covering these bubbles making it almost impossible for them to be diffused away. This entrapment of hydrogen in the deposited films not only makes them porous but also causes the embrittlement when the films are annealed at higher temperatures.

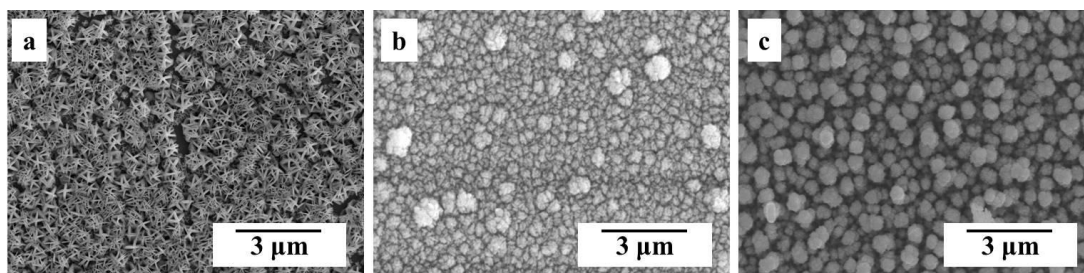


Figure 3.1: The morphology of CIS thin-films deposited at a voltage of a) -0.7, b) -1.0 and c) -1.5 V

A two-electrode system with higher deposition voltage using the DC electrodeposition though succeeded in improving the In content in the films but yielded a rough and porous morphology. In addition, films are rich in copper indicating the possibility of detrimental copper selenide phases which are often observed in copper rich samples. The films are not investigated further for the phase constitution and other properties as the DC deposition is out of the scope of present work. To avoid above mentioned difficulties, use of complexing agents, employing a three-electrode system and an additional selenization step in addition to the post deposition treatments such as etching with KCN, Br₂, etc. were practiced to fabricate phase pure compact CIS thin-films by DC electrodeposition technique. These aspects not only make the technique expensive but might also result in poor quality CIS

films. For instance, the use of KCN etching makes the film rough and use of complexing agents might result in impurities in the deposited CIS films which ultimately reduce the device performance. Hence, it would be essential to achieve stoichiometric phase pure chalcopyrite CIS thin-films by avoiding the above mentioned aspects. In this context, the present study proposes a novel pulse electrodeposition technique for the preparation of CIS thin-films as follows.

3.2 Pulse electrodeposition (PED) of CIS thin-films

The optimized potential during the DC electrodeposition of CIS thin-films are considered for the initiation of pulse electrodeposition (PED) of the CIS thin films. The same precursor concentrations are used as mentioned above for DC deposition and the pH of the electrolyte is maintained in the range of 2.15 to 2.40. The potential of -1.5 V which resulted in a considerable amount of In incorporation during the DC deposition is used for PED too with a deposition time of 15 min. The typical applied pulse-voltage and the corresponding current density curves are shown in Figure 3.2. It can be noted that there is a small positive current density ($\approx 0.5 - 1.5 \text{ mA/cm}^2$) during the pulse off-time though a zero voltage is applied (Figure 3.2b). This could be due to the presence of an electric double layer at cathode-electrolyte interface forming a capacitor of molecular dimension [77, 156]. The duty cycle for the application of pulses is varied in the range of 17 to 67 % (varied off-time with fixed on-time). Although higher voltage is employed but due to the pulse-supply the resulting effective plate potential is observed to be only in the range of 0.25 to 1 V. This decreased plate potential also resulted in the effective current density during deposition which is observed to be $\approx 5 - 15 \text{ mA/cm}^2$. The CE calculations are then carried out using Faraday's law and are found to be in the range of 90 - 95 % for various duty cycles employed. The increased CE for PED over DC affirms considerable reduction in the applied current and hence, reduced hydrogen evolution during the deposition. The PED technique employed in the present study did not result in any disruption and dissolution of the deposited film into the electrolyte, which generally happens with higher deposition voltages as previously reported [166]. The PED deposited CIS films are annealed at 550° C for 30 min under Ar atmosphere. Effect of pulse parameters on the composition of individual elements and morphology of the electrodeposited CIS films are studied in detail.

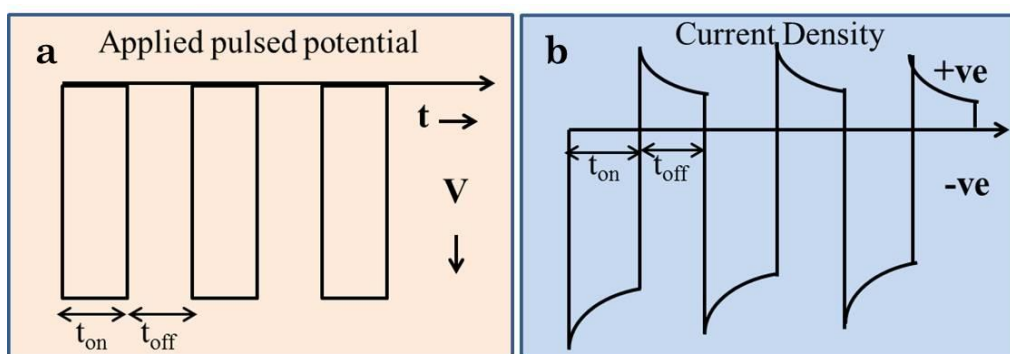


Figure 3.2: Typical curves of a) applied pulse-voltage and b) corresponding current density employed for PED of CIS films

3.2.1 Compositional analysis

Compositional analysis of the PED CIS films is investigated by energy dispersive X-ray spectroscopy. The ideal stoichiometry of copper indium diselenide is CuInSe_2 corresponding to a composition (in at. %) of Cu-25, In-25 and Se-50. The duty cycle (pulse off-time) has been varied in a systematic way to achieve ideal stoichiometry. Variation in content of individual elements in annealed CIS films and the film composition with varied duty cycle are shown in Table 3.2. A drastic variation in the In content is observed with the variation in the pulse off-time (T_{off}) from 5 ms to 50 ms. In order to further investigate, a detailed study on the optimization of In content with variation in pulse off-time is employed.

Table 3.2: Variation in content of individual elements and film composition with pulse off-time. (At constant $T_{\text{on}} = 10$ ms)

Off-time (ms)	Content (at. %)			Film stoichiometry
	Cu	In	Se	
5	24.75	40.20	35.00	$\text{Cu}_{0.99}\text{In}_{1.61}\text{Se}_{1.40}$
8	26.00	24.78	49.25	$\text{Cu}_{1.04}\text{In}_{0.99}\text{Se}_{1.97}$
10	24.25	24.69	51.25	$\text{Cu}_{0.97}\text{In}_{0.98}\text{Se}_{2.05}$
15	32.50	18.75	48.75	$\text{Cu}_{1.30}\text{In}_{0.75}\text{Se}_{1.95}$
18	37.25	15.35	47.75	$\text{Cu}_{1.49}\text{In}_{0.61}\text{Se}_{1.91}$
50	53.75	1.99	40.50	$\text{Cu}_{2.15}\text{In}_{0.23}\text{Se}_{1.62}$

As it can be seen from Table 3.2, very small amount of In content is observed in the films deposited using a T_{off} of 50 ms. Hence, a drastic reduction in the T_{off} is used for the subsequent deposition wherein a T_{off} of 18 ms is employed resulting in considerable increase in the amount of In. In a similar way, when In is observed in larger contents for a T_{off} of 5 ms, the T_{off} is increased to 8 ms and a reasonably suitable amount of In is detected as required for the formation of stoichiometric CIS films. From the above observation, the T_{off} is systematically varied between 5 and 50 ms. The results are very interesting that with an increase in the T_{off} , a decrease in In content is observed in the films. The reason for the decreased In content is explained as follows: The unintended positive current density observed in Figure 3.2b might oxidize the elements with least electronegativity from the deposited film leading to the dissolution of corresponding element into the electrolyte. In the present study, this positive current density during the pulse off-time is expected to oxidize In, since it has the lowest electronegativity among the three elements. Owing to the dissolution of In during the T_{off} , increase in T_{off} results in increased dissolution leading to the loss of In in the films. Hence, the content of In decreased with an increase in T_{off} . A similar phenomenon was reported previously during the pulse electrodeposition of CIS and CIGS thin-films [156, 167]. It is clearly observed from Table 3.2, that the film composition exhibited a stoichiometry close to ideal value for a film deposited with T_{off} values of 8 ms and 10 ms for a fixed T_{on} value of 10 ms.

3.2.2 Morphological characterization

The morphology of annealed CIS films prepared with different T_{off} values, while T_{on} is kept constant at 10 ms, is shown in Figure 3.3. The morphology of CIS films deposited at 5ms off-time appears similar to the one observed for DC deposited films, which contained elongated agglomerated particles (Figure 3.3a). The morphologies for the CIS films deposited at 8, 10 and 15 ms exhibit a flake like crystallite structure wherein 8 and 10 ms correspond to the near-ideal stoichiometric CIS films. Hence, it can be noted that the stoichiometric CIS films with flake like crystallites morphology are achieved with successful optimization of parameters. This structure is novel and to the best of author's knowledge, is being reported for the first time for CIS thin films. Such a flake-like morphology is expected to be advantageous since they expect to have more surface area of the film which is exposed to light, thereby causing improvement absorption of light and hence, photoresponse. This is expected to be particularly advantageous at the device stage since it facilitates increase in the p-n junction area of the solar cell which directly influences its performance. Zhou et al., have achieved similar morphology and reported that the CZTS

flower like particles increased the performance of the device and also observed the reduction in electrical resistivity [168]. In the present case, flake like crystallite structure is favorable to increase current carrier concentration, electron transmission and thus induce the generation of photocurrent [168]. The formation of flake-like crystallite structure could be due to the dissolution of In that takes place during the off-time of pulse electrodeposition of CIS films, as previously mentioned. As it can be seen from Figure 3.3, the bead-like structures are formed at the beginning which are then transformed to flake-like nature with the increase in off-time until 10 ms. However, with further increase in off-time the size and area of the individual flakes decreased and ultimately the complete dissolution of structure is observed at 50 ms. This could be attributed to the dissolution of In which increases with an increased T_{off} . A systematic manipulation of pulse parameters resulted in a stoichiometric CIS thin-films with a novel flake like morphology.

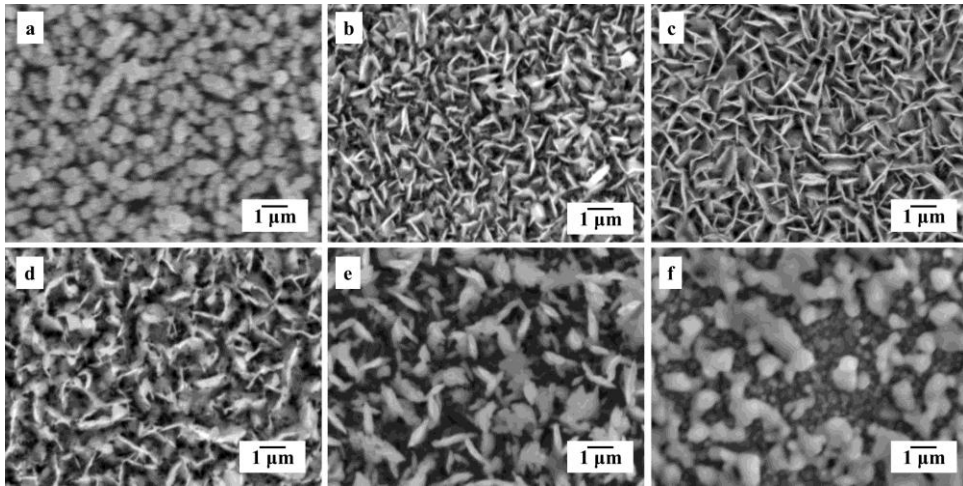


Figure 3.3: Surface morphology of pulse electrodeposited and annealed CIS films at a T_{off} of a) 5, b) 8, c) 10, d) 15, e) 18 and f) 50 ms (at fixed $T_{on} = 10$ ms)

3.2.3 X-ray diffraction of PED CIS films

XRD patterns of annealed CIS films deposited with the variation of T_{off} are shown in Figure 3.4. Though all the samples are characterized the relevant difference is observed for the samples with considerable variation in the composition. Hence, the relevant spectra are discussed here. XRD spectra for all the samples show that the strongest peak corresponds to the (110) preferred orientation of the molybdenum substrate (JCPDS diffraction file no. 42-1120). In addition, the chalcopyrite structure of CIS thin-films (JCPDS diffraction file no. 35-1102) is confirmed by the XRD patterns with preferred diffraction orientation to (112). It has already been explored by several researchers that CIS thin-film has preferred diffraction

orientation to (112); however, it varies with the orientation of the substrate [35, 39, 165]. Orientations of CIS film, corresponding to (220) and (312) are also seen in the patterns. The preferred (112) orientation of CIS thin-films is compared with the variation in T_{off} in the present study. An increase on T_{off} from 8 to 10 ms resulted in an increase in the peak intensity of (112). This is certainly expected as the films deposited at a T_{off} of 10 ms have near ideal stoichiometry. However, with a further increase in T_{off} to 18 and 50 ms resulted in very small intensities for (112) peak since these films have lower In content than the desired amount to form the chalcopyrite structured CIS. Undesired copper selenide phases such as Cu_{2-x}Se , which are generally observed in the DC electrodeposited CIS films, are not observed from the XRD patterns in the present PED deposited CIS films.

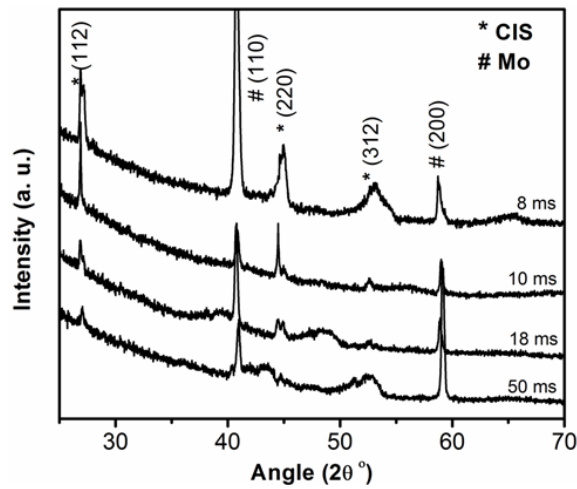


Figure 3.4: XRD patterns of annealed pulse electrodeposited CIS thin-films with varied T_{off}

3.2.4 Micro-Raman analysis of PED CIS films

As discussed previously in section 2.3.4, the specific purpose of the high-resolution micro-Raman studies in the present study is not only to ascertain the vibrational modes of individual phases but also to detect any surface dispersed microcrystallites of Cu_{2-x}Se . In general the detection of phases like CIS, CGS, CIGS, Cu_{2-x}Se is difficult by XRD due to the negligible variation in 2θ values for the dominant (112) orientation of each phase and these can easily be detected by micro-Raman studies [140]. Figure 3.5 shows the Raman spectra of electrodeposited and annealed CIS films for varied T_{off} from 8 to 50 ms. The spectra contain well-defined peaks at wavenumbers of 176, 215, 234 and 260 cm^{-1} . The peaks at 176, 215 and 234 cm^{-1} are attributed to the A_1 , B_2 and E modes of CIS films and the peak at 260 cm^{-1} is attributed to the A_1 mode of Cu_{2-x}Se [140]. Though the Cu_{2-x}Se phase is not observed in XRD, is detected from the Raman spectra in the PED CIS films. If the spectra

are carefully compared, the A₁ mode of CIS takes the maximum peak for the films deposited at a T_{off} of 10 ms and has the minimum amount of copper selenide phase. The films deposited at a T_{off} of 8 and 18 ms have more copper selenide than CIS. Further increase in off-time to 50 ms resulted in only copper selenide films than the desired CIS films which corroborates the compositional analysis wherein the films deposited at 50 ms off-times have hardly any In content. However, the formation of undesired copper selenide phase and its presence even after annealing is detrimental to the performance of CIS films since being a degenerate semiconductor, Cu_{2-x}Se is highly conductive and results in high dark currents [61, 79]. In addition, Cu-Se phases generally segregate to the grain boundaries thereby limiting the grain growth which increases the scattering to the minority carriers [62]. Further, these phases are also expected to segregate to the surface of the films which might eliminate the photovoltaic nature of the CIS thin-films completely [61]. These results from Raman spectra indicate that the PED technique allows good control over phase formation by suitably manipulating the pulse parameters to obtain the required phases. In addition, it is suggested that stoichiometric chalcopyrite CIS thin-films with a novel flake-like morphology are successfully prepared using the pulse condition of T_{on} = 10 ms, T_{off} = 10 ms with a deposition potential of -1.5 V.

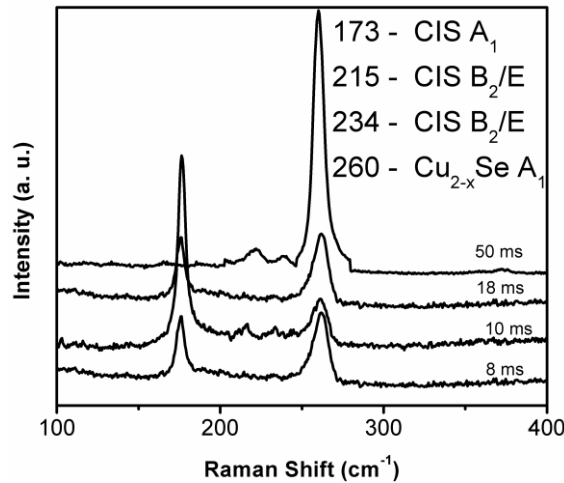


Figure 3.5: Raman spectra of annealed pulse electrodeposited CIS films with varied T_{off}

3.2.5 Cross-sectional analysis using FIB

Focused ion beam analysis is employed to study the cross section of the Mo-CIS thin-film interface. The optimized chalcopyrite thin-film is milled and imaged using FIB. A FIB cross sectional image of the CIS film deposited at 10 ms off-time is shown in Figure 3.6. Cross-sectional analysis of the films is not only intended to determine the thickness but also to

examine the interface carefully since a flake-like morphology is observed. It can be clearly observed that there is a well-defined interface with a continuous layer between the Mo foil (substrate) and the deposited CIS layer. The thickness of the CIS layer around this Mo-CIS interface is of the order of 100 nm. The presence of this interface confirms the fact that a complete coverage of CIS on the Mo surface initially occurs and Mo is not exposed to light during the measurement of photoelectrochemical response of the CIS thin films. The lower dark current during the photoelectrochemical performance confirms the same, as shown later in Figure 3.8, because being a metal; Mo is expected give very high dark currents upon exposure to the electrolyte. In addition, though FIB analysis is also intended to infer the film thickness but due to the high energy of the ion beam the flakes suffered a local melting on the surface. This local melting made it difficult to conclude the thickness of CIS films. However, the flake height (thickness) is approximately observed to be 0.8 to 1 μm .

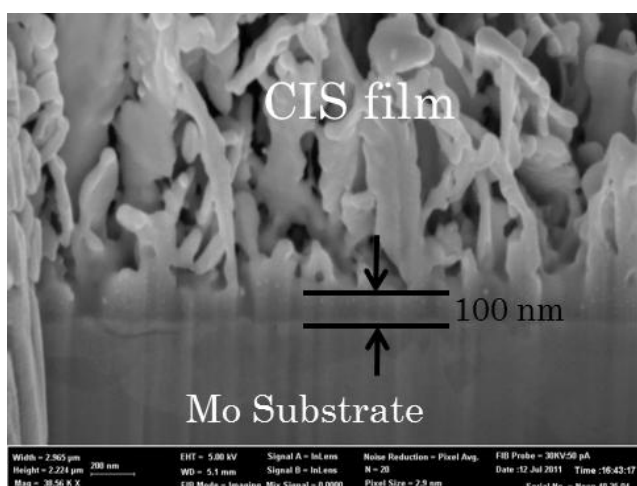


Figure 3.6: Cross-sectional image of optimized pulse electrodeposited annealed CIS thin-film

3.2.6 Optical studies – Determination of bandgap

UV-Vis-NIR diffuse reflectance spectroscopy is used to measure the optical absorption of optimized annealed CIS thin-films. The absorption spectrum is then used and $(\alpha h\nu)^2$ vs. $h\nu$ (Tauc's plot) is plotted as shown in Figure 3.7. Extrapolation of the linear section of this plot yields a bandgap of 1.02 eV, which is close to the reported value of 1.04 eV for CuInSe_2 [13, 14].

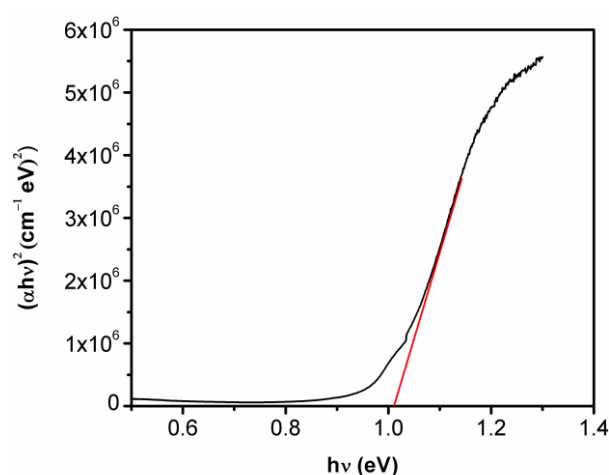


Figure 3.7: Tauc's plot of optimized pulse electrodeposited annealed CIS thin-films

3.2.7 Photoelectrochemical analysis

The photoelectrochemical performance of the electrodeposited CuInSe₂ thin films is studied in a 0.1 M Na₂SO₄ solution (pH = 4.0). Current vs. potential curves are obtained in the range of 0 to -1.0 V vs. SCE with a potential sweep rate of 10 mV/s. Figure 3.8 shows the current-potential curves under dark and AM 1.5 G solar simulated light for the optimized annealed CIS thin-film. The I-V curve is similar to the one reported previously [92]. An increase in cathodic photocurrent, a characteristic of a p-type semiconductor, is observed with increase in cathodic potential. This behavior is attributed to an incomplete photonic conversion, which causes a recombination of charge carriers at the grain boundary of the semiconductor [156, 169]. Photocurrent density observed at a potential of -0.6 V vs. SCE is $\approx 20 \mu\text{A}/\text{cm}^2$. Ugarte *et al.*, observed multinuclear, spherical particle like growth in morphology for the CIS film and reported a photocurrent density of $\approx 10 \mu\text{A}/\text{cm}^2$ at -0.6 V, however glycine acid and EDTA are used during deposition to improve the photocurrent of CIS thin films [92]. Zhou *et al.*, have achieved similar morphology for CZTS films and reported that the CZTS flower like particles increased the performance of the device and also observed the reduction in electrical resistivity [168]. In the present study, the reason for the increment in the photocurrent can be attributed to the flake like crystallite structure of the CIS films achieved through appropriate control of pulse parameters. Flake like crystallite structure is favorable to increase current carrier concentration, electron transmission and thus induce the generation of photocurrent. In addition to the flake like crystallite structure, considerable reduction of undesired Cu_{2-x}Se secondary phases, achieved with suitable variation of pulse parameters, is one of the significant factors in the improvement of photocurrent. Kemell *et al.*, observed that the photoactivity of CIS films was completely lost and have attributed that

it might be due to the segregation of the detrimental Cu_{2-x}Se phase to the surface or at the grain boundaries [61]. Also, the interfacial adhesion between the CIS thin film and the Mo substrate becomes very poor, resulting in an adverse effect on the interface resistance which deteriorates the performance of the solar absorber layer [161]. Hence in the present context, with suitable manipulation of pulse parameters Cu_{2-x}Se phases are reduced which resulted in improved photoelectrochemical performance of the CIS thin films.

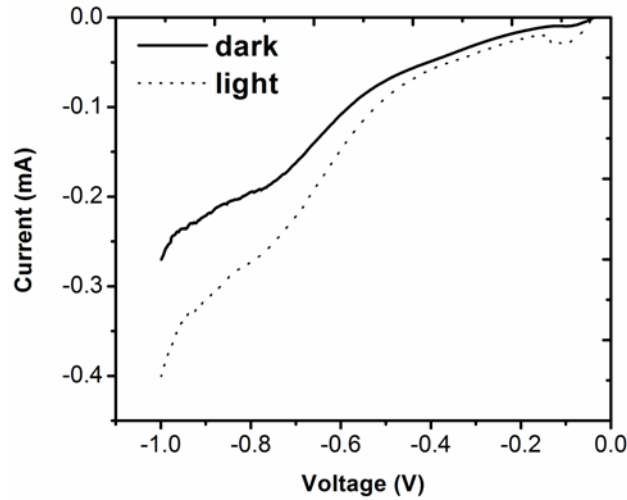


Figure 3.8: PEC measurements: I-V characteristics of the annealed CIS film deposited at the optimized pulse condition under AM 1.5 G solar simulated light.

The photocurrent at -0.8 V is observed to be higher than that at -0.6 V and has been measured for all the CIS films deposited with the variation in T_{off} . The plot of photocurrent vs. pulse off-time is shown in Figure 3.9. It can be clearly observed that the photocurrent increased with increase in T_{off} to 10 ms and then decreased with an increase in T_{off} to 50 ms. This could be attributed to the near-ideal stoichiometry as well as the flake-like morphology achieved for the films at 10 ms off-time. The larger/smaller In content and hence, the deviated film composition from the ideal stoichiometry for the other values of T_{off} resulted in lower photocurrent.

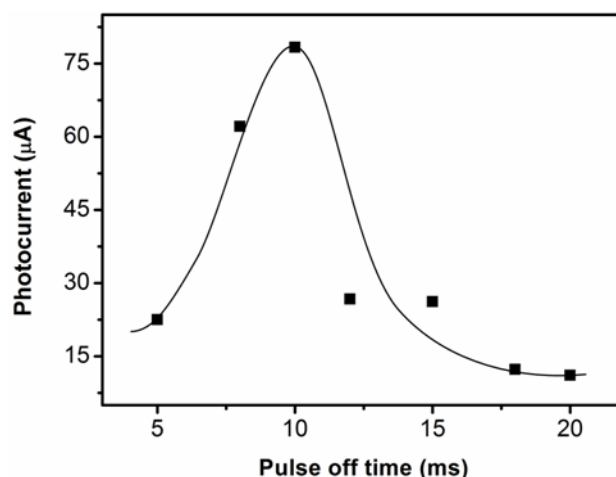


Figure 3.9: Variation in photocurrent density (at -0.8 V) of pulse electrodeposited annealed CIS thin-films with varied T_{off} .

3.3 Conclusions

Optimized CIS thin-films with controlled Cu, In and Se content have been successfully deposited by pulse electrodeposition technique at a cathodic potential of about -1.5 V with the optimized pulse condition being $T_{\text{on}} = 10$ ms and $T_{\text{off}} = 10$ ms. A two electrode system is considered over a three electrode system as mentioned earlier which is economical for scaling up. The optimized CIS thin-films contained flake like crystallite structure which is advantageous because of the high surface area that improves the photoresponse of the film. Flake like crystallite structure is also expected to be advantageous at device stage due to the possible increment in the junction area which further improves the performance of the solar cell. The chalcopyrite structure of the CIS films is confirmed from the XRD and Raman spectroscopic measurements. From the Raman spectra it is also concluded that the undesired secondary phase of Cu_{2-x}Se can be reduced by varying the pulse parameters and is observed to be minimum for the electrodeposited CIS with optimized pulse condition. Optical absorption studies confirmed the bandgap of CIS films as 1.02 eV which is similar to the value reported earlier. Photoelectrochemical response of the CIS films is studied and a photocurrent density of $\approx 20 \mu\text{A}/\text{cm}^2$ is obtained for the CIS film which is deposited at the optimized pulse condition.

Chapter 4

Pulse electrodeposition of Cu(In,Ga)Se₂

Pulse electrodeposition (PED) of Cu(In,Ga)Se₂ (CIGS) thin-films is one of the principal objectives of the present study. In general, optical, electric and electronic properties which influence the ultimate device performance depend directly on the composition and morphology of the CIGS thin-films. Hence, the control over these aspects is an essential concern to look at while fabricating these films. In this context, the relevant advantages of PED and the studies pertaining to the deposition of CIGS films by this technique have been extensively reviewed in previous chapters. Very few reports have appeared on the PED of CIGS films though the technique has shown greater compositional control over the elements in this complex quaternary system. This could be due to the complexity involved in a PED technique because of its additional variables such as pulse on-time (T_{on}) and pulse off-time (T_{off}) compared to a direct current (DC) method. Hence, it is important to understand the variation in composition and morphology of deposited films with the variation in T_{on} and T_{off} so that a suitable manipulation of these variables allows to achieve the desired composition and morphology. The present study focuses on the systematic variation in pulse parameters to achieve stoichiometric phase-pure compact CIGS and also proposes a plausible mechanism to understand the characteristics associated with the compositional and morphological control. In this context, the present chapter covers the following topics:

1. Cyclic voltammetry of Cu-In-Ga-Se system – to infer the reduction potentials
2. Pulse electrodeposition (PED) of CIGS films – optimization of parameters to fabricate stoichiometric compact phase pure CIGS films and to understand the plausible mechanism. Direct current (DC) electrodeposition of CIGS thin-films is also performed to compare the properties between DC and PED plated CIGS films

4.1 Cyclic voltammetry (CV) of Cu-In-Ga-Se system

4.1.1 CV of Cu-Se, In-Se, Ga-Se, Cu-In-Se, Cu-Ga-Se and Cu-In-Ga-Se

The reduction potentials of individual Cu, In, Ga and Se using cyclic voltammetry (CV) have been reported previously. Their possible chemical reduction reactions along with their reduction potentials are mentioned in section 1.10. The CV of binary/ternary phases of Cu-In-Ga-Se system is predominantly interesting due to the fact that the binary selenides of Cu, In and Ga are expected to get reduced at a more positive potential than the individual elements. In this context, CV of the binary/ternary/quarternary systems such as Cu-Se, In-Se, Ga-Se, Cu-In-Se, Cu-Ga-Se and Cu-In-Ga-Se have been investigated in detail. The experimental procedure adopted for carrying the CV of these systems is mentioned in section 2.3.7. The precursor concentrations are used in the same range as shown in Table 2.1. In addition, EDS has been used to detect the qualitative presence of the corresponding elements on the Mo electrode after performing the CV.

Figure 4.1 shows the CV curves of the binary and ternary systems from various combinations of CuCl_2 , InCl_3 , GaCl_3 and H_2SeO_3 . The first of their combination is the mixture of $\text{CuCl}_2 + \text{H}_2\text{SeO}_3$ and the respective CV is shown in Figure 4.1a. It clearly reveals a cathodic reduction peak at -0.32 V vs. SCE and is attributed to the reduction of Cu-Se binary phase as previously reported [88, 98, 156, 170]. The CV of Cu-Se system also suggests the formation of Cu-Se binary phase which precedes the formation of CIS/CIGS during the co-electrodeposition [98, 170]. The CV of the mixture of $\text{InCl}_3 + \text{H}_2\text{SeO}_3$ is performed for the possible detection of In-Se phases. CV of In-Se system (Figure 4.1b) does not reveal any peak even though the potential sweep is increased to -0.9 V compared to -0.5 V employed for Cu-Se system. In a similar way, no reduction peak is observed in the case of Ga-Se system too (Figure 4.1c). These results clearly indicate that In or Se or In-Se and Ga or Se or Ga-Se are not reduced directly onto Mo even if the potential sweep is increased towards more negative values. The results are in consistent with the previous reports that In or Ga and their related binary phases with Se do not directly get deposited onto Mo substrate [71]. The co-deposition of CIS/CIGS often starts with the deposition of Cu and/or Cu-Se followed by the incorporation of In and Ga. It is inferred that the reduction of In and Ga onto Mo occurs only with the aid of Cu suggesting the necessity of Cu's reduction at the initial stages of deposition. Hence, in the present study, In-Se and Ga-Se systems did not produce a reduction peak onto Mo.

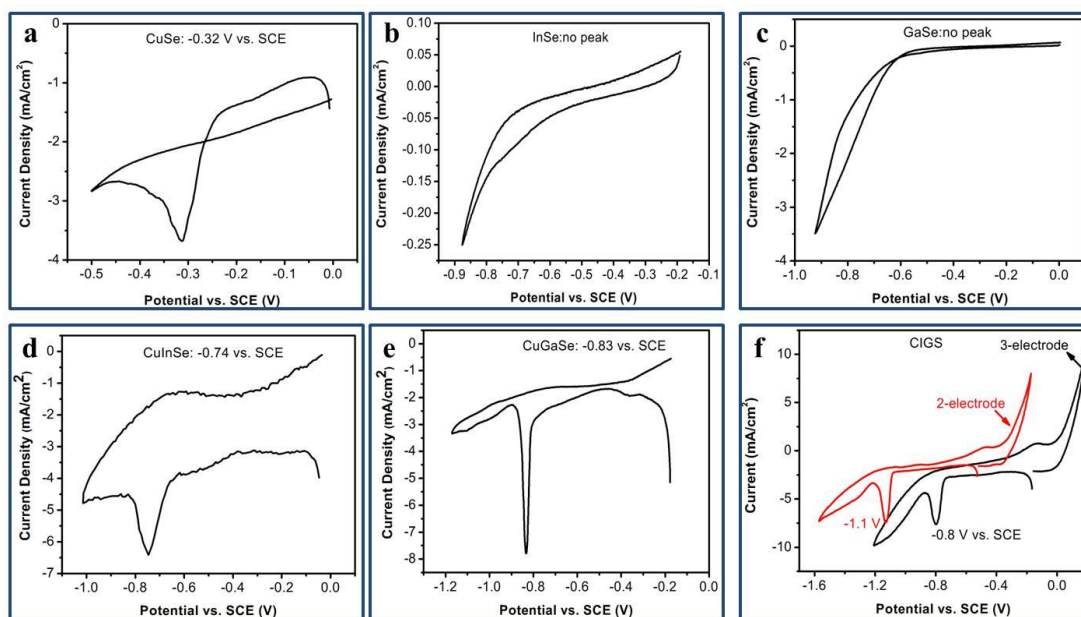


Figure 4.1: Cyclic voltammetry curves of a) $\text{CuCl}_2 + \text{H}_2\text{SeO}_3$, b) $\text{InCl}_3 + \text{H}_2\text{SeO}_3$, c) $\text{GaCl}_3 + \text{H}_2\text{SeO}_3$, d) $\text{CuCl}_2 + \text{InCl}_3 + \text{H}_2\text{SeO}_3$, e) $\text{CuCl}_2 + \text{GaCl}_3 + \text{H}_2\text{SeO}_3$ and f) $\text{CuCl}_2 + \text{InCl}_3 + \text{GaCl}_3 + \text{H}_2\text{SeO}_3$ solutions.

To further investigate the reduction mechanism of CIS and CIGS films, the cyclic voltammogram experiments are conducted on the combination of Cu-In-Se, Cu-Ga-Se and Cu-In-Ga-Se. Figure 4.1d shows the cyclic voltammogram of the mixture of $\text{CuCl}_2 + \text{InCl}_3 + \text{H}_2\text{SeO}_3$. The CV shows a cathodic reduction peak at a potential of -0.74 V vs. SCE , which can be attributed to the reduction of Cu-In-Se phase. This result is also in consistent with previous reports [156, 170]. However, a detailed of the Cu-In-Se is further employed which discusses the mechanism corresponding to CIS formation as explained later. In addition to the CIS system, CGS system has also been investigated using CV and is shown in Figure 4.1e. Similar to the CIS system, CV of CGS system shows a reduction peak at -0.83 V vs. SCE which corresponds to the reduction of Cu-Ga-Se. It can be noted from the CIS and CGS systems that the CGS observed to have a more negative reduction potential than the CIS. It is well known that Ga has more negative reduction potential than that of In due to the lower electronegativity. Hence, the shift in the reduction potential between CIS and CGS is logical. Ultimately, the mixture of $\text{CuCl}_2 + \text{InCl}_3 + \text{GaCl}_3 + \text{H}_2\text{SeO}_3$ is studied, which has a cathodic reduction peak at a potential of -0.8 V vs. SCE corresponding to CIGS, as shown in Figure 4.1f.

The cyclic voltammogram studies of the above systems are consistent with the previous reports when the experiments were carried out using a three-electrode system wherein SCE is used as reference electrode. However, as a key execution, the present work avoids the use of reference electrode and employs a two-electrode system for the electrodeposition of CIS/CIGS thin-films. Hence, it is relevant to explore the cyclic voltammetry of the CIGS systems using a two-electrode system for the observation of possible deviations in the reduction potential compared to a three-electrode system. Figure 4.1f shows the CV of CIGS system using two- and three-electrode systems. As previously mentioned, the reduction peak of CIGS is observed to be around -0.8 V vs. SCE when a three-electrode system is employed. However, the reduction peak of CIGS is detected at -1.1 V with the use of a two-electrode system, indicating considerable shift of about -0.3 V. Apparently, the potential shift is approximately same as the standard electrode potential of SCE vs. normal hydrogen electrode (NHE). However, experiments with different systems might be required to verify the same. The considerable shift in the reduction potential of the CIGS system is an interesting point and supports the use of more negative reduction potential for the deposition of CIS/CIGS thin-films when a two-electrode system is employed. The inference also explains the use of -1.5 V as the applied deposition voltage for the electrodeposition of CIS thin-films, discussed in the previous chapter. It is meaningful to use a slightly more deposition voltage than the reduction potential of the corresponding system, since the applied voltage is simultaneously used for the possible reduction of impurities in the electrolyte and/or reduction of H^+ ions to H_2 (dominant when aqueous electrolytes are used), often leading to lower values for current efficiency.

4.1.2 CV of Cu-In-Se and Cu-In-Ga-Se: Multiple sweeps

Cyclic voltammetry of CIS and CIGS is discussed in the above section; however, the results presented are one of the random runs performed for the corresponding systems. Often multiple sweeps are required to observe the change in reduction peaks which reveal the details of possible mechanism. Hence, to investigate the detailed mechanism, seven sweeps of the CV for CIS and CIGS systems are performed using the same solution on the same electrode. The number of sweeps, however, does not need to be only seven, depends on the stabilization of the reduction peak at the reduction potential of the corresponding system.

Figure 4.2a shows the cyclic voltammetry of $CuCl_2 + InCl_3 + H_2SeO_3$ with increased number of sweeps. During the first sweep of the CV two cathodic peaks around -0.3 and -0.5 V corresponding to the reduction of Cu-Se and In-Se phases are observed. It is important

to note that Cu-Se reduction is initiated first since the reduction of In-Se does not happen without the presence of Cu, as discussed above. As the number of sweeps increased the peak at -0.3 V disappeared and the peak at -0.5 V shifted to more negative values considerably. Further increase in number of sweeps has shown the stabilization of the peak around -0.7 V with an observed increase in the area of the peak. The behavior clearly demonstrates the mechanism of CIS electrodeposition as reported previously [98]. The reduction of Cu-Se and In-Se binary phases occurs at the initial stages of deposition followed by the reduction of overall CIS. This set of cyclic voltammogram studies indicate that Cu is electrodeposited first on the working electrode, which facilitates the deposition of subsequent In for the deposition of CIS. Similarly, cyclic voltammogram of $\text{CuCl}_2 + \text{InCl}_3 + \text{GaCl}_3 + \text{H}_2\text{SeO}_3$ is performed for multiple sweeps, as shown in Figure 4.2b. Two well-defined cathodic reduction peaks at -0.3 and -0.5 V are observed in this case too, which are attributed to the reduction of Cu-Se and In-Se peaks. With increasing the number of sweeps the peak at -0.3 V disappeared similar to the case of CIS system. However, a continuous shift of the peak at -0.5 V towards more negative values is observed with increased number of sweeps. This could be attributed to the more negative reduction potential of Ga which could possibly be incorporated into Cu-In-Se system leading to the formation of CIGS. The observation of peaks and the possible mechanism are in consistent with the previous reports [71, 156].

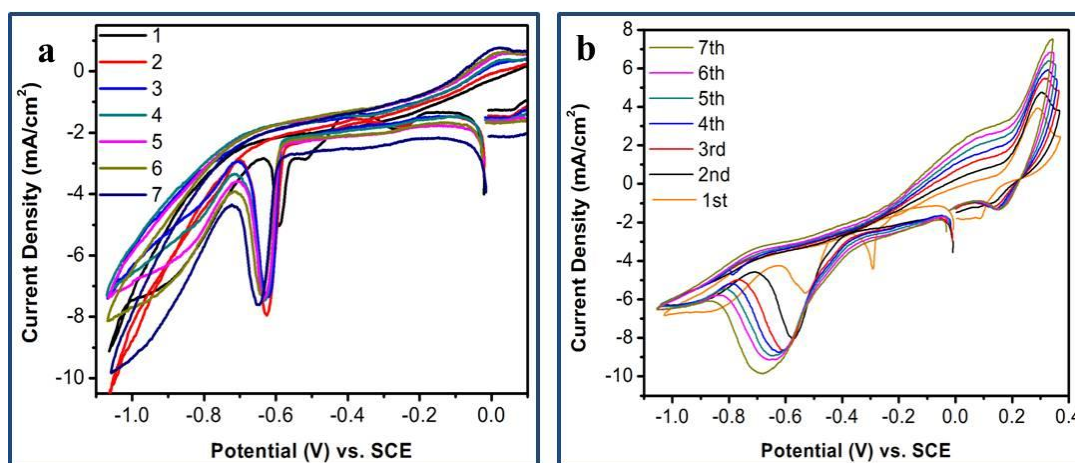


Figure 4.2: Multiple sweeps of CV of a) Cu-In-Se and b) Cu-In-Ga-Se systems.

In conclusion, cyclic voltammetry studies of different systems have been performed to infer the reduction potentials of binary/ternary/quarternary phases and to understand the plausible mechanism for the formation of CIGS thin-films. In addition, shift in reduction potential of CIGS has been observed when a two-electrode system is used by avoiding the reference

electrode. Hence, it is suggested to use a more negative deposition voltage when the deposition of films is aimed using a two-electrode system. These results are used for the initiation of pulse electrodeposition of CIGS thin-films as discussed in the following sections.

4.2 Pulse electrodeposition of CIGS

Pulse electrodeposition (PED) of CIGS thin-films is performed using a two-electrode system on Mo/glass substrate. Preparation of electrolyte and make of electrodes has been detailed in section 2.2.1. The precursor concentrations are chosen based on the optimized reports previously available for the formation of chalcopyrite CIGS thin-films [95]. CuCl_2 (3 mM), InCl_3 (6.4 mM), GaCl_3 (8.5 mM) and H_2SeO_3 (6 mM) are respectively considered for the present case with a final pH maintained between 2.20 – 2.40. The pulse parameters are varied around the optimized set of conditions achieved for the CIS thin-films. Consequently, a variation in duty cycle is employed in the range of 40 to 67 % by the variation in pulse off-time. In addition to the PED technique, direct current (DC) deposition is also performed using the same precursor solutions. The DC deposited films in the present study are referred as PED plated films with a duty cycle 100 % since it indirectly corresponds to an off-time of 0 ms. CIGS thin films are electrodeposited using a deposition voltage of -1.5 V for a deposition time of 15 min at room temperature. Schematic of applied pulse voltage and corresponding current density are similar to the one used for CIS films as shown in Figure 3.2. The need for more negative deposition voltage has been discussed in the previous sections. Electrodeposited CIGS films are annealed under Ar atmosphere for 30 min and are comprehensively characterized.

4.2.1 Compositional analysis of CIGS thin-films

The composition of the pulse electrodeposited annealed CIGS thin-films, as determined by EDS, is shown in Figure 4.3a. In addition, the ratios of $\text{Ga}/(\text{In}+\text{Ga})$ and $\text{Cu}/(\text{In}+\text{Ga})$, which are the decisive factors for efficiency of CIGS solar cell, are shown in Figure 4.3b. The figures also represent the composition of DC deposited CIGS films, shown as 100 % duty cycle. The DC deposited CIGS films are Cu rich in composition and have very less In and Ga. This has often been the case during the DC electrodeposition of CIGS, since In and Ga require higher concentration of respective precursors in addition to the higher deposition voltage. This is also one of the reasons to perform a multi-step deposition to achieve the desired contents of In and Ga into the films. In addition, a complexing agent is frequently used to incorporate sufficient In and Ga content into the films. The DC technique in the

present study explores the same concentration of precursors employed for PED of CIGS films and resulted in Cu rich CIGS films. As a result, the respective ratios of Ga/(In+Ga) and Cu/(In+Ga) are calculated to be 1.92 and 0.19, deviating from the desired range as reported [26, 28, 142, 171]. The stoichiometry of the annealed DC deposited CIGS films, is shown in Table 4.1, which is deviated from the desired stoichiometry of CIGS films.

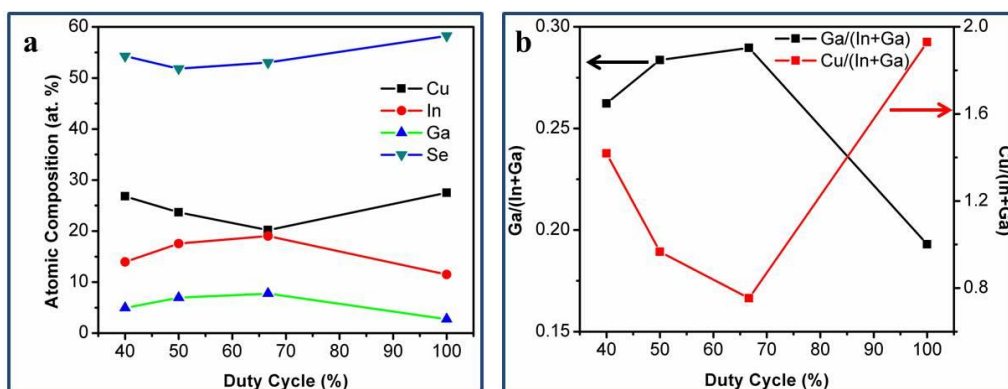


Figure 4.3: Variation in a) elemental composition and b) corresponding Ga/(In+Ga) and Cu/(In+Ga) of PED electrodeposited annealed CIGS thin-films with varied duty cycle

On the other hand, PED electrodeposited CIGS films are observed to have higher In content and hence, lower Cu content in the films, however, the contents vary with a varied duty cycle. As it can be seen from Figure 4.3a, the contents of In and Ga decreased by decreasing the duty cycle from 67 to 40 % whereas the content of Cu increased slightly and does not show a considerable effect on Se. This behavior can be explained using the current-time transient behavior during the PED shown in Figure 3.2. It shows that although applied potential pulses are square in nature, the corresponding current density form is differently modulated. This could be due to the presence of an electric double layer at cathode-electrolyte interface forming a capacitor of molecular dimension [77, 156]. In addition, the current is observed to change from negative during T_{on} to positive during T_{off} , which indicates the film deposition process is a combination of cathodic deposition and anodic dissolution. Accordingly, in the present case, In and Ga dissolve back into the electrolyte due to their lowest electronegativity values corresponding to the positive current during the non-pulse duration i.e. T_{off} , leading to the loss of In and Ga in the deposited film. Similar phenomenon of dissolution of In has been observed during the preparation of CIS/CIGS thin-films [156, 167]. In addition, the similar decrease in In is observed during the pulse electrodeposition of CIS thin-films as discussed in the previous chapter. The stoichiometry of CIGS films deposited at various duty cycle values of 40, 50 and 67 % are shown in Table

4.1. It can be seen that the films deposited at 50 % duty cycle has slightly Cu poor composition with a near ideal stoichiometry as desired for the solar cell application. In addition, the corresponding ratios of Ga/(In+Ga) and Cu/(In+Ga) are approximately 0.28 and 0.96, desirable for high efficiency CIGS absorber layer, at the same duty cycle. It can be suggested that the variation in duty cycle during the pulse electrodeposition of CIGS thin-films has provided a convenient control over the composition of individual elements and aided in achieving stoichiometric CIGS thin-films.

Table 4.1: The stoichiometry of PED deposited annealed CIGS films with varied duty cycle

Duty Cycle (%)	Stoichiometry
100 (DC)	$\text{Cu}_{1.10}\text{In}_{0.46}\text{Ga}_{0.11}\text{Se}_{2.33}$
67	$\text{Cu}_{0.81}\text{In}_{0.76}\text{Ga}_{0.31}\text{Se}_{2.12}$
50	$\text{Cu}_{0.95}\text{In}_{0.70}\text{Ga}_{0.28}\text{Se}_{2.07}$
40	$\text{Cu}_{1.07}\text{In}_{0.56}\text{Ga}_{0.20}\text{Se}_{2.17}$

The bulk composition and thickness of the DC and optimized PED deposited CIGS films are determined by the X-ray fluorescence spectroscopy and are shown in Table 4.2. The bulk composition values are in agreement with the elemental composition determined from the EDS. The thicknesses of 0.97 and 0.85 μm are observed for CIGS films deposited by DC and PED techniques, respectively.

Table 4.2: Elemental composition and thickness of CIGS films obtained from XRF spectroscopy

Method – time (min)	Elemental composition (at. %)				Film stoichiometry	Thickness (μm)
	Cu	In	Ga	Se		
DC – 15	26.8	11.0	3.5	58.7	$\text{Cu}_{1.07}\text{In}_{0.44}\text{Ga}_{0.14}\text{Se}_{2.35}$	0.97
PED – 15	23.3	17.7	6.5	52.5	$\text{Cu}_{0.93}\text{In}_{0.71}\text{Ga}_{0.26}\text{Se}_{2.10}$	0.85

4.2.2 Morphology of CIGS thin-films

Morphological characterization of PED electrodeposited and annealed CIGS thin-films is investigated by scanning electron microscopy. Figure 4.4 shows the morphologies of annealed PED electrodeposited CIGS films with varied duty cycle. For a duty cycle of 40 % the morphology of the CIGS films contain cauliflower like particles, as shown in Figure 4.4a. Though the particles themselves seem compact but the overall surface morphology of the film is rough and porous. This could be due to the excessive dissolution of In back into

the electrolyte during a quite long T_{off} resulting in the depletion of the film bulk and a corresponding rough surface, which is not desirable for photovoltaic application since it accounts for the increased scattering of minority carriers. For an increased duty cycle to 50 %, spherical particle like morphology is observed which is smooth and compact (Figure 4.4b). In addition, the deposited film is homogeneous in appearance and is attributed to the selective dissolution of the projecting parts with high electrochemical activity from the film surface. A homogeneous and compact morphology is necessary in photovoltaic absorber layers since it leads to lower resistance and faster minority carrier diffusion, which ultimately serves to improve the cell performance. When duty cycle is further increased to 67 %, though the overall film surface is smooth but it has plenty of discontinuities which also may lead to increased resistance to the minority carriers. The variation in the morphology and composition of the PED electrodeposited CIGS films with the varied duty cycle, is explained later in detail while discussing the growth mechanism studies.

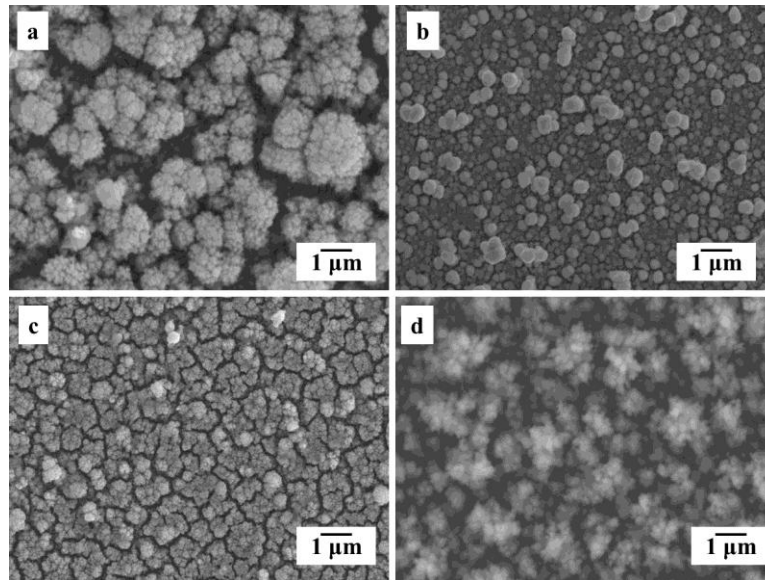


Figure 4.4: Morphology of PED electrodeposited and annealed CIGS thin-films deposited at a duty cycle of a) 40, b) 50, c) 67 and d) 100 % (DC).

The morphology of the DC electrodeposited CIGS films (duty cycle of 100 %) is shown in Figure 4.4d. It can be clearly observed that the morphology of the films is highly porous and rough compared to any of the PED electrodeposited CIGS films. This can be explained based on several reasons as follows: 1) In general, the concentration gradient existing in the electrolyte leads the mass transfer during the electrodeposition process. The reaction rate of the diffusion process of metal ions for a mass-transfer process was slower than that of the

charge-transfer process. Hence, the rate-determining step for the electrodeposition process has been controlled by the diffusion process of metal ions. For the DC electrodeposition technique, the ad-ions or ad-atoms have insufficient time to diffuse to a suitable position on the Mo substrate before reaching a position to attain the lowest Gibbs free energy. Therefore, the surface profile of thin films fabricated by the DC electrodeposition techniques is irregular and these thin films are easy to peel off from the Mo substrate. 2) During the DC deposition of thin-films, due to the continuous supply of constant current, building-up of material takes place at same nucleation sites without the possibility for the creation of new nucleation sites thereby causing the roughness in the deposited films. 3) The evolution of hydrogen during the deposition due to the use of higher negative voltage. The hydrogen evolution reaction is expected to be more prominent and competes with the deposition of CIGS films in the present study since the deposition is carried out in aqueous electrolytes. Hydrogen bubbles evolved during the deposition get entrapped into the films at the cathode. In addition, due to the continuous supply of constant voltage during the DC deposition, the deposition occurs onto these bubbles making it almost impossible for them to be diffused away at that instant. The entrapment of hydrogen leads to the porosity in the deposited films. Unlike the DC electrodeposited CIGS films, highly dense uniform films with coarser spherical particles are observed for PED electrodeposited CIGS films, as explained earlier. PED method can produce relatively more homogeneous surface because the rate-determining step of the deposition process is controlled by a mass-transfer process. Relaxation during the pulse off-time in the PED electrodeposition not only allows the diffusion of ad-atoms but also facilitates the formation of new nucleation sites thereby leading to the homogeneous and compact structure. In addition, during the relaxation time, entrapped hydrogen can get diffused away facilitated by the rearrangement of atoms leading to reduced porosity in the deposited films. The schematic of the deposition of CIGS films by the DC and PED electrodeposition techniques is shown in Figure 4.5.

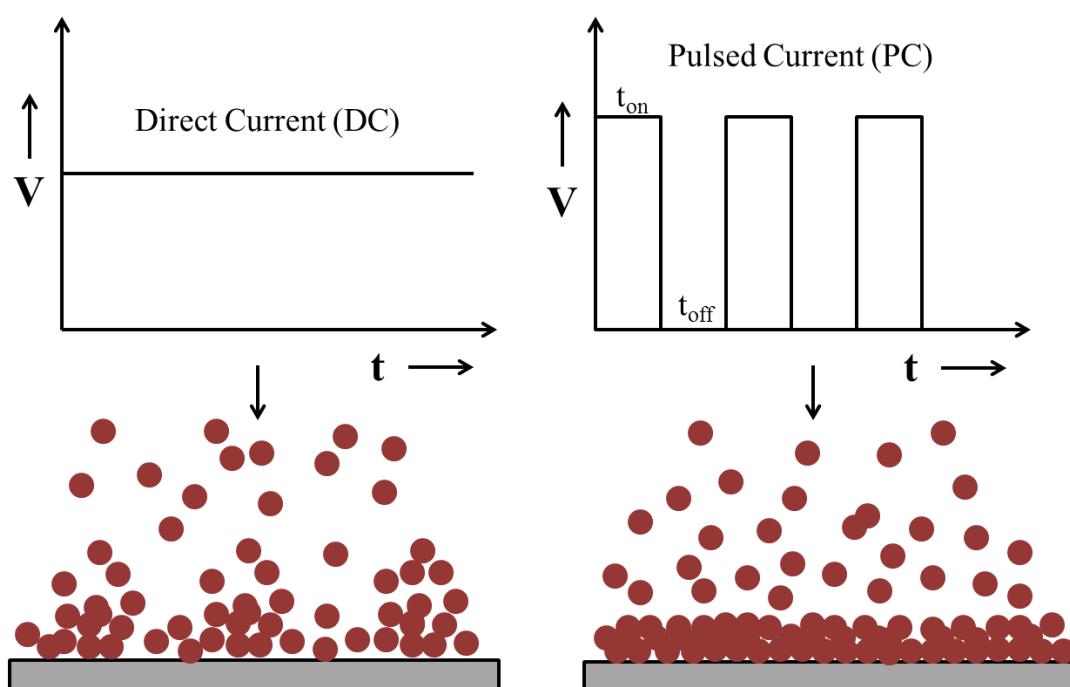


Figure 4.5: Schematic representing the deposition mechanism for DC and PED deposited CIGS films

4.2.3 CIGS thin-films with increased deposition time

Though the near-ideal stoichiometry and compact morphology is observed for the optimized PED deposited CIGS thin-films but the respective thickness values are lower than the typical requirement of $\approx 2 \mu\text{m}$ for CIGS based solar cells. Hence, the deposition time has been increased to 30 min for CIGS thin-films by DC and PED techniques. The composition and the thickness of the CIGS films deposited for 30 min has been determined by XRF spectroscopy and are shown in Table 4.3, which confirm the near ideal stoichiometry of the CIGS thin-films deposited by PED technique and have a thickness of $1.4 \mu\text{m}$. The DC deposited CIGS films seem to have higher In content compared to the films deposited for 15 min but are still Cu-rich in composition and have a film thickness of $1.9 \mu\text{m}$.

Table 4.3: Elemental composition and thickness of DC and PED CIGS films deposited for 30 min, obtained from XRF spectroscopy

Method – time (min)	Elemental composition (at. %)				Film stoichiometry	Thickness (μm)
	Cu	In	Ga	Se		
DC – 30	26.2	13.2	4.1	56.5	$\text{Cu}_{1.05}\text{In}_{0.53}\text{Ga}_{0.16}\text{Se}_{2.26}$	1.93
PED – 30	23.8	18.2	6.1	51.9	$\text{Cu}_{0.95}\text{In}_{0.73}\text{Ga}_{0.25}\text{Se}_{2.07}$	1.32

The morphology of the CIGS films deposited for 30 min is shown in Figure 4.6. It can be clearly observed that the compactness of the films increased with increased deposition time. The PED deposited CIGS films have larger particles and relatively higher compactness than the DC deposited CIGS films. DC deposited CIGS films contain surface dispersed Cu-rich flakes (from EDS), which may correspond to Cu-Se phases (confirmed from XRD and Raman spectra, discussed later). In general, if the films contain copper selenide phases, they get segregated to the grain boundaries thereby limiting the grain growth. Hence, it is suggested that stoichiometric compact CIGS thin-films with desired thickness are prepared by the successful optimization of deposition parameters.

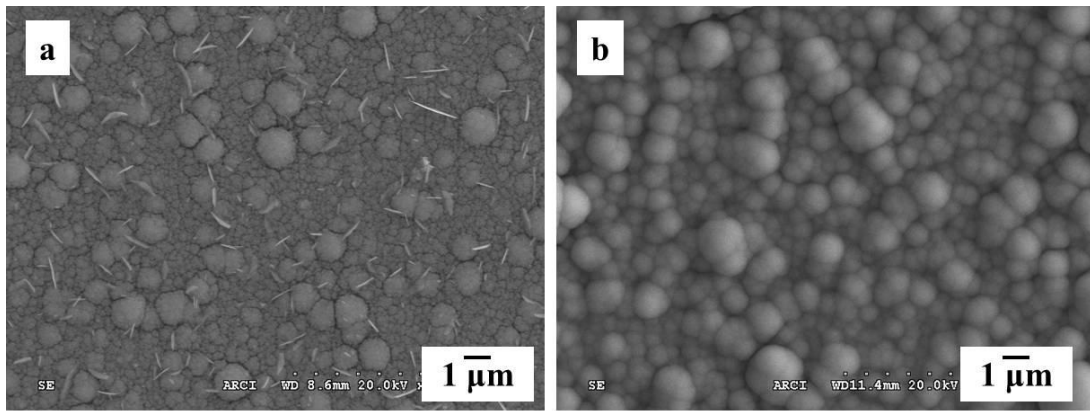


Figure 4.6: Morphology of annealed CIGS films deposited by a) DC and b) PED techniques for 30 min

4.2.4 X-ray diffraction studies of DC and PED deposited CIGS thin-films

CIS/CIGS semiconductors, in general, crystallize in tetragonal chalcopyrite structure as previously discussed in section 1.6. However, due to the presence of four different elements, several binary and ternary phases are expected to be stable along with CIS/CIGS even after annealing. Among these, presence of phases such as binary copper selenides are detrimental and results in reduced device performance. Due to these aspects, it is extremely crucial to detect all the phases that exist in the annealed CIGS films. In this context, the XRD data of various possible phases with their preferred orientations are presented in Table 4.4 along with the relevant 2θ values. The data is extracted from the JCPDS diffraction files of the relevant systems. The JCPDS diffraction file number is also included in the table for reference.

Table 4.4: Various phases and the relevant 2 θ values

Phase	JCPDS file no.	Angle (2 θ)	(hkl)	Preferred Orientation
Molybdenum (Mo)	42-1120	40.5	110	1
		58.6	200	3
		73.66	211	2
		87.6	220	5
		101.41	310	4
Molybdenum Selenide (MoSe ₂)	29-0914	13.7	002	2
		37.9	103	1
		47.5	105	3
		31.4	100	5
		55.96	110	4
Copper Indium Gallium Selenide (CIGS)	35-1102	57.02	008	4
		17.28	101	4
		26.91	112	1
		44.683	220/204	2
		52.99	312/116	3
Copper Indium Selenide (CIS)	40-1487	65.03	400	5
		26.6	112	1
		44.26	220/204	2
Copper Gallium Selenide (CGS)	35-1100	52.43	312/116	3
		27.79	112	1
		46.14	220/204	2
Copper Selenide (Cu _{2-x} Se)	53-0523	54.27	312/116	3
		13.2	111	5
		26.65	222	2
		30.9	115	4
		44.04	404	1
Indium Selenide (In ₂ Se ₃)	40-1407	44.79	414	3
		25.3	102	1
		37.4	110	2
		41.5	006	3
		45.8	202	4
Gallium Selenide (Ga ₂ Se ₃)	44-1012	28.26	131	1

Figure 4.7a shows the XRD patterns of annealed CIGS thin-films prepared by DC and PED electrodeposition techniques. These patterns show preferred orientation corresponding to (112) and other peaks corresponding to (220), (312) and (424) for CIGS (JCPDS diffraction file no. 35-1102) are observed in the film, confirming the presence of crystalline chalcopyrite CIGS phase in the film. As it can be seen from Table 4.4, it is indeed difficult to distinguish between the CIS, CIGS and Cu_{2-x}Se phases due to the narrow variation in the 2 θ values of these phases. Hence, a closer inspection of preferred (112) orientation of CIGS and CIS (optimized by PED in previous chapter) has been carefully performed as shown in

Figure 4.7. It is clearly observed that the (112) peak of CIS occurs at the 2θ of $\approx 26.60^\circ$ whereas for CIGS it is shifted to $\approx 26.90^\circ$. The shift of 0.3° is the characteristic of inclusion of Ga into CIS films. Owing to its lower atomic radius, Ga incorporation into CIS contracts the crystal structure of CIGS as a whole leading to a decrease in the lattice parameter and hence, inter-planar spacing. The decrease in inter-planar spacing in turn leads to a shift in the 2θ of XRD to higher value. The shift observed in Figure 4.7b is in agreement with the previous reports suggesting the formation of chalcopyrite CIGS with the Ga content being $\approx 25 - 30$ at. % [139]. In addition to CIGS, peaks representing MoSe_2 (JCPDS diffraction file no. 29-0914) and Mo substrate (JCPDS diffraction file no. 42-1120) are also observed, as shown in Figure 4.7a. As previously discussed, Wada et al., reported the formation of thin MoSe_2 layer at the Mo/CIGS interface at temperatures higher than 500°C , which not only improves the adhesion between Mo and CIGS but also enhances the ohmic contact. In addition to the above mentioned phases, the Cu_{2-x}Se secondary phase (JCPDS diffraction file no. 53-0523) is observed in the DC electrodeposited CIGS films. This could be attributed to the Cu-rich composition of these films as discussed previously from EDS studies. However, the secondary phase is absent in the PED electrodeposited CIGS films indicating formation of single phase CIGS successfully achieved by the optimization of pulse parameters.

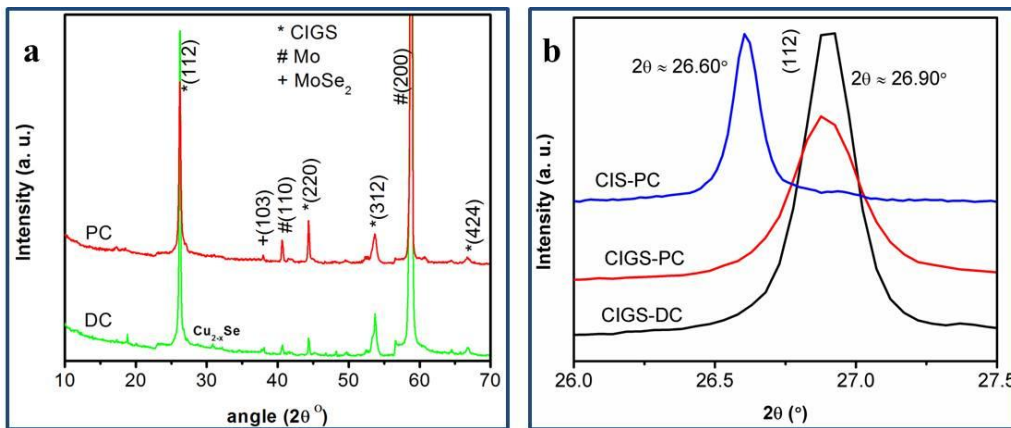


Figure 4.7: a) XRD patterns of annealed DC and PED deposited CIGS films and b) closer inspection of (112) orientation of CIGS and CIS

4.2.5 Micro-Raman analysis of DC and PED deposited CIGS thin-films

As it is observed from XRD spectra that the peak of Cu_{2-x}Se does not evolve noticeably and it could be due to the presence of negligibly small content in the films. In addition, as mentioned above, the narrow variation in the (112) orientation of CIGS and Cu_{2-x}Se makes

it very difficult to detect this phase using XRD. The presence of such phases can be easily detected using the micro-Raman spectroscopy. As discussed earlier in section 2.3.4, in micro-Raman spectra, laser beam can be focused to microscopic scale range and facilitates the detection of surface dispersed microcrystallite (expected form of Cu_{2-x}Se on CIGS and also observed from morphological studies) phases. In the present case, micro-Raman analysis is used to investigate the lattice vibrations of CIGS and to confirm whether the Cu_{2-x}Se secondary phases subsist on the surface of CIGS thin-films. The theoretically possible Raman modes and the active Raman modes are discussed below prior to the results of DC and PED deposited CIGS films.

CIGS has a structure of body centered tetragonal chalcopyrite crystal $\text{A}^{\text{I}}\text{B}^{\text{III}}\text{C}_2^{\text{IV}}$, with space group $\text{I}\bar{4}2\text{d}$ and point group $\text{D}_{2\text{d}}^{12}$. The primitive cell of $\text{A}^{\text{I}}\text{B}^{\text{III}}\text{C}_2^{\text{IV}}$ type compounds is shown in Figure 1.7. The vibrational spectrum of chalcopyrite structure consists of 24 zone-center vibration modes: $1\text{A}_1 + 2\text{A}_2 + 3\text{B}_1 + 4\text{B}_2 + 7\text{E}$. These modes are classified into 3 acoustic ($\text{B}_2 + \text{E}$) and 21 optic-modes ($1\text{A}_1 + 2\text{A}_2 + 3\text{B}_1 + 3\text{B}_2 + 6\text{E}$) of which B_2 and E modes are doubly-degenerated. There are 22 Raman active vibrations: $\text{A}_1 + 3\text{B}_1 + 3\text{B}_2 + 6\text{E}$, 18 IR active: $3\text{B}_2 + 6\text{E}$, and 2 silent modes: 2A_2 . As mentioned by [140, 172] A_1 vibrational mode is the major intense Raman mode located in the range of 172 to 187 cm^{-1} for CIS/CIGS/CGS films, which has been ascribed to the motion of Se relative to Cu atoms with Ga at rest. Neumann proposed that one of the remaining signals in the range of 210 to 215 cm^{-1} is the E mode of the chalcopyrite compound, which is induced by the change in polarization during the vibration of molecular bonds [173]. Xue et al, have reported the structural properties of CuSe phase formed as secondary phase on the surface of CuGaSe_2 due to excess Cu, by the use of micro-Raman spectroscopy [174]. The Raman modes of CuSe and Cu_2Se are observed at 45 and 260 cm^{-1} , respectively.

Figure 4.8a shows the micro-Raman spectra of the annealed DC and PED deposited CIGS thin films. A_1 , B_2 and E modes of the CIGS films are found at 176 , 205 and 232 cm^{-1} respectively for both CIGS thin films. Similar to XRD studies, a closer inspection of dominant A_1 mode has been employed in Raman spectroscopy for CIS and CIGS films and is shown in Figure 4.8b. It can be clearly observed that the CIS A_1 mode is found at a wavenumber of 173 cm^{-1} while that of CIGS is observed at 176 cm^{-1} . This shift is attributed to the incorporation of Ga into CIS films. It is well reported that the A_1 mode is observed at lower wavenumbers in the range of 171 - 173 cm^{-1} for CIGS films with very low Ga content, with the peak shifting to higher wavenumbers of 176 - 178 cm^{-1} for stoichiometric CIGS thin-

films and to 187 cm^{-1} for CuGaSe_2 . In addition to the chalcopyrite CIGS peaks, a less intense peak corresponding to A_1 mode of Cu_{2-x}Se at 260 cm^{-1} is found in case of annealed DC electrodeposited CIGS thin film, as shown in Figure 4.8a. This Cu_{2-x}Se secondary phase is generally dispersed on the surface of CIGS thin-film and its existence leads to the rough surface morphology of the thin-film. It is also well reported that the Cu_{2-x}Se segregates to the grain boundaries thereby limiting the grain growth [62]. Moreover, the interfacial adhesion between the CIGS thin film and the Mo substrate becomes very poor, resulting in an adverse effect on the interface resistance [161]. Deposition of excess Cu during DC electrodeposition caused the deviation from the near ideal stoichiometry and facilitated the formation of undesired Cu_{2-x}Se secondary phase. It can now be confirmed that the flakes that exist on the surface of the DC deposited CIGS films are attributed to the Cu_{2-x}Se phase. Use of complexing agents in the electrolyte during deposition and/or etching of the deposited CIGS film using KCN are in practice for the removal of excess Cu and hence, the secondary Cu_{2-x}Se phase. However, use of complexing agents might lead to the presence of impurities in the film and KCN etching makes the film rough which ultimately causes reduction in the performance, as previously discussed in section 1.10. The A_1 mode of the Cu_{2-x}Se secondary phase, however, is not detected in the thin-film fabricated by the PED technique. Hence, it is suggested that the CIGS thin-film fabricated by the PED technique with a pulse period of 20 ms and duty cycle of 50 % can effectively remove the undesired Cu_{2-x}Se secondary phase and produce a single phase chalcopyrite structured CIGS.

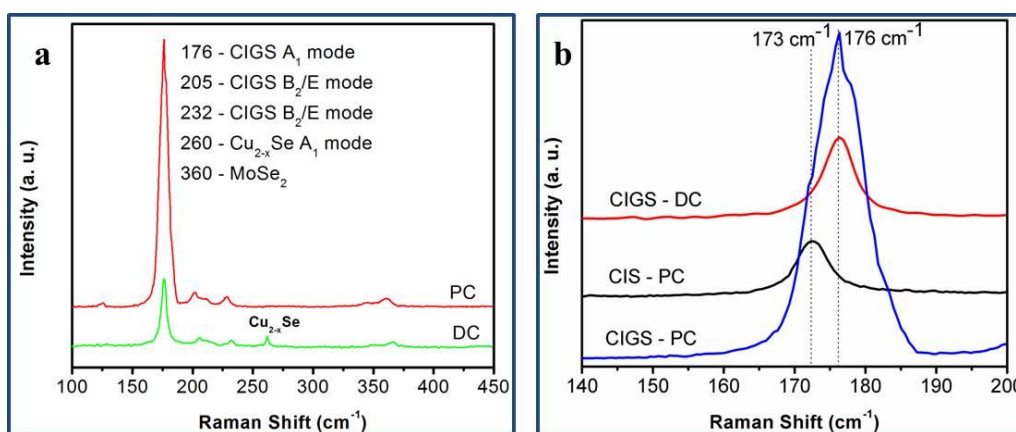


Figure 4.8: a) Raman spectra of annealed DC and PED deposited CIGS films and b) closer inspection of dominant A_1 mode for CIS and CIGS films

4.2.6 Cross-sectional studies of DC and PED deposited CIGS thin-films

Figure 4.9 shows the cross-sectional SEM images of DC and PED deposited annealed CIGS thin-films. The cross-section of the PED deposited CIGS films is more compact than the DC deposited CIGS films which appeared to be porous, indicating the formation of dense CIGS thin-films by PED technique. The thickness of the films is determined to be $\approx 2 \mu\text{m}$ and $1.3 \mu\text{m}$ for DC and PED deposited CIGS films, respectively. The thickness values are in agreement with the XRF results as discussed previously. The thickness values are in the desirable range as required for high efficient CIGS devices [175]. The sputtered Mo layer (200 nm) is also seen in the films.

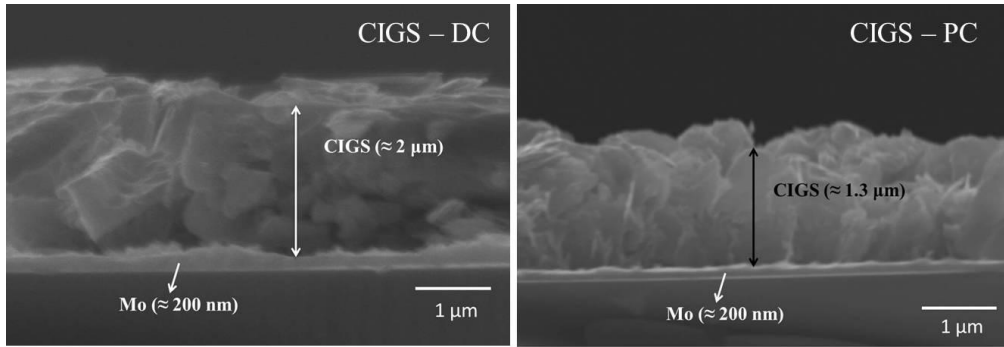


Figure 4.9: Cross-sectional SEM images of DC and PED electrodeposited annealed CIGS thin-films

4.2.7 Optical absorption studies of DC and PED deposited CIGS thin-films

The optical properties of DC and PED deposited CIGS samples are studied by absorption measurements at room temperature with a UV/Visible/NIR diffuse reflectance spectroscopy. Optical bandgap (E_g) and absorption coefficient are well known related to photon energy by following relation:

$$ah\nu = A (h\nu - E_g)^n$$

where A is constant, E_g is the band gap, ν is the frequency of incident photon and h is the Plank's constant. And n takes the value 1/2 for direct allowed transition, value 3/2 for direct forbidden, and values 2 and 3 for indirect allowed and forbidden transitions, respectively. CIS/CIGS thin-films have direct allowed transition as reported by previous researchers [13, 14, 176]. Figure 4.10a shows the absorbance spectra of DC and PED deposited CIGS films. An extended range of absorption from IR through visible to UV can be observed from both the spectra. However, the PED deposited CIGS films show higher absorption over the DC deposited films (For e. g., $\alpha_{\text{PED}} \approx 3.22 \times 10^4 \text{ cm}^{-1}$ is greater than $\alpha_{\text{DC}} \approx 2.78 \times 10^4 \text{ cm}^{-1}$). This

could be attributed to the compact morphology of PED deposited CIGS films. Though the DC films have higher thickness than the PED films but the higher absorption is observed for PED films which might be due to the porosity of the DC plated CIGS films as discussed previously. In addition, the transition in the absorption spectra has been observed at ≈ 960 and 1200 nm for DC and PED deposited CIGS films, respectively, which indirectly points about the larger bandgap of DC plated CIGS thin-films. The absorption coefficient of the CIGS films in both cases has been calculated using the following relation:

$$\alpha = \frac{2.303 \times \log(\text{absorbance})}{\text{thickness (nm)}}$$

The band gap of DC and PED plated CIGS thin-film has been determined using the Tauc's plot of $(\alpha h\nu)^2$ vs. $h\nu$ as shown in Figure 4.10b. Extrapolation of the linear section of the plot to the energy axis yields the band gap of the thin-films. The band gaps of DC and PED electrodeposited CIGS films are 1.28 and 1.21 eV, respectively, which are in the desired range for CIGS thin film as solar absorber layer. The DC plated CIGS thin-films, however, have larger band gap compared to the PED plated CIGS films, which is in agreement with the transition observed in absorbance studies. A possible reason for this phenomenon is carrier degeneracy in $\text{Cu}(\text{In,Ga})\text{Se}_2$ due to continuous distribution of defect states, such as copper vacancies (V_{Cu}), or substitutional indium in copper sites (In_{Cu}).

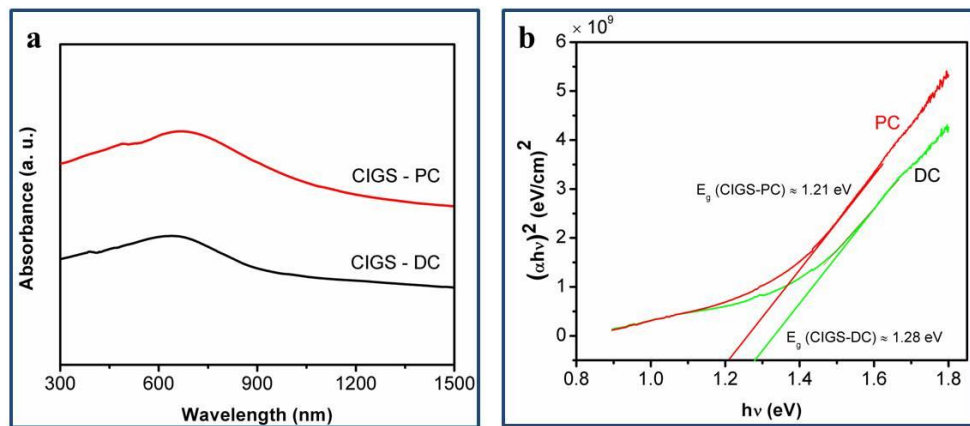


Figure 4.10: a) Absorption spectra and b) Tauc's plot of DC and PED deposited CIGS thin-films

4.2.8 Mott-Schottky studies of DC and PED deposited CIGS thin-films

Mott-Schottky analysis of the annealed DC and PED deposited CIGS thin-films has been carried out. The details are as mentioned in the section 2.3.9. Figure 4.11 shows the Mott-Schottky ($1/C^2$ vs. V) plot of DC and PED deposited CIGS thin-films in 0.5M H_2SO_4 at a frequency of 10 kHz in the dark. The slope of the MS plots is negative in both cases, thereby confirming that the CIGS films are p-type. The flat band potentials of DC and PED plated CIGS films are found to be -0.17 and -0.16 V (vs. SCE), respectively, by extrapolating the linear section to x-axis. In addition, acceptor densities of CIGS films are calculated to be, using the slope of the curve, $2.1 \times 10^{16} \text{ cm}^{-3}$ and $4 \times 10^{16} \text{ cm}^{-3}$, respectively. The flat-band potentials and acceptor densities determined herein are close to the desirable values for stoichiometric CIGS films that have been reported previously [145].

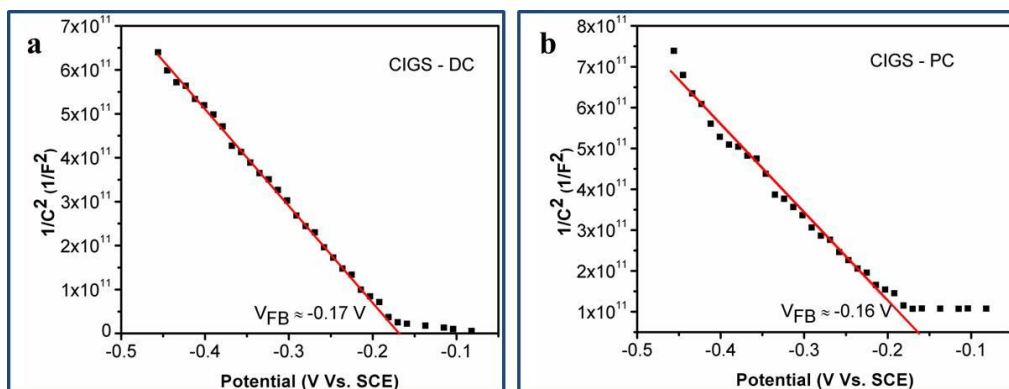


Figure 4.11: Mott-Schottky plots of a) DC and b) PED deposited annealed CIGS thin-films

4.2.9 Photoelectrochemical (PEC) analysis of DC and PED deposited CIGS thin-films

The photoelectrochemical performance of annealed DC and PED deposited CIGS thin-films is studied in 0.5 M Na_2SO_4 . Current vs. potential curves are obtained in the potential range of -0.1 to -0.7 V vs. SCE with a sweep rate of 10 mV/s. Figure 4.12 shows the I-V curve in dark and under AM 1.5 G solar simulated light for the CIGS thin films. An increase in cathodic photocurrent in the third quadrant, a characteristic of a p-type semiconductor, is observed with increase in cathodic potential in both the cases, which also corroborates the above discussed Mott-Schottky studies. This behavior is attributed to an incomplete photonic conversion, which causes a recombination of charge carriers at the grain boundary of the semiconductor [156]. The photoelectrochemical performance of CIGS thin films in aqueous electrolytes exhibited similar behavior as reported previously [156, 177]. Improved photocurrent is observed for the PED deposited CIGS films over DC deposited CIGS films. Near ideal stoichiometry and highly dense uniform morphology of the CIGS films and the elimination of $Cu_{2-x}Se$, an undesired secondary phase by PED, have resulted in the

improved performance. Relatively higher dark current is observed for the DC deposited CIGS over PED deposited CIGS, which could be attributed to the presence of Cu_{2-x}Se secondary phase and the porosity of the CIGS films. Cu_{2-x}Se , being a degenerate semiconductor; is highly conductive and results in high dark currents. In addition to the I-V characteristics, the amperometric current-time (I-t) curve of annealed PED deposited CIGS films obtained at -0.4 V by chopped light as shown in the inset of Figure 4.12. It clearly demonstrates the photoactivity nature of CIGS films with a photocurrent density of $\approx 0.1 \text{ mA/cm}^2$. The I-t curve of the DC deposited films could not be demonstrated due to its high dark current density which is more than the photocurrent density. The improved photoresponse of PED deposited and annealed CIGS films indicate their potential for application in thin-film solar cells. In addition, the photoelectrochemical performance of these films demonstrates their application for photoelectrochemical hydrogen generation.

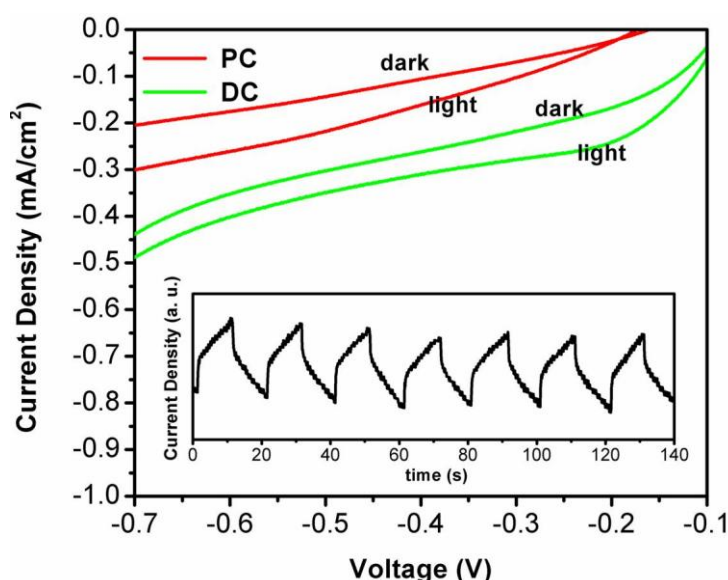


Figure 4.12: Photoelectrochemical I-V characteristics of DC and PED deposited CIGS thin-films

4.3 Growth mechanism studies

This section deals with the growth mechanism studies of DC and PED deposited CIGS films to essentially demonstrate the reasons for obtaining compact CIGS thin-films by PED with the variation in duty cycle (off-time). Prior to the discussion of the results obtained in the present study, the theory explaining the existing mechanisms of electrodeposited species is briefed as follows.

4.3.1 Theory of nucleation mechanism during electrodeposition

The morphology/dispersity of an electrochemically reduced metal/alloy phase depends on the nucleation and growth of individual particles on the substrate. Nucleation is the initial stage of the electro-reduction of metal/alloy species and is regarded as the most critical stage of growth for defining the final film properties. Nucleation mechanism is often explained using electrochemical chronoamperometry studies. In chronoamperometry experiments, the potential is stepped from the open-circuit potential to the reduction potential of active species at which the electro-reduction/deposition of the species would occur. Current transient of the deposition reaction is described the Cottrell equation as:

$$i = \frac{nFD^{1/2}C_0}{\pi^{1/2}t^{1/2}} \quad (4.3)$$

where i is current density, n is number of electrons involved in reduction, F is Faraday's constant, D is diffusion coefficient, C_0 is the bulk concentration of the species and t is time. The i - t curve during the electrodeposition of the species provides the basic information about the nucleation mechanism. Typical I - t curve during the electrodeposition of active species is shown in Figure 4.13. As it can be seen the curve is classified into three zones which are explained below.

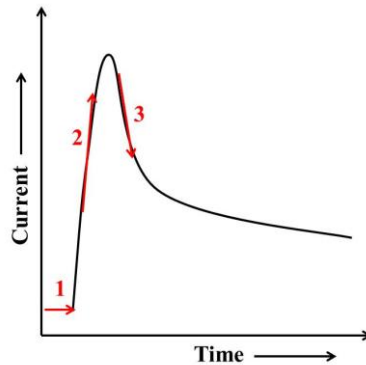


Figure 4.13: Typical I-t curve representing three zones during the electrodeposition of species

A pictorial representation of the substrate/liquid interface for three different zones in Figure 4.13 is depicted in Figure 4.14. Zone 1 represents the initial conditions prior to the onset of reduction reaction. A liquid boundary film adjacent to the solid substrate and a solution bulk are depicted. Here the liquid boundary film is presented in simple form, as described by Scharifker-Hills, thus no double layer properties are considered. Zone 2 represents the onset

of the reduction reaction wherein the reduced atoms sit on the substrate. The distance between the ad-atoms depends on the bulk concentration of the active species in the solution. In general, for smaller concentrations (1 – 10 mM), the ad-atoms are spaced farther apart. Once these species are distributed over the surface in the atomic state, they must travel toward each other to minimize the surface energy. Atoms spaced further apart need to travel longer distances in order to group together to form a nucleus. This is energetically unfavorable because atoms do not have sufficient energy to traverse on the substrate and therefore, they group together with the nearest neighbors, resulting in large number of small nuclei. The nuclei formed on the surface contribute to the active surface area available for reaction. As a result, initial current increases due to the increase in surface area whenever the nucleation is involved (zone 2 in Figure 4.13). Each nucleus defines its own diffusion zone as shown in Figure 4.14, through which the ad-atoms diffuse, representing the mass-transfer mechanism for the continuation of growth. Zone 3 represents the final steady state of electrodeposition wherein growth of independent nuclei and overlapping of diffusion zones occur. These overlapping diffusion zones would eventually include the entire electrode surface area and thereby the reaction is strictly controlled by the mass-transfer i. e. the system is under steady state conditions. As the growth of independent nuclei leads to the coverage of entire surface; it results in the overall active area available on the surface and hence, the decrease in current as observed from Figure 4.13.

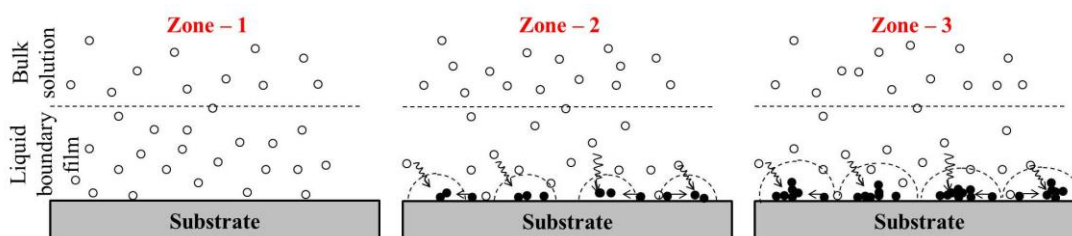


Figure 4.14: Schematic representation of nucleation phenomena during the electro-reduction of active species at various stages of deposition. Depicted zones are 1) prior to electro-reduction, 2) at the onset of reduction and 3) steady state of electrodeposition. Reproduced from [178].

4.3.2 Types of nucleation mechanism

Typical nucleation process and the associated mechanism are briefly explained in the previous section. There are several methods that utilize the coordinates of the chronoamperometric peaks to determine the possible nucleation mechanism and related parameters. Among these, the model developed by Scharifker and Hills is the most widely used since it allows a simple and rapid classification of the experimental transients into two

limiting mechanisms as instantaneous nucleation (IN) and progressive nucleation (PN) [179, 180]. The models are mathematically formulated into following equations [179]:

$$\text{Instantaneous Nucleation} \quad \left(\frac{i}{i_m}\right)^2 = \frac{1.9542}{t/t_m} \left[1 - \exp\left\{-1.2564\left(\frac{t}{t_m}\right)\right\}\right]^2 \quad (4.4)$$

$$\text{Progressive Nucleation} \quad \left(\frac{i}{i_m}\right)^2 = \frac{1.2254}{t/t_m} \left[1 - \exp\left\{-2.3367\left(\frac{t}{t_m}\right)^2\right\}\right]^2 \quad (4.5)$$

where i_m and t_m are the current and time co-ordinates of the peak observed in a typical I-t curve (see Figure 4.13), respectively.

In case of IN, nuclei are formed at the same time and simultaneous growth of the nuclei occurs. In other words, slow growth of nuclei on a small number of active sites takes place which are all activated at the same time. PN corresponds to fast growth of nuclei on many active sites which are activated during the course of electrodeposition. i. e. formation of new nuclei and their rapid growth continuously take place with time during the deposition. The IN and PN models are pictorially demonstrated in Figure 4.15. It can be clearly observed that a small number of nuclei have formed and their slow growth takes place for the case of IN. In case of PN, higher number of nuclei has formed at the initial stage and the number keeps increasing with deposition time with their simultaneous growth. This often results in a rapid coverage of the substrate and hence, the steady state of the electrodeposition. Hence, it can be concluded that the rate of nucleation and their independent growth is much higher for PN than IN leading to the rapid steady state of deposition for PN than IN.

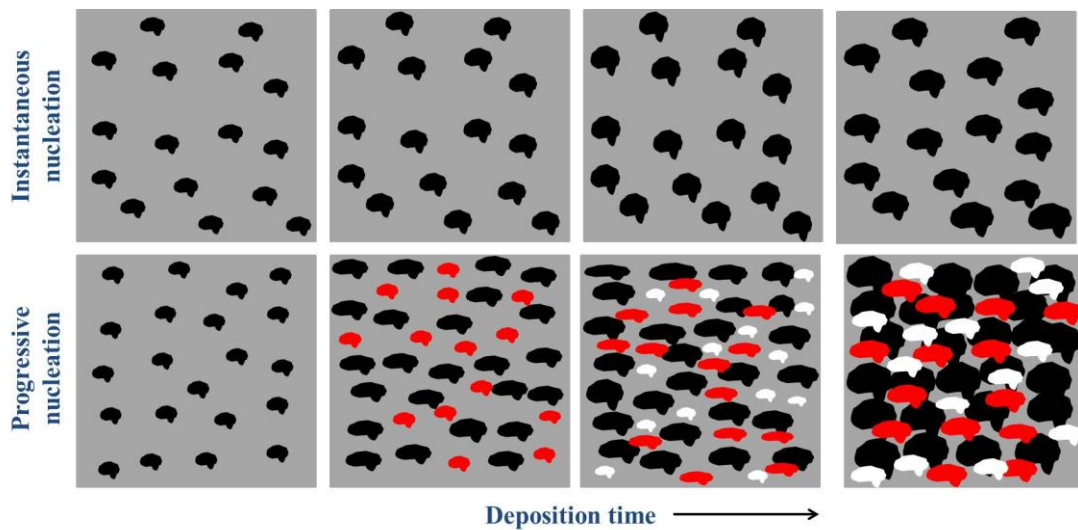


Figure 4.15: Pictorial demonstration of instantaneous and progressive nucleation models with the deposition time

The theory described for the nucleation and the respective mechanisms are further adopted in the present study to explain the growth mechanism of electrodeposition of CIGS thin-films using direct and pulse methods.

4.3.3 I-t curves – DC and PED deposited CIGS films

The I-t curves of DC and PED deposited CIGS films obtained during the deposition are shown in Figure 4.16. The typical I-t curves follow the same trend containing three zones as shown in Figure 4.13. The experimental observations of the I-t curves can be summarized as: 1) a rapid increase in current density in zone 1, 2) a higher peak current density and 3) a rapid decrease in current density for PED deposited CIGS than DC deposition. When compared with the theoretical nucleation mechanism of the electrodeposition as discussed above, the I-t curve for PED deposited CIGS suggests the aspects such as increase in number of nuclei due to the increased current density and rapid growth and overlap of individual nuclei due to the rapid decrease in current density. It is well-known that PED method possesses a relaxation time. The presence of this relaxation time removes the double layer after every pulse which leads to the easier availability of ions in the electrolyte. In addition, the rearrangement of ad-atoms takes place during the relaxation time thereby providing the possibility for new nucleation sites. The number of nuclei is then expected to increase with the increased off-time. However, the possibility of these expectations can be appreciated by the experimental investigation of the nucleation process for DC and PED deposited CIGS films; which is discussed in the following sections.

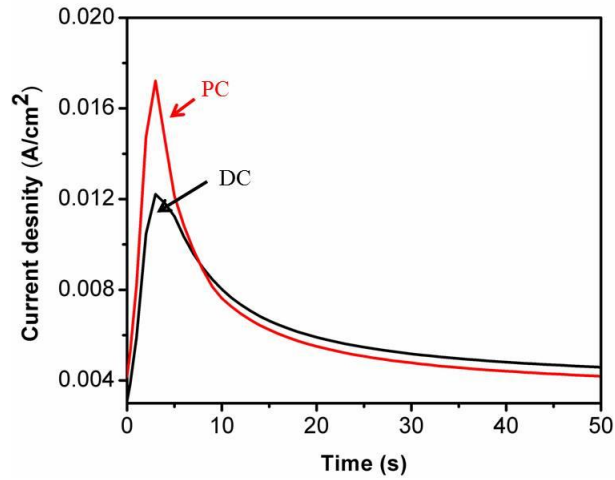


Figure 4.16: Current vs. time curves observed during electrodeposition of DC and PED deposition of CIGS

4.3.4 Growth mechanism of DC and PED deposited CIGS films

The growth mechanism of the deposited films depends on the initial stages of nucleation as demonstrated above. Hence, in the present study, the deposition of CIGS films is carried out in the range of ms to observe the basic difference in the features of the deposit to explore the possible nucleation mechanism. This is essentially due to the fact that the pulse on-time and pulse off-time are varied in ‘ms’ range while optimizing the parameters. It can be noted from the optimized studies for PED deposited CIGS films, the duty cycle of 50 % (corresponds to an on-time and off-time of 10 ms) has resulted in chalcopyrite compact CIGS thin-films. In this regard, preliminarily deposition experiments are performed by increasing the off-time from 1 to 10 ms while fixing an on-time of 10 ms. Deposition is performed only for 5 cycles i. e. for a deposition time of 50 to 100 ms; to explore the nucleation mechanism with varied off-time.

SEM images of PED deposited CIGS films with varied off-time (1 to 10 ms) are shown in Figure 4.17. It can be observed that with increase in off-time from 1 to 10 ms shows an increase in number of particles from Figure 4.17a to d. The particles, here, can be considered as nuclei since they correspond to the initial stages of nucleation. Hence, it can be concluded that the number of nuclei has increased with an increased off-time until 10 ms. However, an important point to be noted that there is no growth of the nuclei since the deposition time (number of pulses) is constant for all the cases. During the nucleation

studies, off-time is not increased beyond 10 ms because it is the optimized parameter during the PED deposition of stoichiometric CIGS films.

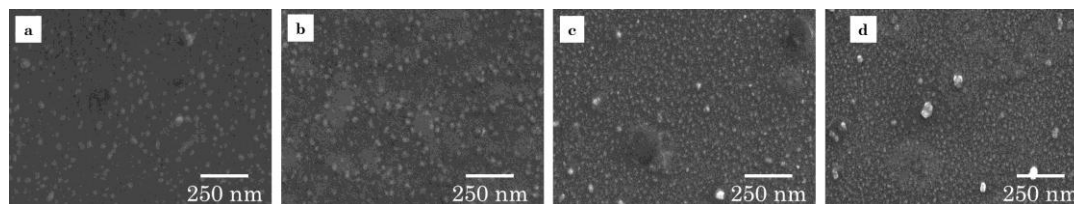


Figure 4.17: SEM images of PED deposited CIGS films with at a pulse off-time of a) 1, b) 2, c) 5 and d) 10 ms, respectively. Depositions are performed for 5 pulses.

The optimized condition is further used to deposit CIGS films using PED technique by increasing the number of cycles i.e. deposition time. SEM images of PED deposited CIGS films with increased deposition time from 20 to 200 ms are shown in Figure 4.18. It can be clearly observed from Figure 4.18 that the number of nucleation sites is increased with an increased deposition time from 20 to 200 ms. In addition, unlike the previous case; growth of the nuclei also took place simultaneously. The increased number of nuclei and their independent growth with increased deposition time essentially reflects the behavior of progressive nucleation mechanism, as discussed in the previous section. However, the confirmation requires an independent analysis of the amperometric I-t curve and fitting it using the equation 4.5. The relevant I-t curves, their simulated curves and discussion pertaining to the PN for PED deposited films are done later in this section.

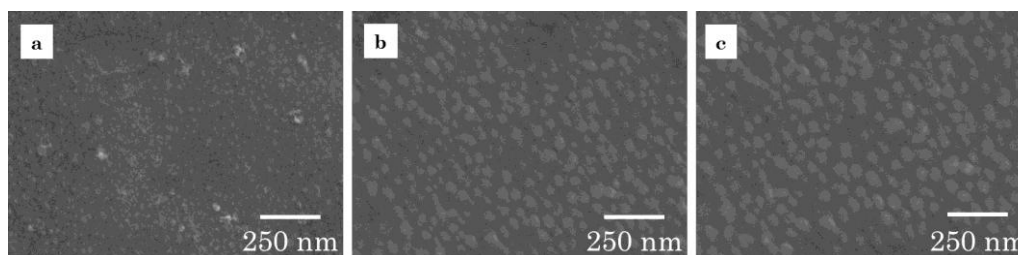


Figure 4.18: SEM images of PED deposited CIGS films for a deposition time of a) 20, b) 100 and c) 200ms, respectively. No. of cycles equivalent is a) 1, b) 5 and c) 10.

To compare the mechanism between the PED deposited and DC deposited CIGS films, the deposition of CIGS films is carried out using DC method for the same deposition time as employed for PED method. Figure 4.19a, b and c show the SEM images of DC deposited CIGS films for the deposition time of 20, 100 and 200 ms, respectively. It can be observed

from the images that the nuclei formed at a deposition time of 20 ms are almost the same for the films deposited for a deposition time of 200 ms. However, an independent growth of the existing nuclei took place with increased deposition time. This phenomenon seems to be consistent with the instantaneous nucleation mechanism, as explained above. The supporting I-t curves and their simulations are explained later in this section.

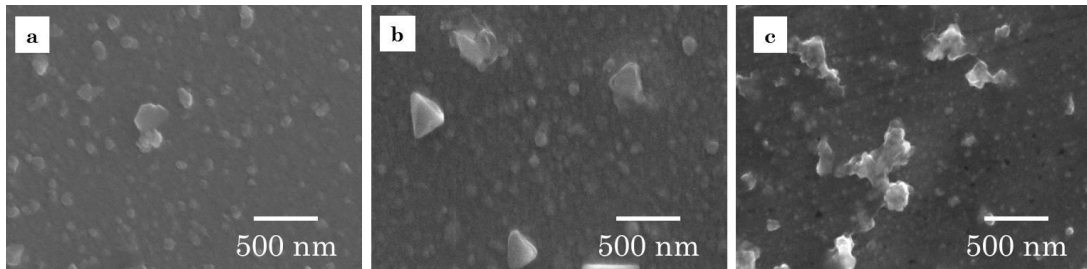


Figure 4.19: SEM images of DC deposited CIGS films for a deposition time of a) 20, b) 100, and c) 200 ms, respectively.

Finally, the deposition of CIGS films is performed for a deposition time of 3 s to study the surface coverage of the deposit on the substrate. Figure 4.20a and b show the SEM images of CIGS films deposited using DC and PED methods, respectively. It can be observed that the growth of the films for PED method is uniform showing the homogeneous coverage of the entire surface. On the other hand, the deposition in case of DC method is observed to be non-uniform and the complete coverage of the surface also does not occur while a rapid coverage of the substrate surface during the PED confirms the progressive nucleation of the CIGS films.

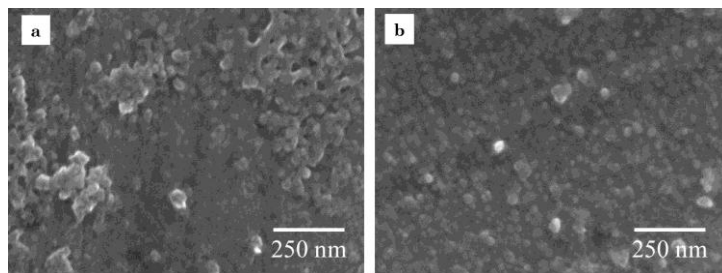


Figure 4.20: SEM images of a) DC and b) PED deposited CIGS films for a deposition time of 3 s.

4.3.5 Simulated and experimental models of DC and PED deposited CIGS films

To further ascertain the nucleation mechanism of DC and PED deposited CIGS films, the experimental I-t curves are theoretically fitted using the simulated models of instantaneous

and progressive nucleation mechanism using equations 4.4 and 4.5. The dimensionless experimental and simulated I-t curves are shown in Figure 4.21. As it can be observed from the figure, the experimental dimensionless I-t curve for DC deposited CIGS films fits the instantaneous nucleation model whereas the curves of PED deposited CIGS films fits the progressive nucleation model. Therefore, it can be clearly concluded from the experimental and theoretical investigations that the DC method follows an instantaneous nucleation and PED method follows progressive nucleation thereby leading to a uniform and compact deposit for PED deposited CIGS films.

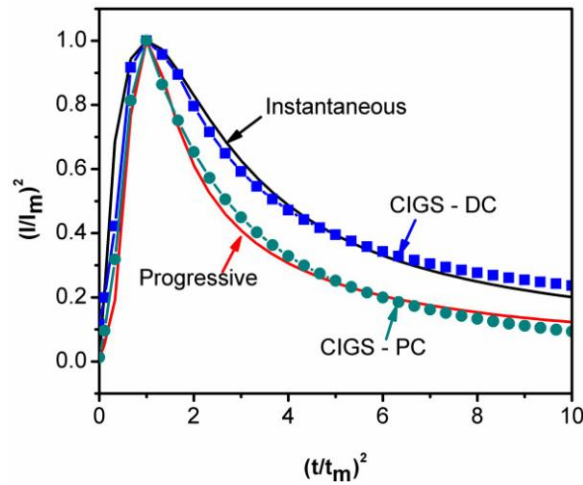


Figure 4.21: The dimensionless experimental and simulated current vs. time curves of DC and PED deposited CIGS films

4.4 Conclusions

Chalcopyrite CIGS thin-films are deposited PED deposition technique in an additive free electrolyte by avoiding the additional step of selenization. For comparison, CIGS films are also deposited using DC deposited films. DC electrodeposited CIGS films are slightly copper rich which resulted in a deviated stoichiometry from the near-ideal one and observed to have porous morphology with surface roughness. In addition, the copper rich CIGS also contained undesired Cu_{2-x}Se secondary phases as confirmed from XRD and Raman studies. However, parameters are successfully optimized for PED deposition to produce near-ideal stoichiometric single phase chalcopyrite structured CIGS films with the elimination of undesired secondary phases. In addition, a highly dense uniform morphology is observed for PED deposited CIGS films which ultimately resulted in superior properties. The characteristic of p-type semiconductor is observed in the both the DC and PED deposited CIGS thin-films, as confirmed from Mott-Schottky as well as PEC studies. Absorption

studies are carried out to determine the band gap of thin-films which are in agreement with the theoretical stoichiometric CIGS band gap. The flat-band potentials and acceptor densities are calculated for both CIGS films from Mott-Schottky analysis. A simplified PED deposition technique has been used by manipulating the parameters to not only achieve control over the composition of elements but also resulted in stoichiometric phase-pure chalcopyrite CIGS thin-films with compact morphology. The typical growth mechanism of CIGS films by DC and PED deposition methods is also investigated experimentally and theoretically. The results demonstrate that the PED deposited CIGS films follow a progressive nucleation mechanism wherein the rapid growth of nuclei with an additional increase in number of nuclei take place with the deposition time leading to a uniform and compact CIGS films. The DC deposited films follow an instantaneous nucleation mechanism wherein non-uniform growth of active nuclei takes place without any increase in the nuclei number density. Further, the PED method used herein has utilized higher precursor concentration of In to achieve desired In content in the CIGS films, which is still a serious concern considering the scarcity of In in addition to its frequent usage in materials for electronic applications. Hence, minimization of In precursor is still a vital concern to be considered prior to the commercialization of the pulse electrodeposition approach for the fabrication of CIGS thin-films.

Chapter 5

Sequential pulse electrodeposition of $\text{Cu}(\text{In,Ga})\text{Se}_2$

It is of general interest to perform the electrodeposition of CIS/CIGS thin-films using a single step approach, as explored in previous chapters. However, the deposition of Ga and In is relatively difficult due to their more negative reduction potentials compared to Cu and Se. The required amount of In (≈ 18 at. %) for the formation of stoichiometric CIGS (theoretically, $\text{CuIn}_{0.7}\text{Ga}_{0.3}\text{Se}_2$) is greater than that of Ga (≈ 7 at. %). In addition, it has been observed that the In content decreases with increase in pulse off-time during the PED of CIGS thin-films as discussed in the previous chapter. These difficulties concerned to deposition of desired amount of In led the researchers to often focus on the optimization of In content in achieving the stoichiometric CIGS films. On the process, often high concentration of In precursor and/or use of complexing agents and/or deposition of In-Se on CIGS as a subsequent step have been used to achieve desired content of In in order to obtain stoichiometric CIGS thin-films [156, 161]. The use of high In precursor concentration is not a viable option due to its scarcity. In this context, the abundance of Cu, In, Ga and Se in earth's crust is shown in Figure 5.1. It can be observed that In and Se are least abundant elements among Cu, In, Ga and Se. In addition, the usage of In in the growing electronic and optoelectronic industries is very high in the form of materials such as indium doped tin oxide (ITO), CIS, CIGS, InP, InN, InGaAs, InAlAs, etc. making it one of the most scarce elements in the near future. Hence, it would be meaningful to use the In precursor as minimum as possible and explore other possibilities such as deposition of In in a separate step or use of complexing agents. In this context, it is also relevant to mention that the deposition of In-Se on CIGS in the second stage by Bhattacharya et al. not only improved the stoichiometry but also resulted in chalcopyrite CIGS films without any surface dispersed Cu-Se phase.

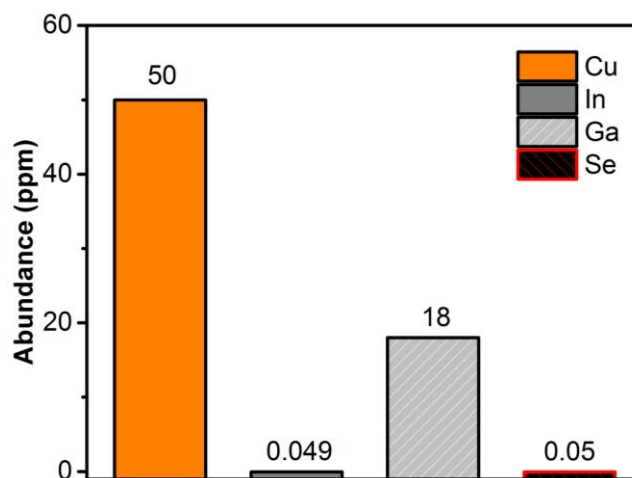


Figure 5.1: Elemental abundance of Cu, In, Ga and Se in earth's crust

In appreciation of the above, the present chapter proposes the fabrication of CIGS thin-films by employing a sequential pulse electrodeposition. The preliminary studies are performed based on the optimized parameters obtained in single stage PED of CIGS thin-films. However, further optimization of parameters in a sequential approach is required and is presented in the second part of this chapter. In the present chapter, the first approach is named as a two-stage PED and the second one as optimized sequential PED to distinguish the two approaches.

5.1 Two-stage deposited CIGS films

The preliminary deposition of CIGS thin-films using a two-stage approach is performed using the conditions that are adopted from PED electrodeposition of CIGS deposited for 15 min, discussed in the section 4.2. Electrodeposition of Cu-Ga-Se is carried out using a bath containing CuCl_2 (3 mM), GaCl_3 (8.5 mM), H_2SeO_3 (8.5 mM) and LiCl (250 mM) dissolved in Hydrion buffer (pH 3), followed by In deposition in the second stage using InCl_3 (2 mM) in Hydrion buffer. A pulse period of 20 ms, duty cycle of 50% and deposition potential of -1.5 V are used in for the deposition of both Cu-Ga-Se and In. The depositions of Cu-Ga-Se and In are carried out for 15 min and 8 min respectively. The electrodeposited CGS/In films are annealed at 550 °C for 30 min under Ar atmosphere to form the chalcopyrite CIGS films by the inter-diffusion of In into Cu-Ga-Se.

5.1.1 Compositional analysis of two-stage PED deposited CIGS thin-films

The elemental composition of individual elements of as-deposited and annealed two-stage CIGS thin-films, as obtained from energy dispersive spectroscopy (EDS), are shown in Table 5.1. The stoichiometry of the annealed CIGS films is determined to be $\text{Cu}_{0.96}\text{In}_{0.73}\text{Ga}_{0.27}\text{Se}_{2.04}$. It may be noted that the stoichiometry is close to the preferred near-ideal stoichiometry ($\text{CuIn}_{0.7}\text{Ga}_{0.3}\text{Se}_2$). While development of a single-stage electrodeposition process to fabricate CIGS thin-films with near-ideal stoichiometry can be interesting, prior efforts using a DC current have often led to formation of undesired Cu-Se phases on the surface, which are detrimental to the performance of the device [161]. Use of complexing agents in the electrolyte during deposition and/or etching of the CIGS film using KCN are commonly practiced in order to remove excess Cu and, hence, the secondary Cu-Se phases, as previously discussed. However, these can lead to presence of impurities in the films and increased film roughness, which adversely influence the performance. Therefore, it is preferable to deposit an In-layer at the surface followed by annealing. In addition, co-deposition of Cu-In-Ga-Se with required stoichiometry is difficult due to the large variation in their deposition potentials, whereas two-stage deposition makes it relatively easier to achieve the required composition of elements. In a similar attempt, Bhattacharya et al. have reported three-stage (CIGS/Cu/In) direct-current (DC) electrodeposition of crack-free dense CIGS thin-films with lower Ga content, attributable to subsequent deposition of Cu and In layers and loss of material during annealing [73]. In the present work, suitable use of optimized parameter (from single-stage PED electrodeposition) in the first stage followed by deposition of In in the second stage, aided the formation of stoichiometric CIGS films.

Table 5.1: Elemental composition of two-stage deposited CIGS thin-film before and after annealing

Element	Composition (at. %)	
	As-deposited	Annealed
Cu	22.31	24.00
In	17.39	18.25
Ga	5.49	6.75
Se	54.81	51.00

5.1.2 Morphology of two-stage PED deposited annealed CIGS thin-films

Figure 5.2 shows the morphology of annealed CIGS thin-films. As it can be seen, though the morphology is dense but the surface of the films is relatively rough. Pulse current (PED) electrodeposition produces a relatively more homogeneous surface as the rate-determining

step is controlled by mass-transfer process. Pulse off-time during deposition allows the diffusion of ad-atoms and facilitates the formation of new nucleation sites, thereby expected to yield a homogeneous and compact structure. A compact morphology is often desirable for the photovoltaic absorber layer since it leads to lower resistance and faster minority carrier diffusion, which ultimately serves to improve cell performance. However, the surface roughness of the films in the present case, could be due to the rapid deposition rate in the first stage at a deposition voltage of -1.5 V, may not be appropriate for solar applications.

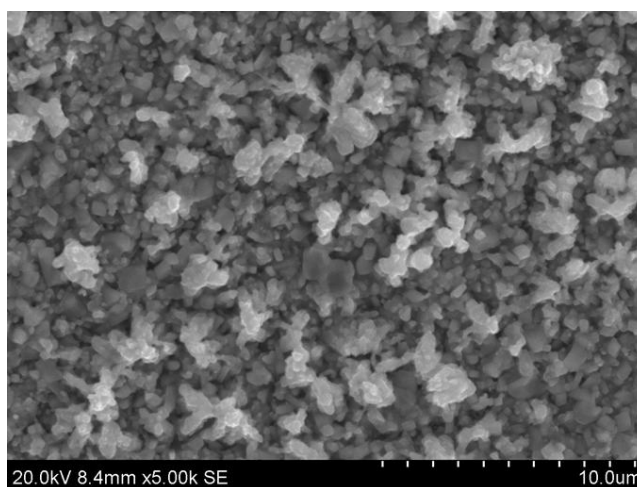


Figure 5.2: SEM image of an annealed two-stage PED electrodeposited CIGS thin-film

5.1.3 Phase constitution of two-stage PED deposited annealed CIGS thin-films

Phase constitution of annealed two-stage deposited CIGS thin-films is examined by X-ray diffraction and Raman spectroscopy. Figure 5.3a shows the XRD pattern of annealed CIGS thin-films prepared by two-stage PED electrodeposition. The pattern reveals a preferred orientation corresponding to (112) of CIGS, other peaks corresponding to (220), (312) and (424) (JCPDS: 35-1102), confirming the presence of crystalline chalcopyrite CIGS phase. In addition, peaks representing MoSe_2 (JCPDS: 29-0914) and Mo substrate (JCPDS: 42-1120) are also observed. Wada et al. have reported that formation of a thin layer of MoSe_2 at temperatures higher than 500 °C enhances adhesion and improves the ohmic contact between Mo and CIGS. It is also interesting to note that no peaks corresponding to the undesired Cu-Se phases are observed. Figure 5.3b shows the Raman spectrum of the annealed CIGS films. The spectrum of annealed CIGS thin films has well-defined peaks of CIGS A_1 mode and B_2/E mode at wave numbers of 176 and 215 cm^{-1} . The undesired $\text{Cu}_2\text{-}_x\text{Se}$ phase is absent in the annealed samples confirming the formation of single phase

chalcopyrite CIGS thin-films, which also corroborates the XRD results. In addition, a mode corresponding to MoSe₂ is also observed at 241 cm⁻¹ in the annealed CIGS thin-films. Appropriate use of pulse parameters during deposition of Cu-Ga-Se in the first stage and In in the second stage, combined with the annealing conditions chosen, plausibly facilitated control over the overall composition and resulted in stoichiometric CIGS thin-films.

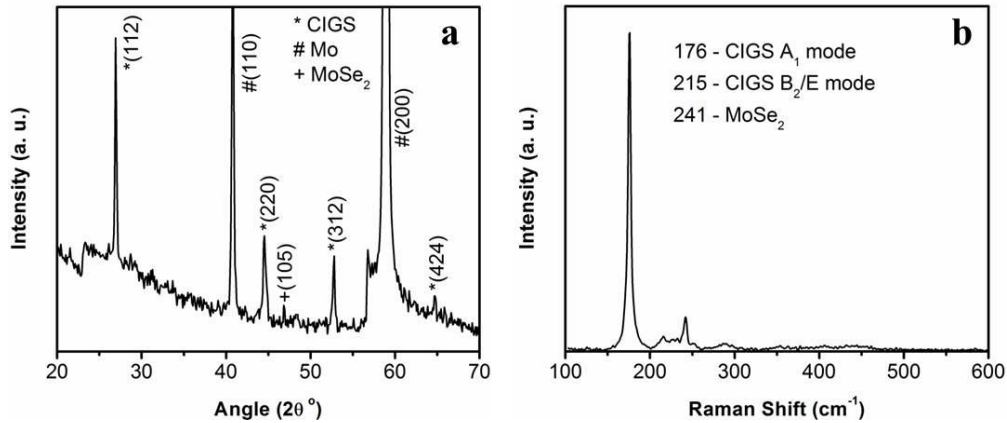


Figure 5.3: : a) XRD pattern and b) Raman spectrum of annealed two-stage PED electrodeposited CIGS thin-films

5.1.4 Band gap of two-stage PED deposited annealed CIGS thin-films

The band gap of the annealed two-stage deposited CIGS thin-films is determined using UV-Vis-NIR diffuse reflectance spectroscopy. Figure 5.4 shows the $(\alpha h\nu)^2$ vs. $h\nu$ plot of annealed two-stage deposited CIGS thin-films. Extrapolation of the linear section of the plot yields a bandgap of 1.27 eV, which compares well with the desired value as reported earlier.

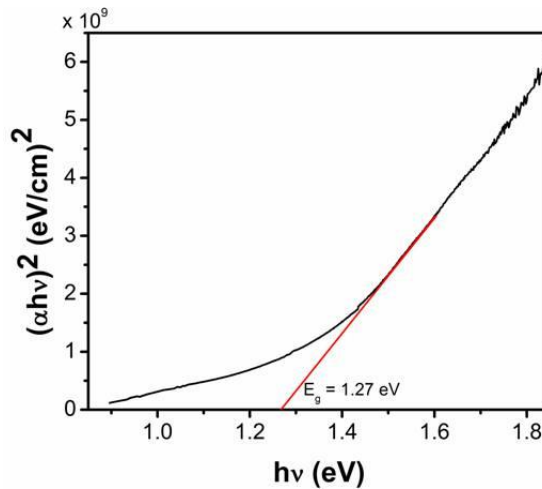


Figure 5.4: $(\alpha h\nu)^2$ vs. $h\nu$ plot of annealed two-stage PED electrodeposited CIGS thin-films

5.1.5 Photoelectrochemistry of two-stage PED deposited annealed CIGS thin-films

The photoelectrochemical performance of two-stage deposited annealed CIGS thin-films is investigated in 0.5 M Na₂SO₄. Current vs. potential curves are obtained in the potential range of 0 to -0.7 V vs. SCE at a sweep rate of 10 mV/s. Figure 5.5 shows the I-V curves in dark and under AM 1.5G solar simulated light for the CIGS films. I-V curve of one-stage PED electrodeposited CIGS films is also included for comparison. An increase in cathodic photocurrent, characteristic of a p-type semiconductor, is observed with increase in cathodic potential. This behavior can be attributed to incomplete photonic conversion, which causes a recombination of charge carriers at the grain boundary of the semiconductor. A photocurrent density of $\approx 0.2 \text{ mA/cm}^2$ at a potential of -0.6 V vs. SCE is observed. It is pertinent to note that significant reduction in the dark current and a considerable improvement in the photocurrent are observed compared to single-stage electrodeposited CIGS films discussed in the previous chapter, which yielded a photocurrent of $\approx 0.089 \text{ mA/cm}^2$ at a potential of -0.6 V vs. SCE. The near-ideal stoichiometry and dense morphology achieved by the two-stage electrodeposition process, combined with complete elimination of the undesirable Cu-Se phase, could have resulted in the reduction of dark current and improved photocurrent. It is important to note that Cu-Se is present in the CIGS films deposited by DC deposition and, being a degenerate semiconductor, is highly conductive. Consequently, its ability to sit at grain boundaries and/or at the surface of the film facilitates electron flow without any resistance even in the absence of light thereby contributing to high dark currents.

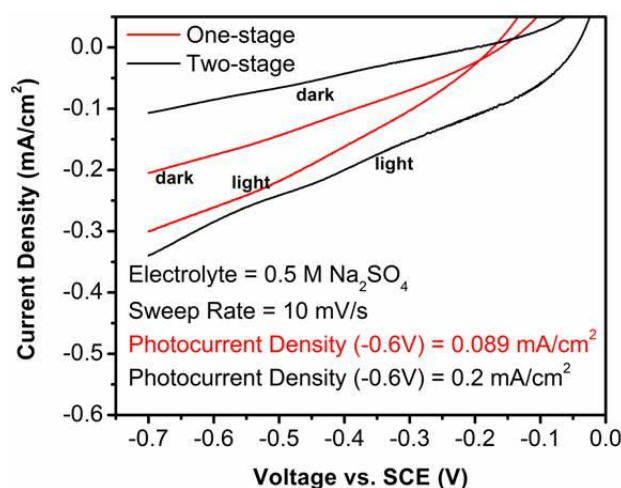


Figure 5.5: Photoelectrochemical response of annealed one-stage and two-stage PED electrodeposited CIGS thin-films

The above discussed approach has employed a two-stage method to obtain stoichiometric CIGS films and also satisfies the use of lower In precursor concentration as intended at the beginning of the chapter. However, the resulting morphology of the CIGS films is rough and porous which ultimately yielded lower photocurrent density. The morphology is still a serious concern as it plays a crucial role in the performance of the absorber layer. Hence, to improve the quality of the films, the approach is further systematically optimized to fabricate chalcopyrite CIGS thin-films.

Optimization of the two-stage PED electrodeposition is performed as follows:

1. Deposition of Cu-Ga-Se films in first stage wherein optimization of deposition voltage has been performed to achieve the necessary Cu, Ga and Se contents as desired for stoichiometric CIGS thin-films.
2. Fabrication of chalcopyrite CIGS thin-films by the deposition of In on Cu-Ga-Se films deposited in stage – I and annealing of the CGS/In films followed by their comprehensive characterization.

Schematic representation of the procedure adopted for the sequential pulse current electrodeposition of CIGS thin-films is shown in Figure 5.6. The applied pulse sequence and the corresponding current density during deposition are similar to that of PED electrodeposition of CIS/CIGS films, as shown in Figure 3.2.

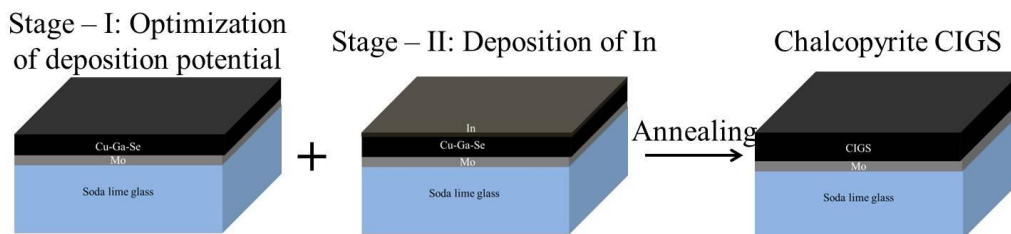


Figure 5.6: Schematic representation of the procedure adopted for CIGS thin-films deposition

5.2 Deposition of Cu-Ga-Se films – optimization of applied voltage

Electrodeposition of Cu-Ga-Se is carried out using CuCl_2 (3 mM), GaCl_3 (6 mM), H_2SeO_3 (8.5 mM) and LiCl (250 mM) dissolved in Hydrion buffer (pH 3). The final pH of the solution is maintained between 2.15 and 2.35 using HCl . The deposition voltage is optimized while keeping a constant duty cycle of 50 % and a deposition time of 30 min.

5.2.1 Compositional analysis of Cu-Ga-Se thin-films

The elemental composition of Cu-Ga-Se films prepared at different deposition voltages, as determined from energy dispersive X-ray spectroscopy, is shown in Figure 5.7. The amount of Ga is noted to increase from ≈ 3 to 6.8 at.% with the change in deposition voltage from -1.0 to -1.2 V. An increased negative voltage is expected to increase the Ga content since Ga has more negative reduction potential, as discussed in section 1.10. In addition, the use of two-electrode system has witnessed the requirement of higher deposition voltages than that required for a three-electrode system, as demonstrated in section 4.1.1. Hence, increase in Ga content is attributed to the increased deposition voltage to -1.2 V. Further change in deposition voltage to -1.5 V, however, leads to a decrease in the amount of Ga to ≈ 4 at.%. The pulse deposition voltage applied for the deposition and the corresponding current density during the deposition are shown Figure 3.2, respectively. It can be observed that there is a positive current density during the pulse off-time even without the application of any voltage. Such an unintended positive current density might oxidize the elements with least electronegativity from the deposited film leading to the dissolution of corresponding element into the electrolyte. In the present case, at the deposition voltage of -1.5 V, the magnitude of the positive current density during the pulse off-time might be sufficient to oxidize Ga, since it has the lowest electronegativity among the three elements. This could possibly be the reason for the lower Ga content at -1.5 V. A similar phenomenon has also been reported during pulse electrodeposition of CIS and CIGS thin-films [156, 167] and also observed during the PED electrodeposition of CIGS in the previous chapter. Considering that lower Ga content is required for obtaining stoichiometric CIGS, it is easier to optimize the Cu-Ga-Se films at a relatively lower voltage. As it can be seen from Figure 5.7, a deposition voltage of -1.2 V yields nearly ideal Ga content required ultimately for the formation of stoichiometric CIGS thin-films.

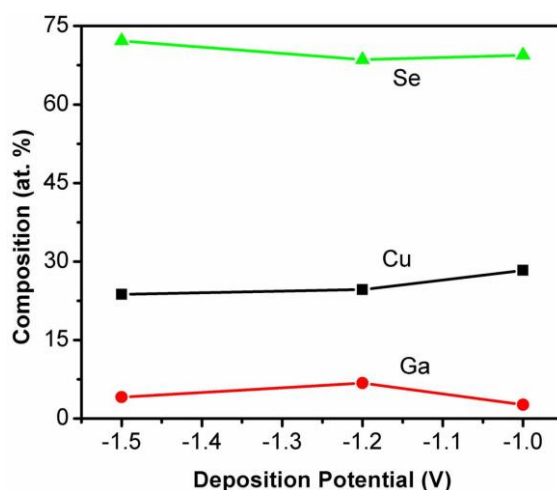


Figure 5.7: Variation in composition of individual elements in as-deposited Cu-Ga-Se films with varied deposition voltage

5.2.2 Morphological and profilometry studies of Cu-Ga-Se thin-films

The surface morphology of Cu-Ga-Se films deposited at different voltages is shown in Figure 5.8. Although the films deposited at -1.0 V show a uniform morphology, increasing the voltage to -1.2 V leads to a smoother and denser morphology (Figure 5.8b). It is plausible that selective dissolution of surface asperities due to relatively higher electrochemical activity leads to the smooth and compact morphology in films deposited at -1.2 V, which is desirable for uniform deposition of In in the second step. However, the films deposited at a further more negative voltage of -1.5 V are rough and porous compared to the other films. This could be attributed to the rapid deposition rate at more negative deposition voltage, as well as to the previously mentioned dissolution of Ga. Besides the morphological characterization, roughness measurements are also carried out using the profilometry. The average surface roughness (R_a) values are 60, 20 and 90 nm, for samples deposited at -1, -1.2 and -1.5 V, respectively. These values clearly demonstrate the fact that films deposited at -1.2 V (Figure 5.8b) are smoothest which further corroborates the morphological studies.

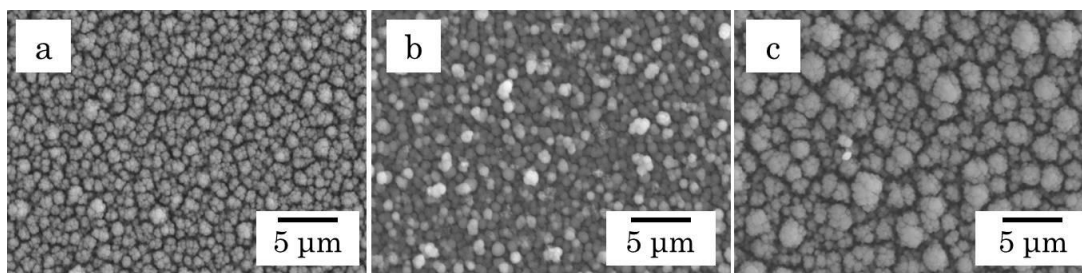


Figure 5.8: SEM images of as deposited Cu-Ga-Se films at a voltage of a) -1.0, b) -1.2, and c) -1.5 V

5.2.3 Micro-Raman spectra of Cu-Ga-Se thin-films

The CIGS films are characterized using micro-Raman spectra for phase analysis before annealing to identify the phases formed during the first deposition step. The specific purpose of the high-resolution micro-Raman studies is also to ascertain the vibrational modes of individual phases and detect any surface dispersed microcrystallites of Cu_{2-x}Se , as detection of phases like CIS, CGS, CIGS, Cu_{2-x}Se is difficult by XRD due to the negligible variation in 2θ values for the dominant (112) orientation of each phase, as shown in Table 4.4. Figure 5.9a shows the micro-Raman spectra of Cu-Ga-Se films deposited at various voltages. Three peaks corresponding to A_1 and E_1 modes of CuGaSe_2 (CGS) and A_1 mode of Cu_{2-x}Se noted at approximately 187, 239 and 260 cm^{-1} , respectively, are of interest [181]. In addition, the broader peak observed at 510 cm^{-1} is attributed to the second harmonic of the A_1 mode of Cu_{2-x}Se . As can be seen from the Figure 5.9a, the peak intensities of the E_1 mode of CGS and A_1 mode of Cu_{2-x}Se vary with the deposition voltage. Cu_{2-x}Se is an undesired secondary phase and, being a degenerate semiconductor, it contributes to higher dark current [61]. In addition, Cu_{2-x}Se is also stable along with CIGS at the annealing temperature ($550\text{ }^\circ\text{C}$) used to improve the crystallinity of CIGS phase and is expected to be present in minimal amounts even after annealing [24, 62, 113, 120]. Hence, reduction of this undesired secondary phase in as-deposited films is essential to improve the quality of CIGS thin-films which can affect the ultimate device performance. Consequently, presence of higher CGS and lower Cu_{2-x}Se is preferable in the as-deposited film. The ratios of E_1 mode of CGS and A_1 mode of Cu_{2-x}Se , as obtained from Raman spectra, are shown in Figure 5.9b, for Cu-Ga-Se films deposited at -1.0, -1.2 and -1.5 V, respectively. As the highest ratio of 0.50 corresponding to the maximum amount of CGS phase is obtained at a deposition voltage of -1.2 V, this value is deemed optimum for codeposition of Cu-Ga-Se films in the first stage.

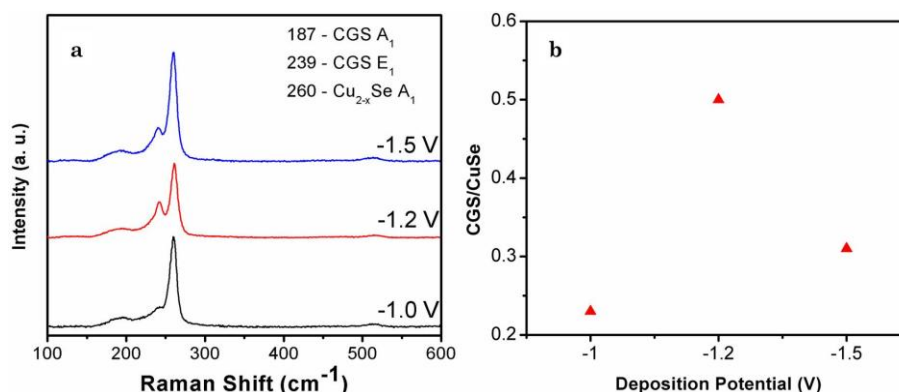


Figure 5.9: a) Raman spectra of as deposited Cu-Ga-Se films at various voltages and b) ratio of CGS to Cu_{2-x}Se intensities from Raman spectra

5.3 Fabrication of CIGS thin-films

As mentioned earlier, deposition of In is subsequently carried out at -1.5 V for 10 min on Cu-Ga-Se films deposited using different voltages in stage – I. A low concentration of In precursor (2 mM) is used to achieve the desired amount of In since the deposition is performed in a separate step. The CGS/In films are annealed at 550 °C under Ar atmosphere to form the CIGS by intermixing of the two layers.

5.3.1 Elemental composition of sequentially deposited annealed CIGS thin-films

The elemental composition of annealed films, as well as the relevant compositional ratios Cu/(In+Ga) and Ga/(In+Ga) in the films are depicted in Figure 5.10. It is deemed informative to plot the above as a function of the deposition voltage applied during stage – I because, although In is deposited in a subsequent step, the composition of the Cu-Ga-Se films achieved after stage – I plays a key role in determining the eventual stoichiometry of the annealed CIGS films. This is primarily because, in the tetragonal chalcopyrite structure of CIGS, the Ga and In atoms compete for identical lattice sites [140, 181]. Consequently, the uptake of In during stage – II is influenced by the Ga content in Cu-Ga-Se films after stage – I as clearly revealed in Figure 5.10. The composition of Cu and Se in the annealed sequentially deposited CIGS films does not vary substantially with change in deposition voltage during Stage – I. The Cu and Se content are also found to be close to the ideal values required for formation of stoichiometric CIGS films. In contrast, considerable variation is observed in the Ga and In content in the annealed CIGS thin-films depending on the deposition voltage applied during Cu-Ga-Se deposition in stage – I. When the amount of Ga is relatively lower at stage – I deposition voltages of -1.0 V and -1.5 V, the In content correspondingly increases. However, at -1.2 V, the Ga and In are present in near-ideal

quantities to form stoichiometric CIGS. At the stage – I deposition voltage of -1.2 V, the Cu/(In+Ga) and Ga/(In+Ga) ratios are observed to be 0.97 and 0.27, respectively, for annealed CIGS films, which are close to the desirable values for high efficient CIGS thin-films [30, 31, 143, 182]. The stoichiometries of the films, as obtained from EDS, are $\text{Cu}_{0.97}\text{In}_{0.90}\text{Ga}_{0.10}\text{Se}_{2.03}$, $\text{Cu}_{0.97}\text{In}_{0.73}\text{Ga}_{0.27}\text{Se}_{2.03}$ and $\text{Cu}_{1.02}\text{In}_{0.81}\text{Ga}_{0.19}\text{Se}_{1.98}$ at -1.0 V, -1.2 V and -1.5V, respectively, indicating the near-ideal stoichiometry in the films deposited at -1.2 V.

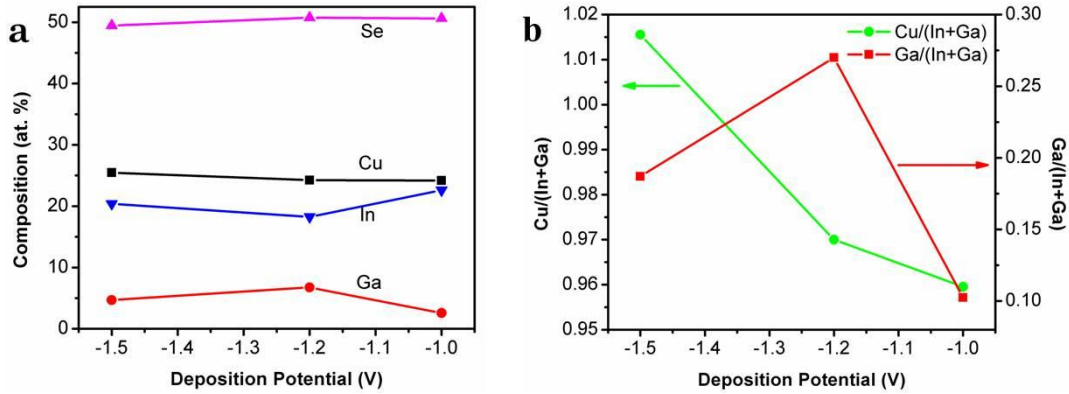


Figure 5.10: Elemental composition and b) Cu/(In+Ga) and Ga/(In+Ga) ratios in sequentially deposited and annealed CIGS thin-films with variation in deposition voltage applied during stage – I

5.3.2 Morphology of sequentially deposited annealed CIGS thin-films

Figure 5.11 shows the morphology of sequential deposited and annealed CIGS thin-films for various deposition voltages employed during stage – I. As can be seen, a rough surface morphology is observed for films deposited at -1.0 and -1.5 V. The films deposited at -1.2 V are noted to have a smooth and compact morphology (Figure 5.11b). Such a dense morphology is well-suited for application as solar absorber layers, since it facilitates easier diffusion of minority charge carriers and reduces recombination, which ultimately yields improved cell performance [71, 175]. Additionally, the surface roughness measurements by profilometry yielded the R_a values as 90, 30 and 130 nm, for the films deposited at -1.0, -1.2 and -1.5 V, respectively, also support the observed SEM results.

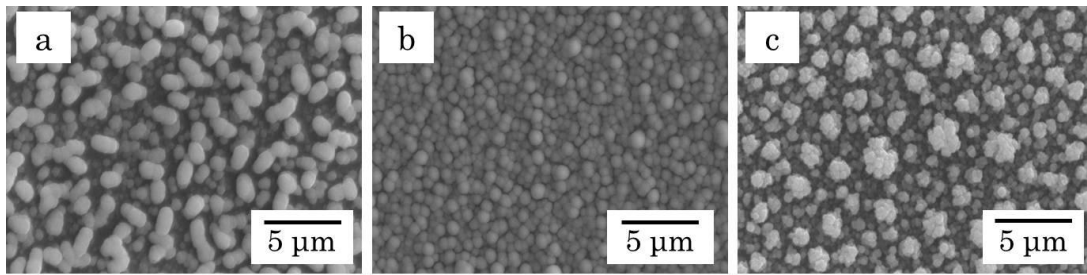


Figure 5.11: Morphology of annealed CIGS thin-films deposited at a voltage of a) -1.0 V, b) -1.2 V and c) -1.5 V in stage – I

5.3.3 XRD patterns of sequentially deposited annealed CIGS thin-films

Figure 5.12 shows the X-ray diffraction patterns of sequential deposited and annealed CIGS thin-films at various deposition voltages used in stage – I. The XRD patterns in each case are observed to have a preferred orientation corresponding to (112) of CIGS, with the presence of other peaks corresponding to (220), (312) and (424) (JCPDS: 35-1102) confirming the presence of crystalline chalcopyrite CIGS phase. In addition, a peak corresponding to Mo from the substrate (JCPDS: 42-1120) is also observed. However, a closer inspection reveals a shift in the (112) orientation of CIGS to a lower 2θ value for the CIGS films deposited at -1.0 V (inset of Figure 5.12). It is well known that with decrease in the amount of Ga the (112) peak shifts to lower 2θ values as the incorporation Ga leads to a decrease in lattice parameter, as discussed previously. As evident from the EDS analysis, the film deposited at -1.0 V has a relatively lower Ga content and is expected to have a CIGS phase with larger lattice parameter. Also, the higher In content results in a secondary indium selenide (In_2Se_3) phase in the films deposited at -1.0 V. The XRD patterns of films deposited at -1.2 V and -1.5 V are, however, found to have well defined peaks corresponding to only ideal stoichiometric chalcopyrite CIGS. No considerable shift is observed for (112) orientation in the films deposited at -1.2 V and -1.5 V owing to a very minor variation in the Ga content. However, such a negligible difference is observed in Raman spectra as explained later. It can also be seen that the peak maximum height is observed in the case of CIGS deposited at -1.2 V in stage – I, affirming -1.2 V to be the optimized voltage. It is also interesting to note that no peaks corresponding to the undesired Cu-Se and In-Se phases are observed for the optimized case.

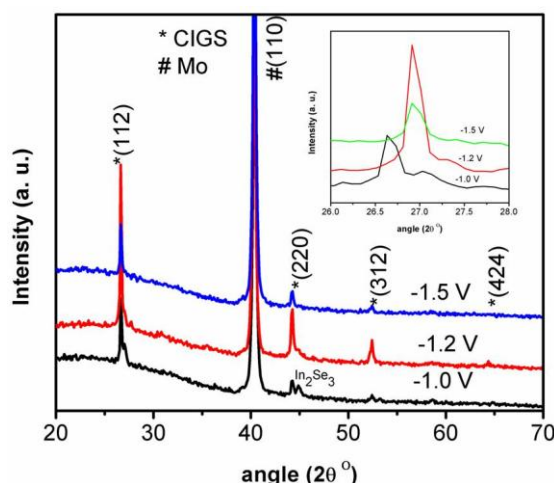


Figure 5.12: XRD pattern of annealed sequentially deposited CIGS thin-films at various voltages in stage I. Inset: Closer inspection of (112) orientation of CIGS thin-films

5.3.4 Raman spectra of sequentially deposited annealed CIGS thin-films

Figure 5.13a shows the Raman spectra of the sequential deposited and annealed CIGS films for various deposition voltages employed during stage – I. The spectra reveal peaks corresponding to A_1 and B_2/E modes of CIGS at wave numbers of 176 , 215 and 232 cm^{-1} , respectively. In addition, a small peak observed at the wavenumber of 480 cm^{-1} can be attributed to the presence of secondary In_2Se_3 phase for the films deposited at -1.0 V . Figure 5.13b shows the shift of A_1 mode of CIGS with deposition voltage. The A_1 mode for CIGS films deposited at -1.0 V in stage – I, is observed at a lower Raman shift of 172 cm^{-1} . This could be attributed to the lower Ga content observed in these films at -1.0 V . It is well reported that the A_1 mode is observed at lower wavenumbers in the range of $171\text{--}173\text{ cm}^{-1}$ for CIGS films with very low Ga content, with the peak shifting to higher wavenumbers of $176\text{--}178\text{ cm}^{-1}$ for stoichiometric CIGS thin-films and to 187 cm^{-1} for CuGaSe_2 . The CIGS films deposited at -1.5 V are also observed to have A_1 mode at a lower Raman shift of 173 cm^{-1} . As it is evident from EDS, the Ga content is higher compared to films deposited at -1.0 V and lower compared to films deposited at -1.2 V . The relatively lower Ga content is accountable for the shift of A_1 mode to lower wavenumbers. However, the films deposited at -1.2 V exhibit a sharp peak at 176 cm^{-1} which corresponds to the stoichiometric CIGS A_1 mode and does not contain any CGS and Cu_{2-x}Se phases which are observed prior to the second step of deposition, thereby confirming formation of a phase-pure chalcopyrite CIGS thin-film. As previously mentioned, elimination of the undesired Cu_{2-x}Se secondary phase in the annealed films is extremely crucial, and is successfully achieved in the present case by

the optimization of deposition voltage in the first stage followed by the deposition of In in the second stage.

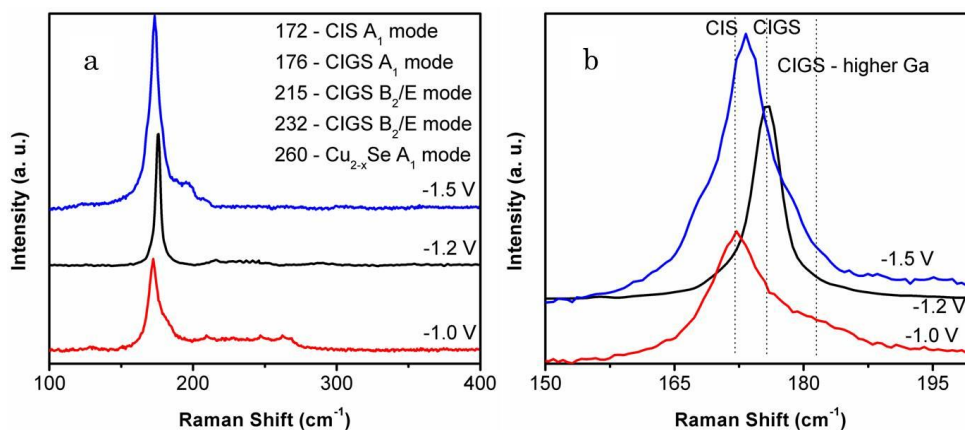


Figure 5.13: a) Raman spectra of annealed sequentially deposited CIGS thin-films at various voltages in stage I and b) a closer inspection of A₁ mode

5.4 Characterization of optimized CIGS thin-films

The optimized stoichiometric annealed CIGS thin-films (stage – I deposited CGS at -1.2 V) are further characterized using XRF, HRTEM, FESEM, UV-Vis-NIR diffuse reflectance spectroscopy, electrochemical impedance spectroscopy and photoelectrochemical analysis.

5.4.1 Compositional analysis of optimized CIGS thin-films by XRF

The bulk composition and thickness of the optimized CIGS films has been determined by XRF spectroscopy and are shown in Table 5.2, which confirm the near ideal stoichiometry of the optimized sequential deposited and annealed CIGS thin-films and have a thickness of 1.6 μm

Table 5.2: Composition and thickness of optimized sequential deposited annealed CIGS films

Composition (at. %)				Stoichiometry	Thickness (μm)
Cu	In	Ga	Se		
24.01	18.52	6.96	50.51	Cu _{0.96} In _{0.74} Ga _{0.28} Se _{2.02}	1.76

5.4.2 Structural analysis of optimized CIGS thin-films by TEM

Optimized sequential deposited annealed CIGS thin-films are further characterized using transmission electron microscopy. The specific use of TEM analysis for these samples is to check the inter-diffusion of In into Cu-Ga-Se films to ultimately yield CIGS thin-films.

SEM-EDS though detects the desired amount of In but it does not detect the In from a localized point or a specific particle. TEM can detect the elements locally and from separate particles too, which is necessary in the present case to check the inter-diffusion of In uniformly across the film. In this context, the transmission electron micrograph, the high resolution TEM image, selected area diffraction (SAD) pattern and TEM-EDS spectrum of CIGS particles are shown in Figure 5.14. The particles are not clearly distinguishable due to the fact that the samples are prepared by scraping the CIGS films from the substrate, as mentioned in section 2.3.5. Hence, analysis of the particle is not considered using TEM. Figure 5.14b shows the high resolution TEM image of CIGS thin-films, which reveals planes with an interplanar spacing of approximately 3.32 and 2.03 Å. These values are in good agreement with the theoretical values for the (112) and (220) orientations of CIGS, which corroborates the presence of polycrystalline chalcopyrite CIGS as observed from XRD analysis. The SAD pattern, in Figure 5.14c, shows the orientations corresponding to (112), (220), (312) and (400) of CIGS, which are in agreement with the previously discussed observation from XRD. TEM-EDS analysis is performed, as shown in Figure 5.14d, reveals presence of Cu, In Ga and Se affirming the inter-diffusion of In (deposited in stage – II) during annealing leading to the formation of CIGS films.

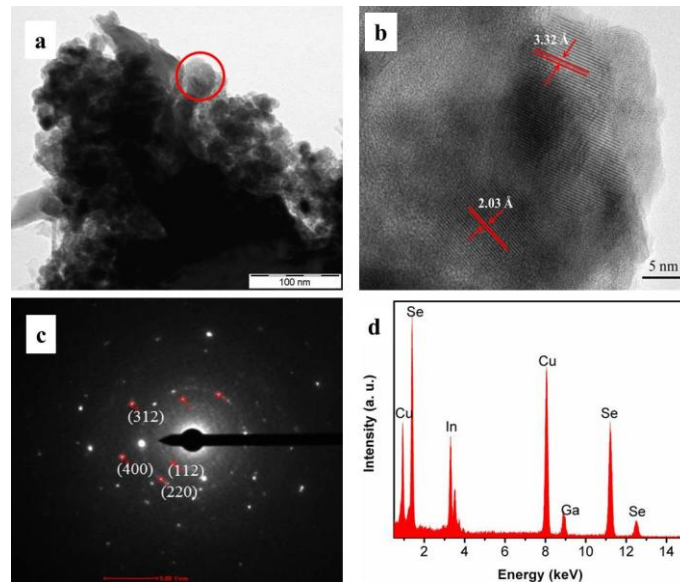


Figure 5.14: a) TEM image, b) HRTEM image, c) SAED and d) TEM-EDS of sequentially deposited CIGS. Red circle in image (a) indicates the position where EDS, SAED and HRTEM are performed

5.4.3 Cross-section analysis of optimized CIGS thin-films by SEM

Figure 5.15 shows the cross-sectional SEM image of optimized sequentially deposited and annealed CIGS thin-films. The cross-section of the film is highly compact, indicating the formation of dense CIGS thin-films. The thickness of the films is determined to be $\approx 1.8 \mu\text{m}$, which is desirable for high efficient CIGS devices. The sputtered Mo layer (200 nm) is also seen in the film.

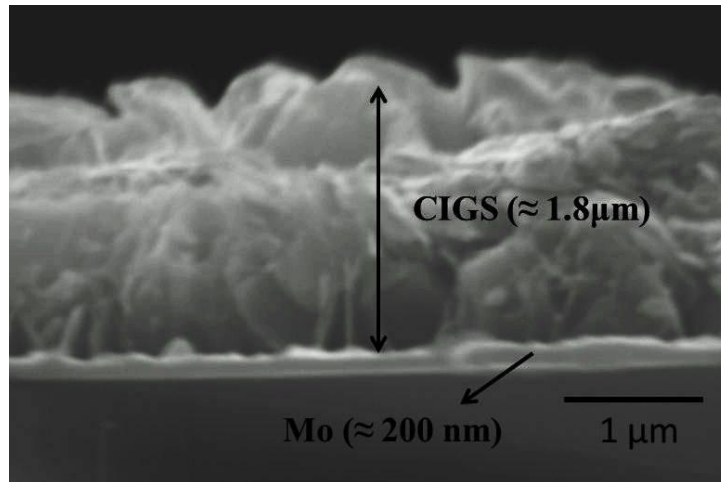


Figure 5.15: Cross-sectional SEM image of optimized sequentially deposited and annealed CIGS thin-film

5.4.4 Optical studies of optimized CIGS thin-films

Figure 5.16 shows $(\alpha h\nu)^2$ vs. $h\nu$ plot of the annealed sequentially deposited CIGS thin-films. The bandgap of the CIGS thin-films is obtained to be $\approx 1.27 \text{ eV}$, determined by extrapolating the linear section of the $(\alpha h\nu)^2$ vs. $h\nu$ plot to x-axis, which is close to the value for stoichiometric CIGS thin-films.

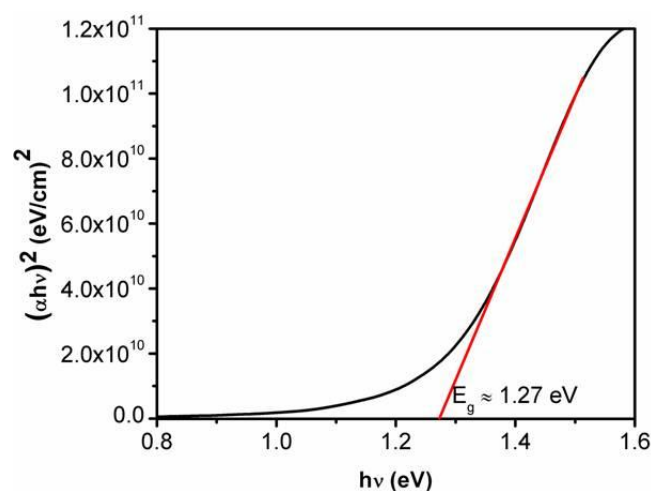


Figure 5.16: $(\alpha h\nu)^2$ vs. $h\nu$ plot of optimized sequentially deposited and annealed CIGS thin-films

5.4.5 Mott-Schottky analysis of optimized CIGS thin-films

Figure 5.17 shows the Mott-Schottky ($1/C^2$ vs. V) plot of CIGS thin-films in 0.5M H_2SO_4 at a frequency of 10 kHz in the dark. The slope of the MS plots is negative, thereby confirming that the CIGS film is p-type. The flat band potential is found to be -0.15 V (vs. SCE) by extrapolating the linear section to x-axis. In addition, the acceptor density, $N_a \approx 2.6 \times 10^{16} \text{ cm}^{-3}$, calculated using the slope of the curve. The flat-band potential and acceptor density values determined herein are close to the desirable values for stoichiometric CIGS films that have been reported previously [145].

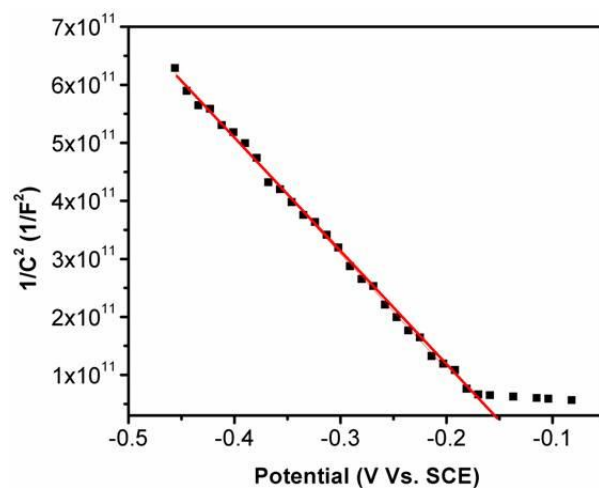


Figure 5.17: Mott-Schottky ($1/C^2$ vs. V) plot (recorded at 10 kHz in the dark) of optimized sequentially deposited and annealed CIGS thin-films

5.4.6 I-V characteristics of optimized CIGS thin-films by PEC

Figure 5.18a shows dark and illuminated current density – voltage characteristics of the optimized annealed CIGS thin-films deposited by sequential PED electrodeposition, measured using a photoelectrochemical analyzer in 0.5 M H₂SO₄ with a sweep rate of 10 mV/s. The nature of the J-V curve confirms the photo-activity of CIGS thin-films. In addition, it shows the increase in cathodic photocurrent with increased cathode potential, which is a characteristic of a semiconductor with p-type conductivity. A photocurrent density of $\approx 800 \mu\text{A}/\text{cm}^2$ at a potential of -0.4 V vs. SCE is observed. This represents a considerable improvement in photocurrent density compared to the value of $\approx 100 \mu\text{A}/\text{cm}^2$ observed for single stage deposited CIGS thin-films, discussed previously in section 4.2.9. The crack-free dense morphology observed in the present optimized CIGS thin-films supports the easier diffusion of minority carriers and is responsible for the improved photoelectrochemical performance. It is also to be noted that the photocurrent increases gradually without attaining a saturated value. This behavior can be attributed to incomplete photonic conversion, which causes a recombination of charge carriers at the grain boundaries of the semiconductor. Figure 5.18b shows the amperometric current-time (I-t) curve of annealed sequential PED electrodeposited CIGS films obtained at -0.4 V by chopped light. It clearly demonstrates the photoactivity nature of CIGS films with a photocurrent density of $\approx 0.8 \text{ mA}/\text{cm}^2$. The improved photoresponse of sequentially deposited and annealed CIGS films indicate their potential for application in thin-film solar cells. In addition, the photoelectrochemical performance of these films demonstrates their application for photoelectrochemical hydrogen generation.

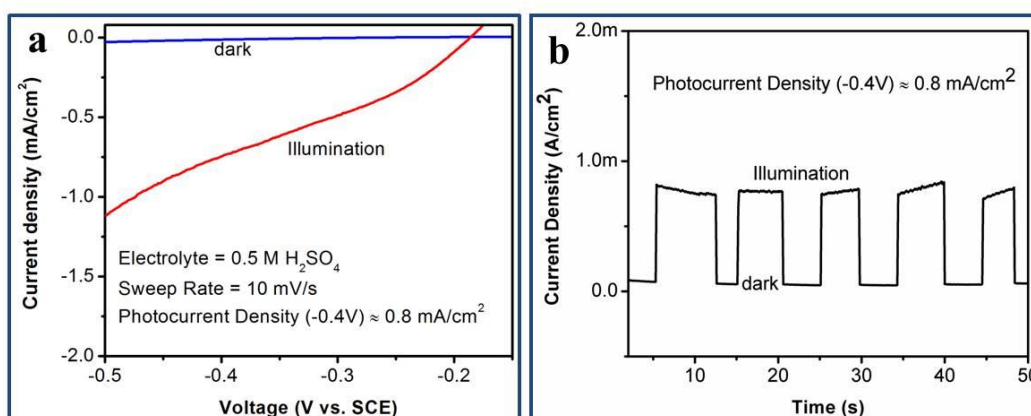


Figure 5.18: a) Photoelectrochemical I-V characteristics (under AM1.5G solar simulated light) and b) Amperometric I-t curve at -0.4 V of optimized sequentially deposited and annealed CIGS thin-films

5.5 Conclusions

A novel sequential pulse current approach has been employed for the fabrication of CIGS thin-films to essentially minimize the In precursor concentration by simultaneously achieving desired In content. Deposition voltage has been optimized for the co-deposition of Cu-Ga-Se films in stage – I followed by deposition of In in the second stage. A convenient control over the composition of individual elements has been achieved by the suitable manipulation of process parameters. Characterization of annealed films using XRD and Raman analyses confirmed the formation of phase-pure stoichiometric chalcopyrite CIGS phase. CIGS films exhibited p-type conductivity as demonstrated from Mott-Schottky as well as PEC studies. Furthermore, a significantly improved photoresponse has been observed. This technique presents a simplified, economic and scalable method for fabrication of CIGS thin-films for solar cell applications.

Chapter 6

Fabrication of Cu(In,Ga)Se_2 nano-flakes by pulse electrodeposition

The minimization of the In precursor during the electrodeposition of CIGS has been discussed in the previous chapter due to the scarcity of In and its frequent usage in electronic and optoelectronic applications. In this context, it has been proposed that various possibilities such as deposition of In in second stage and/or use of complexing agents in the electrolyte during the electrodeposition of CIGS thin-films to improve the content of In. However, as discussed in section 1.11, one of the major implications of the present study is to avoid the use of complexing agents for the deposition of chalcopyrite CIGS thin-films. Supporting this key point, successful fabrication of stoichiometric chalcopyrite compact CIGS thin-films without any secondary phases by avoiding the use of complexing agents in the electrolyte has been demonstrated in previous chapters. Nevertheless, conventional direct current electrodeposition employing the three-electrode system has often used complexing agents in the electrolyte to improve the stoichiometry and morphology of the CIGS thin-films [154, 161]. In this context, use of complexing agents during the pulse electrodeposition of CIGS thin-films can still be a novel objective to fundamentally understand the role of complexing agent on the deposition of CIGS. Tri-sodium citrate has been the most explored complexing agent till date for the electrodeposition of CIGS thin-films. Hence, this chapter focuses on the effect of tri-sodium citrate as complexing agent on the features of CIGS thin-films prepared by pulse electrodeposition. In addition, while optimizing the concentration of tri-sodium citrate for achieving desired composition of CIGS films nanostructured morphology of the deposit is observed for lower concentration of tri-sodium citrate. The condition is further investigated in detail. Therefore, the major aspects of this chapter are classified as follows:

1. Effect of concentration of tri-sodium citrate on the composition and morphology of CIGS thin-films
2. Fabrication of novel hierarchical CIGS nano-flakes using a definite concentration of complexing agent

6.1 Effect of tri-sodium citrate (TSC) on pulse electrodeposition of CIGS

Pulse electrodeposition (PED) of CIGS has been carried out using CuCl_2 (3 mM), InCl_3 (2 mM), GaCl_3 (8.5 mM), H_2SeO_3 (6 mM) and LiCl (250 mM) in Hydrion buffer (pH 3). In addition, tri-sodium citrate (TSC) is used as complexing agent whose concentration has been varied from 40 mM to 120 mM. The pH of the final solution is maintained between 2.15 to 2.35. PED deposition of CIGS thin-films is performed using the optimized pulse conditions as mentioned in chapter 4 with a deposition potential of -1.5 V. For the preliminary optimization of TSC concentration, a deposition time of 15 min has been employed. Later the time is increased to 30 min while the deposition is performed with optimized TSC concentration. Electrodeposited CIGS thin-films are annealed in Ar atmosphere for 30 min and are comprehensively characterized.

6.1.1 Variation in composition of CIGS thin-films with varied TSC concentration

Elemental composition of annealed PED deposited CIGS thin-films with varied tri-sodium citrate (TSC) concentration is shown in Figure 6.1a. It can be clearly seen that Cu content has significantly dropped with increase in TSC's concentration from 40 to 120 mM. On the other hand, In and Ga contents are noted to increase while Se content seems to be almost unaffected with the increase in TSC. It is generally known that the electrodeposition of In and Ga is difficult due to their more negative reduction potentials. However, in the present case, the contents of In and Ga are increased indicating their competing deposition rate with Cu when higher concentration of TSC is used in the electrolyte. This is an interesting finding and has been well reported that it could be due to the formation of complex with Cu that results in a shift in the reduction potentials of Cu, In and Ga. However, the phenomenon lacked a proper explanation for the behavior of TSC in the electrolyte.

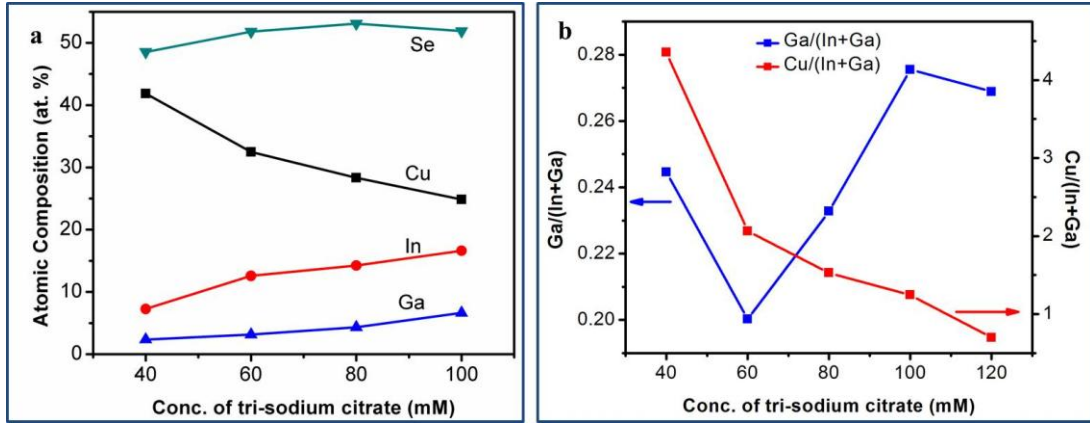
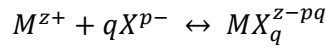


Figure 6.1: a) Atomic composition of individual elements and b) Cu/(In+Ga) and Ga/(In+Ga) ratios of annealed PED deposited CIGS thin-films with varied concentration of tri-sodium citrate

Considering the key point of complex formation into account, a previous study has proposed the possible mechanism of complexing agent role in the electrolyte as follows [183]:

Consider M^{z+} as the metal ions in the electrolyte and X^{p-} as the complexing agent that is externally added to the electrolyte. The possible chemical reaction between the metal ions and the complexing ions that leads to the complex formation is as follows:



where q is the no. of moles of complexing agent that takes part in the reaction and z and p are the charges associated with the metal ions and complexing agent, respectively.

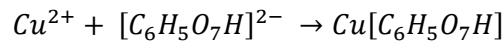
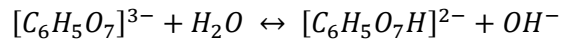
Due to the above reaction the corresponding Nernst's equation of the metal ions involving their reduction potential gets transformed as mentioned below [183]:

$$E = E_{M^{z+}}^0 - \frac{RT}{ZF} \ln \left[\frac{a_{MX_q^{z-pq}}}{(a_{X^{p-}})^q} \right]$$

where E is the shifted reduction potential due to the complex formation, $E_{M^{z+}}^0$ is the standard reduction potential of the metal ions, $a_{MX_q^{z-pq}}$ is the activity of the complex product formed due to the above mentioned reaction, $a_{X^{p-}}$ is the activity of the complexing agent, R universal gas constant, T is the temperature, Z is the no. of electrons participated in the reaction and F is the Faraday's constant. It can be observed from the above equation that

the reduction of metal ions depends significantly on the activities of complexing agent and the resultant complex formed with metal ions. Hence, a shift in the reduction potential is often observed for the metal ions in the presence of a complexing agent.

Based on the above mechanism, the possible reaction in the present study can be described as follows: Tri-sodium citrate forms a complex with Cu^{2+} ions as per the reactions mentioned below:



As a result the Nernst's equation describing the copper ions reduction gets transformed as follows:

$$E = E_{\text{Cu}^{2+}}^0 - \frac{RT}{2F} \ln \left[\frac{a_{\text{Cu}[\text{C}_6\text{H}_5\text{O}_7\text{H}]}}{a_{[\text{C}_6\text{H}_5\text{O}_7\text{H}]^{2-}}} \right] = 0.337 - \frac{RT}{2F} \ln \left[\frac{a_{\text{Cu}[\text{C}_6\text{H}_5\text{O}_7\text{H}]}}{a_{[\text{C}_6\text{H}_5\text{O}_7\text{H}]^{2-}}} \right]$$

where E is the shifted reduction potential, $E_{\text{Cu}^{2+}}^0$ is the standard reduction potential of Cu^{2+} vs. NHE, a represents the corresponding activities and the other symbols have their usual meaning as mentioned above. It clearly shows a shift in reduction potential of Cu to more negative values and the shift depends significantly on the concentration of the TSC in the electrolyte. For higher concentrations, more negative shift can be observed from the above equation. However, much higher concentration of the complexing agents in the electrolyte might not only lead to poor copper content but may also result in the dissolution of deposited films into the electrolyte leading to high surface roughness. This could be due to the fact that when the shift in reduction potential occurs, the oxidation potential of the corresponding element gets equivalently shifted to smaller values. In pulse electrodeposition, due to the unintended positive current density the elements now gets oxidized back into electrolyte leading to the dissolution of film. In addition, higher concentration might also increase the impurities in the deposited films. Hence, optimization of concentration of complexing agent is an important step while performing the electrodeposition of thin-films. The presence of TSC, however, has no effect on In and Ga since these elements do not form any complex with citrate ions [88, 184].

In the present case, the reduction potential of Cu shifts to more negative values resulting in a narrow variation in the reduction potentials of Cu, In and Ga. Hence, In and Ga also compete with the deposition of Cu, however, the competition further depends on the concentration of the tri-sodium citrate in the electrolyte. As seen from Figure 6.1a, the copper content decreases with an increase in TSC's concentration from 40 to 120 mM. With the increased TSC concentration, amount of In and Ga correspondingly increased. However, at much higher concentration of 120 mM of TSC, the copper content is much lower than the desired value for the formation of CIGS thin-films. For 100 mM TSC, the elements have approximately desired composition as required for stoichiometric CIGS. In addition, the corresponding Cu/(In+Ga) and Ga/(In+Ga) ratios are shown in Figure 6.1b. The ratios are observed to have near-ideal values of 1.2 and 0.27 for the TSC concentration of 100 mM. As previously mentioned, the deposition is carried out for 15 min while optimizing the TSC's concentration which will be further increased to 30 min. The composition and morphology of the films deposited with 100 mM of TSC for 30 min is discussed later.

6.1.2 Morphology of annealed CIGS thin-films with varied TSC concentration

The variation in morphology of annealed PED deposited CIGS thin-films with various concentrations of TSC, is shown in Figure 6.2. As it can be observed from the figure that flower like particles are observed for the lower concentration of TSC (40 to 60 mM). However, these particles form into a compact film upon increasing the concentration of TSC to 100 mM leading to a relatively smoother morphology of the CIGS films. Further increase in the concentration of TSC to 120 mM, however, shows a rough morphology. The effect of the complexing agent which leads to different morphologies of electrodeposited thin-films is discussed below.

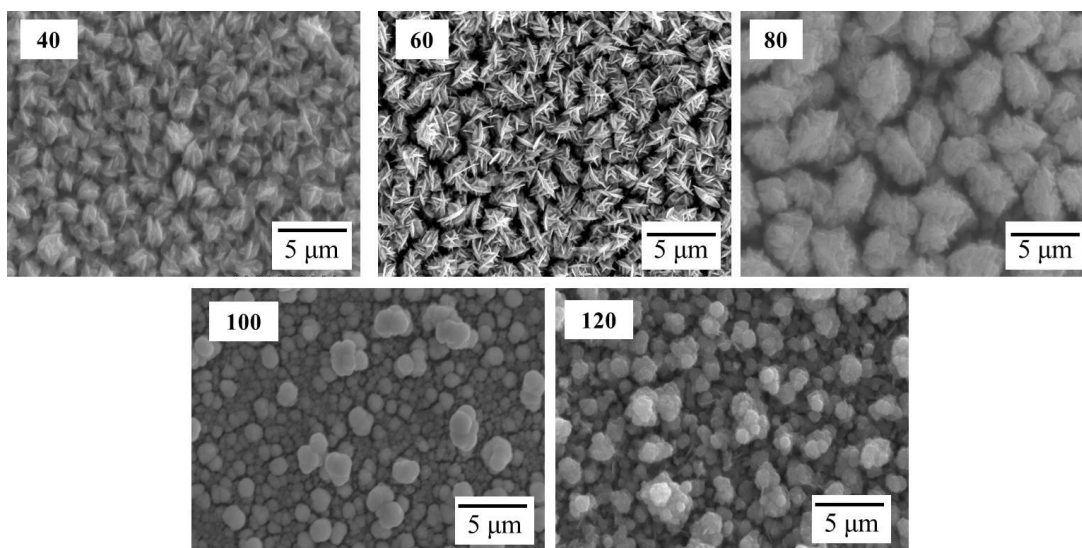


Figure 6.2: Surface morphology of annealed PED deposited CIGS thin-films with varied concentration of tri-sodium citrate

The kinetics of electrodeposition and the growth of the deposit are, in general, affected by the complexing agents in the following ways:

1. Complexing agents involve in the chemical/electrochemical reactions in the electrolyte (at cathode or anode).
2. Complexing agents or their resulting products (of above mentioned chemical reaction) act as additives due to their adsorption at the surface of the cathode.

The chemical/electrochemical reactions of the complexing agents often affect the kinetics of electrodeposition which in turn results in the variable composition of the deposit, as discussed in the previous section. The adsorption of complexing agents or their products affect the growth of the resulting deposit. There are two basic ways of adsorption, namely, the chemisorption (chemical adsorption) and physisorption (physical adsorption). In chemisorption, the chemical attractive forces of adsorption act between the surface and the adsorbate (usually chemical bonds). There is a chemical combination between the substrate and the adsorbate where electrons are shared and/or transferred leading to the formation of new electronic configurations. In physisorption, the physical forces of adsorption such as Vander Waals or electrostatic forces act between the surface and the adsorbate (no electron transfer/sharing). The additives adsorbed by either of these ways affect the growth of the deposit essentially by influencing the concentration of ad-ions/ad-atoms on the surface, the diffusion coefficient and the activation energy of the surface diffusion of ad-ions/ad-atoms. This in turn influences the growth sites on the surface of the cathode. In the presence of an additive, the mean free path for lateral diffusion of ad-ions/ad-atoms is diminished which in turn decreases the diffusivity of ad-ions/ad-atoms. The decreased diffusivity results in an

increase in the concentration of ad-ions/ad-atoms at steady state and thus promotes the two-dimensional nucleation between diffusing ad-ions/ad-atoms. In addition, their preferential adsorption at the high point (peaks of the deposit) inhibits (slows down) the deposition at these points. Due to these aspects, the deposition happens in a well-controlled manner often leading the smooth and compact morphology. However, the smoothness and compactness vary with the variation in concentration of the complexing agents. Very high concentration of complexing agents is also not preferable due to the increased impurity content and also results in disruption and dissolution of the deposit into the electrolyte, as previously discussed [75].

In the present case a smooth and compact morphology is observed for the CIGS films deposited using a concentration of 100 mM, which is deemed optimum. However, the CIGS films deposited with high concentration of TSC (120 mM) resulted in poor composition and morphology. In addition, the disruption and dissolution of these films is observed in the electrolyte and while washing with DI water post the deposition which indicates the poor adhesion of the films to the substrate. Hence, these films are not considered for further characterization.

Deposition of CIGS films with 100 mM of TSC for 30 min:

As previously mentioned, the optimized TSC concentration (100 mM) is used to deposit the CIGS thin-films for a deposition time of 30 min. The pulse conditions and deposition voltage are the same as used for the deposition of CIGS thin-films for 15 min. The composition of individual elements and corresponding ratios $\text{Cu}/(\text{In}+\text{Ga})$ and $\text{Ga}/(\text{In}+\text{Ga})$ for the annealed CIGS films deposited with 100 mM TSC for a deposition time of 15 and 30 min, are shown in Table 6.1. As it can be seen the composition of the individual elements, the contents of In and Ga increased and the corresponding Cu and Se contents decreased relatively. This could be due to the fact that Cu gets deposited first and as the time increases the deposition of In and Ga increase which also results in a relatively lower Cu content. The films deposited for 30 min have near-ideal stoichiometry and desired values of 0.94 and 0.28 for $\text{Cu}/(\text{In}+\text{Ga})$ and $\text{Ga}/(\text{In}+\text{Ga})$, as shown in Table 6.1. Depositions are also performed for intermediate time duration (20 and 25 min), however, 30 min deposition time only yielded in a compact morphological stoichiometric CIGS films. Hence, the studies pertaining to intermediate time duration are not discussed.

Table 6.1: Composition and Cu/(In+Ga) and Ga/(In+Ga) ratios of CIGS thin-films deposited using 100 mM TSC for a time of 15 min and 30 min

Deposition time (min)	Composition (at. %)				$\frac{Cu}{In + Ga}$	$\frac{Ga}{In + Ga}$	Stoichiometry
	Cu	In	Ga	Se			
15	26.86	15.62	5.94	51.58	1.24	0.27	$Cu_{0.95}In_{0.70}Ga_{0.26}Se_{2.07}$
30	23.79	18.37	7.02	50.82	0.94	0.28	$Cu_{0.95}In_{0.73}Ga_{0.28}Se_{2.03}$

The SEM image of the annealed PED deposited CIGS thin-films with 100 mM TSC for 30 min is shown in Figure 6.3. It shows a dense and compact morphology and also contained spherical particles with an average size $\approx 1 - 2 \mu m$. Such dense morphology with coarser particles is expected to be particularly advantageous in solar absorber layer applications as they offer minimum resistance to minority carrier diffusion and reduces the detrimental recombination which ultimately improves the cell performance.

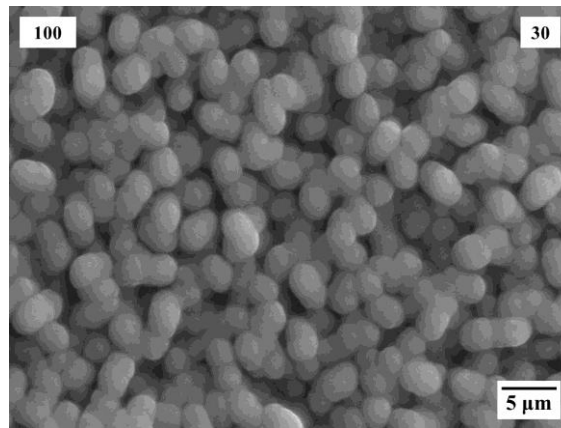


Figure 6.3: SEM image of annealed PED deposited CIGS films with 100 mM tri-sodium citrate for a time of 30 min

6.1.3 XRD analysis of annealed CIGS thin-films with varied TSC concentration

Figure 6.4a shows the X-ray diffraction patterns of annealed CIGS thin-films deposited by PED with varied concentration of TSC (40 – 100 mM). In addition, the film deposited with optimized TSC concentration for 30 min is also included in Figure 6.4a. The patterns, in common, have a preferred orientation corresponding to (112) of CIGS, with the presence of other peaks corresponding to (220), (312) and (424) (JCPDS: 35-1102) confirming the presence of crystalline chalcopyrite CIGS phase. In addition, peaks corresponding to Mo substrate (JCPDS: 42-1120) and $MoSe_2$ (JCPDS: 29-0914) are also observed. The importance of formation of $MoSe_2$ is explained previously while discussing the significance

of annealing CIGS films in section 2.2.1. As previously discussed, the preferred (112) orientation of various phases such as Cu-Se, CIS, CIGS, etc. have a narrow variation that the distinguishability of these phases often requires a closer inspection of this orientation. Hence, a closer inspection of preferred (112) orientation is carried out as shown in Figure 6.4b which clearly reveals that the CIGS films deposited with 40 mM are observed to have two peaks at the 2θ values of 26.6° and 26.9° which are attributed to the of (112) orientation CIS and CIGS. This could be due to the very low Ga content observed for films deposited with 40 mM TSC. The XRD patterns do not reveal any Cu rich phases other than CIS and CIGS. The films deposited with TSC concentration of 40 – 100 mM have a well-defined single peak; however, the peak gets shifted to higher 2θ values with the increase in concentration of TSC from 40 to 100 mM. As it can be observed from compositional analysis, the amount of Ga in the films increased with the increase in TSC concentration. It has also been discussed previously that incorporation of Ga into CIS leads to the contraction of crystal structure thereby leading to the smaller lattice parameter and hence, smaller interplanar spacing. According to Bragg's law, it is well known that the decrease in interplanar spacing leads to the shift in 2θ value to higher angles. Finally, CIGS films deposited with 100 mM of TSC for 15 min and 30 min have well defined (112) peak at 26.9° corresponding to the stoichiometric chalcopyrite CIGS phase. The compositional studies clearly indicate that there is a decrease in the amount of Cu upon increasing the deposition time to 30 min and the relative In and Ga contents are correspondingly increased. Due to this variation, the (112) peak of CIGS films deposited for 30 min is shifted to higher 2θ values indicating the decrease in lattice parameter, as observed from Figure 6.4a. In addition, the peak height is the maximum indicating higher crystallinity of CIGS thin-films deposited for 30 min. Hence, XRD results clearly demonstrate that TSC of 100 mM is the optimized concentration with a deposition time of 30 min for the fabrication of stoichiometric CIGS films. No phases corresponding to undesired Cu-Se and In-Se phases are observed from the XRD results.

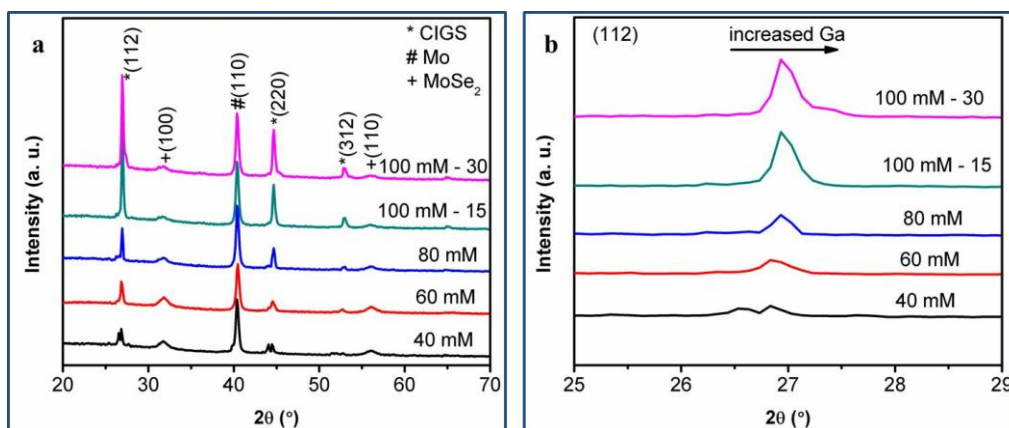


Figure 6.4: a) XRD patterns and b) closer inspection of (112) orientation of annealed PED deposited CIGS thin-films with varied concentration of tri-sodium citrate

6.1.4 Raman spectra of annealed CIGS thin-films with varied TSC concentration

Figure 6.5a shows Raman spectra of the annealed PED deposited CIGS thin-films with varied concentration of TSC (40 – 100 mM). The spectra reveal peak corresponding to A_1 mode of CIGS at the wavenumber of 176 cm^{-1} . In addition, a peak is observed at the wavenumber of 260 cm^{-1} for the films deposited with 40 and 60 mM concentration of TSC and is attributed to the presence of secondary Cu_{2-x}Se phase. This could be attributed to the Cu rich composition of CIGS thin-films deposited with the use of lower concentration of TSC. However, the peak corresponds to secondary Cu_{2-x}Se phase disappears for the films deposited with higher concentration of TSC. As it can be observed, Cu content considerably decreased for the films deposited with the TSC concentration in the range of 80 – 100 mM which in turn led to the disappearance of secondary Cu_{2-x}Se phase. CIGS films deposited with 100 mM of TSC have shown well-defined peaks corresponding to A_1 and B_2/E modes of CIGS at the wavenumbers of 176 and 234 cm^{-1} , respectively. In addition to the overall spectra of CIGS films, a closer inspection of Raman mode is carried out as shown in Figure 6.5b. It shows a shift in the A_1 mode of CIGS with increased concentration of TSC. The A_1 mode for CIGS films deposited with lower concentration of TSC is observed at a lower wavenumber of 171 cm^{-1} and could be attributed to the lower Ga content observed in these films. It is well reported that the A_1 mode is observed at lower wavenumbers in the range of $171\text{-}173\text{ cm}^{-1}$ for CIGS films with very low Ga content, with the peak shifting to higher wavenumbers of $176\text{-}178\text{ cm}^{-1}$ for stoichiometric CIGS thin-films and to 187 cm^{-1} for CuGaSe_2 . The CIGS films deposited with the TSC of 40 -80 mM are also observed to have A_1 mode at a lower Raman shift of 173 cm^{-1} . As it is evident from EDS, the Ga content increased with the increase in concentration of TSC. However, the films deposited with 100

mM of TSC for 15 and 30 min exhibit a sharp peak at 176 cm^{-1} which corresponds to the stoichiometric CIGS A_1 mode and the peak is strongest for the 30 min case. As previously mentioned, elimination of the undesired Cu_{2-x}Se secondary phase in the annealed films is extremely crucial, and is successfully achieved in the present case by the optimization of TSC's concentration.

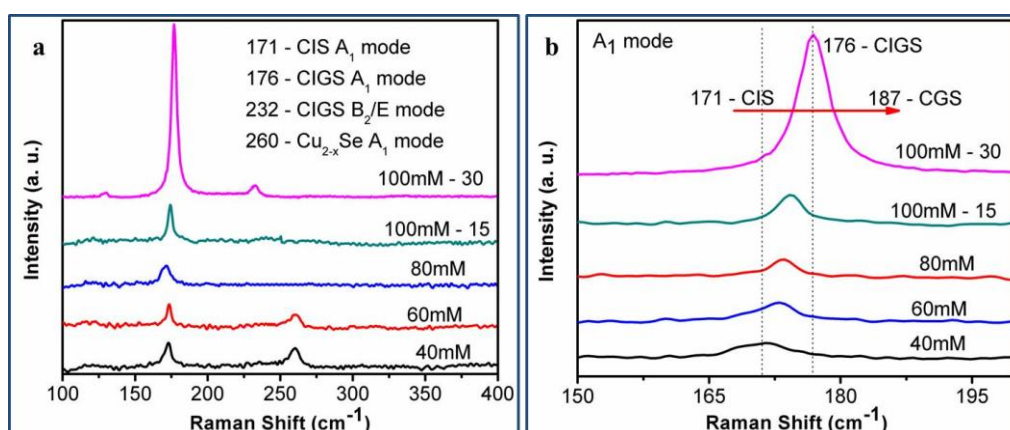


Figure 6.5: a) Raman spectra and b) closer inspection of A_1 mode of annealed PED deposited CIGS thin-films with varied concentration of tri-sodium citrate

The optimized CIGS films deposited by optimizing the concentration of tri-sodium citrate are further characterized to determine the bandgap, flat-band potential, carrier density and photoresponse. The results are discussed in the following sections.

6.1.5 Optical studies of CIGS thin-films deposited with 100 mM TSC

Figure 6.6 shows $[F(R)h\nu]^2$ vs. $h\nu$ plot of the annealed PED deposited CIGS thin-films with the optimized concentration of TSC (100 mM) for 30 min. The bandgap of the CIGS thin-films is obtained to be $\approx 1.28\text{ eV}$, determined by extrapolating the linear section of the plot to x-axis, which is close to the value for stoichiometric CIGS thin-films.

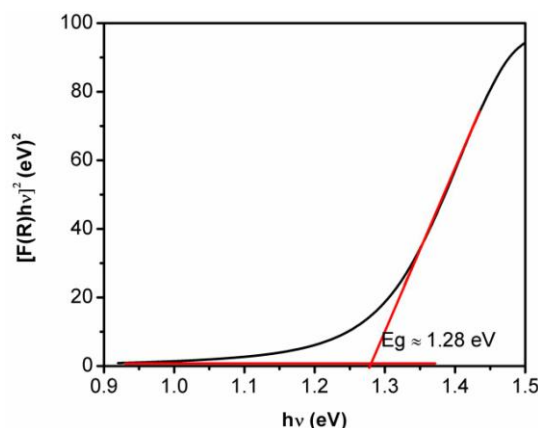


Figure 6.6: $(F(R)hv)^2$ vs. hv plot of annealed PED deposited CIGS thin-films with optimized concentration of tri-sodium citrate

6.1.6 Mott-Schottky analysis of CIGS thin-films deposited with 100 mM of TSC

Figure 6.7 shows the Mott-Schottky ($1/C^2$ vs. V) plot of CIGS thin-films in 0.5M H_2SO_4 at a frequency of 10 kHz in the dark. The slope of the MS plots is negative, thereby confirming that the CIGS film is p-type. The flat band potential is found to be -0.17 V (vs. SCE) by extrapolating the linear section to x-axis. In addition, the acceptor density, $N_a \approx 5 \times 10^{16} \text{ cm}^{-3}$, calculated using the slope of the curve. The flat-band potential and acceptor density values determined herein are similar to the values as obtained for stoichiometric CIGS thin-films mentioned in previous chapters and are in agreement with previous reports [145].

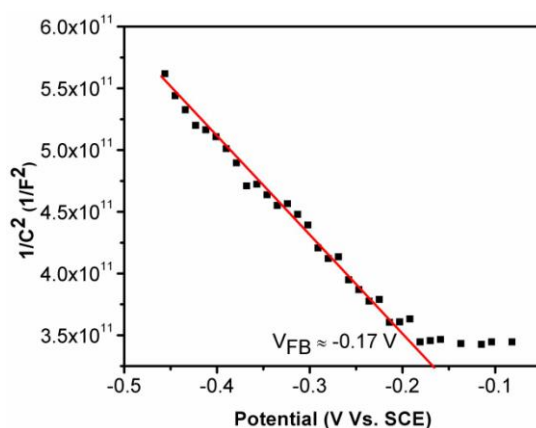


Figure 6.7: Mott-Schottky curve of annealed PED deposited CIGS thin-films with optimized concentration of tri-sodium citrate

6.1.7 PEC studies of CIGS thin-films deposited with 100 mM TSC

Figure 6.8 shows the dark and illuminated current density – voltage characteristics of the annealed CIGS thin-films deposited with 100 mM of TSC by PED electrodeposition,

measured using a photoelectrochemical analyzer in 0.5 M Na₂SO₄ with a sweep rate of 10 mV/s. The nature of the J-V curve confirms the photo-activity of CIGS thin-films. In addition, it shows an increase in the cathodic photocurrent with increased cathode potential, which is a characteristic of a semiconductor with p-type conductivity. A photocurrent density of ≈ 0.25 mA/cm² at a potential of -0.4 V vs. SCE is observed. This represents an improvement in photocurrent density compared to the value of ≈ 100 μ A/cm² observed for PED deposited CIGS thin-films without the use of TSC, discussed previously in section 4.2.9. The dense morphology with increased particle size observed in the present optimized CIGS thin-films supports the easier diffusion of minority carriers and is responsible for the improved photoelectrochemical performance. It is also to be noted that the photocurrent increases gradually without attaining a saturated value. This behavior can be attributed to incomplete photonic conversion, which causes a recombination of charge carriers at the grain boundaries of the semiconductor. The photoelectrochemical performance of these films demonstrates their application for photoelectrochemical hydrogen generation. However, an interesting point to be noted in these studies is that the photocurrent density of the films with the use of TSC is not as good as the value observed for the optimized sequential pulse electrodeposited CIGS thin-films discussed in the previous chapter. This could either be due to the possible impurities caused by the use of tri-sodium citrate or to the slightly porous morphology of CIGS films. Hence, it can be stated that the stoichiometric CIGS thin-films with desired properties can be obtained by avoiding the use of complexing agents as rightly aimed in the present work.

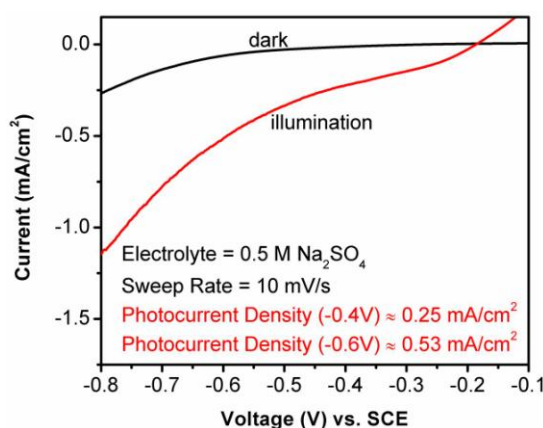


Figure 6.8: Photoelectrochemical I-V characteristics of annealed PED deposited CIGS thin-films with optimized concentration of tri-sodium citrate

6.2 Fabrication of hierarchical CIGS nano-flakes

Previous section has shown the fabrication of stoichiometric compact CIGS thin-films can be achieved by the optimized concentration of tri-sodium citrate. However, from Figure 6.2b, it can be seen that flower like particles are observed for CIGS thin-films deposited with 60 mM of tri-sodium citrate. It has been previously discussed in chapter 3 that flake-like morphological CIS thin-films can be fabricated by pulse electrodeposition technique which resulted in improved photoelectrochemical performance. As previously discussed, flower-like particles or flakes are expected to improve the junction area and enhance the absorption and current transmission properties. The flower-like CIGS films fabricated using 60 mM of TSC do not have the desired composition to form stoichiometric CIGS films. Hence, a further investigation of this study is focused to improve the stoichiometry of flower-like CIGS thin-films. It is previously discussed that with the increase in deposition time the Cu content is decreased relatively and the corresponding In and Ga contents increased. This could be due to the fact that the deposition of Cu occurs at the preliminary stages of deposition followed by facilitating the deposition of In and Ga. Hence, with the increased deposition time Cu content decreases and relative In and Ga contents increase. Hence, the present study employs the variation in deposition time to fabricate stoichiometric CIGS thin-films. In addition, the deposition time is systematically increased from 5 to 25 min to study the possible mechanism for the formation of CIGS films with flower-like structures.

6.2.1 Variation in composition of CIGS thin-films with varied deposition time

Figure 6.9a shows the composition of individual elements of CIGS thin-films deposited using 60 mM of tri-sodium citrate with varied deposition time from 5 to 25 min. It can be clearly observed that the content of Cu decreases with increase in deposition time. And on a similar note, the contents of In and Ga increase with the increased deposition time. This could be attributed to the initial deposition of Cu onto the Mo substrate which then facilitates the deposition of In and Ga. In this way, the content of Cu relatively decreases with the increase in deposition time since the deposition of In and Ga increase with the deposition time. For a deposition time of 25 min, the composition of elements seems ideal to form the stoichiometric CIGS thin-films. This is one of the main reasons to stop the deposition time at 25 min since further increase in deposition time may lead to a further decrease in copper content and relative increase in In and Ga contents. This might lead to highly copper poor CIGS thin-films which is again detrimental solar cell performance due to the plausible presence of In_{Cu} defects (In on Cu vacancies). Hence, a deposition time of 25 min is deemed optimum for the fabrication of stoichiometric CIGS thin-films.

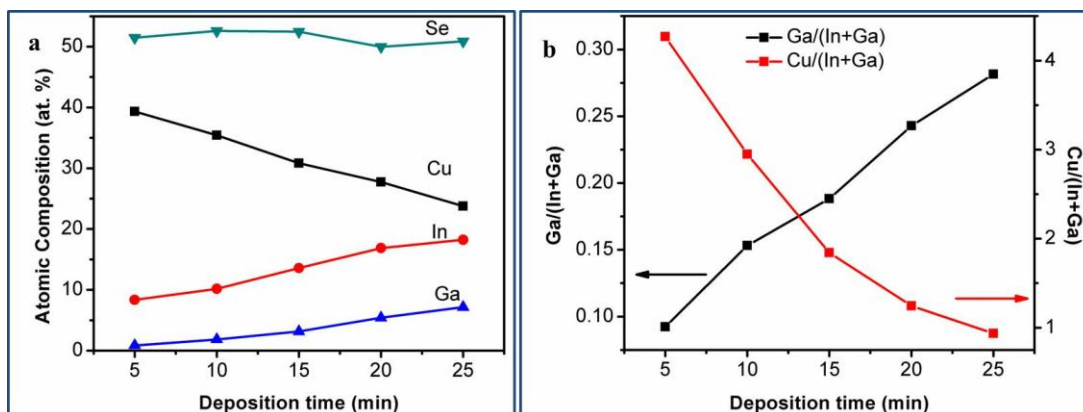


Figure 6.9: a) Elemental composition and b) Cu/(In+Ga) and Ga/(In+Ga) ratios of CIGS thin-films deposited with varied deposition time using 60 mM TSC

6.2.2 Morphology of CIGS thin-films with varied deposition time

Though the stoichiometry of the CIGS thin-films is observed from elemental analysis but the primary aim of this study is to explore for the possible fabrication of flower-like/flake-like CIGS thin-films using 60 mM of tri-sodium citrate. The morphology of CIGS thin-films deposited using 60 mM of TSC and varied deposition time is shown in Figure 6.10. Figure 6.10 a shows the morphology of the CIGS thin-films deposited for a time of 5 min and Figure 6.10f shows the higher magnification of the same. As it can be seen from the figure, the surface morphology of the films contains spherical particles as a whole; however, the higher magnification reveals cluster of bead shaped crystallites in a single particle with an approximate size of 200 nm. With the increase in deposition time to 10 min, the overall compactness of the morphology decreased in addition to the decreased compactness of the bead shaped crystallites whose size is observed to be still around 200 nm (Figure 6.10b and g). Further increase in deposition time to 15 min, the compactness still decreased and seems to have some porosity leading to the formation of flower like particles as shown in Figure 6.10c. The higher magnification of each particle for the deposition time of 15 min contains flake-like crystallites with the thickness of flake is approximately 100 nm (Figure 6.10h). The films deposited for 20 min deposition time contain flake-like crystallites throughout the surface indicating the development of flaky morphology as shown in Figure 6.10d. The magnified image of these films in Figure 6.10i shows the individually grown flakes of size 100 nm. Finally the films deposited for 25 min contain vertically grown nano-flakes of CIGS as shown in Figure 6.10e. The high magnification of image of these films additionally confirm the vertically grown flakes whose size is approximately 50 nm.

A systematic evolution of CIGS nano-flakes deposited using 60 mM of tri-sodium citrate with the increased deposition time is observed in Figure 6.10. In the previous sections, it is explained that the use of complexing agents results in a compact and dense morphology of thin-films by electrodeposition technique. But the flower like and flake like CIGS observed with the use of complexing agent (TSC) contrasts the previous explanation. This could be due to the fact that complexing agents do influence the propagation of micro-steps and cause bunching of ad-atoms or ad-ions leading to the formation of macro-steps [75]. Such a phenomenon occurs essentially when lower concentration of complexing agent is employed, as can be observed from Figure 6.2 wherein the flower like particles are observed when lower concentration of complexing agent is used in the electrolyte. In addition to the effect of complexing agents, the electrochemical dissolution plays a key role in producing such morphology and is dominant when lower concentration of complexing agent is used. Hence, with the combination of selective electrochemical dissolution and use of lower concentration of complexing agent, CIGS nano-flakes are obtained which are expected to exhibit improved photoelectrochemical performance due to the increased surface area of nano-flakes.

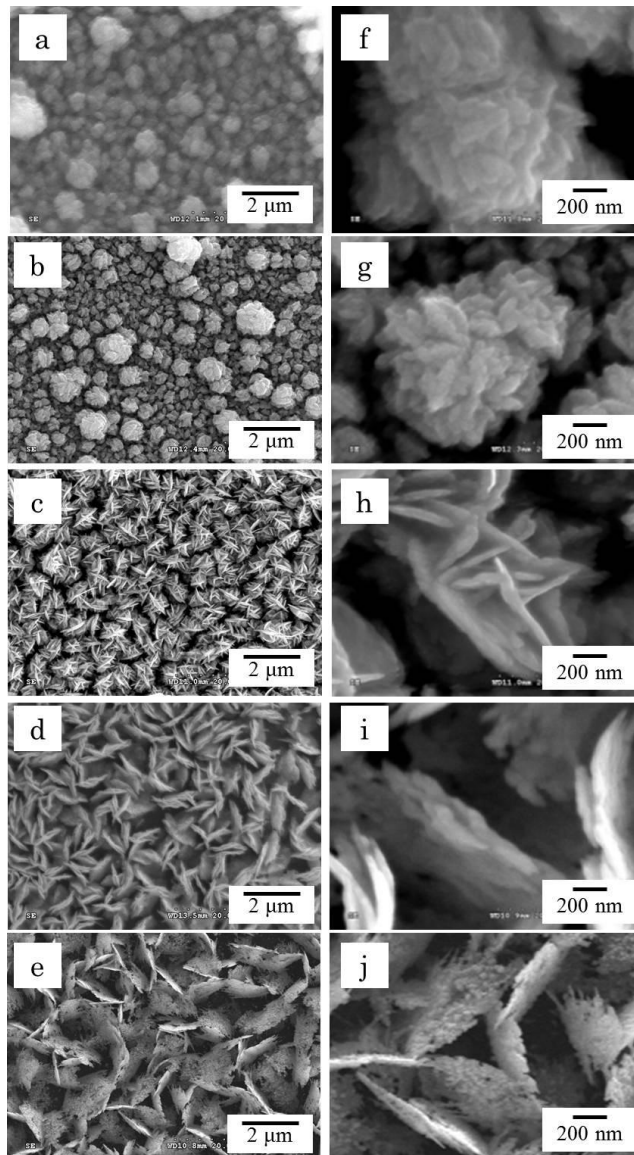


Figure 6.10: Morphology of CIGS thin-films deposited using 60 mM for a time of a) 5, b) 10, c) 15, d) 20 and e) 25 min, respectively. Higher magnification SEM images of these films are shown in f-j.

Vertically aligned CIGS nano-flakes deposited with 60 mM of TSC for 25 min and their high magnification images are shown in Figure 6.11. It can be seen that the typical width of each nano-flake is observed to be $\approx 1 - 1.2 \mu\text{m}$ and the flake height is observed to be $\approx 2 - 2.5 \mu\text{m}$ (confirmed later from cross-sectional analysis). The area of a single flake can then be calculated to be $\approx 2.5 - 3 \mu\text{m}^2$, which shows an increased surface of the CIGS films. The flake-like morphology is expected to be advantageous in the device stage due to its higher surface area which in turn leads to higher junction area. In addition, it is expected to provide superior absorption properties. The nano-flake like CIGS structure also yields a reduced

diffusion length for the minority carriers thereby improving the minority carrier diffusion and is favorable to increase current carrier concentration, electron transmission and thus induce the generation of photocurrent. In addition to the flake-like morphology, a closer observation of each flake shows hierarchically connected nano-particles of ≈ 50 nm. These nanoparticles are advantageous since they reduce recombination due to the large exciton binding energy thereby leading to improved device performance.

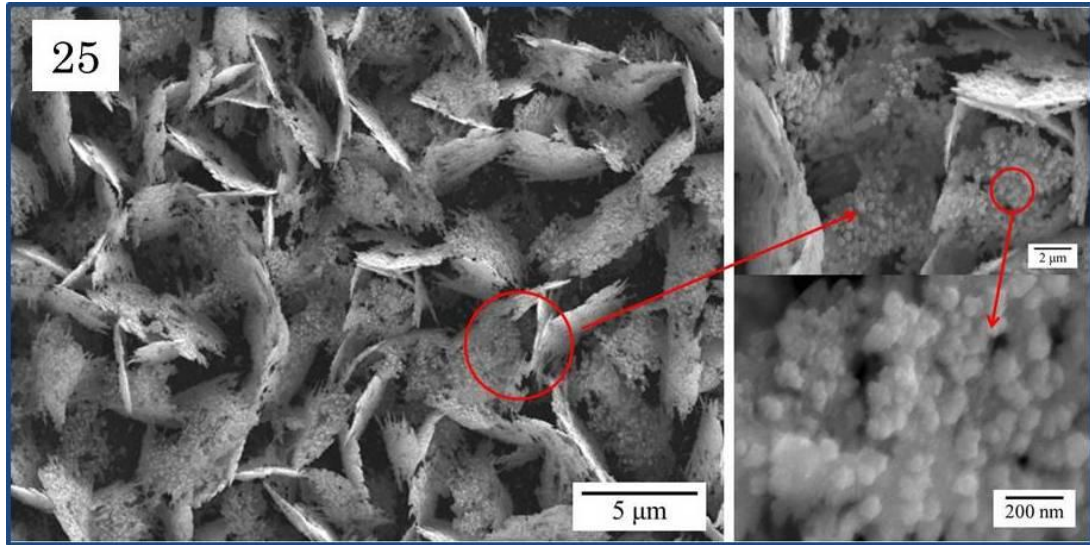


Figure 6.11: CIGS nano-flakes and their high magnification images, deposited with 60 mM of TSC for 25 min

6.2.3 Phase constitution of CIGS thin-films by XRD

Figure 6.12a shows the X-ray diffraction patterns of annealed PED deposited CIGS thin-films using TSC with varied deposition time (5 – 25 min). The patterns have a preferred orientation corresponding to (112) of CIGS, along with other peaks corresponding to (220), (312) and (424) (JCPDS: 35-1102) confirming the presence of crystalline chalcopyrite CIGS phase. In addition, peak corresponding to Mo substrate (JCPDS: 42-1120) is also observed. As previously discussed, the preferred (112) orientation of various phases such as Cu-Se, CIS, CIGS, etc. have a narrow variation in the peak position that the distinguishability of these phases often requires a closer inspection of this orientation. Hence, a closer inspection of preferred (112) orientation is carried out as shown in Figure 6.12b. It clearly reveals that the CIGS films deposited for 5 min are observed to have the (112) peak at a 2θ value of 26.6° . This peak is attributed to the presence of CIS phase and no CIGS phase is observed. This could be due to the lower Ga content observed from compositional analysis. The CIGS films deposited for 10 and 15 min have two peaks at the 2θ values of 26.6° and 26.9° which

are attributed to the of (112) orientation CIS and CIGS. This could be due to the lower Ga content observed for films deposited for 10 and 15 min. The XRD patterns do not reveal any Cu rich phases other than CIS and CIGS although the films are Cu-rich in composition. As it can be observed from compositional analysis, the amount of Ga in the films increased with the increase in deposition time. It has also been discussed previously that incorporation of Ga into CIS leads to the contraction of crystal structure thereby leading to the smaller lattice parameter and hence, smaller interplanar spacing. As per Bragg's law, it is well known that the decrease in interplanar spacing leads to the shift in 2θ value to higher angles. The films deposited for 20 and 25 min have a well-defined single peak at the 2θ value of 26.9° which can be attributed to stoichiometric chalcopyrite CIGS phase. In addition, the peak height for these cases is the maximum which indicates higher crystallinity of CIGS thin-films. Hence, XRD results clearly demonstrate the fabrication of stoichiometric CIGS films for a deposition time of 25 min.

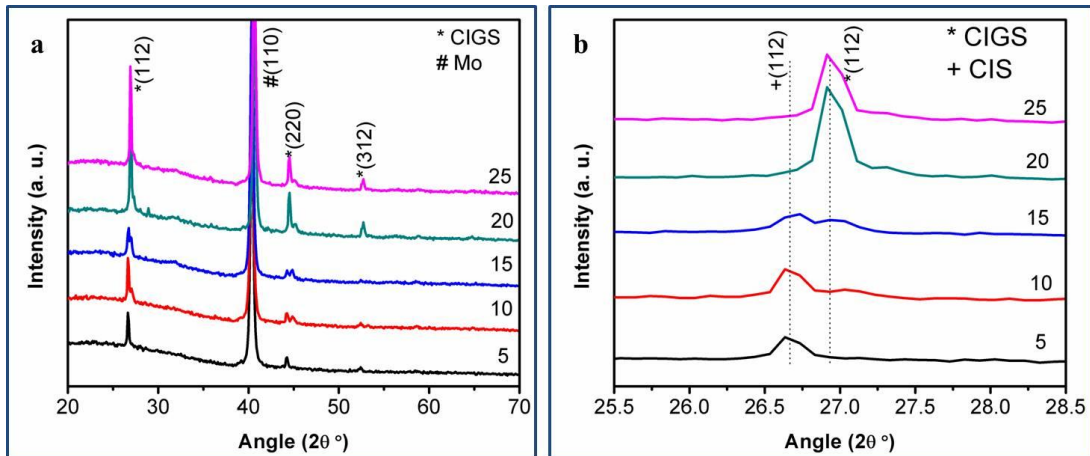


Figure 6.12: a) XRD patterns and b) closer inspection of (112) orientation of annealed PED deposited CIGS thin-films deposited with 60 mM of TSC by varying deposition time

6.2.4 Raman analysis of CIGS thin-films

Figure 6.13a shows Raman spectra of the annealed PED deposited CIGS thin-films with varied deposition time (5 – 25 min). The spectra reveal peak corresponding to A_1 mode of CIGS at the wavenumber of 176 cm^{-1} . In addition, a peak is observed at the wavenumber of 260 cm^{-1} for the films deposited for 5 and 10 min duration and is attributed to the presence of secondary Cu_{2-x}Se phase. This could be due to the Cu rich composition of CIGS thin-films deposited for lower deposition time. However, the peak corresponds to secondary Cu_{2-x}Se phase disappears for the films deposited with higher deposition time. As it can be observed, Cu content considerably decreased for the films deposited for the deposition time

of 15 – 25 min which in turn led to the disappearance of secondary Cu_{2-x}Se phase. The CIGS films deposited for 25 min have shown well-defined peak corresponding to A_1 mode of CIGS at the wavenumber, 176 cm^{-1} . In addition to the overall spectra of CIGS films, a closer inspection of Raman mode is carried out as shown in Figure 6.13b. It shows the shift of A_1 mode of CIGS with increased concentration of TSC. The A_1 mode for CIGS films deposited with lower deposition time is observed at a lower Raman shift of 171 cm^{-1} and could be attributed to the lower Ga content observed in these films. It is well reported that the A_1 mode is observed at lower wavenumbers in the range of $171\text{-}173\text{ cm}^{-1}$ for CIGS films with very low Ga content, with the peak shifting to higher wavenumbers of $176\text{-}178\text{ cm}^{-1}$ for stoichiometric CIGS thin-films and to 187 cm^{-1} for CuGaSe_2 . The CIGS films deposited for deposition time of 10 and 15 min are also observed to have A_1 mode at a lower Raman shift of 173 cm^{-1} . As it is evident from EDS, the Ga content increased with the increased deposition time. However, the films deposited for 25 min exhibit a sharp peak at 176 cm^{-1} which corresponds to the stoichiometric CIGS A_1 mode.

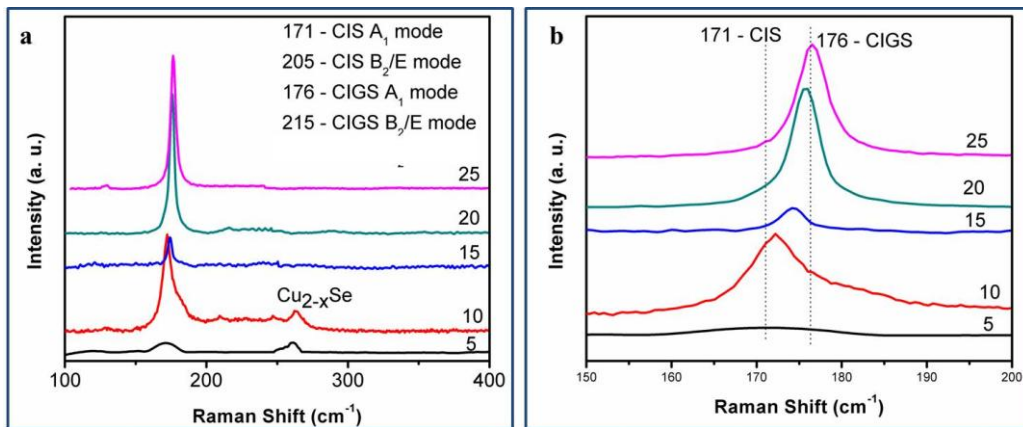


Figure 6.13: Figure 6.5: a) Raman spectra and b) closer inspection of A_1 mode of annealed PED deposited CIGS thin-films using 60 mM of TSC with varied deposition time

6.2.5 Optical absorption studies of CIGS thin-films

The optical studies of the CIGS thin-films have been investigated in previous chapters to determine the bandgap of the films. However, in the present case, a detailed investigation of optical absorption has been carried out to examine the absorption properties of flake like CIGS films. The absorption spectra of CIGS thin-films deposited for 5 – 25 min are shown in Figure 6.14. As it can be clearly observed, absorption of CIGS films increased with the increase in deposition time from 5 to 25 min. The CIGS nano-flakes have maximum absorption as previously mentioned. In addition, a careful observation of the absorption

spectra reveals the absorption edge at a wavelength of ≈ 1200 nm for the films deposited for 5 and 10 min whereas the absorption edge is observed at a wavelength of ≈ 1000 nm for films deposited for 15 – 25 min. A wavelength of 1200 nm corresponds to energy of ≈ 1 eV and 1000 nm corresponds to ≈ 1.24 eV. It is well known that the stoichiometric CIS thin-films have bandgap of ≈ 1.04 eV and stoichiometric CIGS films have a bandgap of ≈ 1.20 eV. Hence, the films deposited with lower deposition time contain CIS and with higher deposition time contain CIGS, corroborating the XRD and Raman results.

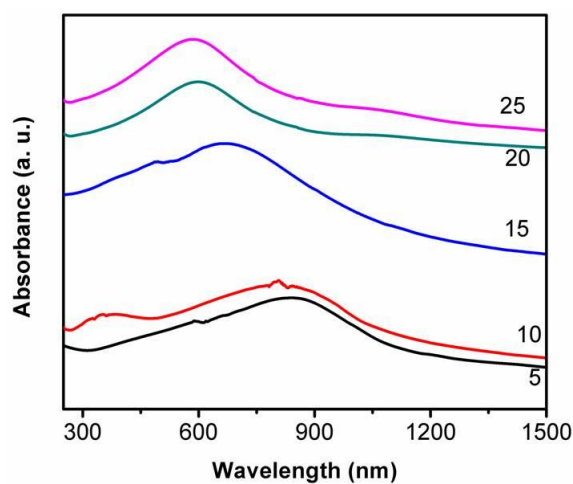


Figure 6.14: Optical absorption spectra of CIGS films deposited using 60 mM of TSC by varied deposition time

6.3 Characterization of stoichiometric CIGS nano-flakes

The stoichiometric hierarchical CIGS nano-flakes are further characterized to TEM, SEM, PEC analyzer, etc. to examine the crystallographic properties, flake height, photoresponse, etc.

6.3.1 TEM analysis of CIGS thin-films

Annealed CIGS nano-flakes fabricated by PED deposition using 60 mM of TSC for a deposition time of 20 min are further characterized using transmission electron microscopy. The transmission electron micrograph, the high resolution TEM image, selected area diffraction (SAD) pattern and TEM-EDS spectrum of CIGS particles are shown in Figure 6.15. The CIGS nano-flakes are clearly observed from the TEM images as shown in Figure 6.15a. Figure 6.15b shows the high resolution TEM image of CIGS thin-films, which reveals planes with an interplanar spacing of approximately 3.31\AA . This value is in good agreement with the theoretical value for the (112) orientation of CIGS. The SAD pattern,

Figure 6.15c, shows the orientations corresponding to (112), (220) and (312) of CIGS, which are in agreement with the previously discussed observation from XRD. TEM-EDS analysis is performed, as shown in Figure 6.15d, reveals presence of Cu, In Ga and Se affirming in the CIGS films.

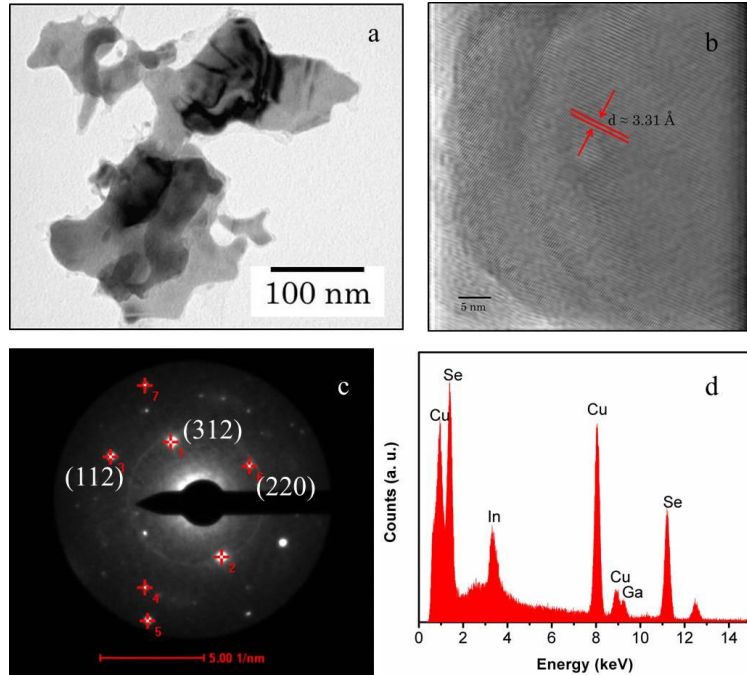


Figure 6.15: a) TEM image, b) HRTEM image, c) SAED and d) TEM-EDS of annealed PED deposited CIGS nano-flakes

6.3.2 Cross-section analysis of CIGS nano-flakes by SEM

Figure 6.16 shows the cross-sectional SEM image of CIGS nano-flakes fabricated by PED electrodeposition using 60 mM of TSC. The cross-section of the films clearly indicates the vertical growth of the CIGS nano-flakes and the thickness of the films which is equivalent to the flake height is determined to be $\approx 2.4 \mu\text{m}$. In addition, width of the flakes is observed to be around $1.2 \mu\text{m}$. Therefore, the typical area of a single nano-flake is calculated to be $\approx 3 \mu\text{m}^2$, corroborating the results observed from the surface morphological analysis. This high surface area is expected to be crucial in improving the properties such as light absorption, junction area, photoresponse, etc. In addition to the CIGS flakes, the sputtered Mo layer (200 nm) is also seen in the film.

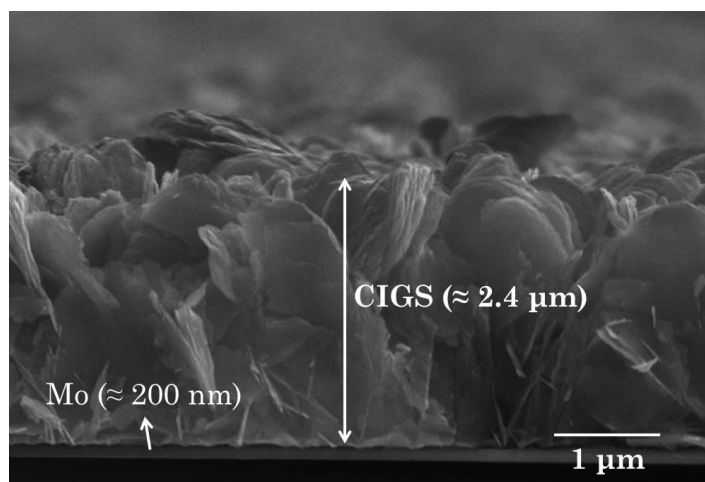


Figure 6.16: cross-sectional FESEM image of CIGS nano-flakes showing flake height

6.3.3 Optical studies of CIGS nano-flakes

Figure 6.17a shows the optical absorbance of CIGS nano-flakes fabricated using 60 mM of TSC. Absorption spectrum of PED deposited dense CIGS thin-films is also included for comparison. As it can be clearly observed, both the films exhibited extended absorption, however, the nano-flake CIGS has higher absorbance compared to the dense CIGS thin-films (Figure 4.6). This could be due to the higher surface area of the nano-flakes as discussed previously. A careful inspection of the Figure 6.17a reveals the absorption edge of the CIGS nano-flakes at around 950 nm whereas that of dense CIGS films is observed to at 1000 nm. The observation indirectly indicates a shift in the bandgap of the CIGS nano-flakes to higher values compared to dense CIGS thin-films. To determine the bandgap of the nano-flake like CIGS absorption coefficient is calculated using the absorbance spectrum in Figure 6.17a and the height of CIGS nano-flakes from cross-sectional analysis. Figure 6.17b show the $(\alpha h\nu)^2$ vs. $h\nu$ (Tauc's) plot of CIGS nano-flakes and that of dense CIGS films (for comparison). The bandgap of the CIGS nano-flakes is determined to be ≈ 1.30 eV, by extrapolating the linear section of the plot to X-axis, which is in the desired range for CIGS thin-film as solar absorber layer. The sequential PED plated CIGS thin-films, however, have larger band gap compared to the PED plated CIGS films, which is in agreement with the transition observed in absorbance studies. A possible reason for this phenomenon is carrier degeneracy in $\text{Cu}(\text{In,Ga})\text{Se}_2$ due to continuous distribution of defect states, such as copper vacancies (V_{Cu}), or substitutional indium in copper sites (In_{Cu}).

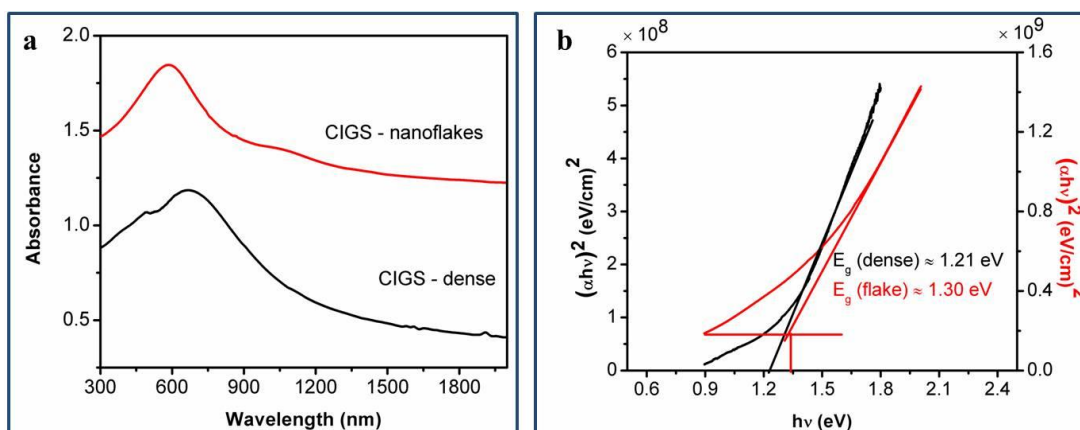


Figure 6.17: a) Optical absorbance and b) corresponding Tauc's plot of annealed CIGS nano-flakes prepared using 60 mM of TSC. Relevant curves of dense CIGS thin-film are also included for comparison

6.3.4 Mott-Schottky analysis of CIGS nano-flakes

Figure 6.18 shows the Mott-Schottky ($1/C^2$ vs. V) plot of CIGS nano-flakes in 0.5M H_2SO_4 at a frequency of 10 kHz in the dark. The slope of the MS plots is negative, thereby confirming that the CIGS nano-flakes exhibit p-type conductivity. The flat band potential is found to be -0.15 V (vs. SCE) by extrapolating the linear section to X-axis. In addition, the acceptor density, $N_a \approx 5.2 \times 10^{16} \text{ cm}^{-3}$, calculated using the slope of the curve. An interesting observation from the Mott-Schottky plot is the reduced $1/C^2$ values of CIGS nano-flakes compared to previously observed values for dense CIGS films. By comparing Figure 6.18 with Figure 4.11, it can be observed that $1/C^2$ values are almost reduced by three orders magnitude indicating significant increase in the value of capacitance for CIGS nano-flakes. The capacitance measured herein is the double layer capacitance observed at the CIGS-electrolyte interface, as discussed previously in section 2.3.9. It is also well known that the capacitance value is directly proportional to the area of the electrodes in a parallel plate capacitor ($C = \epsilon_0 A/d$). Hence, in the present case, the larger capacitance value can be attributed to the increased area of CIGS due to the presence of nano-flakes, as calculated previously.

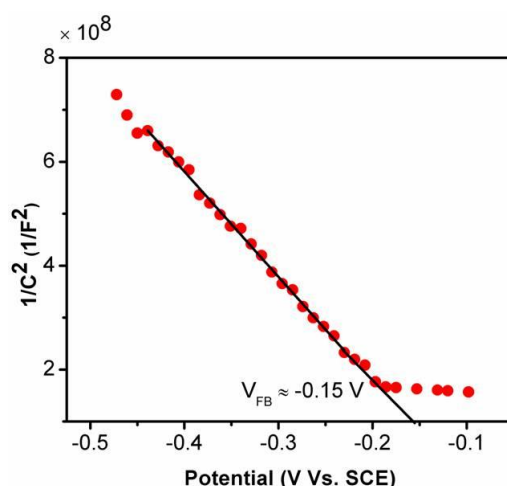


Figure 6.18: Mott-Schottky plot of CIGS nano-flakes prepared using 60 mM of TSC

6.3.5 I-V characteristics of optimized CIGS thin-films by PEC

Figure 6.19a shows dark and illuminated current density – voltage characteristics of the CIGS nano-flakes deposited using 60 mM of TSC for 25 min, measured using a photoelectrochemical analyzer in 0.5 M H₂SO₄ with a sweep rate of 10 mV/s. The nature of the J-V curve confirms the photo-activity of CIGS thin-films. In addition, it shows the increase in cathodic photocurrent with increased cathode potential, which is a characteristic of a semiconductor with p-type conductivity. It is also to be noted that the photocurrent increases gradually without attaining a saturated value. This behavior can be attributed to incomplete photonic conversion, which causes a recombination of charge carriers at the grain boundaries of the semiconductor. A photocurrent density of $\approx 1.71 \text{ mA/cm}^2$ at a potential of -0.4 V vs. SCE is observed. This represents a significant improvement in photocurrent density compared to the values observed in previous chapters. The larger photocurrent value is essentially due to the presence of nano-flakes and can be explained using several reasons. Firstly, increased light absorption due to the nano-flakes yields increased carrier generation thereby leading to the probability for improved photocurrent density. Secondly, the junction area between CIGS nano-flakes and electrolyte is increased which in turn increases depletion field which is responsible for separation of charge carriers thereby leading to improved photocurrent density. In addition, as the junction is between the flake and electrolyte the essential path length need to be traversed by the electron is only the thickness of CIGS nano-flake. The thickness of nano-flakes is only about 50 nm indicating the shorter diffusion length for electrons leading to the possibility of reduction in detrimental recombination.

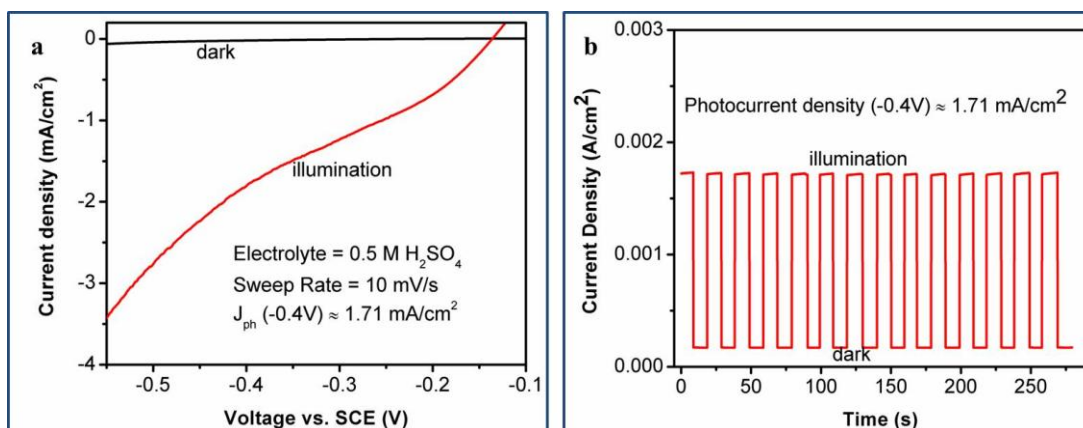


Figure 6.19: a) Photoelectrochemical I-V characteristics and b) amperometric I-t curve of CIGS nano-flakes prepared using 60 mM of TSC

In addition to the PEC I-V characteristics, amperometric current vs. time curve is also obtained for CIGS nano-flakes. Figure 6.19b shows the amperometric current-time (I-t) curve of CIGS nano-flakes obtained at -0.4 V by chopped light. It clearly demonstrates the photoactivity nature of CIGS films with a photocurrent density of $\approx 1.71 \text{ mA/cm}^2$, corroborating the above result. The improved photoresponse of CIGS nano-flakes indicate their potential for application in thin-film solar cells. In addition, the photoelectrochemical performance of these films demonstrates their potential utility for photoelectrochemical hydrogen generation.

6.4 Conclusions

Effect of tri-sodium citrate (TSC) is studied on the pulse electrodeposition of CIGS thin-films. The concentration of TSC is optimized to fabricate stoichiometric chalcopyrite CIGS thin-films. A possible mechanism is proposed to understand the effect of TSC on the deposition of CIGS thin-films. Further, the use of optimized TSC has resulted in highly compact CIGS thin-films but exhibited poor photoresponse which could be due to the possible impurities from the complexing agent. An interesting aspect, however, is the observation of flower like CIGS particles for a lower concentration of TSC (60 mM). This 60 mM of TSC is further used to optimize for the CIGS content by employing a variation in deposition time. Ultimately, the deposition time of 25 min has yielded stoichiometric CIGS films which resulted in an interesting novel nano-flake like morphology. These CIGS nano-flakes have not only shown superior absorption properties but also exhibited significantly improved photocurrent density. These CIGS nano-flakes fabricated by simplified

electrodeposition technique have potential application for thin-film solar cells and photoelectrochemical cells.

Chapter 7

Pulse-reverse electrodeposition of

Cu(In,Ga)Se₂

Pulse electrodeposition technique has been successfully explored for the fabrication of stoichiometric CIGS thin-films in the previous chapters. In addition to the pulse electrodeposition, as mentioned in section 1.11, pulse-reverse electrodeposition (PRED) of CIGS thin-films is also one of the major interests of the present work. The features and the relevant advantages of pulse-reverse electrodeposition have already been detailed in section 1.9.3. To brief out the same in the present context, an anodic (reverse) voltage/current is applied followed by an off-time in PRED in addition to the forward pulse sequence as in pulse electrodeposition. Such a reverse pulse sequence provides additional variables such as pulse reverse voltage, PR on-time and PR off-time. The appropriate variation of these additional variables is expected to offer better control over composition and morphology than the case for pulse electrodeposition. In the present study, the intention to employ PRED for the deposition of CIGS thin-films is to completely eliminate the undesired Cu_{2-x}Se phase. The reason for the appearance of undesired Cu-Se phase and its probable elimination by PRED technique are explained as follows.

In general, it is well known that the amount of Cu is rich in the electrodeposited CIGS thin-films due to its lower reduction potential and higher deposition rate. In addition, deposition of the films at room temperature using an acidic electrolyte (pH \approx 2) also favors the deposition of Cu, leading to its higher amount in the deposited CIGS films. Due to this excess copper content, often undesired secondary Cu-Se phases have been resulted in the electrodeposited CIGS films [61, 161]. Hence, minimization of Cu content to form stoichiometric CIGS is essential. As discussed in section 1.10, though several post deposition treatments have aided in removing this undesired Cu-Se phase but resulted in a

rough and porous morphology which is not desirable for solar cell applications. In this context, PRED is expected to resolve this problem during the deposition stage. The anodic current can be manipulated in such a way that it suffices the oxidation potential of Cu resulting in the dissolution/oxidation of Cu from the deposited films into the solution thereby decreasing the amount of Cu. However, the dissolution should also be controlled since extremely copper poor conditions are again detrimental to solar cell performance. This crucial control over the dissolution can be obtained by manipulating the PR on-time and PR off-time. Hence, appropriate control of these key parameters including reverse potential, reverse on-time and off-time is necessary to achieve stoichiometric CIGS thin-films. In this context, it is also relevant to mention that Fu et al. have successfully explored PRED technique to not only eliminate the undesired Cu_{2-x}Se phase but also to achieve a compact morphology of the CIGS thin-films. However, the report also used tri-sodium citrate as complexing agent to achieve the above result.

The present study avoids the use of complexing agents during the pulse-reverse electrodeposition of CIGS thin-films and essentially focuses on the variation in reverse (anodic) voltage. The study discusses the following aspects:

1. Pulse-reverse electrodeposition of CIGS thin-films by varying the reverse voltage – observation of an interesting fishbone like nano-mesh morphology for CIGS thin-films
2. Characterization of fishbone like CIGS nano-mesh

7.1 Pulse-reverse electrodeposition (PRED) of CIGS thin-films

Pulse-reverse electrodeposition (PRED) of CIGS thin-films is carried out in the same way as that of the pulse electrodeposition technique, by employing a two-electrode system. CuCl_2 (3 mM), InCl_3 (6.4 mM), GaCl_3 (8.5 mM) and H_2SeO_3 (5 mM) are considered for the present case with a final pH maintained between 2.20 – 2.40. A constant forward voltage of -1.5 V is used and the reverse voltage is varied from 0.1 to 0.3 V. A duty cycle of $\approx 97\%$ is used in the present case, which is defined by the equation for PRED case as $T_c/(T_c+T_a)$, where T_c is the cathodic pulse on-time and T_a is the anodic pulse-on time. The typical pulse sequence employed for the present study is shown in Figure 7.1. The deposition is carried out at room temperature for 30 min. The films are not annealed in the present case unlike the previous cases and the reason is discussed during the analysis in the next sections. An important point to mention here is that the deposition conditions are chosen in such a way that Cu and In rich films are primarily observed. This is due to the fact that Cu and In are expected to dissolve back into the electrolyte during the reverse-pulse leading to the

decrease in their respective contents. Though PRED explored in the present case is to eliminate secondary phases but this novel technique is expected to provide a preferential growth of the thin-films which not only leads to novel morphologies but also to the preferential growth of a specific orientation of the deposit.

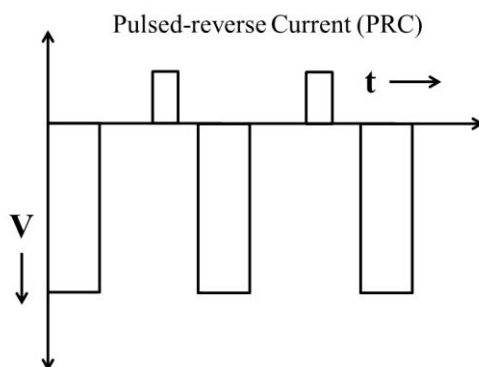


Figure 7.1: Typical pulse sequence employed for pulse-reverse electrodeposition of CIGS thin-films

7.1.1 Compositional analysis of PR electrodeposited CIGS films

The composition of individual elements and corresponding Cu/(In+Ga) and Ga/(In+Ga) ratios of PR electrodeposited CIGS thin-films deposited with varied pulse reverse (PR) voltage are shown in Figure 7.2. It can be clearly observed from Figure 7.2a that Cu rich CIGS thin-films are observed for a PR voltage of 0.1 V which also contain higher content of In and Ga. As previously discussed, the deposition parameters are chosen to achieve higher Cu and In contents in the CIGS thin-films. Further, when the PR voltage is increased to 0.2 V, Cu, and Se contents are observed to decrease while the relative In and Ga content remain almost unaffected. This could be due to the fact that these elements get oxidized leading to their dissolution back into the electrolyte. The PR voltage is further increased to 0.3 V, the films are observed to have the near ideal composition of individual elements which can form the stoichiometric CIGS thin-films. The PRED films deposited at a PR voltage of 0.3 V also exhibited the near-ideal values for the ratios of Cu/(In+Ga) and Ga/(In+Ga) as shown in Figure 7.2b. It can be concluded from the compositional analysis that the contents of individual elements can be conveniently controlled by varying the reverse voltage. However, optimizing the PR voltage is the key for the success since elements like Cu, Se and In get oxidized with the application of reverse-voltage. Though the desired composition of elements is successfully achieved from the PRED method but the results seem to be monotonous and are similar to the previous methods explored for CIGS. Then what is the

novelty of this PRED method? Does it give an interesting morphology or crystallinity or both? These details are explained in the following sections.

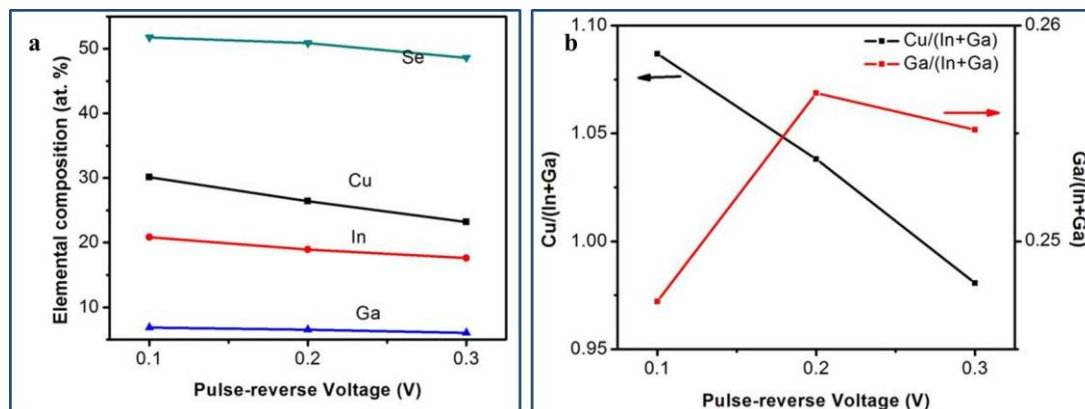


Figure 7.2: a) Atomic composition of individual elements and b) Cu/(In+Ga) and Ga/(In+Ga) ratios of PR electrodeposited CIGS films with varied reverse voltage

7.1.2 Morphology of PR electrodeposited CIGS films

The morphology of the PRED CIGS thin-films deposited with varied pulse-reverse voltage is shown in Figure 7.3. As mentioned previously, an interesting aspect is observed for the morphology of the CIGS films deposited by PRED method. The film deposited using a PR voltage of 0.1 V is observed to have a fully covered rod like growth with attached flakes to it. Such morphology can result either due to the preferential growth of the material on selective sites or due to a possible etching or dissolution of the material. Growth of the material on selective sites by any method generally happen when a pre-deposited seed layer is present on the substrate and often leads to rod like morphology. However, in the present case, such a selective growth may not be possible due to the reasons such as the substrate does not have a pre-deposited seed layer; secondly, the pulse plating (PED or PRED method) expects to provide a uniform and homogeneous growth of the films as discussed in previous chapters. Hence, it could mainly be due to the dissolution of the elements that occurs during the reverse-on time. However, as discussed previously for PED deposition, the dissolution of In and Ga occur even during the forward pulse-off time though no voltage is intentionally applied (Figure 3.2). Hence, the dissolution in the present case occurs for a prolonged period which is equal to the sum of the forward pulse off-time and reverse pulse on-time. In addition, it is important to note that the dissolution during the forward off-time depends on the pulse off-time (since forward voltage is constant) whereas the dissolution during pulse-reverse on time depends both on the applied PR voltage and the duration of PR

on-time. Higher PR voltage might lead to higher dissolution, which is the case observed from the compositional analysis. The prolonged dissolution has resulted in the rod-flake like morphology for a PR voltage of 0.1 V as shown in Figure 7.3a. Upon increasing the PR voltage to 0.2 V, the dissolution is still significantly higher leading to the vertically aligned leaves of CIGS films (Figure 7.3b). It can be observed that the dissolution seems to be an equivalent selective etching process that the material has been removed from the edge of the flakes (which are attached to rod in Figure 7.3a) resulting in a well-defined leaf like structure of CIGS. When the deposition is finally carried out using a PR voltage of 0.3 V, an interesting fishbone like nano-mesh of CIGS rods is observed as shown in Figure 7.3c. The structure is a result of the selective electrochemical etching of the material with a well-controlled reverse voltage applied during deposition.

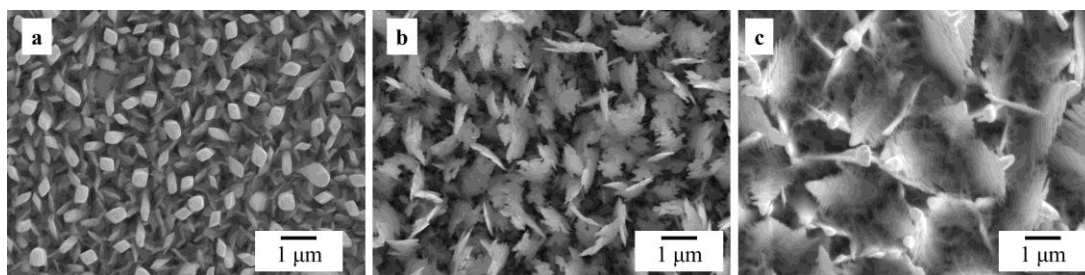


Figure 7.3: Morphology of PRED CIGS thin-films deposited at a reverse voltage of a) 0.1, b) 0.2 and c) 0.3 V, respectively

The schematic representation of the selective electrochemical etching which takes place during the PRED of CIGS films is shown in Figure 7.4. The picture clearly explains the possible dissolution leading to the formation of a well-connected network of fishbone like nano-mesh of CIGS rods. Optimization of PR voltage in a systematic approach has resulted in a stoichiometric fishbone like CIGS nano-mesh structure which is expected to have several advantages for the ultimate device performance as explained later.

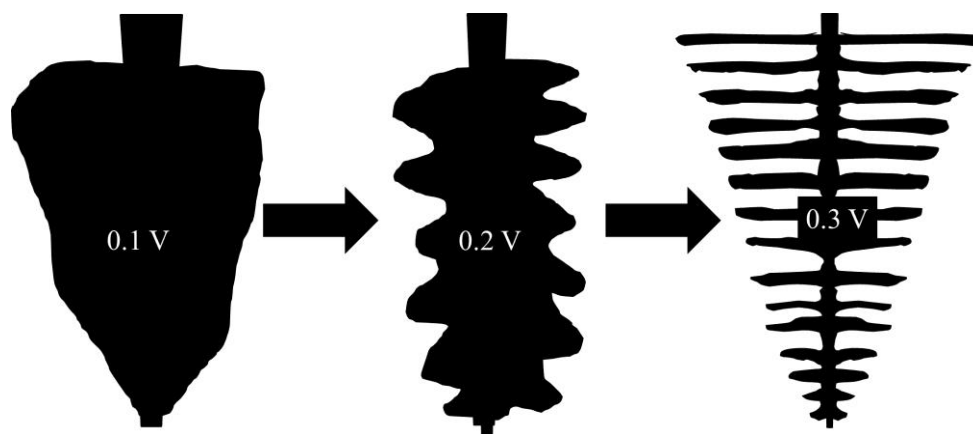


Figure 7.4: Schematic representation of selective electrochemical etching of CIGS films with increased PR voltage

7.1.3 Micro-Raman analysis of PR electrodeposited CIGS films

It has been learnt from previous studies that XRD analysis does not provide a clear picture about the presence of different phases such as CIS, CIGS, Cu-Se, etc. due to the negligible variation in 2θ values of preferred (112) orientation of these phases. Hence, in the present study, micro-Raman analysis is considered over XRD studies to distinctly identify the different phases present in PRED CIGS films. Figure 7.5 shows the micro-Raman spectra of PRED CIGS thin-films deposited with varied reverse voltage. From the spectra, two essential observations can be made viz. the detection of Cu_{2-x}Se mode for the films deposited with reverse voltages of 0.1 and 0.2 V, respectively, and the shift in the A_1 mode of CIGS to lower wavenumbers. The films deposited with PR voltage of 0.1 V have two well-defined peaks corresponding to A_1 mode of CIGS and Cu_{2-x}Se at wavenumbers of 179 and 260 cm^{-1} , respectively. It has been previously discussed that the A_1 mode of CIGS is observed at slightly higher wavenumbers for Ga rich films, which is the case for CIGS films deposited with a reverse voltage of 0.1 V. In addition, these films are observed to be copper rich in composition as observed from compositional analysis, which could be the reason for the presence of undesired secondary Cu_{2-x}Se phase. However, the Raman intensity of this phase is decreased when the PR voltage is increased to 0.2 V wherein a decrease in copper content is observed. In addition, the A_1 mode of CIGS is also observed at 178 cm^{-1} affirming the fact that Ga content is also simultaneously decreased. Finally, when the PR voltage is increased to 0.3 V, the undesired secondary Cu_{2-x}Se phase completely disappeared and well-defined peaks corresponding to CIGS A_1 mode and B_2/E mode are observed at wavenumbers of 176 and 234 cm^{-1} . In addition, the peaks corresponding to CIGS A_1 mode observed for the films deposited at a PR voltage of 0.1 and 0.2 V are slightly broader

compared to the films deposited at PR voltage of 0.3 V. This could be attributed to the probable presence of In rich phases which could be possible due to the excess In observed in these films. However, no separate peaks are observed for any In or Ga related phases. Hence, it can be concluded that application of PR voltage of 0.3 V with a forward voltage of -1.5 V has resulted in single phase chalcopyrite fishbone like CIGS nano-mesh.

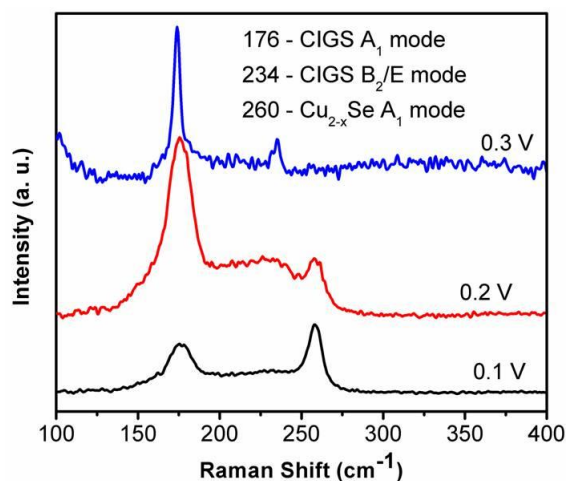


Figure 7.5: Raman spectra of PRED CIGS thin-films deposited with varying reverse voltage as shown

7.2 Characterization of the fishbone like CIGS nano-mesh deposited by PRED

The fishbone like CIGS nano-mesh is further characterized using FESEM, XRD, Raman, TEM, absorption spectroscopy, impedance studies and PEC analysis to study its structural characteristics and other relevant properties.

7.2.1 FESEM characterization of fishbone like CIGS nano-mesh

Figure 7.6a shows the FESEM image of fishbone like CIGS nano-mesh and high magnification images. The morphology clearly reveals vertically aligned CIGS nano-mesh. The high magnification image clearly reveals the nature of fishbone like CIGS mesh which can be compared to the natural fishbone structure as shown in Figure 7.6b. In addition, a closer inspection of mesh reveals the nano-rods of CIGS which have a diameter of ≈ 50 nm. Well-connected one-dimensional nano-rods of CIGS led to the formation of fishbone like CIGS nano-mesh which are vertically aligned across the surface of the CIGS films with a well-connected network. Such structure is expected to be advantageous in improving the absorption as well as transport properties which ultimately improve the device performance.

In addition, the junction area can be significantly increased since the n-type CdS can be deposited over the nano-rods within the fishbone type CIGS.

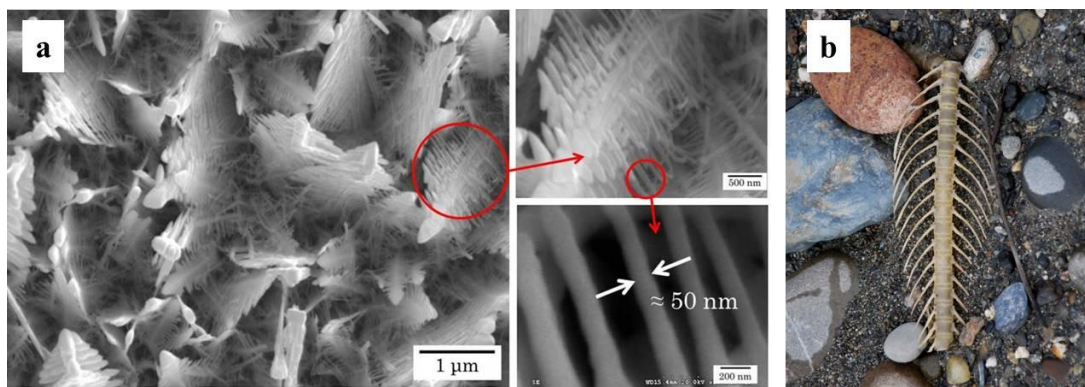


Figure 7.6: a) FESEM image of fishbone like CIGS nano-mesh deposited by PRED and b) a natural fishbone

7.2.2 Phase constitution of fishbone like CIGS nano-mesh

The phase constitution of the CIGS nano-mesh is analyzed using XRD and Raman spectroscopy studies. Figure 7.7a shows the XRD pattern of as-deposited fishbone like CIGS nano-mesh by PRED technique. The pattern reveals two well defined peaks corresponding to (112) preferred orientation of CIGS and (110) orientation of Mo substrate. In addition, a very less intense peak corresponding to (220) orientation of CIGS is observed. Firstly, it is very interesting to notice that a highly crystalline CIGS phase is observed in the as-deposited films and in addition, the nanorods in the mesh seem to exhibit a single crystal nature as the pattern reveals essentially only preferred (112) orientation. The crystalline nature of as-deposited CIGS films can be attributed to the unique PRED technique wherein a very small pulse-reverse on time is employed. This, in turn, results, in a very high power density that can locally influence the structure of the deposited films on the substrate. The high power density provided in the electrochemical form may not only be involved in the possible redox reactions but may also be utilized by the resulting deposit to improve its crystallinity. The single crystal nature of CIGS phase can be attributed to the formation of CIGS nano-rods by the selective etching of the deposit. In addition, (112) orientation needs lesser energy for its growth compared to other orientations of CIGS. The electrochemical power density provided in the present technique might only be sufficient to grow the (112) orientation than the other orientations of CIGS. Hence, highly crystalline CIGS nano-rods which are arranged in a fishbone like mesh are observed by the PRED of CIGS films.

However, analysis of single rod is crucial in confirming this point which is explained in the next section by TEM studies.

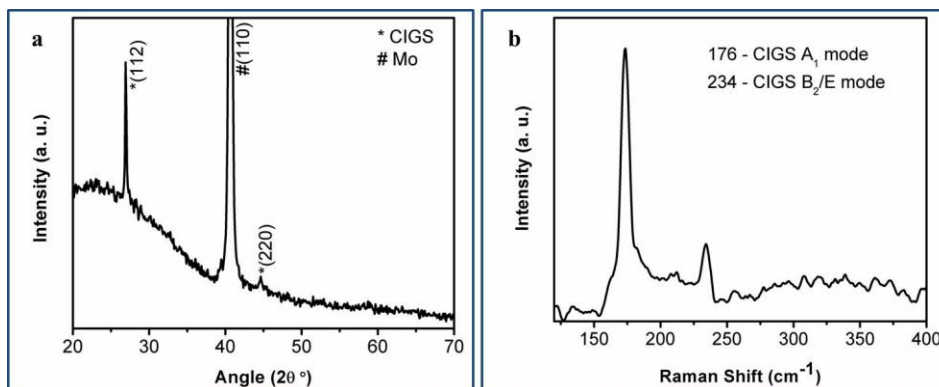


Figure 7.7: a) XRD pattern and b) Raman spectrum of fishbone like CIGS nano-mesh deposited by PRED

The phase constitution of the CIGS nano-mesh is verified by Raman analysis. Figure 7.7b shows the Raman spectrum of the as-deposited CIGS nano-mesh prepared by PRED technique. The spectrum reveals two peaks corresponding to A_1 and B_2/E modes of chalcopyrite CIGS at wavenumbers of 176 and 234 cm^{-1} , respectively. No other secondary phases are observed from the Raman spectrum which corroborates the XRD results suggesting the formation of single phase chalcopyrite CIGS.

7.2.3 Micro-structural characteristics of fishbone like CIGS by TEM

Figure 7.8 shows the TEM characteristics of CIGS nano-rod extracted from the fishbone like CIGS nano-mesh by simple scraping. Figure 7.8a shows TEM image of the nano-rod which reveals the diameter to be ≈ 50 nm, corroborating the FESEM analysis. In addition, HRTEM analysis, SAED and EDS are performed on the nano-rod to further investigate it. Figure 7.8b shows the HRTEM image of the nano-rod which unveils the interplanar spacing to be ≈ 3.3 Å which corresponds to the (112) preferred orientation of CIGS and no other orientations are observed. The result confirms the fact that the CIGS nano-rods are single crystal in nature as observed previously from XRD analysis. In addition, SAED pattern of rod is shown in Figure 7.8c, which reveals the single crystal structure of CIGS nano-rod. Finally, TEM-EDS analysis is performed on the nano-rod to confirm the presence of all the elements. TEM-EDS spectrum of CIGS nano-rod, which reveals the presence of Cu, In, Ga and Se in the rod, is shown in Figure 7.8. A quantitative analysis of the elements is not considered since the analysis is performed on a Cu grid.

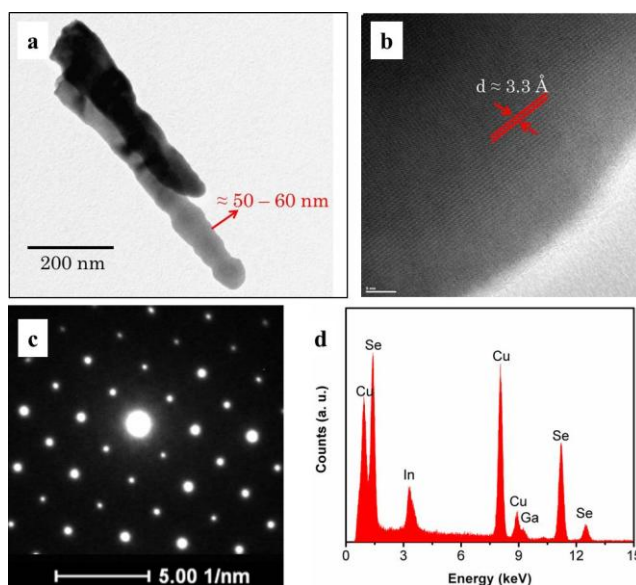


Figure 7.8: a) TEM image, b) HRTEM image, c) SAED and d) TEM-EDS of PRED deposited fishbone like CIGS nano-mesh

7.2.4 Optical absorption studies of the CIGS nano-mesh

Figure 7.9a shows the optical absorbance of fishbone like CIGS nano-mesh fabricated using PRED technique. Absorption spectra of PED deposited dense CIGS thin-films and CIGS nano-flakes are also included for comparison. As it can be clearly observed, the fishbone like CIGS nano-mesh exhibited extended absorption which is very much similar to the other two cases and has recorded the highest absorbance among the three. The higher surface area of the nano-flakes is discussed previously. The fishbone like CIGS is also vertically aligned similar to CIGS nano-flakes which attributes to the higher surface area. In addition, each mesh contains one-dimensional nano-rods similar to that of bones in a fish. It is well known that one-dimensional nano-rods have higher surface area due to their very high aspect ratio (ratio of length to diameter). Hence, the surface area of the fishbone like CIGS nano-mesh is much higher compared to the CIGS nano-flakes and results in an enhanced absorption. A careful inspection of the Figure 7.9a reveals the absorption edge of the fishbone like CIGS nano-mesh at around 950 nm whereas that of dense CIGS films is observed to at 1000 nm. The observation indirectly indicates a shift in the bandgap of the CIGS nano-mesh to higher values compared to dense CIGS thin-films. Figure 7.9b shows the $(\alpha h\nu)^2$ vs. $h\nu$ (Tauc's) plot of the nano-mesh which indicates that the bandgap is determined to be ≈ 1.29 eV, by extrapolating the linear section of the plot to X-axis. The bandgap of dense CIGS films is observed to be 1.21 eV and that of CIGS nano-flakes is 1.30 eV. The bandgap value of the

fishbone like CIGS nano-mesh is almost same as that of CIGS nano-flakes. The nano-rods in the fishbone like CIGS nano-mesh contribute to the possible quantum confinement of charge carriers thereby leading to the quantization of energy levels within valence and conduction bands. This in turn leads to the higher bandgap for fishbone like CIGS nano-mesh, as seen from Figure 7.9b.

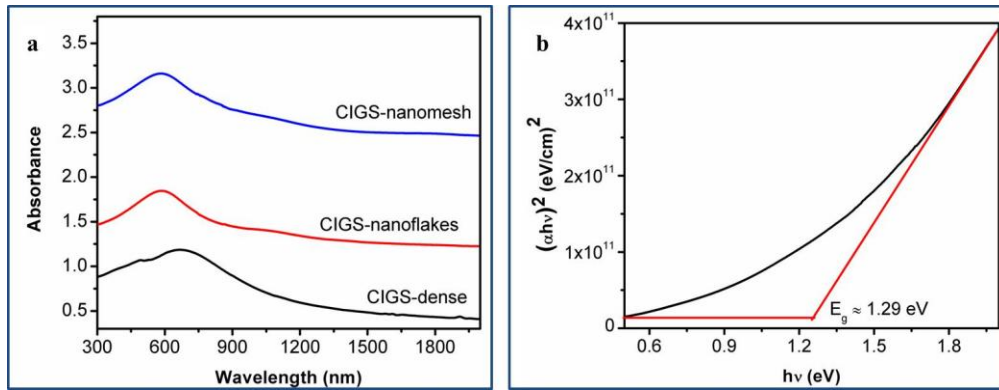


Figure 7.9: a) Optical absorbance and b) Tauc's plot of fishbone like CIGS nano-mesh. Absorbance of dense-CIGS and CIGS nano-flakes are also included for comparison

7.2.5 Mott-Schottky analysis of fishbone like CIGS nano-mesh

Figure 7.10 shows the Mott-Schottky ($1/C^2$ vs. V) plot of fishbone like CIGS nano-mesh in 0.5M H_2SO_4 at a frequency of 10 kHz in the dark. The slope of the MS plots is negative, thereby confirming that the CIGS nano-mesh exhibits p-type conductivity. The flat band potential is found to be -0.195 V (vs. SCE) by extrapolating the linear section to X-axis. In addition, the acceptor density, $N_a \approx 4.95 \times 10^{16} \text{ cm}^{-3}$, calculated using the slope of the curve. An interesting observation from the Mott-Schottky plot is the reduced $1/C^2$ values for the CIGS nano-mesh compared to previously observed values for dense-CIGS films and CIGS nano-flakes.

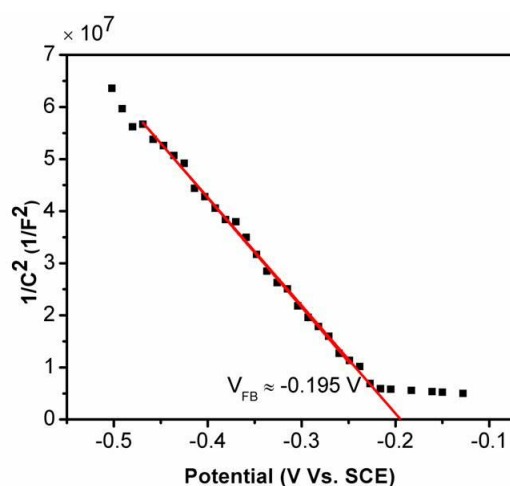


Figure 7.10: Mott-Schottky plot of fishbone like CIGS nano-mesh fabricated using PRED technique

It can be observed that $1/C^2$ values further reduced compared to the previously discussed nano-flakes indicating a higher capacitance for fishbone like CIGS nano-mesh. The capacitance measured herein is the double layer capacitance observed at the CIGS-electrolyte interface, as discussed previously in section 2.3.9. It is also well known that the capacitance value is directly proportional to the area of the electrodes in a parallel plate capacitor ($C = \epsilon_0 A/d$). Hence, in the present case, the larger capacitance value can be attributed to the increased area of CIGS due to the presence of the nano-mesh structure. Figure 7.11 shows the capacitance values for the dense-CIGS films, CIGS nano-flakes and nano-mesh. It can be clearly observed that films containing nano-mesh exhibited highest capacitance among the three which is attributed to its higher surface area compared to CIGS nano-flakes and dense CIGS films.

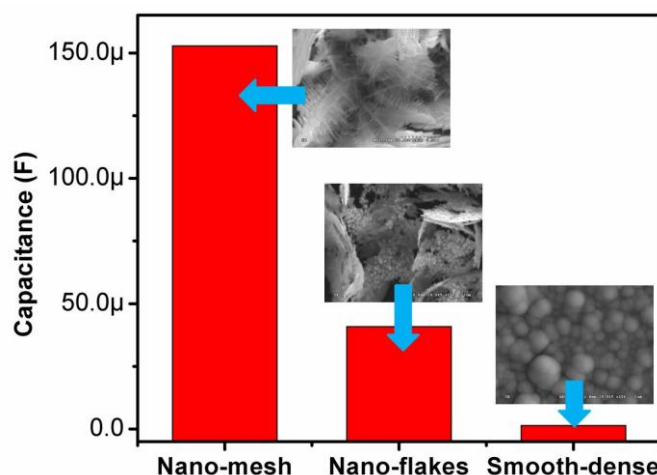


Figure 7.11: Comparison of double layer capacitance measured from impedance analysis for dense-CIGS, CIGS nano-flakes and fishbone like CIGS nano-mesh

7.2.6 Photoelectrochemical studies of fishbone like CIGS nano-mesh

Figure 7.12a shows dark and illuminated current density – voltage characteristics of the CIGS nano-flakes deposited by PRED technique, measured using a photoelectrochemical analyzer in 0.5 M H_2SO_4 with a sweep rate of 10 mV/s. The nature of the J-V curve confirms the photo-activity of CIGS thin-films. In addition, it shows that the increase in cathodic photocurrent with increased cathode potential, which is a characteristic of a semiconductor with p-type conductivity. It is also to be noted that the photocurrent increases gradually without attaining a saturated value. This behavior can be attributed to incomplete photonic conversion, which causes a recombination of charge carriers at the grain boundaries of the semiconductor. A photocurrent density of $\approx 4.31 \text{ mA/cm}^2$ at a potential of -0.4 V vs. SCE is observed. This represents a significant improvement in photocurrent density compared to the values observed in previous chapters for the other CIGS films. The larger photocurrent value is essentially due to the presence of fishbone like nano-mesh and can be explained using several reasons. Firstly, increased light absorption due to fishbone like nano-mesh yields increased carrier generation thereby leading to the probability for improved photocurrent density. Secondly, the junction area between fishbone like nano-mesh and electrolyte is increased which in turn increases depletion field which is responsible for separation of charge carriers thereby leading to improved photocurrent density. In addition, as the junction is formed between the nano-rod and the electrolyte the essential path length that needs to be traversed by the electron is the diameter of the nano-rod which is only about 50 nm indicating the shorter diffusion length for electrons leading to the possibility of reduction in detrimental recombination. One-dimensional nano-rods

improve the electron transmission significantly which results in a higher photocurrent density. In addition, the fishbone like nano-mesh is observed to be single crystal, as confirmed from XRD and TEM analyses, which in turn expects to have less scattering and better transmission of minority carriers thereby leading to increased photocurrent density.

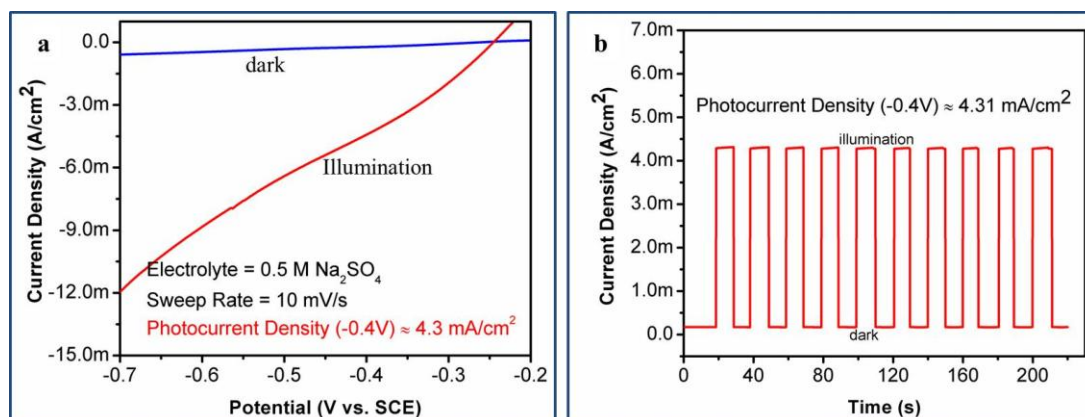


Figure 7.12: a) Photoelectrochemical I-V characteristics and b) amperometric I-t curve of fishbone like CIGS nano-mesh prepared by PRED technique

In addition to the PEC I-V characteristics, amperometric current vs. time curve is also obtained for the films containing nano-mesh structure. Figure 7.12 shows the amperometric current-time (I-t) curve of CIGS nano-flakes obtained at -0.4 V by chopped light. It clearly demonstrates the photoactivity nature of CIGS films with a photocurrent density of ≈ 4.31 mA/cm², corroborating the above result. The improved photoresponse of fishbone like nano-mesh indicate their potential for application in thin-film solar cells. In addition, the photoelectrochemical performance of these films demonstrates their potential utility for photoelectrochemical hydrogen generation.

7.3 Conclusions

Pulse-reverse electrodeposition is successfully explored for the fabrication of stoichiometric chalcopyrite CIGS. Pulse-reverse voltage is optimized to achieve phase pure CIGS films. The optimized PR voltage has yielded a novel fishbone like nano-mesh morphology for CIGS films. The growth mechanism of the fishbone like CIGS nano-mesh is explained with the varied PR voltage and with varied PR parameters. It can be concluded that the convenient optimization of PR voltage and PR on-time resulted in a stoichiometric chalcopyrite fishbone like CIGS nano-mesh. The fishbone like CIGS nano-mesh has not only shown superior absorption properties but also exhibited significantly improved

photocurrent density. The CIGS nano-mesh fabricated by simplified pulse-reverse electrodeposition technique has potential application for thin-film solar cells and photoelectrochemical cells.

Chapter 8

Fabrication and characterization of CIGS/CdS heterojunction

Pulse and pulse-reverse electrodeposition techniques have been successfully explored for the fabrication of stoichiometric CIGS thin-films in the previous chapters. The next major step of the present study is to ascertain the suitability of the pulse electrodeposited CIGS films to realize its application as the solar photovoltaic absorber layer. To ascertain the performance of CIGS absorber layer, devices have often been constructed by sequential deposition of buffer layer (CdS), window layers (i-ZnO and TCO layers), followed by the deposition of metal fingers. Use of distinct methods to deposit each of these layers makes it a difficult and time consuming process, besides leading to increased time for optimization of the absorber layers. A rapid assessment of photoactivity is often desired for screening semiconductor absorber layers for PV applications. This can be achieved without fabricating an entire device by using an electrolyte contact and carrying out photoelectrochemical (PEC) characterization involving a linear/cyclic potential sweep while illuminating the electrode with chopped light [177, 185]. Typically a PEC test utilizes a hydrogen evolution reaction (HER), as related to PEC water reduction, to account for the photocurrent. Such a PEC test not only provides the signature of photoactivity but also demonstrates the potential utility of the CIGS based photoelectrochemical solar cells for hydrogen generation. In general, the hydrogen evolution reaction requires either significant over-potentials or a suitable electro-catalyst [185-188]. As CIGS thin-films do not possess either of the above, they have often yielded poor photocurrent densities when aqueous Na_2SO_4 , K_2SO_4 , H_2SO_4 , etc. have been used as electrolytes [156, 177, 189, 190]. In addition, CIGS thin-films are not adequately stable in aqueous electrolytes, which is often the reason for their lower photocurrent values. An improved photocurrent density, however, has been reported by Ye et al. by using ethyl viologen perchlorate and methyl viologen chloride in acetonitrile as a

redox couple [177]. Use of such non-aqueous solvents with a suitable redox couple might be promising but represents an approach that is both complex and expensive.

On the other hand, CdS has been one of the most widely studied semiconductors for photoelectrochemical water splitting due to its suitable band edge positions [187, 188, 191, 192]. But the larger bandgap of CdS often limits the absorption to UV region thereby limiting the photocurrent density. Use of CIGS/CdS heterojunction not only offers extended absorption range through visible region but also results in improved carrier transport due to the space charge field at the interface. In addition, the most efficient CIGS devices have been known to use CdS as the buffer layer to yield the heterojunction that improves absorption in the space charge region, field assisted electron hole separation and minimizes detrimental interface recombination [30-32, 65, 66, 193-195]. Consequently, the CIGS/CdS heterojunction can be fabricated and tested using photoelectrochemical characterization which not only ascertains the suitability of pulse electrodeposited CIGS film but also yields the performance of CIGS/CdS heterojunction. However, the success of these cells crucially relies on finding an appropriate electrolyte that not only yields larger photocurrent but also enhances stability.

In this context, this chapter focuses on the fabrication and photoelectrochemical characterization of CIGS/CdS heterojunction wherein CdS is chemical bath deposited onto pulse electrodeposited CIGS. The scheme adopted for the fabrication and photoelectrochemical characterization of CIGS/CdS heterojunction is shown in Figure 8.1.

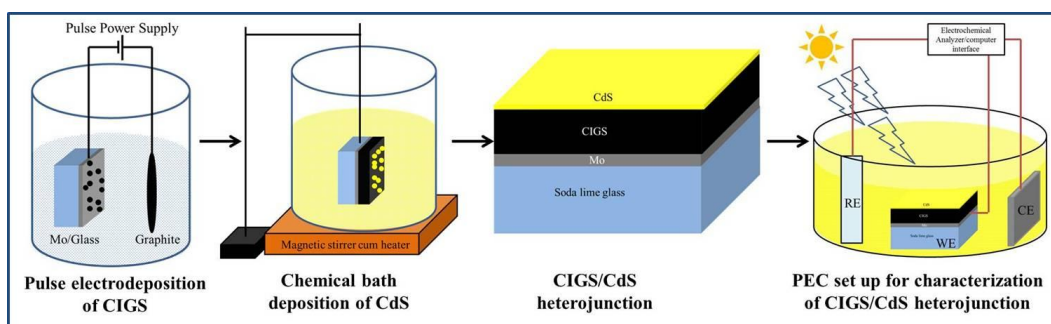
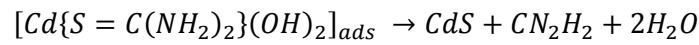
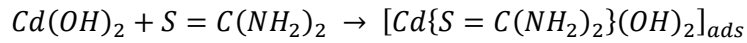
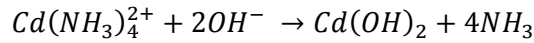


Figure 8.1: Scheme of fabrication and characterization of CIGS/CdS heterojunction

8.1 Fabrication of CIGS/CdS heterojunction

Pulse electrodeposition of CIGS thin-films onto Mo/glass cathode is performed by adopting the optimized pulse conditions mentioned in chapter 4. The deposition of CdS films onto

pulse electrodeposited CIGS is performed by using the chemical bath deposition method wherein 0.0015 M cadmium sulphate and 0.05 M thiourea with ammonia as complexing agent are used. The deposition is carried out at ≈ 65 °C for 8 min. The formation of CdS thin-films by using ammonia as complexing agent involves the following reactions [185, 196]:



CdS deposited CIGS films were then cleaned with DI water and used for further characterization.

8.2 Characterization of CIGS/CdS heterojunction

The CIGS/CdS heterojunction is characterized using SEM, XRD and Raman to essentially demonstrate the presence of CdS on CIGS. In addition, the heterojunction is characterized using photoelectrochemical amperometric I-t characteristics to test the performance of the junction.

8.2.1 Morphology and phase constitution of CIGS/CdS heterojunction

The morphology of bare CIGS films and CIGS/CdS heterojunction is shown in Figure 8.2. The surface morphology of annealed pulse electrodeposited CIGS films is previously discussed in section 4.2.3. The surface morphology of CIGS/CdS heterojunction is shown in Figure 8.2b. The compact morphology of the pulse electrodeposited CIGS films aided in the formation of high-quality heterojunction with conformal coverage of CdS during the chemical bath deposition process. The high conformal coverage obtained in the present study is extremely crucial since it decides the quality of the heterojunction which ultimately affects the performance of the device. In addition to the conformal surface coverage, the CdS particles have a uniform size distribution. These desirable aspects of the CIGS/CdS junction are essentially due to the underlying uniform and compact CIGS films. The pulse electrodeposition technique used herein can produce relatively more homogeneous surface with good adhesion to the substrate because the rate-determining step of the deposition process is controlled by a mass-transfer process. In addition, the relaxation time in the pulse

electrodeposition not only allows the diffusion of ad-atoms but also facilitates the formation of new nucleation sites thereby leading to the smooth and compact structure, as discussed previously.

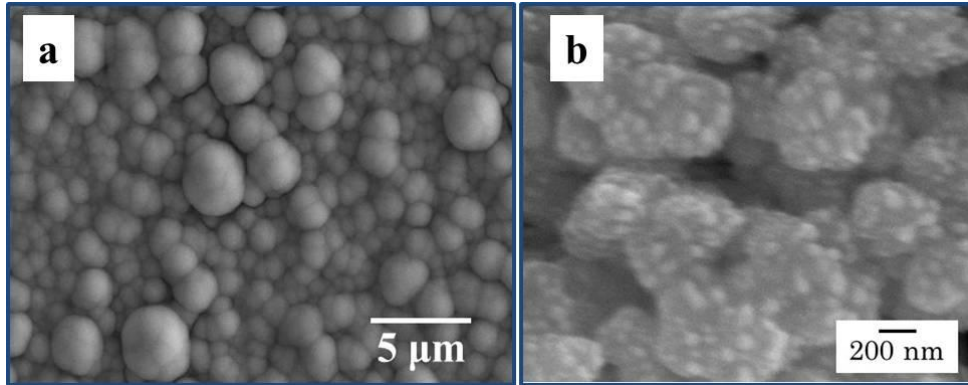


Figure 8.2: Morphology of a) bare CIGS films and b) CIGS/CdS heterojunction

Figure 8.3a shows the XRD patterns of annealed CIGS thin-films and CIGS/CdS heterojunction. The pattern for bare CIGS films reveal the same peaks as mentioned in section 4.2.4. The XRD pattern of CIGS/CdS heterojunction (Figure 8.3a) reveals peaks corresponding to (100) and (002) of CdS in addition to the CIGS peaks confirming the presence of hexagonal CdS layer on pulse electrodeposited CIGS. Figure 3b shows the Raman spectra of the annealed CIGS films and CIGS/CdS heterojunction. The Raman spectrum of CIGS/CdS heterojunction has a peak at 300 cm^{-1} representing the CdS formation in addition to the peaks of CIGS.

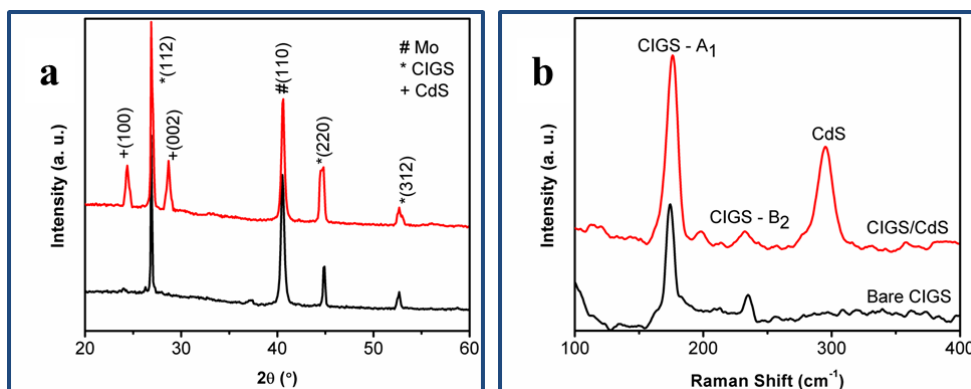


Figure 8.3: a) XRD patterns and b) Raman spectra of bare CIGS films and CIGS/CdS heterojunction

8.2.2 Photoelectrochemical characterization of CIGS/CdS heterojunction

Photoelectrochemical performance of CIGS and CIGS/CdS heterojunction is investigated in 0.5M Na₂SO₄. Amperometric I-t curves of bare CIGS and CIGS/CdS, obtained at -0.4 V vs. SCE, are shown in Figure 8.4a under dark and illumination. The I-t curve of bare CIGS (inset in Figure 8.4a) reveals the photovoltaic activity of CIGS films with a photocurrent density of ≈ 0.5 mA/cm². The pulse electrodeposited CIGS films exhibit a lower dark current and improved photocurrent. The crack-free compact morphology and absence of undesired phases achieved by the appropriate regulation of pulse parameters in the present study are responsible for the lower dark current and improved photoresponse of CIGS films. Though an improved performance is observed at -0.4 V for CIGS films yet the photocurrent is relatively poor and it could be attributed to the fact that the CIGS alone does not possess the desired requirements for an HER reaction, as mentioned earlier.

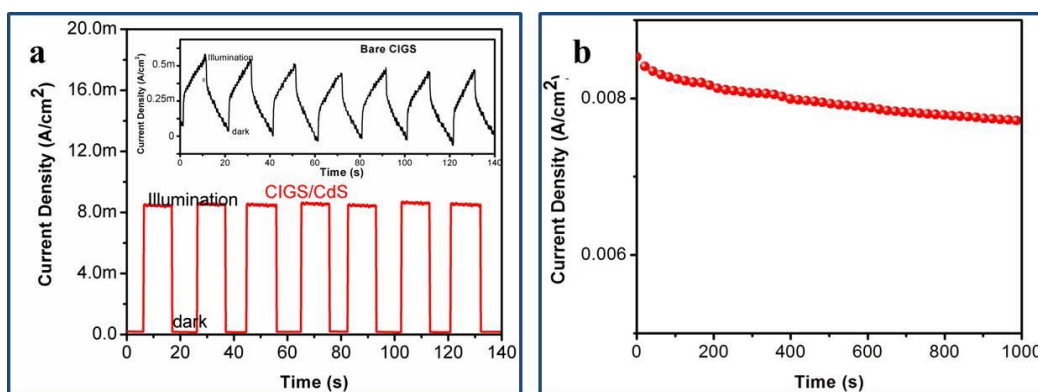


Figure 8.4: a) Amperometric I-t curve and b) stability of CIGS/CdS heterojunction in Na₂SO₄ electrolyte. Inset: I-t curve of bare CIGS films.

Unlike CIGS, the CIGS/CdS heterojunction showed a significantly larger photocurrent density of ≈ 8.5 mA/cm² at -0.4 V vs. SCE. Several aspects which contribute to the increased performance of the junction are discussed here: Primarily, pulse electrodeposited compact phase-pure CIGS is responsible for the formation of high-quality CIGS/CdS heterojunction and its performance. In addition, it is well known that the driving force for the electron-hole separation is assisted by the local electric field created in the space charge region [8, 186]. CIGS/CdS-electrolyte interface has a wider space charge layer beginning from CIGS through CdS to electrolyte than the CIGS-electrolyte interface (Figure 8.5). The increased width of this space charge layer for CIGS/CdS – electrolyte interface, in turn, results in a larger depletion potential affirming the effective electron-hole separation by the minimization of detrimental interface recombination and ultimately resulting in a significantly higher photocurrent density. Another major contribution to improved

photocurrent density arises from the fact that CdS possesses suitable band edge positions for hydrogen evolution reaction. Hence, during the PEC characterization of CIGS/CdS heterojunction, CIGS can largely contribute to the absorption and generation of electron-hole pairs and CdS can effectively separate the generated carriers by utilizing the hydrogen evolution reaction. All these reasons are collectively responsible for the improved photocurrent density thereby making CIGS/CdS as an efficient heterojunction to be applied for CIGS based photoelectrochemical cells.

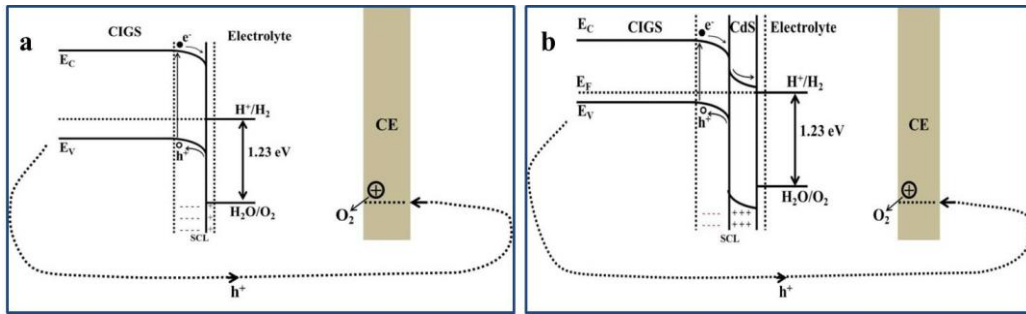


Figure 8.5: Schematic of space charge layer at a) CIGS-electrolyte and b) CIGS/CdS-electrolyte interface

In addition to the PEC performance of the junction, the stability of the heterojunction is also performed as shown in Figure 8.4b. It can be clearly observed that there is a decrease in the photocurrent density with time. The decrease in photocurrent density of the junction is calculated to be $\approx 15\%$ within the duration of about 20 min. This is significant reduction in the photocurrent density and is a major concern prior to the use of the heterojunction for photoelectrochemical as well as thin-film solar cells. Previous studies suggest that the poor stability could be mainly attributed to the surface CdS layer which undergoes photo-corrosion. Sulphur ions from the CdS lattice dissolve into the electrolyte by absorbing the photo-generated holes, thereby resulting in the formation of a passivating sulphur film according to $\text{CdS} + 2\text{h}^+ (\text{h}\nu) \rightarrow \text{Cd}^{2+} (\text{aq}) + \text{S}^0$. This has often been a drawback for Cd based PEC cells leading to their poor stability in aqueous electrolytes. Adequate stabilization of these semiconductor layers is necessary to achieve higher stability by suppressing the decomposition reactions. Hence, choosing the electrolytes which capture carriers before they can react with the semiconductor lattice is the key for the higher stability. Usually, it is preferable to choose redox electrolytes that form Schottky barriers since this ensures that minority carriers will be scavenged. However, in some cases it may be preferable to use an electrolyte in which the electron transfer process is not only fast but also irreversible. One

such case is the use of Na_2SO_3 for CdS since the SO_3^{2-} ion is an excellent hole scavenger, reacting rapidly and irreversibly to form sulphate [185]. Hence, in the present study, sulphide/sulphite electrolyte has been explored for the first time for a CIGS/CdS heterojunction.

Figure 8.6a shows the PEC performance of CIGS/CdS heterojunction in Na_2SO_4 and the sulphide/sulphite electrolytes. As explained above, the use of sulphide/sulphite electrolyte is found to result in a higher photocurrent density, which is observed to be $\approx 11.3 \text{ mA/cm}^2$. The stability of the heterojunction is also tested in both Na_2SO_4 and sulphide/sulphite electrolytes. As shown in Figure 8.6b, the stability of CIGS/CdS heterojunction is compared in Na_2SO_4 and sulphide/sulphite electrolytes. The junction exhibits a constant photocurrent density without any considerable variation in sulphide/sulphite electrolyte for the same duration. The enhanced stability of the junction in the sulphide/sulphite electrolyte compared to sodium sulphate electrolyte can be attributed to the decreased photocorrosion of CdS in sulphite electrolyte. The larger photocurrent density with exceptional stability noted here for the CIGS/CdS heterojunction promises a future for CIGS photoelectrochemical cells and for hydrogen generation by PEC water splitting.

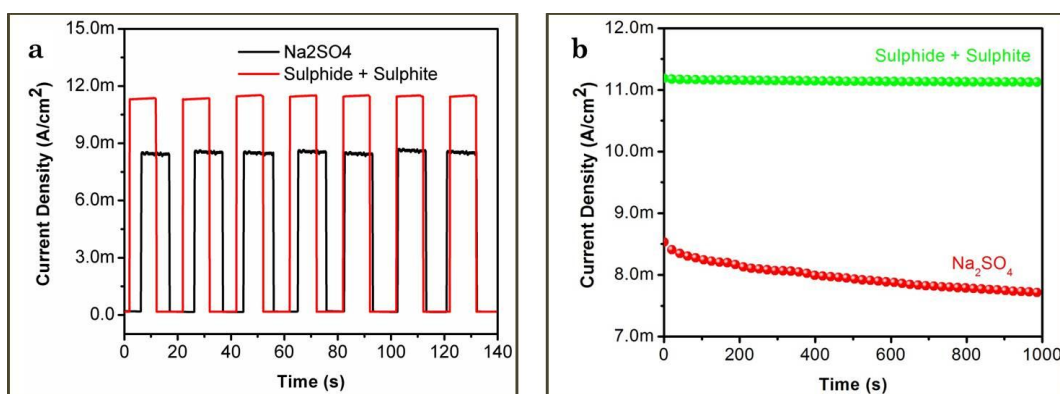


Figure 8.6: a) Amperometric I-t curves b) corresponding stability of CIGS/CdS heterojunction under illumination in Na_2SO_4 and sulphide/sulphite electrolytes

8.3 Conclusions

In summary, CIGS/CdS heterojunction has been fabricated to ascertain the suitability of pulse electrodeposited CIGS thin-films as the solar photovoltaic absorber layer. The morphological and structural characterization demonstrates the high quality heterojunction formed by the chemical bath deposition of CdS onto CIGS. The junction is finally tested using PEC to infer its photoelectrochemical ability. A significantly improved photoresponse

is observed for the CIGS/CdS heterojunction in Na_2SO_4 . However, the poor stability of heterojunction due to the photo-corrosion of CdS is still a concern. The study has, however, revealed that use of a sulphide/sulphite electrolyte can eliminate the above problem and yield enhanced photocurrent density with excellent stability. These results can have important implication in economically realizing CIGS-based photoelectrochemical cells and their potential utility for hydrogen generation.

Summary and Outlook

The research work discussed in the present dissertation is the demonstration of a simplified electrodeposition technique for the fabrication of stoichiometric phase-pure chalcopyrite $\text{Cu}(\text{In,Ga})\text{Se}_2$ (CIGS) thin-films. The thesis work has essentially employed the advanced techniques such as pulse and pulse-reverse electrodeposition for the fabrication of CIGS thin-films. These advanced features of electrodeposition are conveniently optimized to achieve an exceptional control over composition and morphology of the CIGS thin-films. In addition, the selenization which is often employed to correct for the film stoichiometry is completely eliminated in the present study making it an environmental friendly process. The study has also avoided the reference electrode to eradicate the possible impurities from it and employed a two-electrode system wherein the conventionally used expensive platinum counter electrode is replaced by high purity graphite thereby making the system more simple and economical. Furthermore, the majority part of the study avoided the use of complexing agents which are commonly used to improve the features such as composition and morphology of the electrodeposited CIGS films. Hence, a simplified, economic and environmental friendly approach has been proposed in the present study to fabricate the phase-pure stoichiometric CIGS thin-films. The process is systematically modified to improve the quality and performance of the thin-films and the results of the work are summarized chapter-wise below.

At the very beginning, prior to adopting the process for the preparation of CIGS films, the pulse electrodeposition technique is optimized for the fabrication of ternary CuInSe_2 (CIS) system, which has the tetragonal chalcopyrite structure and is the basis for the formation of CIGS. Though the process is optimized to ease it for CIGS films, but the optimized CIS films exhibiting a novel flake-like morphology are formed in addition to the near-ideal stoichiometry. Appropriate regulation of pulse parameters has aided in a well-controlled composition of individual elements and resulted in the formation of chalcopyrite flake-like CIS thin-films with minimal secondary phases in it, as confirmed from SEM-EDS, XRD and Raman analyses. The bandgap of CIS films is determined to be 1.02 eV, from optical absorption studies, is close to the previous reported value. Photoelectrochemical response of the CIS films is studied and a photocurrent density of $\approx 20 \mu\text{A}/\text{cm}^2$ is obtained for the CIS films deposited at the optimized pulse condition.

The optimized pulse electrodeposition approach adopted for CIS films is carried forward to deposit the CIGS films. However, prior to that, to understand the electrochemical activities of various plausible phases among Cu-In-Ga-Se and to understand the sequence of the mechanism during deposition cyclic voltammetry studies are carried out. The analysis is systematically performed on various binary/ternary/quarternary phases using three-electrode and two-electrode systems. There are two essential conclusions that are made from CV measurements: 1) Cu gets deposited first onto the Mo substrate which then facilitates the deposition of In and/or Ga or their binary phases and 2) the use of a two-electrode system shifts the reduction potential of the desired species to more negative values thereby making it a necessity to use higher deposition potential during the electrodeposition.

The inferences from cyclic voltammetry experiments along with the procedure optimized for CIS thin-films aided the pulse electrodeposition method to successfully prepare CIGS thin-films. Principally the duty cycle (variation in off-time with on-time being fixed) has been varied to fabricate compact phase-pure CIGS films wherein it has been observed that the content of In decreased with decrease in duty cycle. A duty cycle of 50 % yielded the desired composition of all the elements to form stoichiometric CIGS without any secondary phases and is deemed optimum. In addition, a highly dense uniform morphology is observed for optimized PED deposited CIGS films. To compare the features of the deposit, CIGS films are also deposited by direct current method, which resulted in Cu-rich samples with rough and porous morphology. In addition, the Cu-richness in the samples led to the formation of undesired Cu_{2-x}Se phases in the films. The characteristic of p-type semiconductor is observed in the both the DC and PED deposited CIGS thin-films, as confirmed from Mott-Schottky as well as PEC studies. Absorption studies are carried out to determine the band gap of the thin-films which are in agreement with the theoretical stoichiometric CIGS band gap. The flat-band potentials and acceptor densities are calculated for both CIGS films from Mott-Schottky analysis. The typical growth mechanism of CIGS films by DC and PED deposition methods is also investigated experimentally and theoretically. The results demonstrate that the PED deposited CIGS films follow a progressive nucleation mechanism wherein the rapid growth of nuclei with an additional increase in number of nuclei take place with the deposition time leading to a uniform and compact CIGS films. The DC deposited films follow an instantaneous nucleation mechanism wherein non-uniform growth of active nuclei takes place without any increase in the nuclei number density.

The optimized PED method in the previous cases has utilized higher precursor concentration of In to achieve desired In content in the CIGS films, which is still a serious concern considering the scarcity of In and its frequent usage in materials for electronic applications. Hence, minimization of In precursor is still a vital concern to be considered prior to the commercialization of the pulse electrodeposition approach for the fabrication of CIGS thin-films. In this context, a novel sequential pulse electrodeposition approach has been proposed for the fabrication of CIGS thin-films to essentially minimize the In precursor concentration by simultaneously achieving desired In content. Deposition voltage has been optimized for the co-deposition of Cu-Ga-Se films in stage – I followed by deposition of In in the second stage. A convenient control over the composition of individual elements has been achieved by the suitable manipulation of process parameters. Characterization of annealed films using XRD and Raman analyses confirmed the formation of phase-pure stoichiometric chalcopyrite CIGS phase. CIGS films exhibited p-type conductivity as demonstrated from Mott-Schottky as well as PEC studies. Furthermore, a significantly improved photoresponse has been observed. This technique minimizes the use of In precursor for fabrication of CIGS thin-films for solar cell applications.

The minimization of In precursor can also be done by the use of complexing agents in the electrolyte. Hence, in the present study, the process has adopted tri-sodium citrate as the complexing agent to minimize In precursor and to study the effect of it on pulse electrodeposition of CIGS films. In this context, the concentration of TSC is optimized to fabricate stoichiometric chalcopyrite CIGS thin-films. A possible mechanism is proposed to understand the effect of TSC on the deposition of CIGS thin-films. Further, the use of optimized TSC has resulted in highly compact CIGS thin-films but exhibited poor photoresponse which could be due to the possible impurities from the complexing agent. An interesting aspect, however, is the observation of flower like CIGS particles for a lower concentration of TSC (60 mM). This 60 mM of TSC is further used to optimize for the CIGS content by employing a variation in deposition time. Ultimately, the deposition time of 25 min has yielded stoichiometric CIGS films which resulted in an interesting novel nano-flake like morphology. These CIGS nano-flakes have not only shown superior absorption properties but also exhibited significantly improved photocurrent density. The CIGS nano-flakes fabricated by simplified electrodeposition technique have potential application for thin-film solar cells and photoelectrochemical cells.

In addition to the pulse electrodeposition, pulse-reverse electrodeposition of CIGS films is also one of the major aims of the present study in order to improve the quality of the films. Pulse-reverse electrodeposition is successfully explored for the fabrication of stoichiometric chalcopyrite CIGS. Pulse-reverse voltage is optimized to achieve phase pure CIGS films. The optimized PR voltage has yielded a novel fishbone like nano-mesh morphology for CIGS films. The growth mechanism of the CIGS nano-mesh is explained with the varied PR voltage. It can be concluded that the convenient optimization of PR voltage and PR on-time resulted in a stoichiometric chalcopyrite fishbone like CIGS nano-mesh. The CIGS nano-mesh has not only shown superior absorption properties but also exhibited significantly improved photocurrent density. The CIGS nano-mesh fabricated by simplified pulse-reverse electrodeposition technique has potential application for thin-film solar cells and photoelectrochemical cells.

The process has been systematically modified to fabricate the compact and nano-structured chalcopyrite CIGS films. The dark current and photocurrent, obtained from PEC analysis, for various CIGS thin-films deposited in the present study are shown in Figure 8.7. It can be observed that the dark current decreased gradually while the photocurrent is increased (see Figure 8.7a and b). The decreased dark current and improved photocurrent values confirm the fact that CIGS films with improved quality have been fabricated by modifying the process. In addition, the nanostructured CIGS films exhibited superior photocurrent density compared to compact morphological CIGS films.

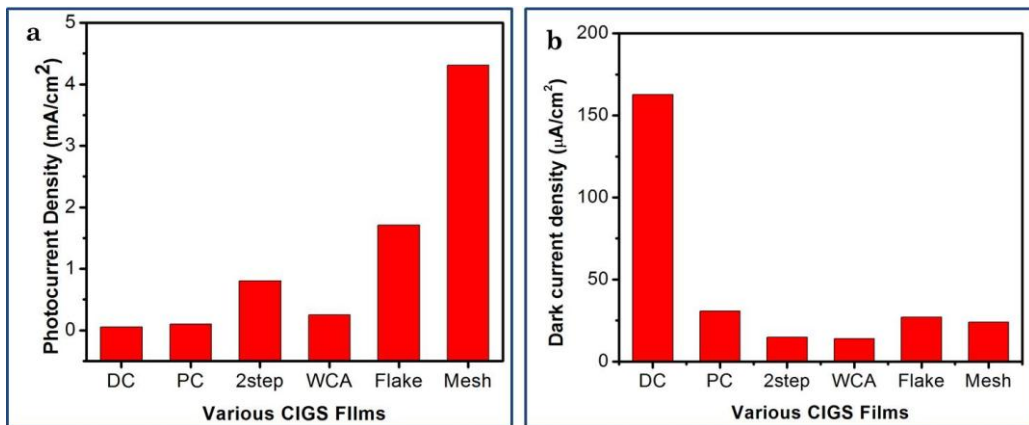


Figure 8.7: Comparison of a) photocurrent density and b) dark current density (both at -0.4 V vs. SCE) of various types of CIGS films deposited in the present study

Ultimately to ascertain the suitability of pulse electrodeposited CIGS thin-films as the solar photovoltaic absorber layer; CIGS/CdS heterojunction has been fabricated. The morphological and structural characterization demonstrates the high quality heterojunction formed by the chemical bath deposition of CdS onto CIGS. The junction is finally tested using PEC to infer its photoelectrochemical performance. A significantly improved photoresponse is observed for the CIGS/CdS heterojunction in Na_2SO_4 . However, the poor stability of heterojunction due to the photo-corrosion of CdS is still a concern. The study has, however, revealed that use of a sulphide/sulphite electrolyte can eliminate the above problem and yield enhanced photocurrent density with excellent stability. These results can have important implication in economically realizing CIGS-based photoelectrochemical cells and their potential utility for hydrogen generation.

In summary, a simplified, economic and environmental friendly pulse and pulse-reverse electrodeposition techniques have been proposed in the present study in order to achieve exceptional control over the composition of individual elements and ultimately, to fabricate stoichiometric single phase chalcopyrite CIGS thin-films with compact as well as nanostructured morphologies. The methods have great run-to-run reproducibility that a minimum of 15 samples have been prepared for each pulse condition revealing the same characteristics. In addition, the process is easily amenable to large area production of CIGS thin-films and in the present work, CIGS thin-films are grown on substrates as large as 10 cm^2 surface area. It is also pertinent to note that electrodeposition technique in general possesses the ability to deposit the films on large area substrates even with complex shapes. The technique also has the potential to grow thin-films on flexible substrates.

Outlook:

The research work in this dissertation mainly focused on the variation of parameters using pulse and pulse-reverse electrochemical techniques for the fabrication of CIGS absorber layers. Though the absorber layer has been characterized individually for its photovoltaic activity, but the real application can only be realized when a full solid state device is constructed and tested for its conversion efficiency. Hence, the immediate possible outlook of the present study is to construct a full device by depositing buffer and window layers. In addition, the films can be characterized using Hall measurements, deep level transient spectroscopy, etc. to study the transport properties, minority carrier lifetime, defect densities, etc. Furthermore, the electrodeposition of CIGS films on the flexible substrates is another important outlook of the present thesis.

References

- [1] V.K. Arora, Ministry of statistics and programme implementation, Govt. of India, New Delhi, (2013) 1-2.
- [2] Wikipedia.org.
- [3] G. Masson, S. Orlandi, M. Rekinge, in: European Photovoltaic Industry Association, 2014, pp. 1-60.
- [4] R.A. Rohde, in, Global Warming Art/wikipedia
- [5] J. Perlin, From Space to Earth, the Story of Solar Electricity, AATEC Publications, Ann Arbor, MI, 1999.
- [6] D.M. Chapin, C.S. Fuller, G.L. Pearson, Journal of Applied Physics, 25 (1954) 676-677.
- [7] M.A. Green, Solar cells: operating principles, technology, and system applications Prentice Hall Inc., Eaglewood Cliffs, N. J., 1982.
- [8] D. Abou-Ras, T. Kirchartz, U. Rau, in, Wiley-VCH Verlag GmbH & Co. KGaA, Weinheim, Germany, 2011.
- [9] I.M. Dharmadasa, Advances in Thin-Film Solar Cells, Singapore, Pan Stanford Publishing, 2013.
- [10] M.A. Green, K. Emery, Y. Hishikawa, W. Warta, E.D. Dunlop, Progress in Photovoltaics: Research and Applications, 22 (2014) 1-9.
- [11] M.A. Green, K. Emery, Y. Hishikawa, W. Warta, E.D. Dunlop, Progress in Photovoltaics: Research and Applications, 21 (2013) 827-837.
- [12] J. Burschka, N. Pellet, S.-J. Moon, R. Humphry-Baker, P. Gao, M.K. Nazeeruddin, M. Graetzel, Nature, 499 (2013) 316-320.
- [13] H. Neumann, Solar Cells, 16 (1986) 317-333.
- [14] W. Horig, H. Neumann, H. Sobotta, B. Schumann, G. Kohn, Thin Solid Films, 48 (1978) 67-72.
- [15] J. Parkes, R.D. Tomlinson, M.J. Hampshire, Journal of Applied Crystallography, 6 (1973) 414-416.
- [16] J.M. Merino, J.L.M.d. Vidales, S. Mahanty, R. Díaz, F. Rueda, M. León, Journal of Applied Physics, 80 (1996) 5610-5616.
- [17] H. Sobotta, H. Neumann, V. Riede, G. Kuhn, J. Seltmülver, D. Opperma, Physica Status Solidi a, 60 (1980) 531-537.

- [18] F. Abou-Elfotouh, D.J. Dunlavy, D. Cahen, I.R. Noufi, L.L. Kazmerski, K.J. Bachmann, *Progress in Crystal Growth and Characterization*, 10 (1984) 15-17.
- [19] H.J.V. Bardeleben, *Solar Cells*, 16 (1986) 381-390.
- [20] G. Dagan, F. Abou-Elfotouh, D.J. Dunlavy, R.J. Matson, D. Cahen, *Chemistry of Materials*, 2 (1990) 286-293.
- [21] R.D. Heyding, R.M. Murray, *Canadian Journal of Chemistry*, 54 (1976) 841-848.
- [22] G. Zahn, P. Paufler, *Crystal Research and Technology*, 23 (1988) 499-507.
- [23] D.S. Albin, J.R. Tuttle, G.D. Mooney, J.J. Carapella, A. Duda, A. Mason, R. Noufi, in: *IEEE*, 1990, pp. 562-569.
- [24] B.J. Stanbery, *Critical Reviews in Solid State and Materials Sciences*, 27 (2002) 73-117.
- [25] S.-H. Wei, S.B. Zhang, A. Zunger, *Applied Physics Letters*, 72 (1998) 3199-3201.
- [26] M. Gloeckler, J.R. Sites, *Journal of Physics and Chemistry of Solids*, (2005) 1891-1894.
- [27] S. Siebentritt, M. Igalson, C. Persson, S. Lany, *Progress in Photovoltaics: Research and Applications*, 18 (2010) 390-410.
- [28] M. Contreras, J. Tuttle, D. Du, Y. Qi, A. Swartzlander, A. Tennant, R. Noufi, *Applied Physics Letters*, 63 (1993) 1824-1826.
- [29] B.E. Miguel A. Contreras, K. Ramanathan, J. Hiltner, A. Swartzlander, F. Hasoon and Rommel Noufi, *Progress in Photovoltaics: Research and Applications*, 7 (1999) 311-316.
- [30] P. Jackson, D. Hariskos, R. Wuerz, W. Wischmann, M. Powalla, *Physica Status Solidi RRL*, 8 (2014) 219-222.
- [31] D.H. Philip Jackson, Erwin Lotter, Stefan Paetel, Roland Wuerz, Richard Menner, Wiltraud Wischmann and Michael Powalla, *Progress in Photovoltaics: Research and Applications*, 19 (2011) 894.
- [32] A. Chirila, S. Buecheler, F. Pianezzi, P. Bloesch, C. Gretener, A.R. Uhl, C. Fella, L. Kranz, J. Perrenoud, S. Seyrling, R. Verma, S. Nishiwaki, Y.E. Romanyuk, G. Bilger, A.N. Tiwari, *nature materials*, 10 (2011) 857-861.
- [33] L.L. Kazmerski, F.R. White, G.K. Morgan, *Applied Physics Letters*, 29 (1976) 268-270.
- [34] T.J. Coutts, *Thin Solid Films*, 90 (1982) 451-460.
- [35] J.H. Scofield, A. Duda, D. Albin, B.L. Ballard, P.K. Predecki, *Thin Solid Films*, 260 (1995) 26-31.
- [36] R.J. Matson, O. Jamjoom, A.D. Buonaquisti, P.E. Russell, L.L. Kazmerski, P. Sheldon, R.K. Ahrenkiel, *Solar Cells*, 11 (1984) 301-305.

- [37] E. Moons, T. Engelhard, D. Cahen, *JEM*, 22 (1993) 275-280.
- [38] R.A. Hoffman, J.C. Lin, J.P. Chambers, *Thin Solid Films*, 206 (1991) 230-235.
- [39] X. Ma, D. Liu, L. Yang, S. Zuo, M. Zhou, in, 2013, pp. 906814-906814-906811.
- [40] G. Gordillo, M. Grizález, L.C. Hernandez, *Solar Energy Materials and Solar Cells*, 51 (1998) 327-337.
- [41] M.A. Martínez, C. Guillén, *Surface and Coatings Technology*, 110 (1998) 62-67.
- [42] L. Assmann, J.C. Bernède, A. Drici, C. Amory, E. Halgand, M. Morsli, *Applied Surface Science*, 246 (2005) 159-166.
- [43] T. Wada, N. Kohara, S. Nishiwaki, T. Negami, *Thin Solid Films*, 387 (2001) 118-122.
- [44] D. Abou-Ras, G. Kostorz, D. Bremaud, M. Kälin, F.V. Kurdesau, A.N. Tiwari, M. Döbeli, *Thin Solid Films*, 480–481 (2005) 433-438.
- [45] N. Kohara, S. Nishiwaki, Y. Hashimoto, T. Negami, T. Wada, *Solar Energy Materials and Solar Cells*, 67 (2001) 209-215.
- [46] D. Schmid, M. Ruckh, H.W. Schock, *Solar Energy Materials and Solar Cells*, 41–42 (1996) 281-294.
- [47] H.W. Schock, U. Rau, *Physica B: Condensed Matter*, 308–310 (2001) 1081-1085.
- [48] J.-F. Guillemoles, L. Kronik, D. Cahen, U. Rau, A. Jasenek, H.-W. Schock, *The Journal of Physical Chemistry B*, 104 (2000) 4849-4862.
- [49] M.A. Contreras, M.J. Romero, B. To, F. Hasoon, R. Noufi, S. Ward, K. Ramanathan, *Thin Solid Films*, 403–404 (2002) 204-211.
- [50] W.S. Chen, J.M. Stewart, B.J. Stanbery, W.E. Devaney, R.A. Mickelsen, in: 19th IEEE Photovoltaic Specialists Conference, New Orleans, 1987, pp. 1445-1447.
- [51] T. Nakada, K. Furumi, A. Kunioka, *Electron Devices, IEEE Transactions on*, 46 (1999) 2093-2097.
- [52] A. Ennaoui, S. Siebentritt, M.C. Lux-Steiner, W. Riedl, F. Karg, *Solar Energy Materials and Solar Cells*, 67 (2001) 31-40.
- [53] T. Negami, T. Aoyagi, T. Satoh, S. Shimakawa, S. Hayashi, Y. Hashimoto, in: Proc. 29th IEEE Photovoltaic Specialist Conference, New Orleans, USA, 2002, pp. 656.
- [54] D. Abou-Ras, D. Rudmann, G. Kostorz, S. Spiering, M. Powalla, A.N. Tiwari, *Journal of Applied Physics*, 97 (2005) -.
- [55] D. Abou-Ras, G. Kostorz, A. Strohm, H.-W. Schock, A.N. Tiwari, *Journal of Applied Physics*, 98 (2005) -.
- [56] M. Konagai, Y. Ohtake, T. Okamoto, in: Mater. Res. Soc. Symp. Proc., 1996, pp. 153.
- [57] A. Yamada, S. Chaisitsak, Y. Othake, M. Konagai, in: Proc. 2nd World Conference of Photovoltaic Energy Conversion, Vienna, Austria, 1998, pp. 1177.

- [58] M. Eron, A. Rothwarf, *Applied Physics Letters*, 44 (1984) 131-133.
- [59] L. Kronik, D. Cahen, H.W. Schock, *Advanced Materials*, 10 (1998) 31-36.
- [60] C. Rincón, S.M. Wasim, G. Marín, E. Hernández, G.S. Perez, J. Galibert, *Journal of Applied Physics*, 87 (2000) 2293-2296.
- [61] M. Kemell, M. Ritala, M. Leskela, *Journal of Materials Chemistry*, 11 (2001) 668-672.
- [62] A. Rockett, F. Abou-Elfotouh, D. Albin, M. Bode, J. Ermer, R. Klenk, T. Lommasson, T.W.F. Russell, R.D. Tomlinson, J. Tuttle, L. Stolt, T. Walter, *Thin Solid Films*, 237 (1994) 1-11.
- [63] T. Nakada, H. Ohbo, T. Watanabe, H. Nakazawa, M. Matsui, A. Kunioka, *Solar Energy Materials and Solar Cells*, 49 (1997) 285-290.
- [64] Y. Nagoya, K. Kushiya, M. Tachiyuki, O. Yamase, *Solar Energy Materials and Solar Cells*, 67 (2001) 247-253.
- [65] K. Ramanathan, M.A. Contreras, C.L. Perkins, S. Asher, F.S. Hasoon, J. Keane, D. Young, M. Romero, W. Metzger, R. Noufi, J. Ward, A. Duda, *Progress in Photovoltaics: Research and Applications*, 11 (2003) 225-230.
- [66] P. Reinhard, A. Chirilă, F. Pianezzi, S. Nishiwaki, S. Buecheler, A.N. Tiwari, in: *Twentieth International Workshop on Active-Matrix Flatpanel Displays and Devices (AMFPD)*, 2013 IEEE, Kyoto, 2013, pp. 79-82.
- [67] A. Chirilă, P. Reinhard, F. Pianezzi, P. Bloesch, A.R. Uhl, C. Fella, L. Kranz, D. Keller, C. Gretener, H. Hagendorfer, D. Jaeger, R. Erni, S. Nishiwaki, S. Buecheler, A.N. Tiwari, *Nature materials*, 12 (2013) 1107-1111.
- [68] in, SNE Research.
- [69] C.J. Hibberd, E. Chassaing, W. Liu, D.B. Mitzi, D. Lincot, A.N. Tiwari, *Progress in Photovoltaics: Research and Applications*, 18 (2010) 434-452.
- [70] S. Aksu, S. Pethe, A. Kleiman-Shwarsctein, S. Kundu, M. Pinarbasi, *38th IEEE Photovoltaics Specialists Conference*, (2012) 003092-003097.
- [71] R.N. Bhattacharya, *Journal of The Electrochemical Society*, 157 (2010) D406-D410.
- [72] R. N.Bhattacharya, *Solar Energy Materials & Solar Cells*, 113 (2013) 96-99.
- [73] R. N.Bhattacharya, M.-K. Oh, Y. Kim, *Solar Energy Materials & Solar Cells*, 98 (2012) 198-202.
- [74] W.B. R. N. Bhattacharya, J. F. Hiltner, and J. R. Sites, *Applied Physics Letters*, 75 (1999) 1431.
- [75] M. PAUNOVIC, M. SCHLESINGER, *Fundamentals of Electrochemical Deposition*, A JOHN WILEY & SONS, INC., PUBLICATION, Hoboken, New Jersey, 2006.

- [76] N.G. Renganathan, M.V. Subramanian, S. Mohan, *International Journal of Science, Engineering and Technology*, 3 (2011) 206-212.
- [77] M.S. Chandrasekar, M. Pushpavanam, *Electrochimica Acta*, 53 (2008) 3313-3322.
- [78] J.F.G. D. Lincot, S. Taunier, D. Guimard, J. Sicx-Kurdi, A. Chaumont, O. Roussel, O. Ramdani, C. Hubert, J.P. Fauvarque, N. Bodereau, L. Parissi, P. Panheleux, P. Fanouillere, N. Naghavi, P.P. Grand, M. Benfarah, P. Mogensen, O. Kerrec, *Solar Energy*, 77 (2004) 725-737.
- [79] M. Kemell, M. Ritala, M. Leskelä, *Critical Reviews in Solid State and Materials Sciences*, 30 (2005) 1-31.
- [80] D. Lincot, *Thin Solid Films*, 487 (2005) 40-48.
- [81] R.N. Bhattacharya, *Journal of The Electrochemical Society*, 130 (1983) 2040-2042.
- [82] G. Hodes, T. Engelhard, D. Cahen, L.L. Kazmerski, C.R. Herrington, *Thin Solid Films*, 128 (1985) 93-106.
- [83] J. Herrero, J. Ortega, *Solar Energy Materials*, 20 (1990) 53-65.
- [84] S. Massaccesi, S. Sanchez, J. Vedel, *Journal of Electroanalytical Chemistry*, 412 (1996) 95-101.
- [85] L. Thouin, S. Massaccesi, S. Sanchez, J. Vedel, *Journal of Electroanalytical Chemistry*, 374 (1994) 81-88.
- [86] X. Wang, G. Wang, B. Tian, S. Wan, Z. Du, *Chin. Sci. Bull.*, 55 (2010) 1854-1858.
- [87] K.K. Mishra, K. Rajeshwar, *Journal of Electroanalytical Chemistry and Interfacial Electrochemistry*, 271 (1989) 279-294.
- [88] F. Chraïbi, M. Fahoume, A. Ennaoui, J.L. Delplancke, *physica status solidi (a)*, 186 (2001) 373-381.
- [89] D. Pottier, G. Maurin, *J Appl Electrochem*, 19 (1989) 361-367.
- [90] T.-J. Whang, M.-T. Hsieh, Y.-C. Kao, S.-J. Lee, *Applied Surface Science*, 255 (2009) 4600-4605.
- [91] F.J. Pern, R. Noufi, A. Mason, A. Franz, *Thin Solid Films*, 202 (1991) 299-314.
- [92] R. Ugarte, R. Schrebler, R. CoÂrdova, E.A. Dalchiele, H. GoÂmez, *Thin Solid Films*, 340 (1999) 117-124.
- [93] M.G. Ganchev, K.D. Kochev, *Solar Energy Materials and Solar Cells*, 31 (1993) 163-170.
- [94] N. Stratieva, E. Tzvetkova, M. Ganchev, K. Kochev, I. Tomov, *Solar Energy Materials and Solar Cells*, 45 (1997) 87-96.
- [95] A.M. Fernáandez, R.N. Bhattacharya, *Thin Solid Films*, 474 (2005) 10-13.

- [96] A. Kampmann, V. Sittinger, J. Rechid, R. Reineke-Koch, *Thin Solid Films*, 361–362 (2000) 309-313.
- [97] J. Vedel, *Inst. Phys. Conf. Ser., Section B*, 152 (1998) 261–268.
- [98] M. Kemell, M. Ritala, H. Saloniemi, M. Leskelä, T. Sajavaara, E. Rauhala, *Journal of The Electrochemical Society*, 147 (2000) 1080-1087.
- [99] A.N. Molin, A.I. Dikumar, *Thin Solid Films*, 237 (1994) 72-77.
- [100] A.N. Molin, A.I. Dikumar, G.A. Kiosse, P.A. Petrenko, A.I. Sokolovsky, Y.G. Saltanovsky, *Thin Solid Films*, 237 (1994) 66-71.
- [101] A.M. Hermann, R. Westfall, R. Wind, *Solar Energy Materials and Solar Cells*, 52 (1998) 355-360.
- [102] Z.-w. Zhang, H.-y. Guo, J. Li, C.-f. Zhu, *Chinese Journal of Chemical Physics*, 24 (2011) 225-230.
- [103] C. Guillén, J. Herrero, *Journal of The Electrochemical Society*, 141 (1994) 225-230.
- [104] M.E. Calixto, P.J. Sebastian, *Solar Energy Materials and Solar Cells*, 63 (2000) 335-345.
- [105] P.J.S. M.E. Calixto, R.N. Bhattacharya, Rommel Noufi, *Solar Energy Materials & Solar Cells*, 59 (1999) 75-84.
- [106] Y. Ueno, H. Kawai, T. Sugiura, H. Minoura, *Thin Solid Films*, 157 (1988) 159-168.
- [107] N. Khare, G. Razzini, L.P. Bicelli, *Thin Solid Films*, 186 (1990) 113-128.
- [108] R.P. Raffaele, H. Forsell, T. Potdevin, R. Friedfeld, J.G. Mantovani, S.G. Bailey, S.M. Hubbard, E.M. Gordon, A.F. Hepp, *Solar Energy Materials and Solar Cells*, 57 (1999) 167-178.
- [109] J. Yang, Z. Jin, C. Li, W. Wang, Y. Chai, *Electrochemistry Communications*, 11 (2009) 711-714.
- [110] E. Saucedo, V. Izquierdo-Roca, C. Ruiz, L. Parissi, C. Broussillou, P.-P. Grand, J. Jaime-Ferrer, A. Pérez-Rodríguez, J. Morante, V. Bermúdez, *Thin Solid Films*, 517 (2009) 2268-2271.
- [111] Y. Oda, M. Matsubayashi, T. Minemoto, H. Takakura, *Journal of Crystal Growth*, 311 (2009) 738-741.
- [112] V. Izquierdo-Roca, X. Fontané, J. Álvarez-García, L. Calvo-Barrio, A. Pérez-Rodríguez, J. Morante, J. Jaime-Ferrer, E. Saucedo, P. Grand, V. Bermúdez, *Thin Solid Films*, 517 (2009) 2163-2166.
- [113] A. Gobeaut, L. Laffont, J.-M. Tarascon, L. Parissi, O. Kerrec, *Thin Solid Films*, 517 (2009) 4436-4442.

- [114] T. Gujar, V. Shinde, J.-W. Park, H.K. Lee, K.-D. Jung, O.-S. Joo, *Journal of The Electrochemical Society*, 156 (2009) E8-E12.
- [115] J. Wellings, A. Samantilleke, S. Heavens, P. Warren, I. Dharmadasa, *Solar Energy Materials and Solar Cells*, 93 (2009) 1518-1523.
- [116] F. Kang, J. Ao, G. Sun, Q. He, Y. Sun, *Materials Chemistry and Physics*, 115 (2009) 516-520.
- [117] F. Long, W. Wang, J. Du, Z. Zou, in: *Journal of Physics: Conference Series*, IOP Publishing, 2009, pp. 012074.
- [118] M. Benaicha, N. Benouattas, C. Benazzouz, L. Ouahab, *Solar Energy Materials and Solar Cells*, 93 (2009) 262-266.
- [119] S. Ikeda, R. Kamai, T. Yagi, M. Matsumura, *Journal of the Electrochemical Society*, 157 (2010) B99-B103.
- [120] Z. Zhang, J. Li, M. Wang, M. Wei, G. Jiang, C. Zhu, *Solid State Communications*, 150 (2010) 2346-2349.
- [121] R. Yu, T. Ren, C. Li, *Thin Solid Films*, 518 (2010) 5515-5519.
- [122] T. Ren, R. Yu, M. Zhong, J. Shi, C. Li, *Solar Energy Materials and Solar Cells*, 95 (2011) 510-520.
- [123] P.-K. Hung, T.-W. Kuo, K.-C. Huang, N.-F. Wang, P.-T. Hsieh, M.-P. Houg, *Applied Surface Science*, 258 (2012) 7238-7243.
- [124] A. Bhatia, M.A. Karmarkar, H. Meadows, M.C. Hymas, E.M. Smith, P.J. Dale, M.A. Scarpulla, in: *Photovoltaic Specialists Conference (PVSC)*, 2012 38th IEEE, 2012, pp. 000879-000883.
- [125] H. Lee, W. Lee, J.Y. Kim, M.J. Ko, K. Kim, K. Seo, D.-K. Lee, H. Kim, *Electrochimica Acta*, 87 (2013) 450-456.
- [126] H.-C. Huang, C.-S. Lin, *Journal of The Electrochemical Society*, 160 (2013) H113-H120.
- [127] H.J. Meadows, A. Bhatia, V. Depredurand, J. Guillot, D. Regesch, A. Malyeyev, D. Colombara, M.A. Scarpulla, S. Siebentritt, P.J. Dale, *The Journal of Physical Chemistry C*, 118 (2014) 1451-1460.
- [128] O. Meglali, N. Attaf, A. Bouraiou, J. Bougdira, M.S. Aida, G. Medjahdi, *Journal of Alloys and Compounds*, 587 (2014) 303-307.
- [129] J. Fischer, J.K. Larsen, J. Guillot, Y. Aida, T. Eisenbarth, D. Regesch, V. Depredurand, N. Fevre, S. Siebentritt, P.J. Dale, *Solar Energy Materials and Solar Cells*, 126 (2014) 88-95.

- [130] F. Kang, J. Ao, G. Sun, Q. He, Y. Sun, *Journal of Alloys and Compounds*, 478 (2009) L25-L27.
- [131] F. Caballero-Briones, A. Palacios-Adrós, F. Sanz, *Electrochimica Acta*, 56 (2011) 9556-9567.
- [132] M.H. Valdés, M. Vázquez, *Electrochimica Acta*, 56 (2011) 6866-6873.
- [133] V. Chitra, S. Vasantha, K.R. Murali, in: *Nanoscience, Engineering and Technology (ICONSET), 2011 International Conference on*, 2011, pp. 429-432.
- [134] S.-Y. Hu, W.-H. Lee, S.-C. Chang, Y.-L. Cheng, Y.-L. Wang, *Journal of The Electrochemical Society*, 158 (2011) B557-B561.
- [135] D. Prasher, P. Rajaram, *Electron. Mater. Lett.*, 8 (2012) 515-518.
- [136] M. Valdés, M. Vázquez, *J Solid State Electrochem*, 16 (2012) 3825-3835.
- [137] A. Shanmugavel, K. Srinivasan, K.R. Murali, *Materials Science in Semiconductor Processing*, 16 (2013) 1665-1671.
- [138] A. Shanmugavel, K. Srinivasan and K. R. Murali, *Journal of Materials Science: Materials in Electronics*, 24 (2013) 2398-2403.
- [139] M. Park, S. Ahn, J.H. Yun, J. Gwak, A. Cho, S.K. Ahn, K. Shin, D. Nam, H. Cheong, K. Yoon, *Journal of Alloys and Compounds*, 513 (2012) 68-74.
- [140] S. Theodoropoulou, D. Papadimitriou, N. Rega, S. Siebentritt, M.C. Lux-Steiner, *Thin Solid Films*, 511 (2006) 690-694.
- [141] J.T.-K. Hai Xiao, and William A. Goddard, *Journal of Physical Chemistry Letters*, 2 (2011) 212-217.
- [142] O. Lundberg, M. Bodegård, J. Malmström, L. Stolt, *Progress in Photovoltaics: Research and Applications*, 11 (2003) 77-88.
- [143] O. Lundberg, M. Edoff, L. Stolt, *Thin Solid Films*, 480 (2005) 520-525.
- [144] R.N. Bhattacharya, H. Wiesner, T.A. Berens, R.J. Matson, J. Keane, K. Ramanathan, A. Swartzlander, A. Mason, R.N. Noufi, *Journal of The Electrochemical Society*, 144 (1997) 1376-1379.
- [145] R.C. Valderrama, P.J. Sebastian, J.P. Enriquez, S.A. Gamboa, *Solar Energy Materials & Solar Cells*, 88 (2005) 145-155.
- [146] M.E. Calixto, K.D. Dobson, B.E. McCandless, R.W. Birkmire, *Journal of The Electrochemical Society*, 153 (2006) G521-G528.
- [147] L. Zhang, F.D. Jiang, J.Y. Feng, *Solar Energy Materials and Solar Cells*, 80 (2003) 483-490.
- [148] R. Friedfeld, R.P. Raffaele, J.G. Mantovani, *Solar Energy Materials and Solar Cells*, 58 (1999) 375-385.

- [149] F. Long, W.M. Wang, J.J. Li, Z.G. Zou, *Key Engineering Materials*, 368 (2008) 472-475.
- [150] Y. Oda, T. Minemoto, H. Takakura, *Journal of The Electrochemical Society*, 155 (2008) H292-H295.
- [151] L. Ribeacourt, G. Savidand, D. Lincot, E. Chassaing, *Electrochimica Acta*, 56 (2011) 6628-6637.
- [152] X. Donglin, X. Man, L. Jianzhuang, Z. Xiujian, *J Mater Sci*, 41 (2006) 1875-1878.
- [153] M. Ganchev, J. Kois, M. Kaelin, S. Bereznev, E. Tzvetkova, O. Volobujeva, N. Stratieva, A. Tiwari, *Thin Solid Films*, 511–512 (2006) 325-327.
- [154] J. Liu, F. Liu, Y. Lai, Z. Zhang, J. Li, Y. Liu, *Journal of Electroanalytical Chemistry*, 651 (2011) 191-196.
- [155] M. Dergacheva, K. Urazov, *Electrochimica Acta*, 107 (2013) 120-125.
- [156] F. Liu, C. Huang, Y. Lai, Z. Zhang, J. Li, Y. Liu, *Journal of Alloys and Compounds*, 509 (2011) L129-L133.
- [157] K. Bouabid, A. Ihlal, A. Manar, A. Outzourhit, E.L. Ameziane, *Thin Solid Films*, 488 (2005) 62-67.
- [158] P.P. Prosini, M.L. Addonizio, A. Antonaia, S. Loreti, *Thin Solid Films*, 288 (1996) 90-94.
- [159] M.E. Calixto, P.J. Sebastian, *J Mater Sci*, 33 (1998) 339-345.
- [160] J. Zank, M. Mehlin, H.P. Fritz, *Thin Solid Films*, 286 (1996) 259-263.
- [161] Y.-P. Fu, R.-W. You, K.K. Lew, *Journal of The Electrochemical Society*, 156 (2009) D553-D557.
- [162] S. Dennison, *Journal of Materials Chemistry*, 4 (1994) 41-46.
- [163] N.B. Chaure, A.P. Samantilleke, R.P. Burton, J. Young, I.M. Dharmadasa, *Thin Solid Films*, 472 (2005) 212-216.
- [164] N.B. Chaure, J. Young, A.P. Samantilleke, I.M. Dharmadasa, *Solar Energy Materials and Solar Cells*, 81 (2004) 125-133.
- [165] H.-C. Huang, C.-S. Lin, W.-C. Chang, *Electrochimica Acta*, 75 (2012) 20-27.
- [166] R.P.B. I.M. Dharmadasa, M. Simmonds, *Solar Energy Materials & Solar Cells*, 90 (2006) 2191-2200.
- [167] S. Endo, Y. Nagahori, S. Nomura, *Japanese Journal of Applied Physics*, 85 (1996).
- [168] Y.-L. Zhou, W.-H. Zhou, M. Li, Y.-F. Du, S.-X. Wu, *The Journal of Physical Chemistry C*, 115 (2011) 19632-19639.
- [169] A.M. Fernandez, P.J. Sebastian, M.E. Calixto, S.A. Gamboa, O. Solorza, *Thin Solid Films*, 298 (1997) 92-97.

- [170] H. Lee, C. Ji, Y. Kim, J.-H. Lee, Y.-H. Hwang, I. Jo, H. Kim, *Journal of the Korean Physical Society*, 64 (2014) 1138-1143.
- [171] A.P.S. T. Delsol, N.B. Chaure, P.H. Gardiner, M. Simmonds, I.M. Dharmadasa, *Solar Energy Materials & Solar Cells*, 82 (2004) 587-599.
- [172] S. Theodoropoulou, D. Papadimitriou, S. Doka, T. Schedel-Niedrig, M.C. Lux-Steiner, *Thin Solid Films*, 515 (2007) 5904-5908.
- [173] H. Neumann, *Solar Cells*, 16 (1986) 399-418.
- [174] C. Xue, D. Papadimitriou, Y.S. Raptis, W. Richter, N. Esser, S. Siebentritt, M.C. Lux-Steiner, *Journal of Applied Physics*, 96 (2004) 1963.
- [175] U.P. Singh, S.P. Patra, *International Journal of Photoenergy*, 2010 (2010) 1-19.
- [176] K. Yoshino, H. Yokoyama, K. Maeda, T. Ikari, A. Fukuyama, P.J. Fons, A. Yamada, S. Niki, *Journal of Applied Physics*, 86 (1999) 4354.
- [177] H. Ye, H.S. Park, V.A. Akhavan, B.W. Goodfellow, M.G. Panthani, B.A. Korgel, A.J. Bard, *Journal of Physical Chemistry C*, 115 (2011) 234-240.
- [178] D. Grujicic, B. Pesic, *Electrochimica Acta*, 47 (2002) 2901-2912.
- [179] B. Scharifker, G. Hills, *Electrochimica Acta*, 28 (1983) 879-889.
- [180] G. Hills, A. Kaveh Pour, B. Scharifker, *Electrochimica Acta*, 28 (1983) 891-898.
- [181] N.E. D. Papadimitriou, and C. Xue, *Physica Status Solidi B*, 13 (2005) 2633-2643.
- [182] T. Nakada, H. Ohbo, M. Fukuda, A. Kunioka, *solar Energy Materials & Solar Cells*, 49 (1997) 261-267.
- [183] Y. Chung, C.-W. Lee, *Journal of Electrochemical Science and Technology*, 3 (2012) 95-115.
- [184] S.M. Lee, S. Ikeda, Y. Otsuka, W. Septina, T. Harada, M. Matsumura, *Electrochimica Acta*, 79 (2012) 189-196.
- [185] R.C. Alkire, D.M. Kolb, J. Lipkowski, P.N. Ross, *Advances in Electrochemical Science and Engineering: Photoelectrochemical Materials and Energy Conversion Processes*, WILEY-VCH Verlag GmbH & Co. KGaA, Weinheim, Germany, 2010.
- [186] L.M. Peter, K.G. Upul Wijayantha, *ChemPhysChem*, 15 (2014) 1983-1995.
- [187] X. Chen, W. Shangguan, *Front. Energy*, 7 (2013) 111-118.
- [188] H. Sheng, L. Yu, Y. Jian-Hua, Y. Ying, CdS-Based Semiconductor Photocatalysts for Hydrogen Production from Water Splitting under Solar Light, in: *Nanotechnology for Sustainable Energy*, American Chemical Society, 2013, pp. 219-241.
- [189] T.J. Jacobsson, C. Platzer-Bjorkman, M. Edoff, T. Edvinsson, *International Journal of Hydrogen Energy*, 38 (2013) 15027-15035.

- [190] R. Inguanta, P. Livreri, S. Piazza, C. Sunseri, *Electrochemical and Solid-State Letters*, 13 (2010) K22-K25.
- [191] A. Pareek, R. Purbia, P. Paik, N.Y. Hebalkar, H.G. Kim, P.H. Borse, *International Journal of Hydrogen Energy*, 39 (2014) 4170-4180.
- [192] Y. Choi, M. Beak, K. Yong, *Nanoscale*, (2014).
- [193] I. Repins, M.A. Contreras, B. Egaas, C. DeHart, J. Scharf, C.L. Perkins, B. To, R. Noufi, *Progress in Photovoltaics: Research and Applications*, 16 (2008) 235-239.
- [194] M.A. Contreras, K. Ramanathan, J. AbuShama, F. Hasoon, D.L. Young, B. Egaas, R. Noufi, *Progress in Photovoltaics: Research and Applications*, 13 (2005) 209-216.
- [195] A. Chirilă, P. Reinhard, F. Pianezzi, P. Bloesch, A.R. Uhl, C. Fella, L. Kranz, D. Keller, C. Gretener, H. Hagendorfer, D. Jaeger, R. Erni, S. Nishiwaki, S. Buecheler, A.N. Tiwari, *Nat Mater*, 12 (2013) 1107-1111.
- [196] S.B. Patil, A.K. Singh, *Applied Surface Science*, 256 (2010) 2884-2889.